From Hard-Sphere Functionals to Square-Well Droplets

Dissertation

der Mathematisch-Naturwissenschaftlichen Fakultät

der Eberhard Karls Universität Tübingen

zur Erlangung des Grades eines

Doktors der Naturwissenschaften

(Dr. rer. nat.)

vorgelegt von

Melih Gül

aus Tübingen

Tübingen

2025

Gedruckt mit Genehmigung der Mathematisch-Naturwissenschaftlichen Fakultät der Eberhard Karls Universität Tübingen.

Tag der mündlichen Qualifikation:	11.02.2026
Dekan:	Prof. Dr. Thilo Stehle
1. Berichterstatter/-in:	Prof. Dr. Roland Roth
2. Berichterstatter/-in:	Prof. Dr. Martin Oettel

Abstract

This thesis studies thermodynamic and structural properties of fluids that can be described by rather simple interparticle interaction potentials. For that, we apply powerful and accurate techniques of classical density functional theory which yields a density distribution through minimizing the grand potential functional of the system at equilibrium. However, in order to perform such minimizations we need to provide the so-called Helmholtz excess free energy functional that only for the most simple systems is known. Having an exact expression of the excess functional would be equivalent to a full knowledge of the underlying partition sum of the system. While there are established, state-of-the-art excess functionals for hard-sphere mixtures in the framework of fundamental measure theory, e.g. the Rosenfeld and White-Bear functionals, for interactions going beyond the pure hard-sphere repulsion solely mean-field approximations are commonly employed. The random phase approximation, for instance, already gives a fairly satisfactory description of attractive fluids despite its crudeness regarding correlations and the proper thermodynamic state of the system under consideration.

We further follow the quest of finding or refining possible excess functionals for hard-sphere systems by investigating key ideas based on dimensional crossover. Herewith, a new class of functionals, that we baptize as Lutsko functionals, can be built that contain yet undetermined parameters. A subset of this class, termed explicitly stable functionals, already show some improvements upon thermodynamic quantities even though the choice of parameters is not motivated by any a-priori reason. We furthermore construct two more classes of functionals relying on the structure of the standard White-Bear and White-Bear mark II functional which are considered to be somewhat more precise than the originally proposed Rosenfeld functional. Then, we can ask the question for which values of these parameters certain equilibrium sum rules, which connect two distinct approaches returning the same thermodynamic quantity, are best fulfilled. Not only do we aim to achieve very good consistency with respect to these sum rules, but in addition improve upon accuracy of the corresponding Lutsko functional. Our main results convincingly show that the optimized Lutsko functionals are more accurate in the equation of state and in the direct pair correlation function for the parameters values obtained in our analysis. Especially, our optimized parameters do not belong to the explicitly stable class which, of course, does not in general render these functionals unstable. Indeed, for special, highly confined systems we can show that the optimized Lutsko functionals still exhibit stability while other established functionals fail to work.

Finally, we consider systems of a binary square-well fluid, such as an interface between liquid and vapor phases of the respective components as well as spherically shaped systems of droplets contained in surrounding vapor. Typically, a classical mean-field approach to the excess functional of square-well is used which, however, is merely reliable for high temperatures and low densities. Inspired by the exact low-density excess functional for hard-sphere systems, we formulate a novel functional for a square-well mixture employing weight functions of fundamental measure theory. Of course, the associated excess free energy density is equivalent to that of the mean-field treatment as long as we identify the mixing rules of Berthelot and Lorentz for energies and ranges of the square-well potentials. This new approach to square-well mixtures promises a more effective description of square-well mixtures. We then study interfacial properties of a binary square-well mixture at equilibrium using the novel functional à la fundamental measure theory. Besides investigating the change of surface tension due to the presence of solute particles (2nd component), we also verify Widom's insertion theorem.

We conclude with the work on droplets suspended with larger solute particles. Driven by the recent Corona pandemic, it is interesting to understand why contagiousness can be still significant even after several days. Again, we consider a binary square-well mixture and solve for stable droplets. The underlying model is given by the capillary approximation model where equilibrium is reached if the change in grand potential is minimized for a specific radius of the droplet. We further take humidity into account by fixing the chemical potential of the solvent close to that of liquid-vapor coexistence. This enables us to study such droplets in different environments with the effect of altering the droplet radius. We provide not only predictions of the capillary model for droplets, but also density distributions inside and outside the droplet by performing sophisticated and numerically challenging continuum density functional theory calculations. Our results are consolidated by comparisons we make for thermodynamic quantities obtained from the capillary model.

Zusammenfassung

Diese Arbeit handelt von thermodynamischen und strukturellen Eigenschaften von Fluiden, die durch einfache Wechselwirkungspotentiale zwischen Teilchen beschrieben werden können. Hierzu wenden wir mächtige und numerisch präzise Methoden der Dichtefunktionaltheorie an, welche über eine Minimierung des großkanonischen Funktionals Dichteverteilungen eines Systems im Gleichgewicht liefert. Solch eine Minimierung jedoch verlangt die Kenntnis eines sogenannten Exzess-Funktionals, das nur für einfachste Systeme bekannt ist. Eine volle Kenntnis des Exzess-Funktionals würde folglich der vollen Kenntnis der Zustandssumme des Systems gleichkommen. Während bereits etablierte Exzess-Funktionale für Harte-Kugel-Mischungen im Rahmen der Fundamentalen Maßtheorie existieren, werden für Wechselwirkungen jenseits harter Kugeln oft nur Mean-Field-Näherungen herangezogen. Die Random-Phase-Approximation z.B. gibt bereits eine zufriedenstellende Beschreibung für attraktive Fluide, trotz ihrer Ungenauigkeit bezüglich Korrelationen und der entsprechenden Zustandsgleichung des Systems.

Wir verfolgen die Aufgabe, Exzess-Funktionale für Harte-Kugel-Systeme zu konstruieren oder zu verbessern, unter Ausnutzung von grundlegenden Ideen, die auf Dimensional Crossover zurückgehen. Hiermit kann eine neue Klasse von Exzess-Funktionalen, den Lutsko-Funktionalen, aufgestellt werden, die noch offene Parameter enthalten. Eine Teilmenge dieser Klasse, die sogenannte explizit stabile Klasse, ist imstande, eine Verbesserung der Zustandsgleichung zu erreichen ohne jedoch einen tieferen Grund für die Wahl der Parameter zu geben. Zudem schlagen wir zwei weitere neue Klassen vor, die auf der Form der White-Bear und White-Bear mark II Funktionale basieren, welche als bessere Funktionale für harte Kugeln betrachtet werden als das ursprüngliche Rosenfeld-Funktional. Somit können wir die Frage stellen, für welche Werte der Parameter des Lutsko-Funktionals die Gleichgewichtssummenregeln am besten erfüllt werden. Letztere gelten als ein Kriterium, das jeweilige Funktional auf seine Konsistenz bezüglich einer thermodynamischen Größe zu prüfen. Unsere Ergebnisse zeigen klar, dass die optimierten Lutsko-Funktionale die Zustandsgleichung sowie die Korrelationsfunktion besser wiedergeben. Insbesondere stellt sich heraus, dass die von uns gefundenen, optimierten Parameter nicht in die explizit stabile Klasse gehören, womit das dazugehörige Funktional im Allgemeinen jedoch nicht unbedingt instabil sein muss. Tatsächlich kann für stark räumlich beschränkte Systeme gezeigt werden, dass die Lutsko-Funktionale stabil bleiben während andere etablierte Funktionale hier versagen.

Schließlich betrachten wir binäre Square-Well Fluide, beispielsweise die Grenzfläche zwischen der flüssigen und der gasförmige Phase der jeweiligen Komponenten, sowie sphärische Systeme wie Tröpfchen, die von Dampf umgeben sind. Typischerweise werden Mean-Field Nähereungen zum Square-Well Exzess-Funktional angewandt, das lediglich für hohe Temperaturen und geringe Dichte vertretbar ist. Dem Grenzfall geringer Dichte für das Harte-Kugel Exzess-Funktional anlehnend, schreiben wir ein neues Funktional für eine Square-Well Mischung auf, das Gewichtsfunktionen analog zu jenen aus der fundamentalen Maßtheorie enthält. Natürlich ist die dazugehörige freie Energiedichte äquivalent zu jener aus der Mean-Field-Näherung, solange wir die Energien und Reichweiten der Square-Well Wechselwirkungen über die Mischregeln nach Berthelot und Lorentz festlegen. Mithilfe dieser neuen Herangehensweise können Berechnungen für Square-Well Mischungen effektiver ausgeführt werden. Zwei Anwendungen dieses neuen Funktionals demonstrieren wir an der Grenzfläche flüssig-gasförmig einer binären Mischung, wo die zweite Komponente sehr verdünnt sein soll. Damit werden die Eigenschaften im

Phasengleichgewicht der ersten Komponente, dem Lösungsmittel, nicht erheblich verändert. Hiermit untersuchen wir die Auswirkungen der Präsenz von Lösungsteilchen an der Phasengrenzfläche auf die Oberflächenspannung. Anschließend verifizieren wir auch das Widomsche Einseztungstheorem.

Wir schließen die Diskussion zu Square-Well Systemen mit der Arbeit über Tröpfchen, suspendiert mit großen Lösungsteilchen, ab. Die letzte Pandemie des Corona-Virus hat unter anderem die Frage aufgeworfen, wie es dazu kommen kann, dass selbst nach einigen Tagen die Ansteckbarkeit durch die Luft erhalten bleibt. Durch die Kondensation an oder Aufnahme von Nanopartikeln wie dem Corona-Virus wird der sonst unaufhaltsame Verdampfungsprozess eines Wassertröpfchens aufgehalten, da durch die Reduktion des Sättigungsdampfdruckes des Tröpfchens das mechanische Gleichgewicht für einen untersättigten Dampf erreicht wird. Daneben verwenden wir ein einfaches thermodynamisches Modell, die Kapillaritäts-Approximation, mit deren Hilfe wir Vorhersagen zu stabilen Tröpfchen machen können. Daneben können wir die Luftfeuchtigkeit mit in die Betrachtung einbeziehen, indem wir das chemische Potential der Flüssigkeit nahe des Koexistenzwertes wählen. Dadurch ist erreicht, dass wir Tröpfchen in verschiedenen Umgebungen untersuchen können, die den Tröpfchenradius beeinflussen. Zudem berechnen wir Dichteprofile des Tröpfchensystems, indem wir numerisch schwer auszuführende Kontinuum-DFT-Berechnungen durchführen. Unsere Ergebnisse werden durch Vergleiche mit thermodynamischen Größen des Systems untermauert.

Aime la vérité, mais pardonne à l'erreur.
— François-Marie Arouet, Voltaire

Contents

Chapter 1

Introduction

1.1 Liquid-State Theory

Liquids are ubiquitous in our daily lives, and their importance extends deeply into the natural sciences particularly within soft matter physics, a subfield of condensed matter physics. Soft matter encompasses materials that are easily deformed by thermal or mechanical forces and occupy a regime between conventional solids and liquids. This includes systems such as simple liquids, colloids, polymers, gels, and liquid crystals. A central goal in soft matter physics is to understand how large numbers of atoms or molecules collectively give rise to complex behaviors, governed by microscopic interactions. A defining feature of soft matter is the emergence of mesoscopic structures much larger than atomic scales, yet still much smaller than the full material that exhibit rich dynamical and structural properties. At this intermediate scale, constituents often self-assemble into transient or metastable patterns, while remaining sensitive to thermal fluctuations. Among all soft matter systems, the liquid phase plays a particularly fundamental role, both as a standalone state of matter and as a host or mediator for more complex soft structures.

Virtually, the liquid phase can be visualized as the erratic motion of particles driven by temperature. The notion of temperature hence is given by the average kinetic energy of a particle. These thermal fluctuations go along with attractive forces between adjacent particles, leading to characteristic structures of liquids on the short-ranged scale.

The description of the liquid state of matter faces several challenges when it comes to an accurate and thorough picture of its nature. Its microscopic structure is complex and has been an issue of long and intense research [1, 2, 3, 4]. In the liquid state, atoms or molecules are packed in a disordered way such that no longer ranged arrangements are present [5, 6], see Fig.1.1. This stays in contrast with the other well-known phases of matter, namely the gas phase and the solid phase. Albeit the fact that gases are disordered, too, the separation between the molecules is large and interactions only occur through molecule-molecule collisions. From a theoretical point of view, a gas allows for perturbation theory where the associated perturbation or small parameter is provided by the density of the gas.

Therefore, the easily accessible ideal gas model serves as a reference onto which additional small interaction terms can be added. This procedure goes under the name of virial expansion wherein higher powers of density, with less significant contributions, are included. In the case of a solid, despite its high packing fraction of atoms, it possesses regular crystalline structures. Here, a reference state would be a perfect crystalline lattice which can be excited by thermal motions around the equilibrium positions or by lattice

defects.

Thus, the liquid state of matter, due to its short-ranged ordering, does neither allow for perturbative approaches nor for approaches based on regular structures. The excluded-volume interactions in all liquids enforce the short-ranged arrangements in molecular positions, such as for argon or krypton. On top to the positional ordering, directional

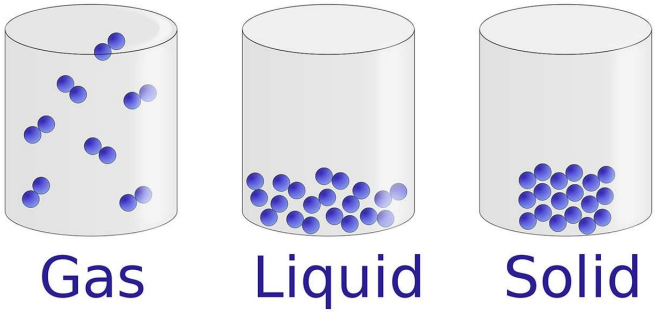

Figure 1.1: The three common phases of matter typically differing in density. The liquid state is particularly difficult to describe.

ordering has to be taken into account for molecules who are themselves not spherically symmetric, such as water molecules. This orientational behavior is among others responsible for cluster formation that are in addition subject to thermal fluctuations due to relatively high temperatures hence being highly dynamic. The inherent properties of liquids can be comprehended by the interplay between entropic and attractive forces. Latter, as the name suggests, keep molecules close to each other along with short-ranged repulsions. Entropic forces, however, are not forces in a mechanical sense but rather arise through the tendency driven by entropy maximization. This natural behavior of fluids to fill the whole accessible volume is closely related to the second law of thermodynamics. Applied to the case of a liquid, both forces are comparable, i.e. the thermal energy is roughly the binding energy of molecules.

In order to describe the state of the liquid several independent thermodynamic quantities have to be known, such as density ρ, temperature T and pressure P. Then, the state of the system is expressed as $f(\rho, T, P) = 0$ where f is the equation of state. Latter is graphically represented by a phase diagram spanned by independent variables, often T and P, which is composed of regions that belong to certain states of the fluid. Figure.1.2 depicts the regions of a monoatomic fluid with temperature T being a function of density ρ. Below the critical point there is a distinction between the vapor and liquid phase which can coexist for temperatures $T_t < T < T_c$. Any horizontal slice ($T = \text{const.}$) in this range would intersect the lines to liquid and vapor respectively, with the corresponding coexistence densities $\rho_v < \rho_l$. However, above the critical point there is only one state called fluid, hence the associated region is termed as supercritical. In contrary, the solid state does not terminate at the critical point so that a continuous path from, for instance, liquid to solid does not exist.

Here, we are only concerned about classical liquids for which we need to quantify when quantum mechanical effects can be neglected. For this, we define the thermal wavelength

$$\Lambda = \sqrt{\frac{2\pi\beta\hbar^2}{m}}, \tag{1.1}$$

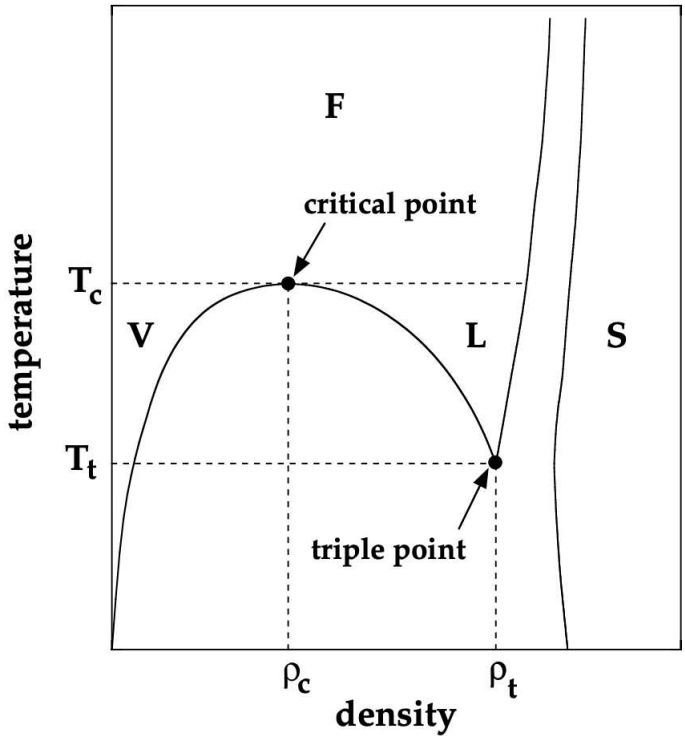

Figure 1.2: A typical phase diagram with boundaries between solid (S), liquid (L), vapor (V) and fluid (F). Picture taken from [7].

where $\beta = 1/k_B T$ is the inverse temperature, $\hbar$ the reduced Planck's constant and m the mass of the particle. The classical limit is reached if $\Lambda \ll d$ where $d \sim \rho^{-1/3}$ represents the nearest-neighbor distance. If we examine the classical limit for several substances then it turns out that except for hydrogen and neon $\Lambda \ll d$ is indeed fulfilled to a good degree. There is an additional constraint if the underlying system is allowed to evolve in time. If τ is a typical time scale of a process in the system, then the classical limit is approached for

$$\tau \gg \frac{h}{k_B T}. \tag{1.2}$$

In general, for liquids at room temperature τ is of the order of 10^{-14}s such that translational motions of particles can be treated often times classically. In total, we can state that quantum mechanical effects become important at low temperatures and small mass.

The characteristic short-ranged ordering of liquids necessitates hard-core repulsions at very short distances, e.g. two molecules whose electron shells create a repulsion. In contrast, attractive forces act smoothly at longer distances with only small influence on the structure of the liquid. This separation between the two competing forces is a common approach to model the liquid state with emphasis on phenomenological data. The widely used model of van der Waals, see Eq.(2.89), is based on this established concept of liquids. The hard-core repulsion is easily given by the model of hard spheres that are subject to an interaction potential $\phi(r)$ of the form

$$\phi_{\text{rep}}(r) = \begin{cases} \infty, & \text{if} \quad r < \sigma \\ 0, & \text{otherwise,} \end{cases} \tag{1.3}$$

where σ is the hard-core diameter. This very simple potential with no physical parameters

and hence energy scale is a common starting point for more sophisticated interaction potentials. Computer simulations play a crucial role in our understanding of hard-sphere fluid, although its application to actual interesting problems is highly restricted. A first attempt to describe a real liquid is to append attractive forces to the hard-core repulsion of Eq.(1.3) by, for instance, introducing the square-well potential

$$\phi_{\text{att}}(r) = \begin{cases} 0, & \text{for} \quad 0 < r < \sigma \\ -\epsilon, & \text{for} \quad \sigma \leq r \leq \lambda\sigma \\ 0, & \text{otherwise} \end{cases} \tag{1.4}$$

in which ϵ is the interaction strength or depth of the square-well potential and λ its range which is often chosen to be 1.5. Adding both potentials Eq.(1.3) and Eq.(1.4) gives overall the interaction potential of a liquid. While the square-well potential of Eq.(1.4) is a very rough estimate of attractive forces between molecules, its efficacy and computational feasibility is indispensable. Its form lead to van der Waals like forces that are proportional to ρ^2 and already provide a simple model for liquid-vapor coexistence. We have applied the square-well potential to several problems presented in Ch.6 and Ch.7 and could show that with such a crude approximation of attractive potentials essential features of liquids and their mixtures can be captured. The hard-core Yukawa potential as a part of more interesting and expressive attractive potentials is also a commonly used model. To mention a last example, the widely employed Lennard-Jones potential accounts for hard-core repulsions and longer ranged attractions by a simple inverse power law r^{-n}, see Eq.(2.102). The corresponding potential is also termed as the 12-6 Lennard-Jones potential with two parameters σ and ϵ. Former again is a hard-core diameter that does not have to coincide with the actual diameter of the molecule. Latter is the depth of the potential-well minimum, see for example Fig.2.9. The physical parameters can be obtained from experimental data, e.g. by observing the critical values of a certain liquid that are directly connected to the physical parameters of the model. In addition, measuring the second virial coefficient B_2 enabled the determination of model parameters of many gases.

One theoretical framework used throughout this thesis is classical density functional theory (cDFT) [8] which we introduce in Ch.3. The history of DFT goes back to Walter Kohn's work on the ground state calculation of the electron gas. The main idea was to circumvent the need of taking into account all degrees of freedom of the electrons in order to obtain the corresponding wave function. Rather, the ground state of an electron gas is uniquely determined by one single electron density depending on three spatial coordinates, which is derived via functional minimization. The classical version later on proved itself to be very successful in describing the structure of inhomogeneous fluids and their thermodynamics on equal footing. Instead of having to know all possible positions and momenta of each particle in the system, the main object of cDFT is the one-body density profile $\rho(\mathbf{r})$ that merely depends on one position vector $\mathbf{r}$ describing the structure of the system at equilibrium. This vast reduction of degrees of freedom is made possible by the unique relationship between $\rho(\mathbf{r})$ and the external potential $V_{\text{ext}}(\mathbf{r})$ the system is subject to, similar to the original idea of quantum DFT. Generically, computations in cDFT are much more efficient than simulations for many-particle systems. However, the prize being paid by cDFT is the fact that the framework relies highly on approximations for interactions that go beyond the ideal gas. Hence, a central task of cDFT is to develop approximations that are robust and reliable. Well-studied cases in cDFT are systems

consisting of hard-spheres that can differ in size and several components are in general allowed [9, 10]. The underlying formalism for hard-sphere mixtures is termed as fundamental measure theory that provides powerful tools to compute hard-sphere equilibrium distributions. Non-trivial interactions such as square-well of Eq.(1.4) or square-shoulder can be added to the hard-sphere repulsion by making use of mean-field theory. The ability of cDFT to account for mixed-fluid systems and even for interactions with directional dependence such as patchy particles [11] consolidates its applicability when it comes to more complex liquids.

1.2 Experimental Techniques

The liquid state can be studied experimentally with respect to its microscopic and macroscopic properties. While microscopic measurements are susceptible to the approximations being used in the specific model of the liquid, macroscopic measurements are much more feasible and accurate. Both type of measurements must be regarded as complementary and aid to further develop models for the liquid state of matter. Typical macroscopic measurements investigate quantities such as pressure or compressibility where former is usually measured as a function of temperature, leading to the corresponding equation of state. Via thermodynamic relations, other thermodynamic quantities can be inferred that characterize the state of the liquid. On the other hand, microscopic measurements

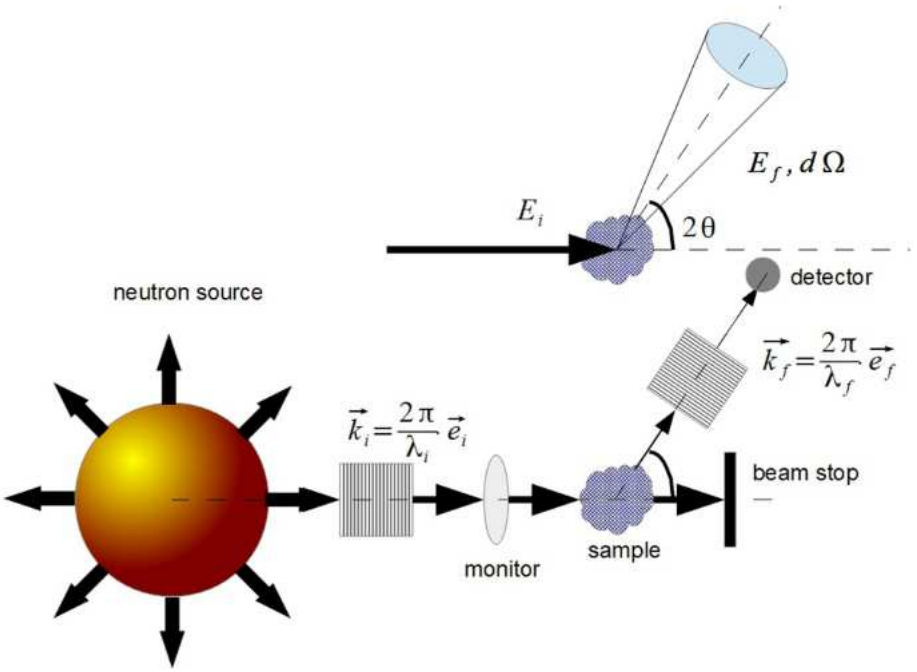

Figure 1.3: Neutron diffraction experiment with a neutron source and a sample that is struck by neutrons with initial momentum $\mathbf{k}_i$ and final momentum $\mathbf{k}_f$ thus a momentum transfer $\mathbf{q} = \mathbf{k}_f - \mathbf{k}_i$. By measuring the differential cross section information about the structure of the sample is obtained. Picture taken from [12].

are conducted, for instance, by performing neutron diffraction or X-ray scattering experiments. The obtained quantity in this case is the cross section that returns the probability of a scattering process for given momentum transfer between the projectile particle and the target. Herewith, the static structure factor $S(q)$ is derived where $q \sim 1/\lambda$ is the wave

number reciprocally depending on the wavelength. Thus, $S(q)$ returns information about the short-ranged order of liquids, i.e. the correlation of a reference or test particle with its neighboring particles that are typically congregated in shells. Equivalently, the radial distribution function $g(r)$ tells how adjacent particles are distributed in the vicinity of the reference particle, see Sec.3.6.

Last but not least, computer simulations are an indispensable corner stone for the study of liquids. Although it cannot be considered as a fully experimental setup, the associated data is considered to be exact where specific, theoretical potentials are employed. Already a few hundred or thousand particles in the system are sufficient to resemble macroscopic systems, i.e. where fluctuations, which would otherwise arise through statistical errors, are negligible. This fact also highlights the feasibility of such computational approaches to study the liquid state. Widely known techniques such as Monte Carlo simulations or Molecular Dynamics serve as quasi-experimental computations to investigate the structure and thermodynamics of a system. Monte Carlo simulations rely on so-called repeated random sampling methods where an otherwise deterministic system is accessed through random computation. Take the simple example of calculating π by randomly distributing points in a unit square that contains a quarter circle in it. On probabilistic grounds, we expect the ratio of points in the quarter circle to the total number of points drawn in the square to be the ratio of the area of the quarter circle to the area of the enclosing square. As the number of drawn points is increased the accuracy of the π estimation is expected to increase, too. Another example is the two dimensional Ising model. It possesses a critical temperature T_c above which the magnetization of the system vanishes with spins that semi-classically either are $+1$ or -1. Initializing the system with a random configuration of spins, the equilibrium state is achieved by applying the Metropolis algorithm that provides the rule based on the Boltzmann distribution.

Molecular dynamics computation, in contrast, is deterministic in the sense that the underlying equations of motion are solved for each time step, e.g. according to the Newtonian laws. The dynamic evolution of a system can be fully captured by such calculations in taking into account all possible forces between atoms or molecules whose trajectories are solved using Newton's equation of motion. Often times it is the case that such calculations are much more intricate, e.g. calculations on a rather long time scale tend to accumulate errors that stem from numerical integration. Additionally, the ergodic hypothesis, essentially connecting time averaged values to thermodynamic quantities, is key in applying these kind of computations in statistical physics.

In summary, computer simulations are an important tool to make predictions on structure, dynamics and thermodynamic properties of complex fluids within the framework of liquid state theory. However, generally speaking the derivation of quantities being of great interest to study the behavior of fluids demands for high computational powers and hence requires a lot of resources, not to mention the algorithms employed that are often very complex and sophisticated. At last, we also want to emphasize that simulations do solely provide data whose underlying mechanism cannot be easily inferred, instead often we can only presume what the associated physical relationships between certain observables are.

1.3 List of Publications

The publications listed below are part of this thesis and ordered chronologically. In each case, I conducted the theoretical and computational work. Co-authors contributed through discussions, supervision and manuscript revisions.

- *Using test particle sum rules to construct accurate functionals in classical density functional theory.*
  Melih Gül, Roland Roth and Robert Evans, Phys. Rev. E, **110**, 064115 (2024), doi.org/10.1103/PhysRevE.110.064115
  Contributions: The project was initiated and supervised by RR. The original draft of the manuscript, editing of the manuscript and data generation was provided by MG. Editing of the manuscript and discussions were done by MG, RR and RE.
  Ch.5 is based on the publication.

- *Effective one-body interactions due to the presence of a liquid–vapor interface.*
  Melih Gül and Roland Roth, Physica A: Statistical Mechanics and its Applications, Volume 674, 130686 (2025), doi.org/10.1016/j.physa.2025.130686
  Contributions: The project was initiated and supervised by RR. The original draft of the manuscript, editing of the manuscript and data generation was provided by MG. Editing of the manuscript and discussions were done by MG and RR.
  Ch.6 is based on the publication.

- *Classical Density Functional Theory for nanoparticle-laden droplets.*
  Melih Gül, Andrew J. Archer, Benjamin D. Goddard and Roland Roth, J. Chem. Phys. 163, 114111 (2025), doi.org/10.1063/5.0292718
  Contributions: The project was initiated and supervised by RR. The original draft of the manuscript, editing of the manuscript and data generation was provided by MG. Editing of the manuscript and discussions were done by MG, AA, BG and RR.
  Ch.7 is based on the publication.

- *Using test particle sum rules to improve approximations in classical density functional theory: White-Bear and White-Bear mark II versions of the Lutsko functional.*
  Melih Gül, Roland Roth and Robert Evans, Phys. Rev. E **113**, 034104 (2026), doi.org/10.1103/3vg8-mbf4
  Contributions: The project was initiated and supervised by RR. The original draft of the manuscript, editing of the manuscript and data generation was provided by MG. Editing of the manuscript and discussions were done by MG, RR and RE.
  Ch.5 is based on the publication.

Chapter 2

Theoretical Background

In this chapter, we want to first outline the foundations and concepts of thermodynamics, statistical physics and classical ensembles. The books of Wolfgang Nolting [13] and Franz Schwabl [14] give a thorough and well-explained introduction on statistical physics making the important connections between the methods developed within the framework of statistical physics or statistical mechanics and the phenomenological findings employed in thermodynamics. Also Reichl's book [15] on statistical physics from a modern point of view gives a concise introduction.

2.1 Essentials: Thermodynamics

Thermodynamics can be understood as the ignorance of a huge number of degrees of freedom of a macroscopic system in equilibrium, such as a gas consisting of a large number of molecules, typically 10^{23} per cm^3. It is basically impossible to gather all the information about particles due to their vast amount and uncertainties. Rather, we are interested in so-called macroscopic quantities that characterize the system, such as its volume, pressure or temperature. Therefore, within thermodynamics we do not care about all the microscopic parts of a macroscopic system but instead use state functions, such as the internal energy U or an equation of state that only contains information about macroscopic quantities putting them into relation. As a consequence, any kind of process where energy and particles are exchanged with the environment can be described solely via few state functions, not including any details about microscopic parts. The ideal gas, for example, consists of N identical, point-like particles not interacting with each other confined in a volume V with pressure p and temperature T. Then, each particle has a momentum $\mathbf{p}$ and a position $\mathbf{r}$ giving in total $6N$ degrees of freedom which would be needed if we wanted to know the exact state of the gas. Given the macroscopic properties of the ideal gas, we can well describe its state through an astonishingly simple equation, called ideal gas law

$$pV = Nk_BT, \tag{2.1}$$

also providing a satisfactory description for low-density fluids. Here, $k_B = 1.3806 \cdot 10^{-23}\mathrm{J/K}$ is the Boltzmann constant. Hence, all the microscopic information of the gas' state, compatible with the macroscopic properties of the gas, is condensed into one equation Eq.(2.1), which is called equation of state of the ideal gas. Johannes Diderik van der Waals proposed an equation of state of a fluid that extends the ideal gas law by including the size of gas molecules and interactions between them depending on the

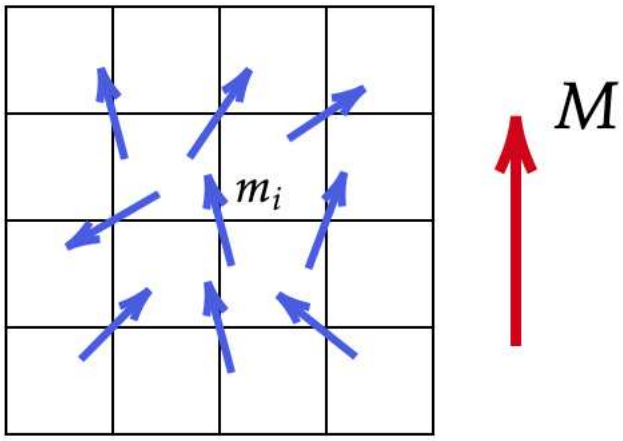

Figure 2.1: A ferromagnet consists of a vast amount of small magnets m_i which interact with their nearest neighbors and are subject to thermal fluctuations. As they tend to align with each other, a magnetization M emerges providing a macroscopic description of the ferromagnet.

specific substance. This simple model for so-called real gases, i.e. gases whose particles undergo interactions, was first to predict liquid-vapor coexistence.

This renders thermodynamics a phenomenological theory, i.e. which only takes into account measurable, macroscopic quantities easily accessed by experiments. As another example, a ferromagnetic material is composed of many small magnets representing the microscopic degrees freedom, see Fig.2.1. Due to interactions between neighboring magnets, these have the tendency to align with each other hence creating a non-vanishing magnetization M of the material. From a phenomenological point of view, instead of considering the small magnets of the material, we only make use of the total magnetization M in order to describe the state of the system. Therefore, the magnetization M is a macroscopic variable representing a key feature of the macroscopic system, the ferromagnetic material.

Thermal fluctuations, however, counteract the collective alignment of the small magnets. If the temperature of the material is too high, thermal fluctuations become so strong that the overall magnetization will vanish. The abrupt change of the macroscopic property of the material is one example of phase transitions. Hence, there is a critical temperature of the ferromagnetic material below which the magnetization is non-zero.

Overall, thermodynamics is a powerful description of macroscopic systems, i.e. having many particles or degrees of freedom, that, in principle, can be applied to any kind of systems being classical or quantum mechanical in thermodynamic equilibrium. Latter is a state where the system does not undergo any further changes in its state variables but remains there. The zeroth law of thermodynamics states that if two systems are separately in thermal equilibrium with a third system, then they are also in thermal equilibrium with each other, defining the notion of temperature.

In thermodynamics, the concept of change of work δW and change of heat δQ is essential in describing the change of internal energy dU which reads

$$dU = \delta Q + \delta W, \tag{2.2}$$

where it is important to know that the differentials of heat, δQ, and work, δW, are not total differentials. This implies that those quantities are no state functions but depend

on how a certain state of a system is reached. Equation(2.2) is referred as the first law of thermodynamics. It was first formulated by Robert Mayer in 1842 stating that the energy content of a body is given by the sum of work and heat put into or taken out of it.

The second law of thermodynamics, first introduced by Clausius and Lord Kelvin in 1850, refers to the entropy S of a system, whose change in a given process can be expressed as

$$dS \geq \frac{\delta Q}{T}, \tag{2.3}$$

where equality holds for reversible processes and inequality in the case of an irreversible change. Therefore, the entropy S is a state function, i.e. via the relation in Eq.(2.3) that its differential dS is a total differential as the temperature T serves as an integrating factor for the heat exchange δQ. There are several, equivalent ways of expressing the second law. One way is the observation that heat never flows from a cold body to a warm one but the other way around. Another is the non-existence of a perpetuum mobile of second kind, i.e. a cyclic machine only cooling a heat reservoir and performing work. For a closed system it holds that the entropy at least stays constant, if the underlying process is reversible, and increases if the process is irreversible. In this regard, the second law of thermodynamics prohibits irreversible processes to be inverted in time, hence the name.

Processes such as the spontaneous separation of milk and coffee, which were mixed with each other before, cannot occur as the mixing process represents an irreversible change of the system. Although from the point of view of the first law this reversed process is not forbidden, the second law would be violated which would correspond to a decrease of entropy. Statistical physics provides an elegant explanation of how irreversibility arises despite the deterministic laws that govern classical systems.

We have already mentioned that state functions or thermodynamics potentials, such as the internal energy U or entropy S, can describe a macroscopic system through associated state variables. Latter are variables that are kept constant throughout a change of the system, minimizing the corresponding state function when equilibrium is reached.

For an isolated system that can neither exchange energy nor particles with its environment, the appropriate state function is the internal energy $U = U(N, V, S)$ being a function of particle number N, volume V and entropy S. From the knowledge of U we can infer other thermodynamic quantities, such as the temperature

$$T = \left(\frac{\partial U}{\partial S}\right)_{N,V}, \tag{2.4}$$

which can also be regarded as a formal definition of it. If the system is only allowed to exchange energy with its environment, then the free energy $F = F(N, V, T) = U - TS$ is minimized when equilibrium is reached.

In Tab.2.1 we list the most important state functions applied in thermodynamics. These yield the same complete thermodynamical information of a system, but depending on the setup of the system, i.e. which quantities we keep fixed, only one state function is extremized when equilibrium is reached. Furthermore, these state functions are connected via a Legendre transformations representing a variable transformation. For instance, the free energy $F(N, V, T)$ can be obtained from the internal energy $U(N, V, S)$ via a Legendre transformation given by

$$F(N, V, T) = U(N, V, S) - S\left(\frac{\partial U}{\partial S}\right)_{N,V}. \tag{2.5}$$

Potential	State variables	Differential
Internal Energy U	N, V, S	$dU = TdS - pdV + \mu dN$
Free Energy F	N, V, T	$dF = -SdT - pdV + \mu dN$
Enthalpy H	N, S, p	$dH = TdS + Vdp + \mu dN$
Gibbs Energy G	N, p, T	$dG = -SdT + Vdp + \mu dN$
Grand Potential Ω	μ, V, T	$d\Omega = -SdT - pdV - Nd\mu$

Table 2.1: Thermodynamic potentials listed together with their state variables and differentials. Given the state variables, the corresponding state function is minimized in equilibrium.

In the same way, other state functions are obtained with the according Legendre transformations.

2.2 Statistical Physics and Phase Space

The kinetic theory of diluted gases initiated a first microscopic view of thermodynamics. James Clerk Maxwell's velocity distribution of particles embedded in a system of given temperature and volume could reproduce the equation of state of the ideal gas which does not include anything about microscopic degrees of freedom. Ludwig Boltzmann wrote down the equally termed transport equation from which he derived the increase of entropy (H-theorem) of an isolated system towards equilibrium. He realized that entropy S of a system characterized by certain macroscopic state variables, e.g. energy U, volume V etc., is given by the following formula

$$S = k_B \log W(U, V, \dots), \tag{2.6}$$

where W counts all states compatible with the macroscopic properties of the system. These compatible states belong to the class of microscopic states, e.g. positions and momenta of all particles of a gas, that the system can occupy.

The quest of statistical physics is to derive macroscopic laws of thermodynamics grounded on phenomenological ideas from microscopic data governed by classical or quantum mechanical equations of motion of many particles. Any attempt to exactly describe the time evolution of all the particles is doomed since this would necessitate the exact knowledge of initial conditions. Besides that, the computational power needed to perform such calculations within a reasonable amount of time would not be feasible. Therefore, the thermodynamic laws being completely ignorant of any microscopic information must be considered as averaged assertions based upon probability theory. Hence, probabilistic concepts like average values, distributions and fluctuations have to be taken into account in order to provide a mathematical description of the microscopic world. Fortunately, as we always speak about macroscopic systems being comprised of many individual particles statistical fluctuations of quantities become negligible despite the huge increase of our microscopic ignorance. This is often termed as thermodynamic limit ($N \to \infty$ and $V \to \infty$ with N/V kept constant) defining asymptotically big systems describable by thermodynamic laws.

The backbone of statistical physics is an assumption that reads as follows

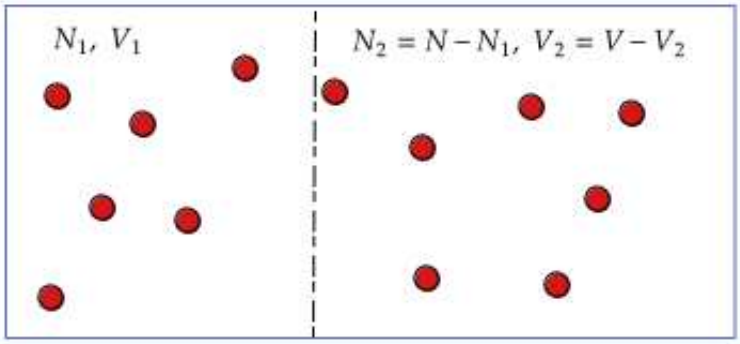

Figure 2.2: N particles (red) of a gas are put into a box of volume V which is fictively divided into two volumina V_1 and V_2. Then, there are in total 2^N possible ways of distributing these particles between V_1 and V_2.

- *For an isolated system of energy U each microstate compatible with this energy is equally probable.*

Also termed as the a-priori probability postulate, this statement is not provable but justified by consequences (a-posteriori) regarding statistical results with empirical data. Of course, such isolated systems do not exist in reality but are rather exposed to some uncertainties. This means that instead of assigning a fixed energy U for the system, it is more sensible to introduce an energy width Δ accounting for fluctuations. It is clear that $|\Delta| \ll U$ will hold for an asymptotically big system so that the energy lies in the interval $E < U < E + \Delta$. Therefore, as we restrict our knowledge to few quantities, here U, Δ, V and N, we encompass all microstates of the system corresponding to the associated macrostate. These microstates, according to the a-priori postulate being equally probable, therefore are located on a hypersurface defined by the aforementioned energy interval.

It remains to clarify what thermodynamic equilibrium and irreversibility mean in statistical physics' perspective. According to macroscopic criteria equilibrium is reached when the macroscopic quantities do not change in time. However, this observation will certainly not hold on a microscopic scale as thermal fluctuations are relevant. As was pointed out before in Sec.2.1, although the deterministic or reversible equations of motion in time prescribe the microscopic motion, irreversibility is a common phenomenon on macroscopic scales. For instance, an isolated system will eventually reach its equilibrium state through irreversible processes maximizing its entropy. The emergence of irreversibility is explained by the enormous amount of degrees of freedom of an asymptotically big system, rendering thermodynamics correct only in the sense of the thermodynamic limes.

In order to illuminate the above arguments, let us consider a simple model of N particles in an isolated system of volume V being partitioned into two volumina V_1 and V_2. Then, a given particle will either be in V_1 or V_2 where the precise location within these volumina shall not be considered. If we assume that N_1 particles are in volume V_1 then there are $N_2 = N - N_1$ particles in volume V_2, i.e. this configuration can be realized in

$$W(N, N_1) = \binom{N}{N_1} = \frac{N!}{N_1!(N - N_1)!} \tag{2.7}$$

ways. Hence, in total we have

$$\sum_{N_1=0}^{N} \binom{N}{N_1} = 2^N \tag{2.8}$$

configurations the system could occupy which we expect as for each particle we can either choose V_1 or V_2 for insertion. The probability p for a particle to be in V_1 is given by $p = V_1/V$ and thus the probability $1-p$ for being in V_2. Apparently, the overall probability $P(N, N_1)$ to find N_1 particles in V_1 reads

$$P(N, N_1) = W(N, N_1) p^{N_1} (1-p)^{N-N_1}, \tag{2.9}$$

where the correct normalization is easily checked. At this point, we want to emphasize that the total number of possible microstates the system can occupy increases exponentially with N. This has the consequence that if N is taken to be a huge number, as is the case of a macroscopic system, then the amount of microstates becomes enormous. More importantly, what will happen is that those configurations are much more probable (almost with certainty) that maximize the probability distribution given in Eq.(2.9). These will be configurations close to the averaged number $\bar{N}_1 = Np$ of particles being in V_1. For such a macroscopic system, we can show that the probability distribution $P(N, N_1)$ is a Gaussian distribution around $\bar{N}_1$

$$P(N, N_1) \approx P(N, \bar{N}_1) \exp\left(-\frac{(N_1 - \bar{N}_1)^2}{2Np(1-p)}\right). \tag{2.10}$$

The important message here is that the probability distribution in Eq.(2.10) has a strongly pronounced peak at $N_1 = \bar{N}_1$, i.e. that the system will, with almost certainty, occupy those configurations that are close to $\bar{N}_1$. In addition, if we examine the relative error, $\Delta N_1/N$, we see that it scales as $1/\sqrt{N}$.

Via Boltzmann's relation of entropy and possible microstates, Eq.(2.6), we see that the most probable configuration maximizes the entropy S verifying the second law of thermodynamics. We can even understand how irreversibility arises and hence how equilibrium is reached: Suppose that we prepare the system such that all the particles are in volume V_1 corresponding to a configuration that can only be achieved by one microstate. Then, after a sufficiently long time the particles will distribute themselves in such a way that the most probable configuration ($N_1 \approx \bar{N}_1$) is assumed. This configuration almost covers all microstates, i.e. the system will remain (with almost certainty) in this configuration. Given this observation, we find that the system has reached a state that can be interpreted as equilibrium. The fact that the probability of the system leaving its equilibrium state is vanishingly small explains also how irreversibility arises. The spontaneous demixing of coffee and milk mentioned in Sec.2.1 would therefore be extraordinarily improbable but in principle allowed. In the same manner, the spontaneous clustering of air molecules in a room into one corner could occur however this would take a time span exceeding the life time of the universe.

Let us consider an isolated system that has N degrees of freedom being assigned to generalized coordinates $\mathbf{q} = (q_1, q_2, \ldots, q_N)$ and momenta $\mathbf{p} = (p_1, p_2, \ldots, p_N)$, e.g. coordinates and momenta of particles of a gas. The associated space spanned by these N-dimensional vectors is called phase space or Γ-space. It is natural to consider the $2N$-dimensional vector $\pi = (\pi_1, \pi_2, \ldots, \pi_{2N}) = (q_1, \ldots, q_N, p_1, \ldots, p_N)$. Then, a microstate is given by a phase space point $\pi(t)$ that defines a phase space trajectory prescribed by the Hamiltonian $H(\mathbf{q}(t), \mathbf{p}(t))$ equations of motion

$$\dot{p}_i = -\frac{\partial H}{\partial q_i}, \quad \dot{q}_i = \frac{\partial H}{\partial p_i}, \quad i = 1, \ldots, N \tag{2.11}$$

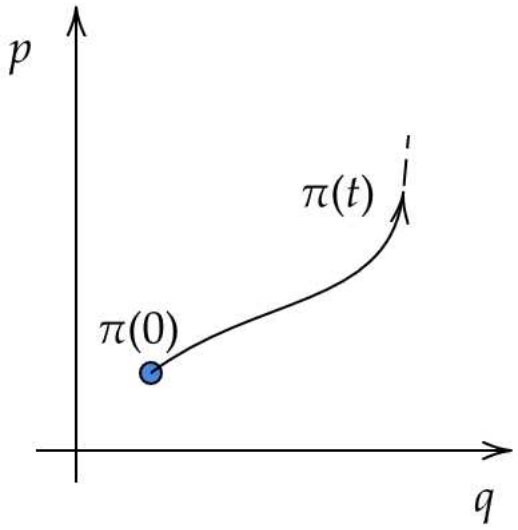

Figure 2.3: A trajectory in a two-dimensional phase space starting at $\pi(0)$ and evolving according to Hamiltonian equations of motion, Eq.(2.11).

with initial conditions $\mathbf{q}(0)$ and $\mathbf{p}(0)$, see Fig.2.3. Since the system is isolated, i.e. no energy exchange with its environment is allowed, the Hamiltonian H must be constant in time being equal to the total energy $H(\mathbf{q}, \mathbf{p}) = U$. As the differential equations in Eq.(2.11) are of first order, the corresponding solutions $\pi(t)$ are unique, i.e. there cannot be intersections between these trajectories. Furthermore, these trajectories are bound to the $2N - 1$-dimensional energy hypersurface.

Any observable quantity A of the system must be therefore a function of generalized coordinates and momenta, $A = A(\mathbf{q}, \mathbf{p}, t)$ including explicit time dependence. We know that the microstate $\pi(t)$ of the system is evolving in time which would entail also a change of the observable A. However, when we refer to an observable A we actually refer to its time averaged value of a time span T

$$\bar{A} = \frac{1}{T} \int_0^T dt\, A(\mathbf{q}(t), \mathbf{p}(t), t), \tag{2.12}$$

which should in principle exist. It is crucial to note that by defining the time average via Eq.(2.12), we neglect any information prior to the averaging process so that it does not depend on the initial conditions the system has been. This assumption used in statistical physics is fundamental which despite being plausible was not yet mathematically proven in a strict manner. It corresponds to the quasi ergodic hypothesis, formulated by P. and T. Ehrenfest in 1911, stating that

- *A phase space trajectory bound on a hypersurface $H(\mathbf{q}, \mathbf{p}) = U$ comes arbitrarily close to any point on the hypersurface.*

No matter how plausible this statement might seem there are counter examples (non-ergodic systems) that can be achieved by special systems. For most systems of interest in statistical physics, this assumption is taken to be true. We want to remind that the quasi-ergodic hypothesis is equivalent to the postulate of equal a-priori probability.

In coarse-graining the phase space into volumina $\Delta^N q \Delta^N p$, we can also ask the question how often the system has visited a region in phase space, see Fig.2.4. Herewith, a

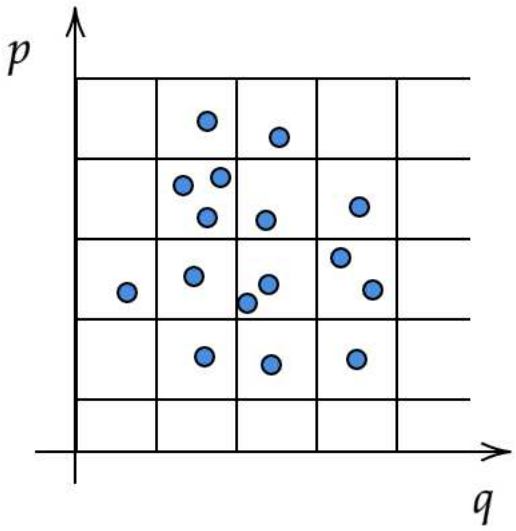

Figure 2.4: If we coarse-grain the phase space we can define a phase space distribution $\varrho(\mathbf{q},\mathbf{p})$. Each member of the ensemble is represented by blue points occupying different microstates.

density distribution $\varrho(\mathbf{q},\mathbf{p})$ can be defined giving the probability

$$\varrho(\mathbf{q},\mathbf{p})\, d^N q d^N p \tag{2.13}$$

that the system is to be found at $\pi = (\mathbf{q},\mathbf{p})$. Then, for a given observable $A(\mathbf{q},\mathbf{p})$ the phase-space average

$$\bar{A} = \int d^N q d^N p\, \varrho(\mathbf{q},\mathbf{p}) A(\mathbf{q},\mathbf{p}) \tag{2.14}$$

is defined assuming that after a sufficiently long time the phase-space probability density $\varrho(\mathbf{q},\mathbf{p})$ exists. This is again very important as the result obtained in Eq.(2.14) should not depend on the initial condition the system once has been. The reasoning behind it is justified by taking into account the quasi-ergodic hypothesis. Gibbs and Boltzmann laid down the foundations of this very important concept of statistical physics which is termed as an ensemble average arising from statistical ensembles. Latter are defined as physically equal copies of the original system compatible with all constraints. These copies can therefore occupy all microstates of the isolated system. At this point, the quasi-ergodic hypothesis enters in asserting that eventually all microstates will be visited by the system therefore the ensemble representing the full time evolution of it. From this argument we can infer the following crucial statement in statistical physics

- *Time Average = Ensemble Average.*

Taking the equivalence of these conceptually different averages for granted, we can circumvent the need of solving the Hamiltonian equations of motion in order to make sense of macroscopic quantities. The point is that an ensemble average is taken at a single time thus time evolution of the system is no longer needed.

The underlying equations of motion, Eq.(2.11), imply that an initial region in phase space at time t_0 can be understood as an incompressible fluid. For that, we consider the total time derivative of the phase space distribution

$$\frac{d\varrho}{dt} = \frac{\partial \varrho}{\partial t} + \sum_{i=1}^{N} \frac{\partial \varrho}{\partial q_i}\dot{q}_i + \sum_{i=1}^{N} \frac{\partial \varrho}{\partial p_i}\dot{p}_i. \tag{2.15}$$

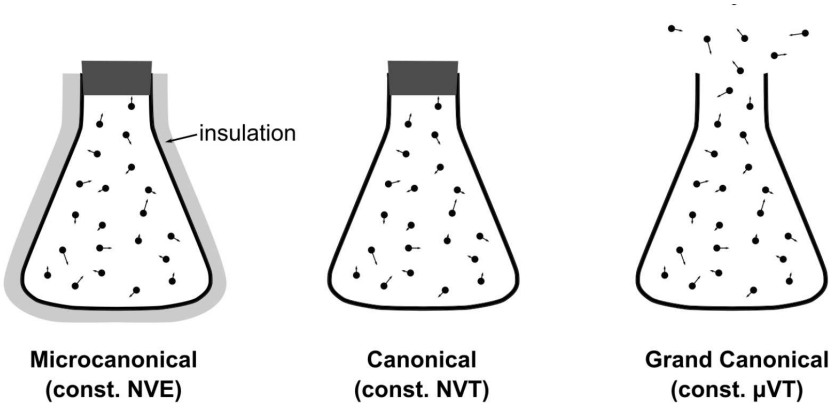

Figure 2.5: The three classical ensembles often used in statistical physics. The microcanonical ensemble refers to an isolated system for which energy E, volume V and particle number N are fixed. The canonical ensemble instead is embedded in an environment of constant temperature T. The grand-canonical ensemble finally is also able to exchange particles with its environment, i.e. the chemical potential μ is fixed.

By further introducing a density current $\mathbf{j} = \varrho\mathbf{v}$ where $\mathbf{v} = (\dot{\mathbf{q}}, \dot{\mathbf{p}})$ is the phase space velocity vector, we can consider the set of ensembles as a fluid moving in phase space. As the phase space is not supposed to have any sinks or sources the phase space current $\mathbf{j}$ has to fulfill the following continuity equation

$$\frac{\partial \varrho}{\partial t} + \nabla \cdot \mathbf{j} = 0, \tag{2.16}$$

where the $2N$-dimensional gradient ∇ is given as $\nabla = (\nabla_{\mathbf{q}}, \nabla_{\mathbf{p}})$. Using Eq.(2.16) in Eq.(2.15), we see that the total derivative of the phase space probability vanishes. Hence, the set of ensembles or the ensemble fluid is moving in phase space as an incompressible fluid. Equation(2.15) is termed as Liouville's theorem stating that phase space volume is conserved if the underlying equations of motion are described by Hamiltonian dynamics, Eq.(2.11).

In the next section, we will introduce the classical ensembles frequently used in statistical physics. After having defined the ensembles, we will derive a very important quantity, called partition sum, which essentially contains all the thermodynamic information of the system under consideration. Put in other words, fully knowing the partition sum of a system enables us to derive thermodynamic quantities connecting the concepts employed in statistical physics with macroscopic quantities employed in thermodynamics.

2.3 Classical Ensembles

In the previous section we motivated an approach to many-body or macroscopic systems by considering a phase space distribution ϱ. Virtually, it represents a set of copies of the original system that evolve according to the same equations of motion. Herewith, we do not need to know all the microscopic information of the system, i.e. its full time evolution.

In the following, we will investigate classical systems embedded into a sufficiently big environment such that energy and particle exchange do not alter its equilibrium state. From this idea we derive an expression for the phase space distribution of the system

allowing us to easily access thermodynamic quantities, such as energy, pressure, chemical potential etc. We will see that the partition sum plays the main role when it comes to an ensemble description of a system, i.e. knowing the exact partition sum is equivalent to a complete knowledge of the thermodynamic state of the system.

2.3.1 Microcanonical Ensemble

For the arguments made in Sec.2.2, we solely considered an isolated system in a fixed volume V with N particles, i.e. a system that can neither exchange energy nor particles with its environment. We elucidated how equilibrium and irreversibility arise from a microscopic point of view. Since the system is isolated (or quasi-isolated), its energy $U = H(\mathbf{q}, \mathbf{p})$ lies within a range $E < U < E + \Delta$ where Δ refers to some width of the energy hypersurface with $\Delta/U \ll 1$, see Fig.2.6. We furthermore know that each microstate located on this energy hypersurface has an equal probability.

Then, the phase space distribution ϱ_{MC} of the microcanonical ensemble must have the following form

$$\varrho_{\mathrm{MC}} = \begin{cases} 1/Z_{\mathrm{MC}}, & U \in (E, E + \Delta) \\ 0, & \text{otherwise}, \end{cases} \tag{2.17}$$

where we introduced the quantity

$$Z_{\mathrm{MC}} = C \int_{E<H(\mathbf{q},\mathbf{p})<E+\Delta} d^N q \, d^N p \tag{2.18}$$

which only gets contributions of the energy shell $(E, E + \Delta)$. C is a constant whose meaning will be clear later on. Equivalently, by letting $\Delta \to 0$ we can use the Dirac delta function

$$Z_{\mathrm{MC}} = C \int d^N q \, d^N p \, \delta(E - H(\mathbf{q}, \mathbf{p})) \tag{2.19}$$

so that Eq.(2.17) can be re-expressed as

$$\varrho_{\mathrm{MC}} = \frac{1}{Z_{\mathrm{MC}}} \delta(E - H(\mathbf{q}, \mathbf{p})) \tag{2.20}$$

providing a more compact expression for the microcanonical phase space distribution. Therefore, we see that Eq.(2.18) or Eq.(2.19) count the number of microstates of the isolated system.

Given this interpretation of the quantity Z_{MC}, we can relate it to the entropy S of the system in a similar fashion for Boltzmann's formula

$$S = k_B \log Z_{\mathrm{MC}}. \tag{2.21}$$

Having this relation for the entropy in the microcanonical ensemble, we can infer other thermodynamic quantities, e.g. pressure p and chemical potential μ

$$\frac{p}{T} = \left(\frac{\partial S}{\partial V} \right)_{E,N}, \quad \frac{\mu}{T} = - \left(\frac{\partial S}{\partial N} \right)_{E,V}. \tag{2.22}$$

Let us consider an ideal gas as a simple example. The Hamiltonian H has the form $H = \mathbf{p}^2/(2m)$ where every particle shall have the same mass m. Recall that for an ideal gas by definition there is no potential. In order to find an expression for its entropy S

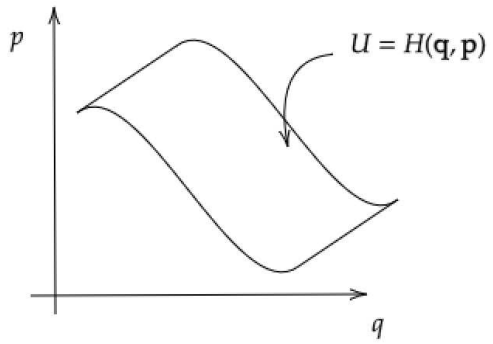

Figure 2.6: The energy hypersurface $U = H(\mathbf{q}, \mathbf{p})$ contains all microstates the isolated system can occupy.

we have to compute the microcanonical sum of states, Eq.(2.19), or the microcanonical partition sum

$$Z_{\mathrm{MC}} = C \int d^N q \, d^N p \, \delta \left(E - \frac{\mathbf{p}^2}{2m} \right). \tag{2.23}$$

As the Hamiltonian of the ideal gas has no $\mathbf{q}$-dependency, the corresponding volume integrals in Eq.(2.23) factorize giving in total V^N. The remaining momentum integral can be evaluated by using spherical coordinates for $3N$ dimensions

$$\begin{aligned} Z_{\mathrm{MC}} &= CV^N \int d^N p \, \delta \left(E - \frac{\mathbf{p}^2}{2m} \right) \\ &= CV^N \int d\Omega_{3N-1} \int_0^\infty dp \, p^{3N-1} \delta(E - \frac{\mathbf{p}^2}{2m}) \\ &= CV^N \Omega_{3N-1} \int_0^\infty dp \, p^{3N-1} \sqrt{\frac{m}{2E}} \delta(\sqrt{2mE} - p) \\ &\approx CV^N \Omega_{3N-1} \, (2mE)^{3N/2}, \end{aligned} \tag{2.24}$$

where we used in the last line that $N \gg 1$. The momentum integral is bound to the hypersurface represented by a $3N$-dimensional sphere of radius $\sqrt{2mE}$. Inserting $\Omega_{3N-1} = 2\pi^{3N/2}/\Gamma(3N/2)$ into Eq.(2.24) we obtain

$$Z_{\mathrm{MC}} = CV^N \frac{2\pi^{3N/2}}{\Gamma(\frac{3N}{2})} (2mE)^{3N/2}. \tag{2.25}$$

If we set $C = 1/N!$, accounting for the indistinguishability of identical particles, the entropy S of an ideal gas becomes

$$S = k_B N \log \left(\frac{V}{N} \left(\frac{4\pi mE}{3N} \right)^{3/2} \right) + \frac{5}{2} k_B N, \tag{2.26}$$

which is also known as the Sackur-Tetrode equation. From Eq.(2.26) we can derive from the formal definition of temperature, Eq.(2.4),

$$\begin{aligned} \frac{1}{T} &= \left(\frac{\partial S}{\partial E} \right)_{N,V} \\ &= \frac{3k_B N}{2E}, \end{aligned} \tag{2.27}$$

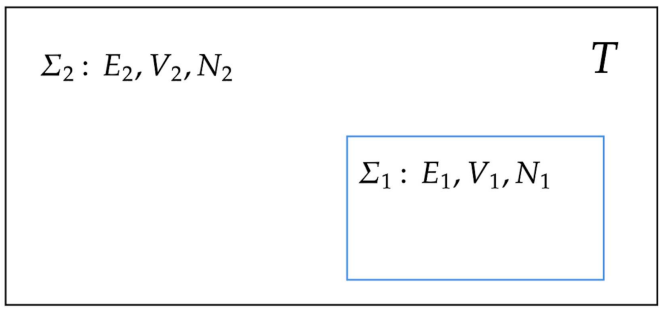

Figure 2.7: The system Σ_1 of interest is put into a heat bath Σ_2 of tempeprature T that is much larger that the former, i.e. Σ_2 is not affected by the thermal contact.

or solving for the energy

$$E = \frac{3}{2} N k_B T \tag{2.28}$$

yielding the correct caloric equation of state of the ideal gas. Similarly, examining the relations Eq.(2.22) we obtain the correct equation of state and chemical potential

$$\begin{aligned} \frac{p}{T} &= \left(\frac{\partial S}{\partial V}\right)_{E,N} \Rightarrow pV = N k_B T \\ \frac{\mu}{T} &= -\left(\frac{\partial S}{\partial N}\right)_{E,V} \Rightarrow \mu = k_B T \log\left(\frac{V}{N}\left(\frac{4\pi m E}{3N}\right)^{3/2}\right). \end{aligned} \tag{2.29}$$

2.3.2 Canonical Ensemble

Often it is the case that an experimental setup is put in an environment of predefined temperature T, also called heat bath. Latter is understood as a macroscopically large system that can take or give an arbitrarily high amount of energy to its subsystem without altering its own thermodynamic state. Imagine the heat bath as a laboratory of temperature T in which an experiment, being in thermal contact, is conducted. Let us denote the heat bath as system Σ_2 having the energy E_2, volume V_2 and particle number N_2 whereas the system of interest is denoted by Σ_1 with energy, volume and particle number correspondingly, see Fig.2.7.

The total system consisting of Σ_1 and Σ_2 has therefore a fixed amount of energy $E_1 + E_2$ being described microcanonically. As we assume Σ_1 to be much smaller than the heat bath Σ_2, the Hamiltonian H of the total system is just a sum of H_1 and H_2 of the subsystem and the heat bath, respectively. In equilibrium, the vast amount of microstates will be assigned to an energy $E_1 \approx \bar{E}_1$ of the subsystem, hence $E_2 \approx E - \bar{E}_1$.

The microcanonical phase space distribution ϱ of the total system reads

$$\varrho = \varrho(\mathbf{q}_1, \mathbf{p}_1, \mathbf{q}_2, \mathbf{p}_2) \tag{2.30}$$

that we can interpret as the probability to find Σ_1 in the microstate $(\mathbf{q}_1, \mathbf{p}_1)$ and Σ_2 in $(\mathbf{q}_2, \mathbf{p}_2)$.

Now, we are merely interested in the marginal phase space distribution $\varrho_1(\mathbf{q}_1, \mathbf{p}_1)$

which we obtain by integrating out the degrees of freedom of the heat bath

$$\begin{aligned}\varrho_1(\mathbf{q}_1,\mathbf{p}_1) &= C\int d^{N_2}q_2\, d^{N_2}p_2\, \varrho(\mathbf{q}_1,\mathbf{p}_1,\mathbf{q}_2,\mathbf{p}_2) \\ &= \frac{C}{Z_N(E,V)}\int d^{N_2}q_2\, d^{N_2}p_2\, \delta\left(E - H_1(\mathbf{q}_1,\mathbf{p}_1) - H_2(\mathbf{q}_2,\mathbf{p}_2)\right) \\ &= \frac{Z_{N_2}(E_2 = E - E_1, V_2)}{Z_N(E,V)},\end{aligned} \tag{2.31}$$

where we defined the partition sums $Z_N(E,V)$ and $Z_{N_2}(E_2,V_2)$ according to Eq.(2.19). Since we have $E_1 \approx \bar{E}_1 \ll E - \bar{E}_1 \approx E$, it is meaningful to consider the following Taylor expansion

$$\begin{aligned}k_B \log Z_{N_2}(E_2 = E - E_1, V_2) = k_B \log Z_{N_2}(E_2 = E, V_2) - \\ E_1 \left(\frac{\partial\, k_B \log Z_{N_2}(E_2,V_2)}{\partial E_2}\right)_{N_2,V_2}(E_2 = E) + \cdots,\end{aligned} \tag{2.32}$$

in which we recognize the entropy $S_2 = k_B \log Z_{N_2}(E_2,V_2)$ of the heat bath so we obtain

$$k_B \log Z_{N_2}(E_2 = E - E_1, V_2) = k_B \log Z_{N_2}(E_2 = E, V_2) - \frac{E_1}{T} + \cdots, \tag{2.33}$$

where we make use of the temperature definition, Eq.(2.4). Introducing the inverse temperature $\beta = 1/(k_B T)$, we can write for the phase space distribution of Σ_1

$$\varrho_1(\mathbf{q}_1,\mathbf{p}_1) \propto \exp\left(-\beta H_1(\mathbf{q}_1,\mathbf{p}_1)\right), \tag{2.34}$$

where we have replaced the energy E_1 with the corresponding Hamiltonian H_1. Herewith, we finally define the canonical phase space distribution (discarding the indices)

$$\varrho(\mathbf{q},\mathbf{p}) = \frac{\exp\left(-\beta H(\mathbf{q},\mathbf{p})\right)}{Z_{\mathrm{C}}} \tag{2.35}$$

with the canonical partition sum

$$Z_{\mathrm{C}} = C\int d^N q\, d^N p\, \exp\left(-\beta H(\mathbf{q},\mathbf{p})\right). \tag{2.36}$$

For any observable $A(\mathbf{q},\mathbf{p})$ we define its canonical ensemble average as

$$\langle A\rangle = \frac{\int d^N q\, d^N p\, A(\mathbf{q},\mathbf{p}) \exp\left(-\beta H(\mathbf{q},\mathbf{p})\right)}{\int d^N q\, d^N p\, \exp\left(-\beta H(\mathbf{q},\mathbf{p})\right)}. \tag{2.37}$$

In the case of $A = H$ we can infer for the average energy U of the system the succinct formula

$$U = -\frac{\partial}{\partial\beta}\log Z_{\mathrm{C}}. \tag{2.38}$$

More specifically, for a Hamiltonian $H(\mathbf{q},\mathbf{p}) = \frac{\mathbf{p}^2}{2m} + V(\mathbf{q})$ with an arbitrary potential $V(\mathbf{q})$, the canonical partition sum, Eq.(2.36), can be expressed concisely as

$$Z_{\mathrm{C}} = \frac{1}{\lambda_T^{3N} N!}\int_V d^N q\, \exp\left(-\beta V(\mathbf{q})\right), \tag{2.39}$$

where we have set $C = 1/(h^{3N}N!)$ and defined the thermal wavelength

$$\lambda_T = \frac{h}{\sqrt{2\pi m k_B T}}. \tag{2.40}$$

Recall that for an ideal gas, as $V(\mathbf{q}) \equiv 0$, the canonical partition sum in Eq.(2.39) reduces to

$$Z_{\mathrm{C}}^{\mathrm{id}} = \frac{1}{\lambda_T^{3N} N!} \tag{2.41}$$

from which the correct equations for an ideal gas can be derived.

For a system possessing discrete energy states E_i, the associated partition sum reads

$$Z_{\mathrm{C}} = \sum_i \exp(-\beta E_i), \tag{2.42}$$

so that the probability p_i for the system being in state E_i is given by

$$p_i = \frac{\exp(-\beta E_i)}{Z}. \tag{2.43}$$

Finally, one can easily examine that the free energy $F(T, V, N)$ is directly given by Z_{C}

$$F(T, V, N) = -k_B T \log Z_{\mathrm{C}} \tag{2.44}$$

fulfilling all necessary requirements, e.g. extensivity. The entropy S, pressure p and chemical potential μ are thus given by

$$\begin{aligned} S &= -\left(\frac{\partial F}{\partial T}\right)_{V,N} \\ p &= -\left(\frac{\partial F}{\partial V}\right)_{T,N} \\ \mu &= -\left(\frac{\partial F}{\partial N}\right)_{T,N}. \end{aligned} \tag{2.45}$$

One important remark is a relationship connecting the fluctuations of the energy U of the system and its heat capacity C_V. Using the definition

$$C_V = \left(\frac{\partial U}{\partial T}\right)_{V,N} \tag{2.46}$$

we can show that

$$C_V = k_B \beta^2 \left(\langle H^2 \rangle - \langle H \rangle^2\right) = k_B \beta^2 \langle (H - \langle H \rangle)^2 \rangle, \tag{2.47}$$

i.e. the heat capacity C_V is connected to the thermal fluctuations of the system and is positive showing thermal stability. Furthermore, it should be noted that in contrast to the microcanonical ensemble the canonical ensemble allows to in principle occupy all energies, however with a sharply peaked, Gaussian shaped maximum at $H \approx \langle H \rangle$. From this fact we make the important conclusion that for asymptotically big systems, $N \gg 1$, although all energies are present, only those close to $\langle H \rangle$ contribute noticeably, i.e. providing an equivalent description to the microcanonical ensemble.

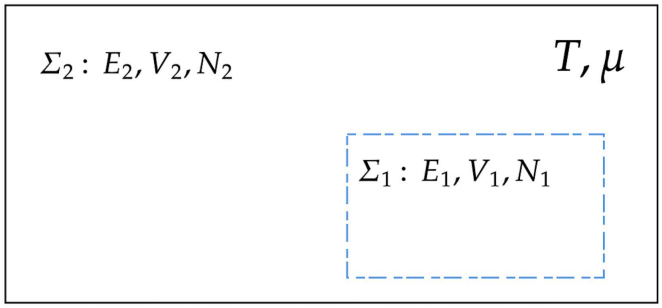

Figure 2.8: The system Σ_1 of interest is put into a heat bath Σ_2 of tempeprature T also being a particle reservoir with chemical potential μ.

2.3.3 Grand-canonical Ensemble

Now we consider an experimental setup where not only do we allow the subsystem Σ_1 to exchange energy with the heat bath Σ_2 of temperature T but also to exchange particles rendering Σ_2 as a particle reservoir with chemical potential μ, see Fig.2.8. This can be illuminated, for instance, with an experiment conducted in a laboratory that can provide the experiment with particles without altering its thermodynamic state, e.g. the atmosphere. Therefore, we again assume that Σ_2 is much bigger than Σ_1, i.e. $N_2 \gg N_1$ and $E_2 \gg E_1$. In equilibrium, the temperature T and chemical potential μ are equal everywhere in the total system and Σ_1 will attain a state with $E_1 \approx \bar{E}_1$ and $N_1 \approx \bar{N}_1$ representing equilibrium.

Once more, we are solely interested in the marginal phase space distribution $\varrho_1(\mathbf{q}_1, \mathbf{p}_1)$ which is obtained the same way as was done in Eq.(2.31). Here, we further have to take into account the change in particle number N_1, i.e. $Z_{N-N_1}(E - E_1, V_2)$. Again, Taylor expanding now around E and N, we find

$$k_B \log Z_{N-N_1}(E_2 = E - E_1, V_2) = k_B \log Z_N(E_2 = E, V_2) - \frac{E_1}{T} + \frac{\mu N_1}{T} + \cdots , \tag{2.48}$$

where we made use of the second equation in Eq.(2.22). Hence, we make the following conclusion for ϱ_1

$$\varrho_1(\mathbf{q}_1, \mathbf{p}_1) \propto \exp\left(-\beta H_1(\mathbf{q}_1, \mathbf{p}_1) + \beta\mu N_1\right). \tag{2.49}$$

In a similar fashion, we define the phase space distribution of the grand-canonical ensemble (again discarding indices)

$$\varrho(\mathbf{q}, \mathbf{p}) = \frac{1}{Z_{\mathrm{GC}}} \exp\left(-\beta\left(H(\mathbf{q}, \mathbf{p}) - \mu N\right)\right) \tag{2.50}$$

with the grand-canonical partition sum running over all particle numbers

$$Z_{\mathrm{GC}} = \sum_{N=0}^{\infty} C_N \int d^N q\, d^N p \, \exp\left(-\beta\left(H_N(\mathbf{q}, \mathbf{p}) - \mu N\right)\right). \tag{2.51}$$

Defining the fugacity $z = \exp(\beta\mu)$, Z_{GC} can be rewritten as

$$Z_{\mathrm{GC}} = \sum_{N=0}^{\infty} C_N z^N Z_{\mathrm{C},N}, \tag{2.52}$$

where we defined the canonical partition sum $Z_{\mathrm{C},N}$, given in Eq.(2.36), now for N particles. Recall that Eq.(2.52) is straightforwardly extended for systems with discrete energy states where each canonical partition sum is replaced with that of Eq.(2.42).

The ensemble average here takes the form

$$\langle A\rangle = \frac{1}{Z_{\mathrm{GC}}}\sum_{N=0}^{\infty} C_N \int d^N q\, d^N p\, A_N(\mathbf{q},\mathbf{p}) \exp\left(-\beta(H_N(\mathbf{q},\mathbf{p}) - \mu N)\right) \tag{2.53}$$

With Eq.(2.52) we can compute once again in the case of an ideal gas using the partition sum Eq.(2.41) of an ideal gas for N particles

$$Z_{\mathrm{GC}}^{\mathrm{id}} = \sum_{N=0}^{\infty} \frac{z^N V^N}{\lambda_T^{3N} N!} = \exp\left(\frac{zV}{\lambda_T^3}\right). \tag{2.54}$$

In the grand-canonical ensemble the grand potential $\Omega(\mu, V, T) = -pV$ is the quantity which becomes minimal at equilibrium and is given by

$$\Omega(\mu, V, T) = -k_B T \log Z_{\mathrm{GC}}. \tag{2.55}$$

Here, we have the important relations to other thermodynamic quantities

$$\begin{aligned} S &= -\left(\frac{\partial\Omega}{\partial T}\right)_{V,N} \\ p &= -\left(\frac{\partial\Omega}{\partial V}\right)_{T,N} \\ N &= -\left(\frac{\partial\Omega}{\partial \mu}\right)_{V,N}. \end{aligned} \tag{2.56}$$

Also in this ensemble, we can relate a thermodynamic quantity, namely the isothermal compressibility κ_T, with the fluctuations of the system. The formal definition of κ_T reads

$$\kappa_T = -\frac{1}{V}\left(\frac{\partial V}{\partial p}\right)_T \geq 0, \tag{2.57}$$

which, due to the mechanical stability criterium, has to be positive. Performing the calculations for the averages values $\langle N^2\rangle$ and $\langle N\rangle^2$, we can find the following relationship

$$\frac{\kappa_T}{\beta V} = \frac{\langle N^2\rangle - \langle N\rangle^2}{\langle N\rangle^2} = \frac{\langle (N - \langle N\rangle)^2\rangle}{\langle N\rangle^2}. \tag{2.58}$$

proving Eq.(2.57) to be positive. With the same reasoning as in the canonical ensemble, basically all ensemble members will have particle numbers that are close to the mean value $\langle N\rangle$ as the width of the distribution is vanishingly small. This observation shows the equivalence of canonical and grand-canonical ensembles in the thermodynamic limit.

2.4 Shannon Entropy and Ensembles

The classical ensembles introduced in the previous sections provide us with the main quantity of statistical physics, namely the partition sum. For its derivation, we had to work in the phase space description of a system being embedded in an environment with certain thermodynamic properties. In the thermodynamic limit these ensembles become equivalent, i.e. macroscopic quantities attain values that correspond to their equilibrium value.

In this section we would like to connect the ideas of information theory introduced by Claude Shannon in his works[16, 17] to an alternative derivation of the classical partition sums. Shannon defined for a discrete random variable X the entropy $H(X)$ in the following way

$$H(X) = -\sum_{x\in\mathcal{X}} p(x)\log p(x), \tag{2.59}$$

where the sum runs over all values in some set $\mathcal{X}$ and p is the probability distribution on that set. $H(X)$ becomes maximal if the probability distribution $p(x)$ is uniform, i.e. we have no information about the system. Shannon provided a quantity named surprisal $\log(1/p(x))$ accounting for events that are very unlikely to occur. The more unlikely the event x, the bigger is the surprisal. In this sense, Eq.(2.59) can be understood as the mean value of surprisal

If we understand the random variables X as the energies of the microstates of a system at temperature T then Eq.(2.59) is formally identical to Gibb's formula for entropy. Therefore, let $p_i = p(\varepsilon_i)$ be the probability that the system is found at energy ε_i, then we declare for the corresponding entropy

$$S = -k_B \sum_i p_i \log p_i \tag{2.60}$$

which is extremal in the case of an isolated system in equilibrium. Imposing further conditions on the entropy in Eq.(2.60) allows us to derive the partition sums we derived from phase space arguments. The formula Eq.(2.60) is well-known in statistical physics, being equivalent to Boltzmann's concise and beautiful entropy formula (see also Eq.(2.6))

$$S = k_B \log W, \tag{2.61}$$

where W is the number of microstates that fit to the given macrostate of the system. Recall that the transition from Eq.(2.60) to Eq.(2.61) is achieved by making use of $p_i = 1/W$, i.e. a uniform probability distribution for the microstates. Therefore, in terms of information theory, the notion of entropy in information theory can be considered to be missing information needed to determine a microstate for given macrostate.

- **Microcanonic Ensemble**

  If the isolated system has reached its equilibrium state the entropy S becomes extremal. According to Eq.(2.60), the associated probability distribution p_i has to maximize the entropy at the same time having the right normalization $\sum_i p_i = 1$

which we take into account by adding a Lagrange multiplier λ_1. This means

$$\begin{aligned} 0 &= -k_B \frac{\partial}{\partial p_i} \left[\sum_j p_j \log p_j + \lambda_1 \left(\sum_j p_j - 1 \right) \right] \\ &= -k_B \sum_j (\log p_j + 1 + \lambda_1) \delta_{ij} \\ &= -k_B (\log p_i + 1 + \lambda_1). \end{aligned} \tag{2.62}$$

Hence, we find

$$p_i = \exp(-1 - \lambda_1) \equiv \frac{1}{Z} > 0, \tag{2.63}$$

that means each probability p_i is equally valued where we introduced a positive constant Z that we can interpret as the partition sum of the system. We conclude that for a uniform probability distribution, i.e. each microstate is equally probable, the entropy is maximized.

- **Canonical Ensemble**

  Let us add one more information about the system: Its average energy value $\bar{\varepsilon} = \sum_i p_i \varepsilon_i$. Then, we again maximize the entropy now with two Lagrange multipliers λ_1 and λ_2

$$\begin{aligned} 0 &= -k_B \frac{\partial}{\partial p_i} \left[\sum_j p_j \log p_j + \lambda_1 \left(\sum_j p_j - 1 \right) + \lambda_2 \left(\sum_j p_j \varepsilon_j - \bar{\varepsilon} \right) \right] \\ &= -k_B \sum_j (\log p_j + 1 + \lambda_1 + \lambda_2 \varepsilon_j) \delta_{ij} \\ &= -k_B (\log p_i + 1 + \lambda_1 + \lambda_2 \varepsilon_i) \end{aligned} \tag{2.64}$$

  from which we obtain

$$p_i = \exp\left(-1 - \lambda_1 - \lambda_2 \varepsilon_i\right). \tag{2.65}$$

  Again, using $1/Z = \exp(-1 - \lambda_1)$ we arrive at

$$Z = \sum_i \exp(-\lambda_2 \varepsilon_i). \tag{2.66}$$

  It remains to fix the Lagrange multiplier λ_2 which we can achieve by looking at the entropy

$$\begin{aligned} S &= -k_B \sum_i p_i \left(-\lambda_2 \varepsilon_i - \log Z\right) \\ &= k_B \left(\lambda_2 \bar{\varepsilon} + \log Z\right). \end{aligned} \tag{2.67}$$

  Via the relation Eq.(2.4) we find

$$\frac{1}{T} = k_B \lambda_2, \quad \Leftrightarrow \quad \lambda_2 = \beta \tag{2.68}$$

  giving in total for the probability distribution

$$p_i = \frac{\exp(-\beta \varepsilon_i)}{Z} \tag{2.69}$$

  which is just the right probability distribution of an energy state ε_i in the canonical ensemble.

- **Grand-canonical Ensemble**

  Finally, we also include the knowledge of an average value $\bar{N}$ of the particle number $\bar{N} = \sum_i p_i N_i$ with corresponding Lagrange multiplier λ_3. We find in the same way as in Eq.(2.64) for the probability distribution

$$p_i = \exp\left(-1 - \lambda_1 - \lambda_2 \varepsilon_i - \lambda_3 N_i\right), \tag{2.70}$$

  where we again have

$$Z = \sum_i \exp\left(-\lambda_2 \varepsilon_i - \lambda_3 N_i\right). \tag{2.71}$$

  Inserting Eq.(2.71) into the entropy we get

$$\begin{aligned} S &= -k_B \sum_i p_i(-\lambda_2 \varepsilon_i - \lambda_3 N_i - \log Z) \\ &= k_B(\lambda_2 \bar{\varepsilon} + \lambda_3 \bar{N} + \log Z) \end{aligned} \tag{2.72}$$

  and it remains again to fix the Lagrange multipliers. λ_2 we fix the same way as was done in the canonical case, $\lambda_2 = \beta$, and λ_3 can be identified via Eq.(2.22) so that $\lambda_3 = -\beta\mu$. Hence, we have found the probability distribution

$$p_i = \frac{\exp(-\beta(\varepsilon_i - \mu N_i))}{Z} \tag{2.73}$$

  correctly describing the grand-canonical ensemble.

We can thus conclude that the new perspective offered by Shannon entropy provides a deeper insight into the concept of entropy itself. It can be interpreted as a measure of the observer's ignorance about the microscopic details of the system under consideration. In other words, the observer does not possess complete knowledge of the system's microscopic states but only of a limited set of accessible quantities, such as average values corresponding to macroscopic observables. By maximizing the entropy subject to these known averages, one can recover the correct probability distributions of the classical ensembles.

2.5 Simple Liquids

The study of real gases is of fundamental interest as daily phenomena such as freezing of water, evaporation and other changes of aggregate states into each other can be understood already quite well with simple models for liquids, hence simple liquids. Phase transitions therefore are only predicted by assuming that interactions of hard-core repulsion and a longer, attractive tail are present allowing the particles to coordinate themselves with each other depending on the temperature of the system. In theory, real gases refer to any kind of liquid models including interactions, i.e. going beyond the ideal gas. Properties such as critical points, condensation and the Joule-Thomson effect can only be comprehended using real gas models. Going further, interactions not possessing any isotropic properties such as patchy particles are studied extensively [18, 19, 20]. Patchy particles are colloidal particles that either have non-spherical shaped surfaces or surfaces decorated with so-called patches that can be docked by charged particles, such as ions. Hence, patchy particles are able to bind with each other in certain orientational

constellations leading to anisotropic surface chemistry. Many material science related fields benefit from the patchy particle model [21, 22, 23]. This chapter shall only include isotropic interactions.

Suppose we have a gas of N identical particles each with three degrees of freedom inside a volume V with a surface F. The particles with diameter σ can mutually interact with each other with a interparticle potential $U(\mathbf{r}_i, \mathbf{r}_j) = U(|\mathbf{r}_i - \mathbf{r}_j|) = U(r_{ij})$ only depending on the distance r_{ij} between particle i and particle j, see Fig.2.9. The Hamiltonian of the system is therefore given by

$$H = \sum_{i=1}^{N} \left(\frac{\mathbf{p}_i^2}{2m} + V_{\text{ext}}(\mathbf{r}_i) \right) + \sum_{i<j} U(r_{ij}), \tag{2.74}$$

where the external potential confines the particles into the accessible volume $\mathcal{V}$

$$V_{\text{ext}}(\mathbf{r}) = \begin{cases} 0, & \text{for} \quad \mathbf{r} \in \mathcal{V} \\ \infty, & \text{otherwise.} \end{cases} \tag{2.75}$$

The accessible volume $\mathcal{V}$ accounts for the finite size of a particle, i.e. the volume that can be reached by the center of a given particle. In the classical ensemble, we already showed that after integrating out the momentum integrals, Eq.(2.39) the partition sum reads (dropping subscript C)

$$Z = \frac{1}{\lambda_T^{3N} N!} \prod_{i<j} \int_{\mathcal{V}} d^N\mathbf{r} \, \exp\left(-\beta U(r_{ij})\right), \tag{2.76}$$

where it is important to note that the external potential restricted the real space integrations to the volume $\mathcal{V}$. Again, if we had $U(r_{ij}) \equiv 0$ we would recover the case of an ideal gas.

Hence, it remains to solve the real space integrals of Eq.(2.76). We want to point out that with the general form of the interaction potential, Fig.2.9, we can grasp the main features of inter-molecular interactions, i.e. a hard-core repulsion and a long-ranged attractive tail enabling the particles to bind with each other. Imagine molecules attracting each other via electrical forces generated by their dipole moments but not able to penetrate each other, thus possessing a hard-sphere like behavior for very short distances.

In order to be able to further continue from Eq.(2.76), we assume that the kinetic thermal energy of the particle is larger than the binding energy, which is to a good degree reliable for fairly dilute gases. Then, $\beta U(r_{ij}) \leq 1$ is an appropriate expansion parameter, so that the product of exponentials of Eq.(2.76) become

$$\prod_{i<j} \exp\left(-\beta U(r_{ij})\right) \approx \prod_{i<j} (1 - \beta U(r_{ij})) \approx 1 - \beta \sum_{i<j} U(r_{ij}) \tag{2.77}$$

so we are left with a sum of the interaction potential. We have to evaluate the integral

$$\int_{\mathcal{V}} d^N\mathbf{r} - \beta \sum_{i<j} \int_{\mathcal{V}} d^N\mathbf{r} \, U(r_{ij}), \tag{2.78}$$

where the first one is easily obtained

$$\int_{\mathcal{V}} d^N\mathbf{r} = \mathcal{V}^N = (V - F\sigma - Nv)^N \tag{2.79}$$

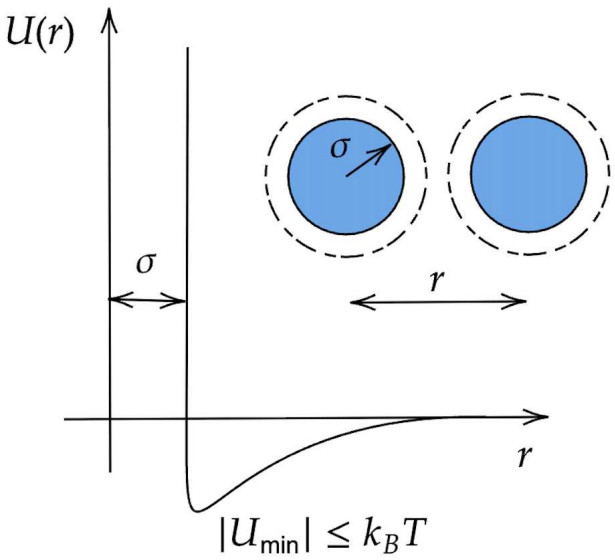

Figure 2.9: Interparticle interaction potential as a function of the distance r. For $r \leq \sigma$ the particles (blue) behave as hard spheres and are attractive when coming close to each other. The dashed circles represent regions where attractions are present. We further assume that the binding energy $|U_{\min}|$ is much smaller than the thermal energy $k_B T$ of the particles allowing for a perturbative calculation.

in which we used that the accessible volume is given by the total volume V minus the volume due to the surface, $F\sigma$, and the volume of a particle, v. Note that the last term of Eq.(2.79) is actually $(N-1)v$, however $N \gg 1$ justifies the overall result.

The second term of Eq.(2.78) is performed for each contribution of particle j so that the remaining expression is still a function of the positions $\mathbf{r}_1, \ldots, \mathbf{r}_{j-1}, \mathbf{r}_{j-1}, \ldots, \mathbf{r}_N$

$$\int_{\mathcal{V}} d\mathbf{r}_j \, U(r_{ij}) = a(\mathbf{r}_1, \ldots, \mathbf{r}_{j-1}, \mathbf{r}_{j-1}, \ldots, \mathbf{r}_N) \tag{2.80}$$

and with the assumption that, for instance, particle j is very close to particle i compared to other particles the integral Eq.(2.80) can further be simplified to

$$\int_{\mathcal{V}} d\mathbf{r}_j \, U(r_{ij}) = 4\pi \int_{\sigma}^{\infty} dr \, r^2 U(r) = -b, \tag{2.81}$$

which is valid since the interparticle potential does not get any contributions from the other particles due to their very large distance where $U(r_{ij}) \approx 0$. This also allowed us to extend the upper bound of the integral in Eq.(2.80) to infinity for convenience. The positive constant b thus measures the strength and range of the interaction potential $U(r)$. Therefore, for a diluted gas we can write

$$\prod_{i \neq j} \int_{\mathcal{V}} d\mathbf{r}_i \int_{\mathcal{V}} d\mathbf{r}_j \, U(r_{ij}) = -b\mathcal{V}^{N-1} \tag{2.82}$$

and in the case of a non-diluted gas we formally have

$$\prod_{i \neq j} \int_{\mathcal{V}} d\mathbf{r}_i \int_{\mathcal{V}} d\mathbf{r}_j \, U(r_{ij}) = \prod_{i \neq j} \int_{\mathcal{V}} d\mathbf{r}_i a(\mathbf{r}_1, \ldots, \mathbf{r}_{j-1}, \mathbf{r}_{j+1}, \ldots, \mathbf{r}_N) = \bar{a}\mathcal{V}^{N-1}, \tag{2.83}$$

where we introduced the averaged quantity

$$\bar{a} = \frac{\prod_{i\neq j}\int_{\mathcal{V}} d\mathbf{r}_i a(\mathbf{r}_1,\ldots,\mathbf{r}_{j-1},\mathbf{r}_{j+1},\ldots,\mathbf{r}_N)}{\mathcal{V}^{N-1}} \tag{2.84}$$

being a function of the particle density $\rho = N/V$, thus we expect $a = -b(\rho)$ with the property that $b(\rho \to 0) = b$ for the constant b defined in Eq.(2.81). Since the second term in Eq.(2.78) is summed over all possible pairs of particles, for which there are $\binom{N}{2} = \frac{N(N-1)}{2} \approx N^2/2$, in total we find

$$\mathcal{V}^N + \frac{N^2}{2}\beta b(\rho)\mathcal{V}^{N-1}, \tag{2.85}$$

so that the partition sum reads

$$Z = \frac{\mathcal{V}^N}{\lambda_T^{3N} N!}\left(1 + \frac{N^2\beta b(\rho)}{2\mathcal{V}}\right). \tag{2.86}$$

From the partition sum in Eq.(2.86) the pressure P can be derived

$$P = \frac{Nk_BT}{\mathcal{V}} - \frac{N^2 b(\rho)}{2\mathcal{V}^2} \tag{2.87}$$

and keeping in mind that $\mathcal{V} = V - Nv$ for a large volume V (its surface can be neglected) and $a = N^2 b(\rho)/2$ we end up with

$$P = \frac{Nk_BT}{V - Nv} - \frac{a}{(V - Nv)^2} \tag{2.88}$$

which almost captures the van-der Waals (vdW) equation of state

$$P = \frac{Nk_BT}{V - Nv} - \frac{a}{V^2}. \tag{2.89}$$

The difference arises through the fact that in the derivation of Eq.(2.87) we assumed a sufficiently diluted gas. As $P \geq 0$, the expression found in Eq.(2.87) is only valid for $\mathcal{V} \geq N\beta b(\rho)/2$ whereas in the vdW equation the volume can be sent to zero. Consequently, the branch for the liquid phase cannot be described with Eq.(2.87) but rather is reliable for $V \gg Nv$ coinciding with the vdW equation of state and resembling the ideal gas.

Still, with the above derivation from a statistical mechanical point of view, we could provide a relatively simple description of a real gas also enlightening the underlying assumptions. We see that in the case of a sufficiently diluted gas the parameters of the vdW equation of state, b and a, find their interpretations from this approach. The constant b takes into account the finite size of the particles, i.e. the actual volume the particles can access is less than the total volume. In addition, the parameter a describes an average value of mutual particle interactions interpretable as a background field acting on the particles. Due to the attractive pair potential, the total pressure P of the system is lowered compared to the ideal gas which can also be pictured through the fact that particles close to the surface of the system are only pulled towards the bulk therefore the overall pressure is lower.

The vdW equation of state was the first to predict liquid-gas phase coexistence.

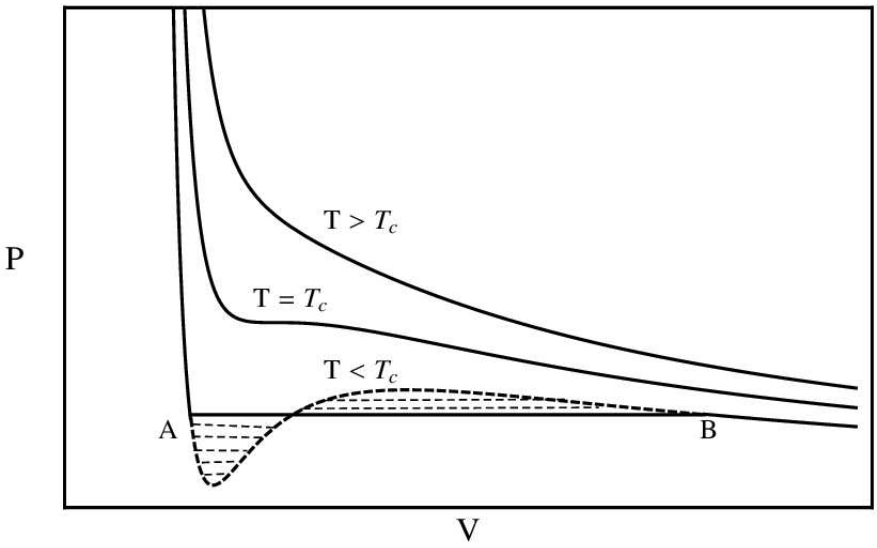

Figure 2.10: van-der Waals isotherms for several values of temperature T. For $T < T_C$ Maxwell's construction has to be considered. Picture taken from [24].

In Fig.2.11 several isotherms of the vdW fluid are displayed. What we can infer from the shape of these isotherms is that there is a temperature $T = T_C$, called the critical temperature, at which the $P - V$ curve exhibits an inflection point, i.e. where

$$\left(\frac{\partial P}{\partial V}\right)_{T_C} = 0, \quad \left(\frac{\partial^2 P}{\partial V^2}\right)_{T_C} = 0 \tag{2.90}$$

is fulfilled. These relations define the critical point of the fluid. Examining the first and second derivative of P with respect to V, we find the critical values

$$P_C = \frac{a}{27b^2}, \quad T_C = \frac{8a}{27bR}, \quad V_C = 3b, \tag{2.91}$$

where b is the particle molar volume and $R = N_A k_B$ the universal gas constant. Going below the critical temperature, $T < T_C$, has the effect of giving rise to regions in the $P-V$ diagram where the slope of the corresponding isotherm becomes positive, see Fig.2.11. This would mean that the compressibility of the fluid, Eq.(2.57), is negative which is unphysical. Put in other words, compressing a system would further lower its pressure rendering it mechanically unstable. The subcritical region of the fluid corresponds to a state where two phases, gas and liquid, coexist, i.e. chemical and mechanical equilibrium is reached. Denoting ρ_v and ρ_l as the coexisting densities of the gas and liquid respectively, the chemical potential $\mu(\rho)$ and total pressure $P(\rho)$ have to satisfy

$$\mu(\rho_v) = \mu(\rho_l), \quad P(\rho_v) = P(\rho_l). \tag{2.92}$$

The chemical equilibrium, first part of Eq.(2.92), ensures that the rate of particles going from vapor to liquid is the same as going from liquid to vapor. The fact that the system of liquid and vapor has everywhere the same pressure is guaranteed by the second part of Eq.(2.92). In order to remedy the problem of the metastable regions at phase coexistence, Maxwell applied the following construction: The area of the dashed regions above and below the isotherm $T < T_C$ in Fig.2.11 have to cancel out each other. Herewith,

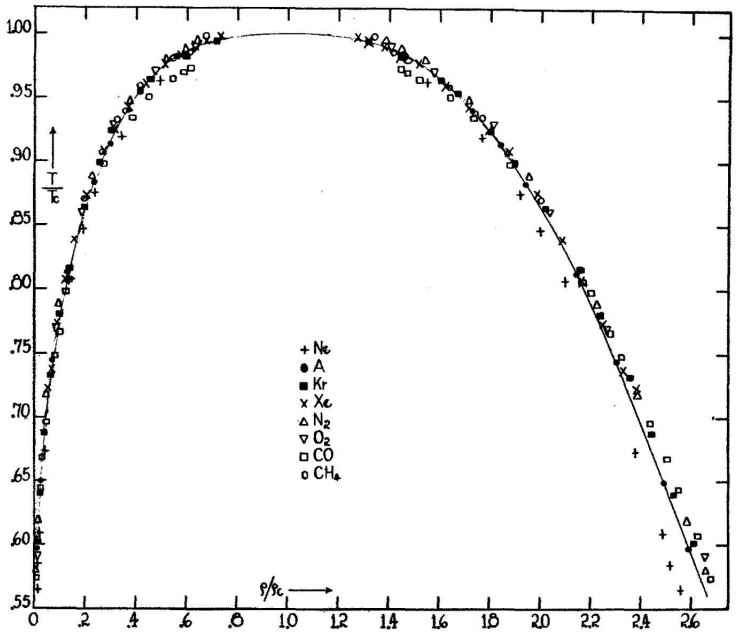

Figure 2.11: Reduced temperature and reduce density diagram for several gases. The agreement with the law of corresponding states is very good. Picture taken from [25].

the subcritical isothermals of the vdW equation of state are modified properly correctly describing chemical and mechanical equilibrium.

As another implication, the vdW equation of state leads to the law of corresponding states, i.e. the equation of state is solely expressed by reduced variables with respect to the critical values. By doing that, we obtain a material-independent description of fluids. Therefore, defining the dimensionless quantities $\pi = P/P_C$, $\nu = V/V_C$ and $t = T/T_C$ the vdW equation Eq.(2.89) can be rewritten as

$$\left(\pi + \frac{3}{\nu^2}\right)(3\nu - 1) = 8t. \tag{2.93}$$

Thus, fluids having the same values (π, ν, t) that obey Eq.(2.93) imply that they are in corresponding states.

Often, a suitable measure for the deviation from the ideal gas is the compressibility factor $Z = PV/(RT)$ which, in the case of an ideal gas, would be unity. For real gases, however, the compressibility factor will be different giving insights to the underlying interactions. In most cases an exact analytical expression for the equation of state is not given and expansions around a reference system, taken to be the ideal gas usually, are performed. The virial expansion is such a procedure wherein terms as powers of the density are added

$$Z = 1 + B_2\rho + B_3\rho^2 + \ldots, \tag{2.94}$$

where the B_i are called virial coefficients. For the vdW fluid, we find

$$B_1 \equiv 1, \quad B_2 = b - \frac{a}{RT}, \quad B_i = b^i,\ i \geq 3. \tag{2.95}$$

In particular, the compressibility factor Z_C at the critical point is $Z_C = 3/8$. For most real gases $Z_C < 3/8$ while the ideal gas has $Z = 1$, i.e. the vdW equation of state is

already a big improvement. The second virial coefficient often times provides a reasonable description for fluids beyond the ideal gas and can be well accessed via experimental setups [26]. Hence, finding the first virial coefficients already enable us to study the most important features of such systems.

The virial coefficients can be defined in statistical mechanics providing a systematic approach to their calculation. Introducing the Mayer-function

$$f(r) = \exp(-\beta U(r)) - 1 \tag{2.96}$$

the virial coefficients describing the interparticle interactions according to $U(r)$ read

$$\begin{aligned} B_2(T) &= -\frac{1}{2V}\int\int d\mathbf{r}_i d\mathbf{r}_j\, f(r_{ij}) \\ B_3(T) &= -\frac{1}{3V}\int\int\int d\mathbf{r}_i d\mathbf{r}_j d\mathbf{r}_k f(r_{ij}) f(r_{jk}) f(r_{ki}) \\ &\vdots \\ B_n(T) &= -\frac{1}{nV}\int d\mathbf{r}_{i_1}\cdots\int d\mathbf{r}_{i_n}\prod_{i,j} f(r_{ij}), \end{aligned} \tag{2.97}$$

where in the last line all pairs (i, j) have to be taken into account. While the second virial coefficient B_2 contains two-particle interactions, B_3 has three-particle interactions etc. Diagrammatic descriptions of these multidimensional integrals turn out to be efficient in comprehending the various contributions of a given virial coefficient [7, 27]. Higher order virial coefficients can only be obtained numerically [28].

2.5.1 Hard Spheres

The hard-sphere system is insofar unique as it is essentially a geometrical problem, i.e. rigid bodies that cannot penetrate each other. This means for the corresponding Mayer function

$$f(r) = \begin{cases} -1, & \text{if} \quad r \leq \sigma \\ 0, & \text{otherwise.} \end{cases} \tag{2.98}$$

implying that the virial coefficients are temperature independent [7, 29]. The first three virial coefficients were obtained analytically whereas the higher order ones were computed numerically [30, 31, 32, 33].

The equation of state for hard spheres in three dimensions hence is given by

$$\begin{aligned} Z = 1 + 4\eta + 10\eta^2 + 18.365\eta^3 + 28.225\eta^4 + \\ 39.74\eta^5 + 53.5\eta^6 + 70.8\eta^7 + \ldots \end{aligned} \tag{2.99}$$

with the packing fraction $\eta = \frac{\pi}{6}\rho\sigma^3$. It was the remarkable insight of Carnahan and Starling to realize that the virial coefficients B_n for hard spheres can be well approximated by $B_n = n^2 + n - 2$, $n \geq 2$ [35]. For instance, the first virial coefficients would be $4, 10, 18, 28, 40$ and so forth coming really close to the exact values of Eq.(2.99). In particular, given these virial coefficients the sum can be expressed in a closed form using identities for the geometrical series

$$Z = 1 + \sum_{n=2}^{\infty}(n^2 + n - 2)\eta^{n-1} = \frac{1 + \eta + \eta^2 - \eta^3}{(1-\eta)^3} \tag{2.100}$$

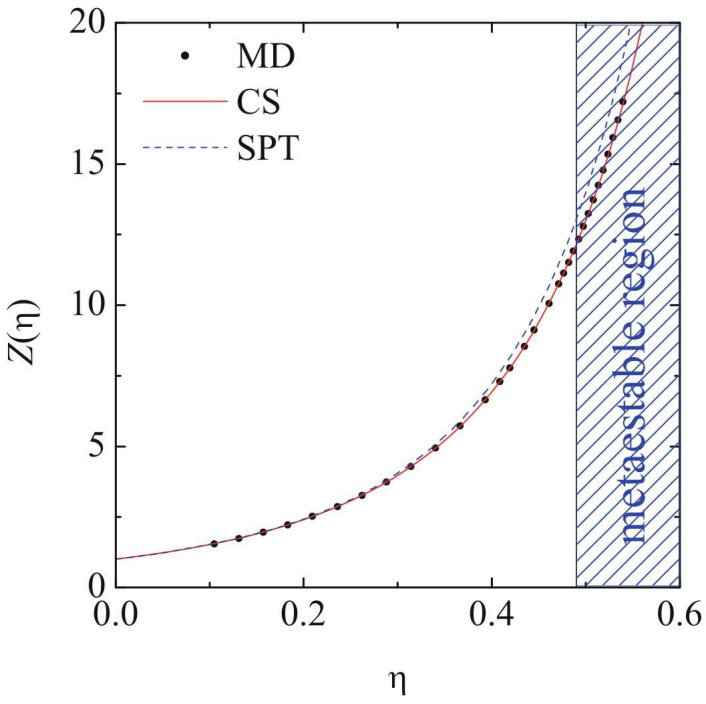

Figure 2.12: Compressibility factor $Z = \beta P/\rho$ obtained from Molecular Dynamics (MD) [34], scaled-particle theory (SPT) Eq.(3.57) and the Carnahan-Starling equation of state Eq.(2.101). Picture taken from [27].

yielding the very accurate Carnahan-Starling equation of state. It is in very good agreement with computer simulations for fluid densities with highest deviations being around 1% for very high densities. In fact, it performs better than the Percus-Yevick equation of state Eq.(3.57) which overestimates the pressure for higher densities, see Fig.2.12. It corresponds to the scaled-particle relation Eq.(3.94) for the one-component case $m = 1$ where each scaled-particle variable is expressed in terms of the packing fraction η. The equation of state in Eq.(2.101) leads to the excess free energy density already mentioned in Eq.(3.69) through the relation [7]

$$\frac{\beta F_{\text{ex}}}{N} = \int_0^\eta \frac{d\eta'}{\eta'} \left(Z(\eta') - 1\right), \tag{2.101}$$

meaning that only off-ideal terms ($Z \neq 1$) contribute in Eq.(2.101).

2.5.2 Square Well

One simple model for interaction potentials mentioned above for real gases is the square-well (SW) interaction. The underlying parameters of the attractive potential $U_{\text{sw}}(r)$ are the SW range λ and energy ε. The SW model can be understood as a rough simplification of more sophisticated interaction potentials, e.g. the Lennard-Jones interaction

$$U_{\text{LJ}}(r) = 4\varepsilon \left(\left(\frac{\sigma}{r}\right)^{12} - \left(\frac{\sigma}{r}\right)^{6} \right) \tag{2.102}$$

which is often employed to model interactions between molecules or between atoms, i.e. forces of neutrally charged particles. The shape of the Lennard-Jones potential is well

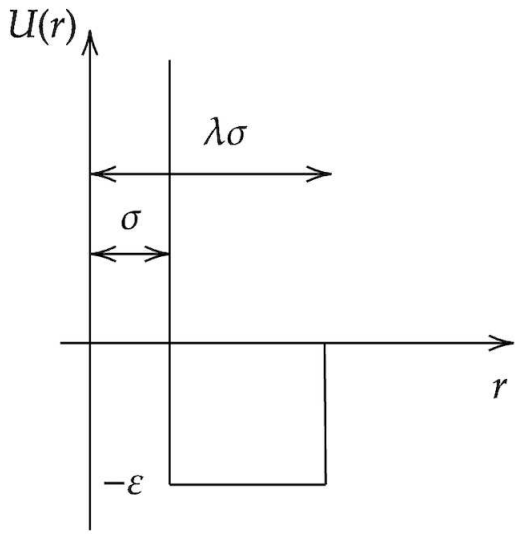

Figure 2.13: Interaction potential $U(r)$ with hard-core repulsion for $r \leq \sigma$ and attractive, square-well region for $\sigma < r < \lambda\sigma$ with range λ and energy ε.

resembled by Fig.2.9, hence a repulsion for very short distances and attractions in the immediate neighborhood of the reference particle.

Aligning to the assumptions being made above for a real gas, i.e. sufficiently diluted gas at high temperatures, we can derive an equation of state for the SW fluid merely taking into account the second virial coefficient B_2. The total interaction potential $U(r)$ is decomposed into a hard-sphere potential $U_{\mathrm{HS}}(r)$ and a SW potential $U_{\mathrm{SW}}(r)$

$$U(r) = U_{\mathrm{HS}}(r) + U_{\mathrm{SW}}(r), \tag{2.103}$$

where U_{HS} is infinite for $r \leq \sigma$ and zero otherwise and $U_{\mathrm{SW}}(r) = -\varepsilon\,\Theta(\lambda\sigma - r)$.

Here, it is important to note that we extended the SW potential into the core ($r \leq \sigma$) in order to remedy correlation effects in a numerical analysis. Due to our assumptions, we are only concerned with the second virial coefficient, Eq.(2.97), of the SW interaction, i.e. only including two-particle interactions with $\beta\varepsilon \ll 1$

$$\begin{aligned} B_2 &= -\frac{1}{2V}\int\int d\mathbf{r}\, d\mathbf{r}'\, f(|\mathbf{r}-\mathbf{r}'|) \\ &= -\frac{1}{2V}\left(\int d\mathbf{r}'\right)\int d\mathbf{r}\ (\exp(-\beta U(r)) - 1) \\ &\approx -\frac{1}{2}4\pi\left(-\int_0^{\sigma} dr\, r^2 + \beta\varepsilon\int_0^{\lambda\sigma} dr\, r^2\right) \\ &= \frac{2\pi\sigma^3}{3} - \frac{2\pi\sigma^3}{3}\lambda^3\beta\varepsilon, \end{aligned} \tag{2.104}$$

where from the first to the second line we used $\mathbf{r}' = 0$, split into the hard-core and attractive contributions in the third line assuming $\beta\varepsilon \ll 1$ and finally performed the integrations to give the fourth line. Hence, we can read off the virial coefficient of the SW interaction

$$B_{2,\mathrm{SW}} = -\frac{2\pi\sigma^3}{3}\lambda^3\beta\varepsilon \tag{2.105}$$

for low-densities and high temperatures, leading to the SW pressure

$$\beta P_{\mathrm{SW}} = B_{2,\mathrm{SW}}\rho^2. \tag{2.106}$$

The total pressure of the system is then a sum of hard spheres, βP_{HS}, and SW, Eq.(2.106),

$$P = P_{\mathrm{HS}} + P_{\mathrm{SW}}, \tag{2.107}$$

which we can rewrite using the reduced pressure $\tilde{P} \equiv \beta P v$ with the particle volume v and the packing fraction η

$$\tilde{P} = \eta\frac{1+\eta+\eta^2-\eta^3}{(1-\eta)^3} - 4\beta\varepsilon\lambda^3\eta^2, \tag{2.108}$$

where we inserted the CS equation of state, Eq.(2.101). The chemical potential μ is given by

$$\beta\mu = \log(\eta) + \eta\frac{8-9\eta+3\eta^2}{(1-\eta)^3} - 8\beta\varepsilon\lambda^3\eta + \text{const.} \tag{2.109}$$

which can be found via thermodynamic relations. We see that Eq.(2.108) describes a vdW-like interaction, i.e. where attractive forces are treated as a mean field. Accordingly, due to the attractive part of the potential we expect liquid-vapor phase separation. The critical point, defined in Eq.(2.90), of the SW fluid is obtained by solving the two equations

$$\left(\frac{\partial\tilde{P}}{\partial\eta}\right)_{T_C} = 0, \quad \left(\frac{\partial^2\tilde{P}}{\partial\eta^2}\right)_{T_C} = 0 \tag{2.110}$$

which yield the critical packing fraction $\eta_C = 0.1287$ and the critical temperature $k_B T_C = 0.375 \cdot \varepsilon\lambda^3$ which depends on the specific choice being made on the SW parameters.

Furthermore, solving for phase coexistence, Eq.(2.92), defines the so-called binodal of the SW fluid separating the stable region from the metastable which is enclosed by the binodal and spinodal, see Fig.2.14. Latter represents points of the phase diagram where the first derivative of the pressure with respect to density, first part of Eq.(2.90), vanishes. Thus, a phase point inside the spinodal is unstable.

If we choose $\lambda = 1.5$, then the critical temperature is $k_B T_C/\varepsilon \approx 1.266$ and for a temperature $T/T_C = 0.658$, which refers to $\beta\varepsilon = 1.2$, we for example have the coexisting packing fractions of vapor η_v and liquid η_l

$$\eta_v = 0.00586050, \quad \eta_l = 0.38022500. \tag{2.111}$$

approximating relatively well the coexisting densities of water and its vapor. In general, for a specific temperature $T < T_C$ below the critical temperature the associated horizontal line in the phase diagram of Fig.2.14 intersects with the binodal at two points referring to the low and high density, i.e. that of vapor and liquid, respectively. As the temperature T approaches its critical value T_C, the coexisting densities or packing fractions converge to each other, as can be seen at the top of the binodal Fig.2.14.

So far, we have seen that the SW fluid already exhibits phase coexistence of liquid and vapor despite its simplicity. We derived its equation of state, Eq.(2.106), assuming a diluted gas where only two-particle interactions are relevant and high temperatures, such that $\beta\varepsilon \ll 1$. Of course, for certain parameter regions, e.g. low temperatures, these assumptions are not reliable anymore and more accurate equation of states have to be

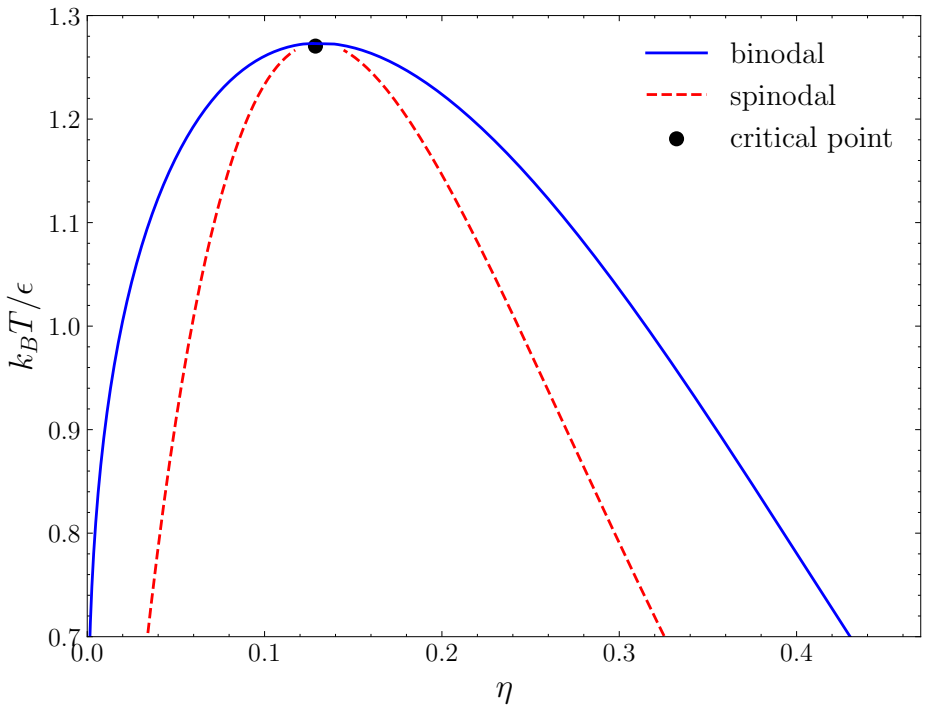

Figure 2.14: Phase diagram of the SW fluid with $\lambda = 1.5$ showing the binodal and the spinodal. By reaching the critical point, the coexisting liquid and vapor densities coincide.

taken into account. In particular, for one-dimensional systems of next-neighbor interactions exact equation of states, especially for SW, could be found [27] which, in principle, could be extended to three dimensions. Finally, other thermodynamic properties of the SW fluid can be obtained within classical density functional theory, Ch.3, e.g. the surface tension of a liquid-vapor interface.

Chapter 3

Classical Density Functional Theory

Density functional theory (DFT) was conceived in the attempt to overcome intricate and time consuming tasks of solving the Schrödinger equation for a system consisting of many electrons at $T = 0$. Instead, DFT proposes a functional containing solely a one-body density distribution that encapsulates all the information of the system. Walter Kohn could find using a variational principle the equilibrium density distribution of an electron gas in its ground state [36, 37] for which he received the Nobel prize in chemistry in 1998. It was also shown that the functional is unique in the electron density, i.e. independent of any external potential. Mermin further extended this idea of describing electronic systems for non-zero temperatures such as electron liquids [38]. Classical density functional theory (cDFT) arose in the 1970s when a corresponding functional was applied to classical fluids [39] and liquid-vapor interface [8].

The uniqueness of the functional with respect to the local density distribution or density profile implies that latter is sufficient to fully describe the thermodynamic system, i.e. equivalent to an exact knowledge of the partition sum.

3.1 Grand-canonincal Ensemble Revisited

Before we go into the details of cDFT, it is first necessary to lay out the basic framework which is the grand-canonical or μVT ensemble. Suppose we have a one-component system (generalization to mixtures is straightforward) of N particles with equal mass m. The generic Hamiltonian reads

$$H_N = T + U + V, \tag{3.1}$$

where $T = \sum_i \mathbf{p}_i^2/(2m)$ is the kinetic, $U = U(\mathbf{r}_1, \ldots, \mathbf{r}_N)$ the interparticle interaction energy and $V = \sum_i V_{\text{ext}}(\mathbf{r}_i)$ the external potential of the system. We know from Sec.2.3.3 that the grand-canonical partition sum is given by

$$Z_{\text{GC}} = \text{Tr}\left(\exp(-\beta(H_N - \mu N))\right), \tag{3.2}$$

where we introduced the classical trace

$$\text{Tr} \equiv \sum_{N=0}^{\infty} \frac{1}{h^{3N} N!} \int dq_1\, dp_1 \cdots \int dq_N dp_N \tag{3.3}$$

as a short-hand notation. In principle, knowing Z_{GC} exactly would render the problem of solving for a many-body system as completed. However, for most cases an exact

calculation of the partition sum is out of reach, especially when external potentials V_{ext} are present. This motivates the application of cDFT in using approximative approaches to better describe systems with complicated interactions.

To recapitulate, denoting the grand-canonical equilibrium distribution by f_0 we define it by

$$f_0 \equiv \frac{1}{Z_{\text{GC}}} \exp(-\beta(H_N - \mu N)) \tag{3.4}$$

which fulfills the normalization $\text{Tr} f_0 = 1$. Ensemble averages of operators $\mathcal{O}$ can be obtained by

$$\langle \mathcal{O} \rangle = \text{Tr} f_0 \mathcal{O}. \tag{3.5}$$

The main object within cDFT is the one-body density operator

$$\hat{\rho}(\mathbf{r}) = \sum_{i=1}^{N} \delta(\mathbf{r} - \mathbf{r}_i) \tag{3.6}$$

whose ensemble average

$$\rho_0(\mathbf{r}) = \langle \hat{\rho}(\mathbf{r}) \rangle \tag{3.7}$$

is giving rise to the equilibrium density profile $\rho_0(\mathbf{r})$. In the next sections we will promote the grand potential Ω to a functional $\Omega[f]$ of the phase space distribution and will prove that instead we can consider $\Omega[\rho]$ providing a much more simple description of liquids. This step is crucial in that we drastically reduce the dimensionality of the problem, $6N$ degrees of freedom of phase space, to just three of real space.

Similar to the definition of the one-body density operator, Eq.(3.6), we can define the n-body density operator

$$\hat{\rho}^{(n)}(\mathbf{r}_1, \ldots, \mathbf{r}_n) = \sum_{i_1=1}^{N} \sum_{i_1<i_2}^{N} \cdots \sum_{i_1<i_2<\cdots<i_n}^{N} \delta(\mathbf{r}_1 - \mathbf{r}_{i_1}) \delta(\mathbf{r}_2 - \mathbf{r}_{i_2}) \ldots \delta(\mathbf{r}_n - \mathbf{r}_{i_n}) \tag{3.8}$$

keeping track of n particles located at positions $(\mathbf{r}_1, \ldots, \mathbf{r}_n)$ and also providing information about correlations between these particles. The corresponding n-body distribution function $\rho^{(n)}(\mathbf{r}_1, \ldots, \mathbf{r}_n)$ is obtained then the we integrate over the remaining $N - n$ degrees of freedom, i.e. calculating the marginal distribution of $n < N$ particles

$$\begin{aligned} \rho^{(n)}(\mathbf{r}_1, \ldots, \mathbf{r}_n) &= \text{Tr}(f_0 \hat{\rho}^n(\mathbf{r}_1, \ldots, \mathbf{r}_n)) \\ &= \sum_{N=n}^{\infty} \frac{1}{h^{3N}(N-n)!} \int d\mathbf{r}^{N-n} \int d\mathbf{p}^N \, f_0(\mathbf{r}^N, \mathbf{p}^N), \end{aligned} \tag{3.9}$$

where we have to correctly normalize with respect to the particle number n. As an example, the n-body distribution function $\rho_{\text{id}}^{(n)}(\mathbf{r}_1, \ldots, \mathbf{r}_n)$ of the ideal gas, where $H_N = T$ and $U = V = 0$, is given by

$$\begin{aligned} \rho_{\text{id}}^{(n)}(\mathbf{r}_1, \ldots, \mathbf{r}_n) &= \frac{1}{Z_{\text{GC}}} \sum_{N=n}^{\infty} \frac{1}{h^{3N}(N-n)!} \int d\mathbf{r}^{N-n} \int d\mathbf{p}^N \, \exp\left(-\beta \frac{\mathbf{p}^2}{2m} + \beta\mu N\right) \\ &= \frac{1}{Z_{\text{GC}}} \sum_{N=n}^{\infty} \frac{z^N}{\lambda_T^{3N}(N-n)!} V^{N-n} \\ &= \frac{1}{Z_{\text{GC}}} \frac{z^n}{\lambda_T^{3n}} \sum_{N=0}^{\infty} \frac{z^N V^N}{N!} \\ &= \rho^n, \end{aligned} \tag{3.10}$$

where in the last step we used the uniform ideal gas density $\rho = z/\lambda_T^3$. With the definition of the n-body density distribution, Eq.(3.9), the n-body distribution function

$$g^{(n)}(\mathbf{r}_1, \ldots, \mathbf{r}_n) = \frac{\rho^{(n)}(\mathbf{r}_1, \ldots \mathbf{r}_n)}{\prod_{k=1}^{n} \rho(\mathbf{r}_k)} \tag{3.11}$$

is introduced. Its interpretation is much more comprehendible as, for instance, in the case of an ideal gas $g^n = 1$ holds therefore any deviation from unity provides information about the structure of the underlying system. The pair distribution function $g^{(2)}(\mathbf{r}_1, \mathbf{r}_2)$ for example is an important quantity regarding the pairwise structure of a fluid and makes crucial connections to thermodynamical quantities, as is pointed out in Sec.3.6.

One important observation is that the n-body distribution function Eq.(3.11) gives rise to the following property

$$\frac{1}{V^n} \int d\mathbf{r}^n \, g^{(n)}(\mathbf{r}_1, \ldots, \mathbf{r}_n) = \frac{1}{\langle N \rangle^n} \left\langle \frac{N!}{(N-n)!} \right\rangle \tag{3.12}$$

which in the case of $n = 2$ reduces to

$$\frac{1}{V} \int d\mathbf{r} \, g(\mathbf{r}) = \frac{\langle N^2 \rangle}{\langle N \rangle^2} - \frac{1}{\langle N \rangle} \tag{3.13}$$

which is just the relation Eq.(2.58) connecting the isothermal compressibility κ_T with the particle number fluctuation, $\langle N^2 \rangle - \langle N \rangle^2$. In particular, when approaching the thermodynamic limit, $\langle N \rangle \to \infty$, $V \to \infty$, we know that $\langle N^2 \rangle / \langle N \rangle^2 \to 1$ (except the critical point where κ_T diverges) so we infer from Eq.(3.13) that $1/V \int d\mathbf{r} \, g(\mathbf{r}) \approx 1$. Latter implies that for macroscopic distances $r \to \infty$ we have $g(r) \approx 1$ dominating the integral of Eq.(3.13). This bulk limit virtually means that spatial correlations between to particles are smeared out as the distance between them is arbitrarily increased.

3.2 Grand-Potential Functional

For an arbitrary phase space distribution f fulfilling $\mathrm{Tr} f = 1$ we define the grand functional

$$\Omega[f] = \mathrm{Tr} \, f(H_N - \mu N + \frac{1}{\beta} f) \tag{3.14}$$

that has the correct property in reducing to the grand potential for $f = f_0$

$$\begin{aligned} \Omega[f_0] &= \mathrm{Tr} \, f_0 (H_N - \mu N + \frac{1}{\beta} f_0) \\ &= -\mathrm{Tr} \, f_0 \frac{\log Z_{GC}}{\beta} \\ &= -\frac{1}{\beta} \log Z_{\mathrm{GC}} \\ &= \Omega. \end{aligned} \tag{3.15}$$

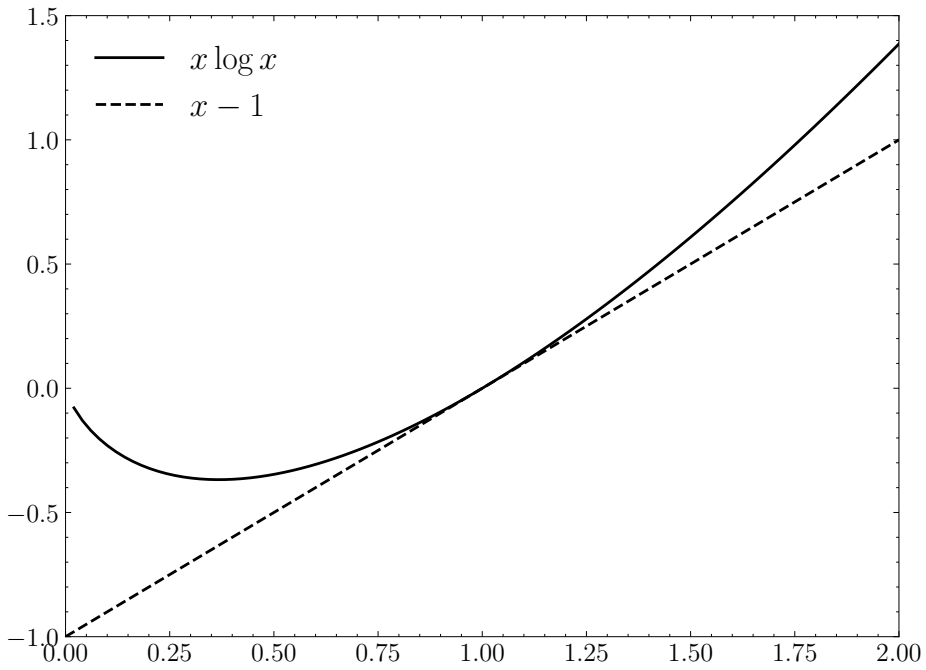

Figure 3.1: Plot visualizing the Gibbs inequality.

Now, we want to show that for any $f \neq f_0$ we have the inequality $\Omega[f] > \Omega[f_0]$

$$\begin{aligned}
\Omega[f] &= \mathrm{Tr}\, f(H_N - \mu N + \frac{1}{\beta}\log Z_{\mathrm{GC}}) \\
&= \mathrm{Tr}\, f(\Omega[f_0] + \frac{1}{\beta}(\log f - \log f_0)) \\
&= \Omega[f_0] + \frac{1}{\beta}\mathrm{Tr}\, f(\log f - \log f_0) \\
&= \Omega[f_0] + \frac{1}{\beta}\mathrm{Tr}\, f_0(x\log x + 1 - x), \quad x = \frac{f}{f_0} \\
&> \Omega[f_0]
\end{aligned} \tag{3.16}$$

where we used the Gibbs inequality $x \log x \geq x - 1$. Figure3.1 displays the Gibbs inequality.

To sum up, we showed that the functional of the grand potential, Eq.(3.14), has the right properties, i.e. reduces to the grand potential Ω if taken at the equilibrium phase space probability distribution f_0 also representing the minimum of the functional $\Omega[f]$. A rigorous proof of the Gibbs inequality can be found at [40].

3.3 Variational Principle

So far, we introduced the grand functional $\Omega[f]$ via the phase space probability distribution f. Through Eq.(3.4), the equilibrium phase space probability distribution f_0 becomes a functional of the external potential $V_{\mathrm{ext}}(\mathbf{r})$. Furthermore, as the equilibrium one-body density distribution $\rho_0(\mathbf{r})$ is calculated via Eq.(3.7), it has to also be a functional of $V_{\mathrm{ext}}(\mathbf{r})$. Now, in the following we want to show that this implies that f_0 must be a functional of ρ_0 relying on the fact that latter is uniquely determined by V_{ext}.

In order to prove the above statement let us consider two distinct external potentials $V_{\text{ext}}(\mathbf{r})$ and $V'_{\text{ext}}(\mathbf{r})$ and hence two phase space distributions f and f_0 leading to the same equilibrium density profile $\rho_0(\mathbf{r})$. We will see that this assumption leads to a contradiction rendering it to be false [40].

We have the Hamiltonians

$$\begin{aligned} H_N &= T + U + V \\ H'_N &= T + U + V' \end{aligned} \tag{3.17}$$

associated to f_0 and f, respectively. Remind that we can write $H'_N = H_N - V + V'$. Then, the grand potential $\Omega[f']$ reads as follows

$$\begin{aligned} \Omega[f'] &= \mathrm{Tr} f'(H'_N - \mu N + \frac{1}{\beta}\log f') \\ &= \mathrm{Tr} f'(H_N - \mu N - V + V' + \frac{1}{\beta}\log f') \\ &= \mathrm{Tr} f'(-\frac{1}{\beta}\log f_0 + \Omega[f_0] - V + V' + \frac{1}{\beta}\log f') \\ &= \Omega[f_0] + \mathrm{Tr} f'(V' - V) + \frac{1}{\beta}\mathrm{Tr} f' \log\left(\frac{f'}{f}\right), \end{aligned} \tag{3.18}$$

where we inserted the expression for $\Omega[f_0]$. The second term in Eq.(3.18) can be re-expressed using the density operator Eq.(3.6)

$$\begin{aligned} V(\mathbf{r}_1, \ldots, \mathbf{r}_N) &= \sum_{i=1}^{N} V_{\text{ext}}(\mathbf{r}_i) \\ &= \int d\mathbf{r} \sum_{i=1}^{N} \delta(\mathbf{r} - \mathbf{r}_i) V_{\text{ext}}(\mathbf{r}) \\ &= \int d\mathbf{r}\, \hat{\rho}(\mathbf{r})\, V_{\text{ext}}(\mathbf{r}) \end{aligned} \tag{3.19}$$

simply using the property of the Dirac-delta. Herewith, the second term of Eq.(3.18) becomes

$$\mathrm{Tr} f'(V' - V) = \int d\mathbf{r}\, \rho_0(\mathbf{r})\, (V'_{\text{ext}}(\mathbf{r}) - V_{\text{ext}}(\mathbf{r})) \tag{3.20}$$

having used the fact that $\mathrm{Tr} f' \hat{\rho}(\mathbf{r}) = \rho_0(\mathbf{r})$ which is just our assumption from above. Again, according to the Gibbs inequality the last term in Eq.(3.18) is positive. Thus, putting all together we find the inequality

$$\Omega[f'] < \Omega[f_0] + \int d\mathbf{r}\, \rho_0(\mathbf{r})\, (V'_{\text{ext}}(\mathbf{r}) - V_{\text{ext}}(\mathbf{r}))\,. \tag{3.21}$$

However, we could have done the above steps replacing f' with f_0 with the result

$$\Omega[f_0] < \Omega[f'] + \int d\mathbf{r}\, \rho_0(\mathbf{r})\, (V_{\text{ext}}(\mathbf{r}) - V'_{\text{ext}}(\mathbf{r}))\,, \tag{3.22}$$

so that adding Eq.(3.21) Eq.(3.22) gives

$$\Omega[f_0] + \Omega[f'] < \Omega[f_0] + \Omega[f'] \tag{3.23}$$

which apparently cannot be true. Going back to our previous assumption made at the beginning, we must infer that for two distinct external potentials these cannot imply the same equilibrium density profile. This conclusion is crucial insofar as the high-dimensional equilibrium phase space distribution f_0 is a functional of the equilibrium density profile ρ_0

$$f_0 = f_0[\rho_0] \tag{3.24}$$

and accordingly for the grand functional

$$\Omega[f_0] = \Omega[\rho_0]. \tag{3.25}$$

Given these, we can re-express the grand functional $\Omega[\rho]$ in terms of the density profile ρ

$$\begin{aligned}\Omega[\rho] &= \mathrm{Tr} f(H_N - \mu N + \frac{1}{\beta}\log f) \\ &= \mathrm{Tr} f(T + U + \frac{1}{\beta}\log f) + \mathrm{Tr} f(V - \mu N) \\ &= \mathcal{F}[\rho] + \int d\mathbf{r}\, \rho(\mathbf{r})(V_{\mathrm{ext}}(\mathbf{r}) - \mu N),\end{aligned} \tag{3.26}$$

where we introduced the unique Helmholtz-free energy functional

$$\mathcal{F}[\rho] = \mathrm{Tr} f(T + U + \frac{1}{\beta}\log f). \tag{3.27}$$

With the important representation in Eq.(3.26) at hand, we have arrived at a point where we can succinctly formulate the core of cDFT. The minimum property of Eq.(3.16) now becomes

$$\Omega[\rho(\mathbf{r})] > \Omega[\rho_0(\mathbf{r})], \quad \rho \neq \rho_0 \tag{3.28}$$

and the main result of these considerations

$$\left.\frac{\delta\Omega[\rho(\mathbf{r})]}{\delta\rho(\mathbf{r})}\right|_{\rho(\mathbf{r})=\rho_0(\mathbf{r})} = 0, \quad \Omega[\rho_0] = \Omega. \tag{3.29}$$

In summary, cDFT is performed using Eq.(3.29) that provides us in principle with the equilibrium density profile $\rho_0(\mathbf{r})$ which enables us to not only obtain thermodynamic quantities of the system but also its structure. All we need is to find expressions for the Helmholtz-free energy functional, Eq.(3.27), that contains all the information of the system. As it turns out, for most cases an exact functional $\mathcal{F}[\rho]$ is hardly achieved, rather certain approximations have to be employed. In general, $\mathcal{F}[\rho]$ is decomposed into an ideal part denoted as $\mathcal{F}_{\mathrm{id}}[\rho]$ and a so-called excess part $\mathcal{F}_{\mathrm{ex}}[\rho]$ accounting for interactions going beyond the ideal gas. Latter is the object of focus that provides the features of interacting systems that can only be described in an approximative manner.

3.4 Functional of the Ideal Gas

Suppose we have a system of N non-interacting, point-like particles of an ideal gas that can be subject to an external potential $V = \sum_i V_{\mathrm{ext}}(\mathbf{r}_i)$, i.e. the Hamiltonian is given by

$H_N = T + V$. Then, as we have already found in Sec.2.3.3, the grand partition sum is obtained by

$$\begin{aligned} Z_{\mathrm{GC}} &= \mathrm{Tr}\exp\left(-\beta(H_N-\mu N)\right) \\ &= \sum_{N=0}^{\infty}\frac{1}{h^{3N}N!}\int d^N\mathbf{r}\,d^N\mathbf{p}\exp\left(-\beta\sum_{i=1}^{N}\left(\frac{\mathbf{p}_i^2}{2m}+V_{\mathrm{ext}}(\mathbf{r}_i)\right)+\beta\mu N\right) \\ &= \sum_{N=0}^{\infty}\frac{z^N}{h^{3N}N!}\left(\int d\mathbf{r}\,\exp\left(-\beta V_{\mathrm{ext}}(\mathbf{r})\right)\right)^N\left(\int d\mathbf{p}\exp\left(-\frac{\beta\mathbf{p}^2}{2m}\right)\right)^N \\ &= \sum_{N=0}^{\infty}\frac{1}{N!}\left(\frac{zQ}{\lambda_T^3}\right)^N, \quad Q\equiv\int d\mathbf{r}\,\exp\left(-\beta V_{\mathrm{ext}}(\mathbf{r})\right) \\ &= \exp\left(\frac{zQ}{\lambda_T^3}\right), \end{aligned} \tag{3.30}$$

where we used the definitions of the fugacity z and thermal wavelength λ_T outlined in Sec.2.3.3. Hence, the grand potential can be found with Eq.(2.55) to give

$$\beta\Omega_{\mathrm{id}} = -\log Z_{\mathrm{GC}} = -\frac{zQ}{\lambda_T^3}. \tag{3.31}$$

The next step is to consider the ensemble average $\langle\hat{\rho}(\mathbf{r})\rangle$

$$\begin{aligned} \langle\hat{\rho}(\mathbf{r})\rangle &= \mathrm{Tr} f_0\hat{\rho}(\mathbf{r}) \\ &= \frac{1}{Z_{\mathrm{GC}}}\sum_{N=1}^{\infty}\frac{z^N}{\lambda_T^{3N}N!}\int d\mathbf{r}_1\cdots\int d\mathbf{r}_N\,\exp\left(-\beta\sum_{i=1}^{N}V_{\mathrm{ext}}(\mathbf{r}_i)\right)\sum_{j=1}^{N}\delta(\mathbf{r}-\mathbf{r}_j) \\ &= \frac{1}{Z_{\mathrm{GC}}}\sum_{N=1}^{\infty}\frac{z^N}{\lambda_T^{3N}N!}\sum_{i=1}^{N}\left[\exp\left(-\beta V_{\mathrm{ext}}(\mathbf{r})\right)\left(\int d\mathbf{r}'\exp\left(-\beta V_{\mathrm{ext}}(\mathbf{r}')\right)\right)^{N-1}\right] \\ &= \frac{1}{Z_{\mathrm{GC}}}\sum_{N=1}^{\infty}\frac{z^N}{\lambda_T^{3N}N!}N\exp\left(-\beta V_{\mathrm{ext}}(\mathbf{r})\right)Q^{N-1} \\ &= \frac{z}{\lambda_T^3}\exp\left(-\beta V_{\mathrm{ext}}(\mathbf{r})\right)\frac{1}{Z_{\mathrm{GC}}}\sum_{N=0}^{\infty}\left(\frac{zQ}{\lambda_T^3}\right)^N \\ &= \frac{z}{\lambda_T^3}\exp\left(-\beta V_{\mathrm{ext}}(\mathbf{r})\right), \end{aligned} \tag{3.32}$$

where we inserted Eq.(3.6), rearranged the multiple real space integrals as they factorize and finally used Eq.(3.30) in the last line of Eq.(3.32). Combining Eq.(3.31) and Eq.(3.32), we find for the grand functional of an ideal gas

$$\beta\Omega_{\mathrm{id}}[\rho] = -\int d\mathbf{r}\,\rho(\mathbf{r}), \tag{3.33}$$

which for constant bulk density $\rho_b = N/V$ reduces to the known result $\beta\Omega_{\mathrm{id}} = -N$. If we use Eq.(3.32) to replace $V_{\mathrm{ext}}(\mathbf{r}) - \mu$ in Eq.(3.26) by $-\frac{1}{\beta}\log(\lambda_T^3\rho(\mathbf{r}))$, we obtain

$$\beta\mathcal{F}_{\mathrm{id}}[\rho] = \int d\mathbf{r}\,\rho(\mathbf{r})\left(\log(\lambda_T^3\rho(\mathbf{r}))-1\right). \tag{3.34}$$

We want to emphasize that the Helmholtz-functional in Eq.(3.27) of an ideal gas is exact.

3.5 Euler-Lagrange Equations

In cDFT we must provide the full Helmholtz functional, Eq.(3.27), which can be split into an ideal $\mathcal{F}_{\text{id}}[\rho]$ and excess part $\mathcal{F}_{\text{ex}}[\rho]$

$$\mathcal{F}[\rho] = \mathcal{F}_{\text{id}}[\rho] + \mathcal{F}_{\text{ex}}[\rho], \tag{3.35}$$

where the excess contribution contains any interactions going beyond the ideal gas. We have already derived the exact expression of $\mathcal{F}_{\text{id}}[\rho]$ in Eq.(3.34).

From the minimization of the grand functional, Eq.(3.29), the following equation is found for the equilibrium density profile $\rho(\mathbf{r})$

$$0 = \log\left(\lambda_T^3 \rho(\mathbf{r})\right) + \beta\left(\frac{\delta \mathcal{F}_{\text{ex}}[\rho]}{\delta \rho(\mathbf{r})} + V_{\text{ext}}(\mathbf{r}) - \mu\right) \tag{3.36}$$

to which we often refer to as the Euler-Lagrange equation of cDFT. If we further split the chemical potential $\mu = \mu_{\text{id}} + \mu_{\text{ex}}$ into an ideal gas contribution $\beta\mu_{\text{id}} = \log(\lambda_T^3 \rho_b)$, where ρ_b denotes the bulk density of the system, and an excess contribution μ_{ex} we can rewrite the Euler-Lagrange equation

$$\rho(\mathbf{r}) = \rho_b \exp\left(c^{(1)}(\mathbf{r}) - \beta\left(V_{\text{ext}}(\mathbf{r}) - \mu_{\text{ex}}\right)\right), \tag{3.37}$$

where we have introduced the one-body correlation function

$$c^{(1)}(\mathbf{r}) \equiv -\beta \frac{\delta \mathcal{F}_{\text{ex}}[\rho]}{\delta \rho(\mathbf{r})} \tag{3.38}$$

in which the interparticle interactions are encoded. We can furthermore see in the absence of any external potentials V_{ext} that $-c^{(1)}(\mathbf{r}) = \beta\mu_{\text{ex}}$, i.e. we can interpret $c^{(1)}(\mathbf{r})$ as the excess part of the intrinsic chemical potential. We can extend to higher-order derivatives

$$c^{(n)}(\mathbf{r}_1, \ldots, \mathbf{r}_n) = -\beta \frac{\delta^n \mathcal{F}_{\text{ex}}}{\delta\rho(\mathbf{r}_1) \cdots \delta\rho(\mathbf{r}_n)}, \tag{3.39}$$

where particularly for uniform systems $c^{(2)}(\mathbf{r}_1, \mathbf{r}_1)$ equals pair-correlation function $c^{(2)}(r)$ [8]

$$c^{(2)}(r) = c^{(2)}(|\mathbf{r} - \mathbf{r}'|). \tag{3.40}$$

It is important to note that in general Eq.(3.37) cannot be solved analytically but rather numerical methods have to be applied. The reason lies in the fact that these equations are merely implicit equations for the equilibrium density profile as latter also appears in the calculation of one-body correlation function.

3.5.1 Picard-Iteration

An often used minimization scheme is the Picard iteration [41, 42] which is comprised by the following steps

1. First, we have to provide a first guess, i.e. an initial profile $\rho^{(0)}(\mathbf{r})$ that is suitable for the problem, especially satisfying boundary conditions, for example the bulk density ρ_b for away from any surfaces. For instance, the external potential $V_{\text{ext}}(\mathbf{r})$ prescribes the shape and range of the equilibrium density profile $\rho_0(\mathbf{r})$. Furthermore, certain symmetries the system possesses, e.g. translational or spherical symmetry, can give additional hints on the first guess.

2. Having provided the initialization, the Picard iteration scheme yields the next, closer solution $\rho^{(i+1)}(\mathbf{r})$ of the i-th step in calculating

$$\tilde{\rho}^{(i)}(\mathbf{r}) = \rho_b \exp\left(c^{(1)}(\mathbf{r}) - \beta(V_{\text{ext}}(\mathbf{r}) - \mu_{\text{ex}})\right) \tag{3.41}$$

where for the calculation of $c^{(1)}(\mathbf{r})$ the intermediate density profile $\rho^{(i)}(\mathbf{r})$ is used.

3. Then, we mix $\rho^{(i)}(\mathbf{r})$ and $\tilde{\rho}^{(i)}(\mathbf{r})$ with an associated mixing parameter $\alpha \in (0, 0.1]$ in order to obtain the new solution

$$\rho^{(i+1)}(\mathbf{r}) = (1-\alpha)\rho^{(i)}(\mathbf{r}) + \alpha\tilde{\rho}^{(i)}(\mathbf{r}) \tag{3.42}$$

4. We return to the second step until the solution has sufficiently converged, i.e. up to a given accuracy the converged solution is equal to the equilibrium density profile.

It should be emphasized that the initial guess of the density profile also often comes along with a certain intuition of the problem. The closer it is to the equilibrium solution, the more stable and faster the Picard iteration scheme performs. The external potential $V_{\text{ext}}(\mathbf{r})$ plays a crucial role in this regards, as its overall properties determine the general shape of the equilibrium profile $\rho_0(\mathbf{r})$. Of course, if we put latter as a first guess into the Picard iteration, we would directly obtain it again by definition. We also have introduced a mixing parameter α in order to find the next density profile.

Choosing a suitable value for α is very important and the concrete magnitude strongly depends on the nature of the problem to be minimized. The mixing procedure in general guarantees that no too rapid changes can occur, keeping the numerics stable. Finally, at each step of the iteration it is necessary to calculate the one-body correlation function $c^{(1)}(\mathbf{r})$ basically encapsulating all the physics of the problem. In the framework of Fundamental Measure Theory, see Ch.4, we need to perform several convolutional integrals in order to obtain $c^{(1)}(\mathbf{r})$, i.e. computing weighted densities and the functional derivative of $\mathcal{F}_{\text{ex}}[\rho]$.

Besides this numerical challenge, we must further provide an expression for the excess functional $\mathcal{F}_{\text{ex}}[\rho]$. Certain approximative schemes are needed in order to construct such functionals. Of particular interest is the hard-sphere system that on the one hand is important as a reference model for simple fluids or colloidal mixtures and on the other hand more approachable.

3.5.2 Gradient Descent

The technique of gradient descent plays a key role when it comes to computations that seek the minimum of a function, such as is currently done in the field of Machine Learning. The underlying idea is to perform successive iteration steps on the location, where the functions is evaluated, in such a way that the direction is opposite to the gradient. In our case, the minimization of the grand functional $\Omega[\rho]$ can be achieved by applying the following step

$$\rho^{(i+1)}(\mathbf{r}) = \rho^{(i)}(\mathbf{r}) - \eta\frac{\delta\beta\Omega[\rho^{(i)}]}{\delta\rho^{(i)}(\mathbf{r})}, \tag{3.43}$$

where η is the so-called learning parameter typically in the range 0.01 to 0.1. Latter is crucial regarding stability of gradient descent as too large steps might leave the region where the true minimum lies. At the same time, too small steps can prolong the overall

minimization procedure unnecessarily. Therefore, the iteration steps in Eq.(3.43) are repeated until the Euler-Lagrange equation, $\delta\Omega[\rho]/\delta\rho$=0, is fulfilled sufficiently well. We should remark here that in contrast to Eq.(3.42), Eq.(3.43) is not as stable, since the gradient in Eq.(3.43) can generally change its sign. This entails the fact that the new density profile $\rho^{(i+1)}(\mathbf{r})$ of the minimization procedure may become negative, which is of course undesirable. Thus, the following constraint has to be taken into account

$$\eta < \min_{\mathbf{r}} \left| \frac{1}{\rho^{(i)}(\mathbf{r})} \frac{\delta\beta\Omega[\rho^{(i)}]}{\delta\rho^{(i)}(\mathbf{r})} \right| \tag{3.44}$$

which ensures stability of gradient descent procedures throughout the whole space under consideration. Comparing the Picard-iteration scheme with gradient descent for hard-sphere calculations within DFT shows in general that gradient descent is similar to Picard in time and accuracy. However, gradient descent is much more prone to diverge when systems of high packing fractions are considered. There are several more advanced versions of gradient descent, among others stochastic gradient descent wherein the actual gradient is replaced by an estimate of it. The Adam optimizer is a more sophisticated method of gradient descent making use of momentum and root mean square propagation (RMSprop) [43]. Former is useful in the sense that local minima can inhibit the progress of gradient descent and even let it stuck there. RMSprop helps avoiding the corresponding learning rate to diminish too much which would slow down gradient descent unwillingly. In Machine Learning, the Adam optimizer is a widely used and established algorithm for optimization problems due to its efficiency and reliability. It employs a dynamical learning rate rendering the algorithm save from local minima and oscillations with additional bias correction.

3.6 Radial Distribution Function

We would like to know the conditional probability of finding a particle at position $\mathbf{r}$ and another particle at position $\mathbf{r}'$ which is obtained by considering the two-body density distribution $\rho^{(2)}(\mathbf{r},\mathbf{r}')$ containing information about correlations between these two particles. We define [7]

$$\rho^{(2)}(\mathbf{r},\mathbf{r}') = \langle \sum_{i\neq j} \delta(\mathbf{r}-\mathbf{r}_i)\delta(\mathbf{r}'-\mathbf{r}_j) \rangle \tag{3.45}$$

with the property that for non-interacting particles $\rho^{(2)}(\mathbf{r},\mathbf{r}')$ simply factorizes $\rho(\mathbf{r})\rho(\mathbf{r}')$ so that there are no spatial correlations. If we further assume isotropy, then $\rho^{(2)}(\mathbf{r},\mathbf{r}') = \rho^{(2)}(|\mathbf{r}-\mathbf{r}'|)$, i.e. only the relative distance $r = |\mathbf{r}-\mathbf{r}'|$ is relevant. Thus, we introduce the radial distribution function

$$g(r) = \frac{\rho^{(2)}(r)}{\rho_b^2} \tag{3.46}$$

which describes density-density correlations of an homogeneous fluid compared to an ideal gas. The concept of the radial distribution function $g(r)$ becomes more illuminating by taking the example of a test particle [44]. Suppose that we fixate a reference particle of given diameter as the origin of the coordinate system, see Fig.3.2. This reference particle acts as an external potential $V_{\text{ext}}(r) = \phi(r)$ onto the surrounding particles of the gas being equal to the interparticle potential $\phi(r)$.

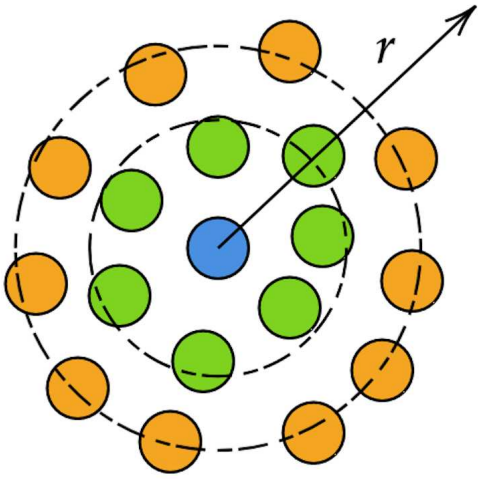

Figure 3.2: A test particle (blue) is surrounded by particles in the first shell (green) and second shell (orange) etc. According to Percus' interpretation the radial distribution function $g(r)$ is the one-body density profile $\rho(r) = \rho_b g(r)$.

Therefore, the radially symmetric one-body density profile $\rho(r)$ is directly connected to the radial distribution function

$$\rho(r) = \rho_b g(r) \tag{3.47}$$

providing us with the important picture for the structure of a fluid: The radial distribution function $g(r)$ taken at a radial distance r from the reference or test particle gives the average number of particles $4\pi r^2 g(r)dr$ to be found in the shell $[r, r + dr]$. Hence, peaks that occur in the radial distribution function correspond to shells of surrounding particles or neighbors. Figure3.3 displays a typical shape of $g(r)$ of Argon where we can clearly infer the diameter of the reference particle by locating the first peak or shell. These peaks become weaker as the radial distance is increased, i.e. spatial correlations start to vanish. Due to the fluid being disordered spatial correlations vanish as $r \to \infty$ thus $g(r \to \infty) = 1$. Monte-Carlo (MC) and Molecular Dynamics (MD) techniques [45, 46] can be applied to access $g(r)$.

Through the radial distribution function $g(r)$, the total pair correlation function $h(r) = g(r) - 1$ is defined. Its 3d-Fourier transform

$$\hat{h}(\mathbf{k}) = \int d\mathbf{r}\, h(\mathbf{r}) \exp(-i\mathbf{k}\mathbf{r}) \tag{3.48}$$

is a quantity that can be inferred from scattering experiments where the structure factor $S(\mathbf{k})$ is measured

$$S(\mathbf{k}) = 1 + \rho_b \hat{h}(\mathbf{k}). \tag{3.49}$$

3.7 Ornstein-Zernike Relation

The Ornsein-Zernike relation [48] connects different correlation functions with each other and in combination with a so-called closer relation provides an access to the structure

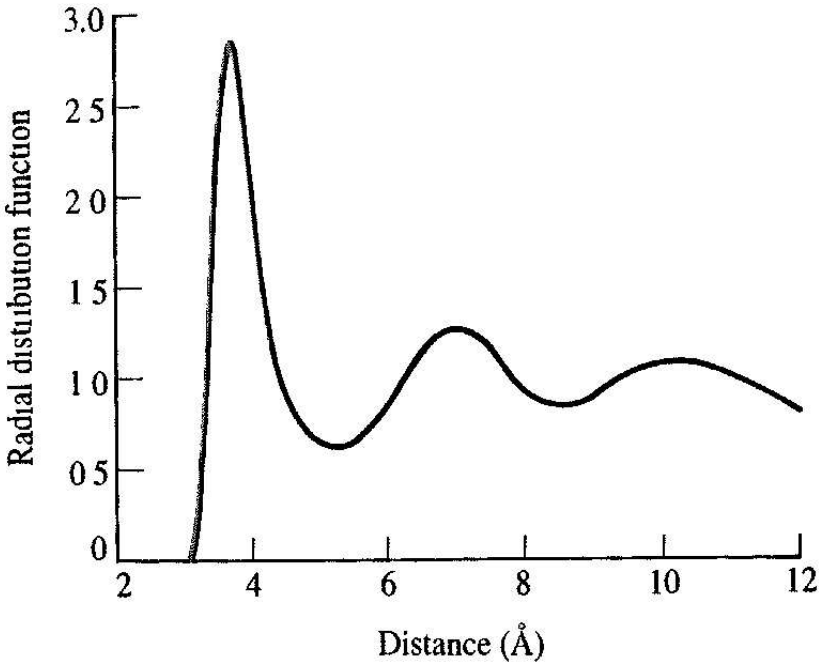

Figure 3.3: Radial distribtion function of Argon. The maxima represent congregation shells (see Fig.3.2) of neighboring particles with a width roughly of the order of hard-core diameter. As the distance is increased, correlations tend to damp out, i.e. here approach unity. Picture taken from [47].

factor $S(\mathbf{k})$ from which thermodynamic quantities can be obtained. The total correlation function $h(\mathbf{r}_1, \mathbf{r}_2)$ thus obeys

$$h(\mathbf{r}_1, \mathbf{r}_2) = c(\mathbf{r}_1, \mathbf{r}_2) + \int d\mathbf{r}' c(\mathbf{r}_1, \mathbf{r}')\rho(\mathbf{r}')h(\mathbf{r}', \mathbf{r}_2), \tag{3.50}$$

i.e. is split into a direct and indirect contribution. The direct contribution defines the direct correlation function, $c(r)$. The indirect contribution on the other hand accounts for the influence of a third particle located at position $\mathbf{r}'$ that influences particle two at $\mathbf{r}_2$ again directly and indirectly integrated for all possible positions $\mathbf{r}'$. For a uniform and isotropic system Eq.(3.50) can also be written as

$$h(r) = c(r) + \rho_b \int d\mathbf{r}' c(|\mathbf{r} - \mathbf{r}'|)h(r'). \tag{3.51}$$

In Fourier space, Eq.(3.51) reads

$$\hat{h}(\mathbf{k}) = \frac{\hat{c}(\mathbf{k})}{1 - \rho_b \hat{c}(\mathbf{k})} = \frac{S(\mathbf{k}) - 1}{\rho_b}, \tag{3.52}$$

where we have used Eq.(3.49). One important quantity, namely the reduced isothermal compressibility χ_T, is closely related to the structure factor

$$\rho_b k_B T \chi_T = \frac{1}{1 - \rho_b \hat{c}(0)}. \tag{3.53}$$

The Percus-Yevick approximation [49] relates $c^{(2)}(r)$ with $g(r)$ providing a closure relation. We have

$$c^{(2)}(r) \approx (1 - \exp(\beta\phi(r)))g(r) \tag{3.54}$$

being consistent with the fact that $g(r) \approx 1$ for $r \to \infty$ as at the same time $\exp(\beta\phi(r)) \approx 1 + \beta\phi(r)$. Furthermore, the low-density expansion [7] is also satisfied since $g(r) \approx \exp(-\beta\phi(r))$. Especially, this approximation enables the exact analytical solution for hard spheres [50]. Introducing the packing fraction $\eta = \frac{\pi}{6}\rho_b\sigma^3$, the corresponding correlation function reads

$$c^{(2)}(x) = \left[a_0(\eta) + a_1(\eta)x + a_3(\eta)x^3\right]\Theta(1-x), \quad x = \frac{r}{\sigma} \tag{3.55}$$

with the coefficients

$$\begin{aligned} a_0(\eta) &= -\frac{(1+2\eta)^2}{(1-\eta)^4} \\ a_1(\eta) &= \frac{3\eta(2+\eta)^2}{2(1-\eta)^4} \\ a_3(\eta) &= -\frac{\eta(1+2\eta)^2}{2(1-\eta)^4} \end{aligned} \tag{3.56}$$

and the Percus-Yevick equation of state for hard spheres

$$\frac{\beta P}{\rho_b} = \frac{1+\eta+\eta^2}{(1-\eta)^3} \tag{3.57}$$

being in good agreement with computer simulations.

The random-phase approximation (RPA) relies upon the simple observation that $c(r) \approx -\beta\phi_{\text{att}}(r)$ for $r \to \infty$ where $\phi = \phi_{\text{HS}} + \phi_{\text{att}}$ is decomposed into hard-sphere (HS) and attractive part (att). Thus, the following assumption is made

$$c^{(2)}(r) = c_{\text{HS}}(r) - \beta\phi_{\text{att}}(r) \tag{3.58}$$

in which $c_{\text{HS}}(r)$ has to be provided by certain expressions for hard-sphere fluids.

3.8 Excess Functional

Following the ideas of [8], we can construct an excess functional for systems of hard-core repulsion and longer attractive tail. The two-body density $\rho^{(2)}(\mathbf{r}, \mathbf{r}')$ is obtained by taking the functional derivative of the excess functional $\mathcal{F}_{\text{ex}}[\rho]$ with respect to the pair interaction potential $\phi(\mathbf{r}, \mathbf{r}')$

$$\rho^{(2)}(\mathbf{r}, \mathbf{r}') = 2\beta\frac{\mathcal{F}_{\text{ex}}[\rho]}{\delta\phi(\mathbf{r}, \mathbf{r}')}. \tag{3.59}$$

The pair potential can be decomposed into a reference part $\phi_0(\mathbf{r}, \mathbf{r}')$ and a perturbation part $\phi_{\text{p}}(\mathbf{r}, \mathbf{r}')$

$$\phi_\xi(\mathbf{r}, \mathbf{r}') = \phi_0(\mathbf{r}, \mathbf{r}') + \xi\phi_p(\mathbf{r}, \mathbf{r}'), \tag{3.60}$$

where $\xi \in [0, 1]$ is a parameter with which we can turn on the perturbation smoothly. Reverting the functional derivative of Eq.(3.59), we find a formal solution to the excess functional

$$\mathcal{F}_{\text{ex}}[\rho] = \mathcal{F}^0_{\text{ex}}[\rho] + \frac{1}{2}\int_0^1 d\xi \int\int d\mathbf{r}\, d\mathbf{r}'\, \rho^{(2)}(\mathbf{r}, \mathbf{r}'; \xi)\phi_p(\mathbf{r}, \mathbf{r}'), \tag{3.61}$$

where $\mathcal{F}^0_{\rm ex}[\rho]$ is the excess functional of the reference fluid. Furthermore, using the generic form of the pair correlation function, $g^{(2)}(\mathbf{r},\mathbf{r}') = \rho^{(2)}(\mathbf{r},\mathbf{r}')/(\rho(\mathbf{r})\rho(\mathbf{r}'))$ we can rewrite Eq.(3.61) as

$$\mathcal{F}_{\rm ex}[\rho] = \mathcal{F}^0_{\rm ex}[\rho] + \frac{1}{2}\int_0^1 d\xi \int\int d\mathbf{r}\, d\mathbf{r}'\, \rho(\mathbf{r})\rho(\mathbf{r}')g^{(2)}(\mathbf{r},\mathbf{r}';\xi)\phi_p(\mathbf{r},\mathbf{r}'). \tag{3.62}$$

To further simply Eq.(3.62), we expand the pair correlation function $g^{(2)}(\mathbf{r},\mathbf{r}';\xi)$ at $\xi = 0$

$$g^{(2)}(\mathbf{r},\mathbf{r}';\xi) = g^{(2)}(\mathbf{r},\mathbf{r}';0) + \xi\frac{\partial g^{(2)}(\mathbf{r},\mathbf{r}';\xi)}{\partial\xi}\bigg|_{\xi=0} + \dots \tag{3.63}$$

and only include the lowest order, $g^{(2)}(\mathbf{r},\mathbf{r}';\xi) \approx g^{(2)}(\mathbf{r},\mathbf{r}';0) \equiv g^{(2)}_0(\mathbf{r},\mathbf{r}')$

$$\mathcal{F}_{\rm ex}[\rho] = \mathcal{F}^0_{\rm ex}[\rho] + \frac{1}{2}\int\int d\mathbf{r}\, d\mathbf{r}'\, \rho(\mathbf{r})\rho(\mathbf{r}')g^{(2)}_0(\mathbf{r},\mathbf{r}')\phi_p(\mathbf{r},\mathbf{r}') \tag{3.64}$$

or, considering isotropic pair interactions

$$\mathcal{F}_{\rm ex}[\rho] = \mathcal{F}^0_{\rm ex}[\rho] + \frac{1}{2}\int\int d\mathbf{r}\, d\mathbf{r}'\, \rho(\mathbf{r})\rho(\mathbf{r}')g(|\mathbf{r}-\mathbf{r}'|)\phi_p(|\mathbf{r}-\mathbf{r}'|), \tag{3.65}$$

where $g(r = |\mathbf{r}-\mathbf{r}'|)$ is now the radial distribution function. Since we do not have any information about $g(r)$ the first roughest approximation we can make is to assume $g(r) \approx 1$, which is just the random phase approximation (RPA) for $c(r)$. Hence, the RPA functional reads

$$\mathcal{F}_{\rm ex}[\rho] = \mathcal{F}^0_{\rm ex}[\rho] + \frac{1}{2}\int\int d\mathbf{r}\, d\mathbf{r}'\, \rho(\mathbf{r})\rho(\mathbf{r}')\phi_p(|\mathbf{r}-\mathbf{r}'|). \tag{3.66}$$

We can better interpret the RPA functional of Eq.(3.68) if we introduce the quantity

$$n_p(\mathbf{r}) = \frac{1}{2}\int d\mathbf{r}'\, \rho(\mathbf{r}')\phi_p(|\mathbf{r}-\mathbf{r}'|), \tag{3.67}$$

so that Eq.(3.68) attains a concise form

$$\mathcal{F}_{\rm ex}[\rho] = \mathcal{F}^0_{\rm ex}[\rho] + \int d\mathbf{r}\; n_p(\mathbf{r})\rho(\mathbf{r}) \tag{3.68}$$

which is termed as the mean-field (MF) approximation. The name accounts for the fact that the "weighted" density $n_p(\mathbf{r})$ represents an average value of the pair interaction or perturbation potential $\phi_p(\mathbf{r})$ which is weighted with the local density $\rho(\mathbf{r})$. Therefore, $n_p(\mathbf{r})$ can be conceived as a background field acting on a particle located at position $\mathbf{r}$. We want to emphasize once again, that the derivation of Eq.(3.65) relies on pair interactions. In addition, we also have to provide an expression for the reference functional $\mathcal{F}^0_{\rm ex}[\rho]$ which is almost always given by an excess functional for hard spheres.

There are several attempts to construct excess functionals for hard spheres. One attempt is to make use of the so-called local-density approximation (LDA), i.e. assuming that the bulk free energy density $f_{\rm ex}(\rho_b)$ can be promoted also for inhomogeneous fluids. For instance, the Carnahan-Starling (CS) free enregy denisty

$$f^{\rm CS}_{\rm ex}(\rho_b) = \rho_b\frac{4\eta - 3\eta^2}{(1-\eta)^3}, \quad \eta = \frac{\pi}{6}\sigma^3\rho_b \tag{3.69}$$

becomes an excess functional

$$\beta\mathcal{F}_{\rm ex}[\rho] = \int d\mathbf{r}\,\rho(\mathbf{r})\frac{4\eta(\mathbf{r}) - 3\eta^2(\mathbf{r})}{(1-\eta(\mathbf{r}))^3}, \tag{3.70}$$

i.e. the bulk quantities are raised to be spatially dependent. As it turns out, the approach of Eq.(3.70) is only reliable for slowly varying density profiles and especially does not fulfill the exact low-density limit of $c(r)$. Alternatively, the Ramakrishnan-Yussouff approximation [51] also provides an excess functional for hard spheres where latter is expanded at bulk density ρ_b truncating at second order. If, for example, the Percus-Yevick expression for $c^{(2)}(r)$ is used for the second functional derivative, a good description for hard-sphere fluids is obtained for a wide range of densities when compared to simulations [51, 52]. Suppose that a given reference system has the interparticle interaction potential $\phi_{\rm ref}(\mathbf{r})$ with an excess free energy functional $\beta\mathcal{F}_{\rm ref}$. Then, for any system under consideration deviating from the reference system we can write its underlying interparticle interaction potential $\phi(\mathbf{r})$ as a perturbation of the form

$$\phi(\mathbf{r}) = \phi_{\rm ref}(\mathbf{r}) + \xi w(\mathbf{r}), \tag{3.71}$$

where ξ is a perturbation parameter recovering the full potential of the system if $\xi = 1$. The associated excess functional therefore is understood as a correction to the excess functional of the reference system, which has as a consequence that the deviation of the direct correlation function to the reference system is given by RPA.

The one-body density profile $\rho(\mathbf{r};\xi)$ is written as [7]

$$\rho(\mathbf{r};\xi) = \rho_{\rm ref}(\mathbf{r}) + \xi\Delta\rho(\mathbf{r}) \tag{3.72}$$

from which the excess free energy functional $\beta\mathcal{F}_{\rm ex}[\rho]$ is obtained as

$$\begin{aligned}\beta\mathcal{F}_{\rm ex}[\rho] &= \beta\mathcal{F}_{\rm ex}[\rho_{\rm ref}] - \int_0^1 d\xi \int d\mathbf{r}\,\frac{\partial\rho(\mathbf{r})}{\partial\xi}c^{(1)}(\mathbf{r}) \\ &= \beta\mathcal{F}_{\rm ex}[\rho_{\rm ref}] - \int_0^1 d\xi \int d\mathbf{r}\,\Delta\rho(\mathbf{r})c^{(1)}(\mathbf{r})\end{aligned} \tag{3.73}$$

together with

$$c^{(n-1)}(\mathbf{r}) = c_{\rm ref}^{(n-1)}(\mathbf{r}) + \int_0^\xi d\xi' \int d\mathbf{r}'\,\Delta\rho(\mathbf{r}')c^{(n)}(\mathbf{r},\mathbf{r}';\xi'). \tag{3.74}$$

Equation(3.73) can be found by expanding the excess functional around $\xi = 0$

$$\begin{aligned}\beta\mathcal{F}_{\rm ex}[\rho] &= \beta\mathcal{F}_{\rm ex}[\rho_{\rm ref}] + \int_0^1 d\xi\,\frac{\partial\beta\mathcal{F}_{\rm ex}[\rho(\mathbf{r};\xi)]}{\partial\xi} \\ &= \beta\mathcal{F}_{\rm ex}[\rho_{\rm ref}] + \int_0^1 d\xi \int d\mathbf{r}\,\frac{\delta\beta\mathcal{F}_{\rm ex}[\rho(\mathbf{r};\xi)]}{\delta\rho(\mathbf{r})}\frac{\partial\rho(\mathbf{r})}{\partial\xi} \\ &= \beta\mathcal{F}_{\rm ex}[\rho_{\rm ref}] - \int_0^1 d\xi \int d\mathbf{r}\,c^{(1)}(\mathbf{r};\xi)\frac{\partial\rho(\mathbf{r})}{\partial\xi}.\end{aligned} \tag{3.75}$$

Hence, putting together Eq.(3.73) and Eq.(3.74) we find

$$\begin{aligned}\beta\mathcal{F}_{\rm ex}[\rho] = \beta\mathcal{F}_{\rm ex}[\rho_{\rm ref}] - \int_0^1 d\xi \int d\mathbf{r}\,\Delta\rho(\mathbf{r})c_{\rm ref}^{(1)}(\mathbf{r}) - \\ \int_0^1 d\xi \int_0^\xi d\xi' \int d\mathbf{r} \int d\mathbf{r}'\,\Delta\rho(\mathbf{r})\Delta\rho(\mathbf{r}')c^{(2)}(\mathbf{r},\mathbf{r}';\xi')\end{aligned} \tag{3.76}$$

which can be further simplified using the facts that the ξ-integral of the second term trivially gives unity and in the third term we can use the relation Eq.(3.74) for $n = 2$. Thus, the following formally exact expression is found

$$\beta\mathcal{F}_{\text{ex}}[\rho] = \beta\mathcal{F}_{\text{ex}}[\rho_{\text{ref}}] - \int d\mathbf{r}\,\Delta\rho(\mathbf{r})c^{(1)}_{\text{ref}}(\mathbf{r}) - \frac{1}{2}\int d\mathbf{r}\int d\mathbf{r}'\,\Delta\rho(\mathbf{r})\Delta\rho(\mathbf{r}')c^{(2)}_{\text{ref}}(\mathbf{r},\mathbf{r}') + \dots \tag{3.77}$$

that, truncating after the second term, only requires the the excess functional of the reference system and the direct correlation function. The reference system is often taken to be a homogeneous fluid $\rho_{\text{ref}}(\mathbf{r}) = \rho$ with the excess free energy being derived from an equation of state. Lastly, the direct correlation is obtained by the excess chemical potential.

Ramakrishnan and Yussouff employed the Percus-Yevick approximation in order to provide the direct correlation function and the Carnahan-Starling equation of state, Eq.(2.101), for the hard-sphere fluid. The corresponding functional is capable of describing solid-fluid coexistence of hard spheres. Its results are comparable to those of exact MC simulations [53].

The weighted-density approximation (WDA) of Tarazona [54] is regarded, besides Rosenfeld's Fundamental Measure Theory (FMT) Ch.4, as one of the most reliable density functionals for hard spheres. Starting with the exact low-density expansion for the excess functional

$$\beta\mathcal{F}_{\text{ex}}[\rho] = -\frac{1}{2}\int\int d\mathbf{r}\,d\mathbf{r}'\,\rho(\mathbf{r})\rho(\mathbf{r}')f(|\mathbf{r}-\mathbf{r}'|) - \tag{3.78}$$

$$\frac{1}{6}\int\int\int d\mathbf{r}d\mathbf{r}'d\mathbf{r}''\rho(\mathbf{r})\rho(\mathbf{r}')\rho(\mathbf{r}'')f(|\mathbf{r}-\mathbf{r}'|)f(|\mathbf{r}''-\mathbf{r}|)f(|\mathbf{r}'-\mathbf{r}''|) + \dots \tag{3.79}$$

Tarazona showed that the leading term of Eq.(3.78) can be captured if the weighted density

$$\bar{\rho}(\mathbf{r}) = -\frac{1}{8}\int d\mathbf{r}\,\rho(\mathbf{r}')f(r) \tag{3.80}$$

is defined which replaces the local density $\eta(\mathbf{r})$ of Eq.(3.70). Due to rather poor results regarding computer simulations [55], Tarazona improved his idea [56] fulfilling the expansion in Eq.(3.78) up to second order in proposing the functional

$$\beta\mathcal{F}_{\text{ex}}[\rho] = \int d\mathbf{r}\,\rho(\mathbf{r})\beta\Psi(\bar{\rho}(\mathbf{r})), \tag{3.81}$$

where $\Psi(\bar{\rho}(\mathbf{r}))$ is understood as the bulk free energy per particle. In this case, the weighted density $\bar{\rho}(\mathbf{r})$ is defined via a more general ansatz including weight functions $\omega(|\mathbf{r}-\mathbf{r}'|,\tilde{\rho}(\mathbf{r}))$

$$\bar{\rho}(\mathbf{r}) = \int d\mathbf{r}'\,\rho(\mathbf{r}')\omega(|\mathbf{r}-\mathbf{r}'|,\tilde{\rho}(\mathbf{r})) \tag{3.82}$$

with the constraint $\rho(\mathbf{r}) = \bar{\rho}(\mathbf{r}) = \tilde{\rho}(\mathbf{r}) = \rho_b$ in the bulk and hence

$$\int d\mathbf{r}\,\omega(\mathbf{r},\rho_b) = 1 \tag{3.83}$$

Of course, the weight function ω is yet unknown and we need to find an access in order to specify it further. Tarazona expanded the weight function with respect to the density

$$\omega(r,\rho) = \omega_0(r,\rho) + \rho\omega_1(r,\rho) + \rho^2\omega_2(r,\rho) + \dots \tag{3.84}$$

which in turn has a corresponding expansion for the weighted density $\bar{\rho}(\mathbf{r})$. If these expansions are inserted into the correlation function $c(r)$ derived from Eq.(3.81) and compared to the low-density expansion of $c(r)$ we find for instance

$$\omega_0(r,\rho) = \frac{3}{4\pi\sigma^3}\Theta(\sigma - r). \tag{3.85}$$

Further works [57] could improve upon the averaged density $\tilde{\rho}(\mathbf{r})$, which in the case of Tarazona equals $\bar{\rho}(\mathbf{r})$, by defining it as the global average of the density $\rho(\mathbf{r})$ requiring less computational effort.

We want to conclude this section in mentioning that the excess free energy density for any pair potential must find its functional part in order to apply cDFT. While for hard-sphere fluids we could present some approaches to construct reliable and accurate functionals, any interactions going beyond the hard spheres is hardly captured by reasonable methods. In these cases, MFA, Eq.(3.68) is often employed to describe simple liquids, i.e. liquids with a fairly simple pair potential $\phi(r)$ solely depending on the distance r. In principle, if we knew an accurate equation of state of the associated fluid we could derive via thermodynamic relations the excess free energy density that would provide a starting point to construct more accurate functionals for simple liquids. Especially for one-dimensional systems exact equation of states can be found [27] that could enable the development of new functionals even for higher dimensional systems.

3.9 Scaled-Particle Theory

The simple idea of inserting a hard sphere of radius R into a mixture of m hard spheres of radii R_i, $i = 1,\ldots,m$ provides an alternative approach to the thermodynamics of such systems. The required work of this insertion, especially in the cases of $R \to 0$ and $R \to \infty$, is equivalent to the excess chemical potential $\mu_{\text{ex}}(R)$ [7, 58, 59]. Suppose we have N_i particles of species i confined in a volume of size V hence with particle density $\rho_i = N_i/V$. Then, the insertion of a particle of radius $R \ll R_i$ can also be viewed as a spontaneous fluctuation of the hard-sphere mixture in such a way that a cavity of the same radius as the inserted particle is produced. Therefore, there is the probability

$$p(R) = \exp(-\beta\mu_{\text{ex}}(R)) \tag{3.86}$$

which is at the same time also the probability of finding a cavity of radius $R + R_i$, i.e. an exclusion sphere the particle of radius R_i cannot enter. With Eq.(3.86), we define the probability that such an insertion is not possible as $\bar{p}(R) = 1 - p(R)$.

Let us now think of cavities that fulfill $R + R_i \leq R_i$, i.e. unphysical cavities where the radius attains negative values. In this case, the corresponding cavity can at most hold one particle and consequently the probability that a particle of species i occupies this cavity is a sum over all species

$$\bar{p}(R) = \sum_{i=1}^{m} \frac{4\pi}{3}(R + R_i)^3\rho_i \tag{3.87}$$

or taking into account Eq.(3.86)

$$\beta\mu_{\text{ex}}(R) = -\log\left(1 - \sum_{i=1}^{m} \frac{4\pi}{3}(R + R_i)^3\rho_i\right) \tag{3.88}$$

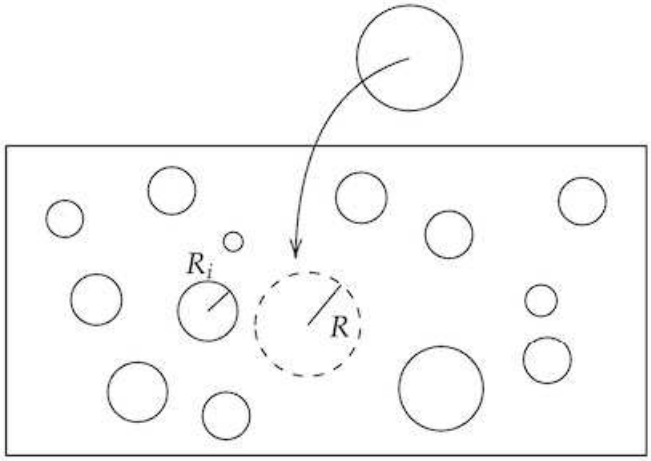

Figure 3.4: If a particle of radius R is inserted into a mixture of m hard-sphere species with radius R_i, an exclusion sphere or cavity of size $R + R_i$ is created.

On the other hand, the case of $R \to \infty$ corresponds to the reversible work of a large cavity accounting for the expansion against the surrounding pressure P of the hard-sphere mixture

$$\lim_{V\to\infty} \frac{\mu_{\text{ex}}}{V} \approx \frac{4\pi}{3} R^3 P. \tag{3.89}$$

A geometrical interpretation of Eq.(3.89) allows for interpolating for medium-sized cavities, i.e. not only do we add a volume term accompanied by the pressure but also terms accounting for lower dimensional measures of the cavity such as its surface. Hence, we extend Eq.(3.89) to

$$\mu_{\text{ex}}(R) = \frac{4\pi}{3} R^3 P + 4\pi R^2 \gamma + 4\pi R \kappa + \bar{\kappa}, \tag{3.90}$$

where the remaining physical quantities γ, κ and $\bar{\kappa}$ are found by imposing continuity of $\mu_{\text{ex}}(R)$ and its derivative at $R = 0$. Performing these calculations leads to

$$\begin{aligned} \beta\bar{\kappa} &= -\log(1-\xi_3) \\ 4\pi\beta\kappa &= \frac{\xi_2}{1-\xi_3} \\ 4\pi\beta\gamma &= \frac{4\pi\xi_1}{1-\xi_3} + \frac{\xi_2^2}{2(1-\xi_3)^2}, \end{aligned} \tag{3.91}$$

where the scaled-particle variables

$$\begin{aligned} \xi_3 &= \frac{4\pi}{3}\sum_{i=1}^{m} \rho_i R_i^3, \quad \xi_2 = 4\pi \sum_{i=1}^{m} \rho_i R_i^2 \\ \xi_1 &= \sum_{i=1}^{m} \rho_i R_i, \quad \xi_0 = \sum_{i=1}^{m} \rho_i. \end{aligned} \tag{3.92}$$

represent these geometrical measures weighted with densities of species. Given the expression Eq.(3.90) for the chemical potential in geometrical terms and the relations Eq.(3.91), the excess chemical potential of inserting a hard sphere of radius R_i reads

$$\beta\mu_{\text{ex},i}(R_i) = \frac{4\pi}{3} R_i^3 \beta P + \frac{4\pi R_i^2 \xi_1 + R_i \xi_2}{1-\xi_3} + \frac{R_i^2 \xi_2^2}{2(1-\xi_3)^2} - \log(1-\xi_3). \tag{3.93}$$

Finally, utilizing the thermodynamic relationship between pressure and chemical potential, latter can be derived to give

$$\beta P = \frac{\xi_0}{1-\xi_3} + \frac{\xi_1\xi_2}{(1-\xi_3)^2} + \frac{\xi_2^3}{12\pi(1-\xi_3)^3}, \tag{3.94}$$

where we should note that it reduces to the Percus-Yevick equation of state in the single component case, $m = 1$

$$\begin{aligned}
\beta P^{\mathrm{PY}} &= \frac{\rho}{1-\eta} + \frac{\rho R \cdot 4\pi R^2 \rho}{(1-\eta)^2} + \frac{(4\pi\rho R^2)^3}{12\pi(1-\eta)^3} \\
&= \frac{\rho}{1-\eta} + \frac{3\rho\eta}{(1-\eta)^2} + \frac{36\pi\rho\eta^2}{12\pi(1-\eta)^3} \\
&= \rho\left(\frac{1}{1-\eta} + \frac{3\eta}{(1-\eta)^2} + \frac{3\eta^2}{(1-\eta)^3}\right) \\
&= \rho\frac{1+\eta+\eta^2}{(1-\eta)^3},
\end{aligned} \tag{3.95}$$

where we used the packing fraction $\eta = 4\pi R^3\rho/3$. The excess free-energy density of the hard-sphere mixture is

$$\beta f_{\mathrm{ex}} = -\xi_0 \log(1-\xi_3) + \frac{\xi_1\xi_2}{1-\xi_3} + \frac{\xi_2^3}{24\pi(1-\xi_3)^2}. \tag{3.96}$$

The ideas of scaled-particle theory laid out in this section played an important role in the development of constructing functionals for hard spheres, e.g. as Rosenfeld attempted to find an ansatz for the excess free energy density. Additionally, we have seen that such relatively simple ideas can connect the structure of hard spheres to thermodynamic quantities of the system.

Chapter 4

Fundamental Measure Theory

In section Sec.3.8 we have introduced several ideas and formalism to construct excess functionals for systems including hard-sphere or other possible interactions. Especially former serve as a reference for more complicated interactions whose functionals are expanded around the hard-sphere part. In particular, the scaled particle theory approach of Sec.3.9 demonstrated that the geometrical properties of the underlying particles, such as spheres, already define the thermodynamics of the system, e.g. pressure, isothermal compressibility and so forth which can be also seen in the fact that only the packing fraction η appears in the mathematical description. Yasha Rosenfeld [9] presented novel ideas of a density functional theory of hard-sphere mixtures making use of the geometrical properties of the spheres, e.g. volume, surface etc. Consequently, the formalism is termed as Fundamental Measure Theory (FMT) that employs quantities that "measure" the effects of the finite size of the spheres in order to construct an excess functional. There was a lot of progress regarding inhomogeneous cases of hard-sphere fluids [60, 9].

The stable crystalline phase could not be captured by FMT, igniting some improvements and refinements [61, 62] of FMT considering the $0D$-limit, i.e. a narrow cavity capable of at most holding one particle. In detail, the requirement of an exact reduction to the $0D$ free energy density provided further insights into the structure of FMT with more accurate functionals giving satisfactory descriptions for extreme confinement. This reproduction of the $0D$-limit therefore enabled the construction of hard-sphere excess functionals solely depending on this concept, as was described by Tarazona and Rosenfeld [63, 64, 65]. Important thermodynamic features, e.g. equation of state or correlation function, are no more input but output of the formalism [64, 66].

One of the drawbacks of the original FMT is the fact that the Percus-Yevick (PY) equation of state Eq.(3.57) is obtained for the homogeneous fluid, similar to scaled particle theory. As was pointed out earlier in Sec.2.5.1, the PY equation of states overestimates the pressure of the hard-sphere fluid, near to bulk freezing [7]. In contrast, the Carnahan-Starling equation of state, Eq.(2.101), improves for high densities. Former can be incorporated in the construction of the so-called White-Bear functionals [62, 67] and the more recent White-Bear Mark II functional [68].

4.1 Hard Rods $D = 1$

To easily introduce the framework of FMT, we consider the most simple example of hard spheres: hard rods in $D = 1$. The system consists of m hard rods of diameter $\sigma_i = 2R_i$ that can only move along the z-axis and hence can interact only with their next

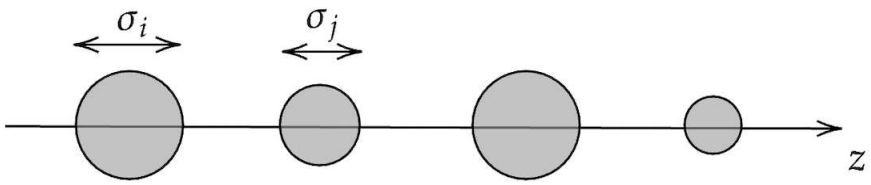

Figure 4.1: The one-dimensional hard-rod mixture where species i has diameter σ_i. There is only one degree of freedom along the z-axis with next-neighbor interaction.

neighbors, left and right. The structure of Rosenfeld's FMT follows the exact excess free energy density of a hard-rod mixture [69, 70].

We make the following ansatz for the excess functional for hard rods in $D = 1$

$$\beta\mathcal{F}_{\text{ex}}[\{\rho_\alpha\}] = \int dz\, \Phi(\{n_\alpha\}), \tag{4.1}$$

where Φ is the free energy density being a function of weighted densities n_α defined by

$$n_\alpha(z) = \sum_{i=1}^{m} \int dz'\, \rho_i(z)\omega_\alpha^i(z - z'). \tag{4.2}$$

The weighted densities n_α are therefore a sum of convolutions of the local density ρ_i and the weight function ω_α^i representing the geometrical properties of component i. Here in the one-dimensional case $D = 1$, the volume and the surface of the hard rods provide all geometric information of the particle. The surface, actually the edges of a given hard rod, is defined as

$$\omega_0^i(z) = \frac{1}{2}\left(\delta(z - R_i) + \delta(z + R_i)\right), \tag{4.3}$$

i.e. we get contributions only from the surface. Similarly, the second weight function

$$\omega_1^i(z) = \Theta(R_i - |z|) \tag{4.4}$$

describes the volume. The Mayer function $f_{ij}(z)$ between hard-rod species i and j is, of course, given by

$$f_{ij}(z) = \begin{cases} -1, & |z| < R_i + R_j \\ 0, & \text{otherwise,} \end{cases} \tag{4.5}$$

which can be expressed as convolutions of the weight functions

$$-f_{ij}(z) = \omega_1^i \otimes \omega_0^j + \omega_0^i \otimes \omega_1^j \tag{4.6}$$

with the abbreviation

$$\omega_i^\alpha \otimes \omega_j^\beta\,(z = z_i - z_j) = \int dz'\, \omega_i^\alpha(z' - z_i)\omega_j^\beta(z' - z_j). \tag{4.7}$$

The one-dimensional case $D = 1$ is unique since a given particle in the chain can only interact with its next neighbors, thus merely two-body interactions are possible. As a consequence, the representation of Eq.(4.6) fully encapsulates the interactions of the hard rods, i.e. can be exactly described with the aid of the weighted densities. So far, we do not know anything about the free energy density Φ. However, using dimensional

analysis we can make an ansatz for it. Let us assume a one-component hard-rod system of diameter σ and bulk density ρ_b. Then, it is easily shown that the weighted densities have the following bulk limits

$$n_1(z) \to \rho_b \sigma = \eta, \quad n_0(z) \to \rho_b, \tag{4.8}$$

i.e. n_1 is dimensionless whereas n_0 has the dimension of a density. Given this information, the only possibility of an excess free energy density $\Phi(n_0, n_1)$ of dimension density is

$$\Phi(n_0, n_1) = n_0 f(n_1), \tag{4.9}$$

where $f(n_1)$ is an arbitrary function of n_1 which we have still to specify. The excess chemical potential μ_{ex} is formally defined as

$$\beta\mu_{\text{ex}} = \frac{\partial\Phi}{\partial\rho_b} = \frac{\partial\Phi}{\partial n_0}\frac{\partial n_0}{\partial\rho_b} + \frac{\partial\Phi}{\partial n_1}\frac{\partial n_1}{\partial\rho_b}, \tag{4.10}$$

where we applied the chain rule. With the bulk properties given in Eq.(4.8) we obtain

$$\beta\mu_{\text{ex}} = \frac{\partial\Phi}{\partial n_0} + \sigma\frac{\partial\Phi}{\partial n_1}. \tag{4.11}$$

Now, we make use of the scaled-particle observation that if a very large cavity is considered the reversible work is given by the contribution accounting for the pressure P. The reversible work is at the same time the excess chemical potential, i.e. the energy needed to insert a particle into the system. Therefore, we have argued that

$$\lim_{\sigma\to\infty} \frac{\beta\mu_{\text{ex}}}{\sigma} = \beta P \tag{4.12}$$

must hold, where the volume here is, of course, just the diameter σ. From Eq.(4.12) and Eq.(4.11) it thus follows the important relation

$$\beta P = \frac{\partial\Phi}{\partial n_1}. \tag{4.13}$$

On the other hand, we have the thermodynamic relation for the pressure P

$$\beta P = -\Phi + n_0\left(\frac{\partial\Phi}{\partial n_0} + \sigma\frac{\partial\Phi}{\partial n_1}\right), \tag{4.14}$$

where we already replaced the bulk density ρ_b with n_0. Inserting Eq.(4.13) into Eq.(4.14), we encounter a differential equation for Φ

$$\frac{\partial\Phi}{\partial n_1} = -\Phi + n_0\left(\frac{\partial\Phi}{\partial n_0} + \sigma\frac{\partial\Phi}{\partial n_1}\right) \tag{4.15}$$

which, using the ansatz Eq.(4.9), reduces to

$$\frac{df(n_1)}{dn_1} = 1 - n_1 \tag{4.16}$$

with the solution

$$f(n_1) = -\log(1 - n_1) + C. \tag{4.17}$$

The remaining constant C must be zero as for $n_1 \to 0$ we must have $\Phi \to 0$ corresponding to having no particles in the system. In total, we have derived a simple and exact expression for the free energy density

$$\Phi(n_0, n_1) = -n_0 \log(1 - n_1) \tag{4.18}$$

giving rise to the equation of state

$$\beta P = \frac{n_0}{1 - n_1} \tag{4.19}$$

or, if we restrict ourselves to the one-component case ($n_0 \to \rho_b$ and $n_1 \to \eta$)

$$\beta P = \frac{\rho_b}{1 - \eta}. \tag{4.20}$$

We want to also give an alternative derivation of the equation of state in Eq.(4.20) using the canonic partition sum, Eq.(2.39). This means, that we have to evaluate

$$Z = \frac{1}{\lambda_T^N} \int d^N z \, \exp(-\beta U(z_1, \ldots, z_N)), \tag{4.21}$$

where we adjusted the dimensions properly and kept in mind that since the hard rods are aligned in a fixed chain of finite length L no permutations have to be considered, therefore no factor of $N!$ in Eq.(4.21). The integral in Eq.(4.21) only contributes when the particles do not penetrate each other, i.e. its evaluation is of pure geometric nature. Suppose we take the first particle in the chain. Its center-of-mass coordinate z_1 has the following bounds $z_1 \in [R, L - R - (N-1) \cdot 2R]$, for the second particle $z_2 \in [z_1 + 2R, L - R - (N-2) \cdot 2R]$ etc., that means in general for the k-th particle in the chain $z_k \in [z_{k-1} + 2R, z_k^{\max}]$, $k > 1$ where $z_k^{\max} = L - R - (N-k) \cdot 2R$. The partition sum Eq.(4.21) then reads

$$Z = \frac{1}{\lambda_T^N} \int_R^{z_1^{\max}} dz_1 \int_{z_1+2R}^{z_2^{\max}} dz_2 \cdots \int_{z_{N-2}+2R}^{z_{N-1}^{\max}} dz_{N-1} \int_{z_{N-1}+2R}^{L-R} dz_N. \tag{4.22}$$

The integrals have to be taken from the right to the left as they are nested. Arriving at the k-th step in Eq.(4.22), we find

$$\frac{1}{k!} (L - (2k-1)R - z_k)^k \tag{4.23}$$

so that the last integral in Eq.(4.22) is

$$\int_R^{L-R-2(N-1)R} dz_1 \, \frac{1}{(N-1)!} (L - (2N-1)R - z_1)^{N-1} \tag{4.24}$$

leading to the final expression for the partition sum

$$Z = \frac{1}{\lambda_T^N N!} (L - N\sigma)^N. \tag{4.25}$$

The one-dimensional bulk density is given by $\rho_b = N/L$ with the packing fraction $\eta = \rho_b \sigma$, so Eq.(4.25) is rewritten as

$$Z = \frac{1}{N!} \left(\frac{L}{\lambda_T} \right)^N (1 - \eta)^N \tag{4.26}$$

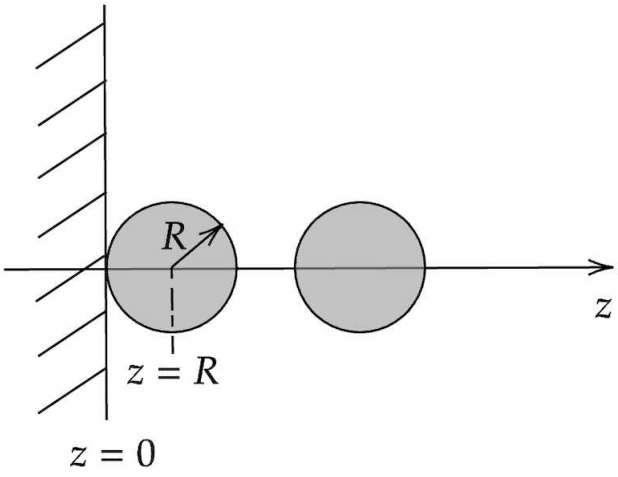

Figure 4.2: Hard rods of radius R in the vicinity of a hard wall.

from which we obtain the free energy

$$\beta F = \log(N!) - N \log\left(\frac{L(1-\eta)}{\lambda_T}\right) \tag{4.27}$$

and via the relation

$$P = -\left(\frac{\partial F}{\partial L}\right)_{T,N} \tag{4.28}$$

we finally get

$$\beta P = \frac{\rho_b}{1-\eta} \tag{4.29}$$

which is equal to what we have found within FMT, Eq.(4.20). As the statistical mechanical derivation of the equation of state of hard rods in $D = 1$ did not use any approximations, it is exact and therefore verifying the FMT approach to be exact, too.

4.1.1 Hard Rods at a Hard Wall

One simple but yet insightful application of FMT is a system of one-component hard rods at a hard wall, see Fig.4.2. We ask for the equilibrium density profile $\rho(z)$ in the presence of a hard, impenetrable wall modeled as an external potential

$$V_{\text{ext}}(z) = \begin{cases} \infty, & z < R \\ 0, & \text{otherwise.} \end{cases} \tag{4.30}$$

As we can provide an exact expression for the excess functional, Eq.(4.1), a corresponding density profile minimizing the grand functional can be found. The minimization is of the grand functional is achieved by applying the Picard iteration scheme often used in the framework of cDFT, Sec.3.5. The initial profile $\rho^{(0)}(z)$ here is, according to the external potential, taken as $\rho^{(0)}(z) = \rho_b\,\Theta(z-R)$ also obeying the boundary condition in the bulk.

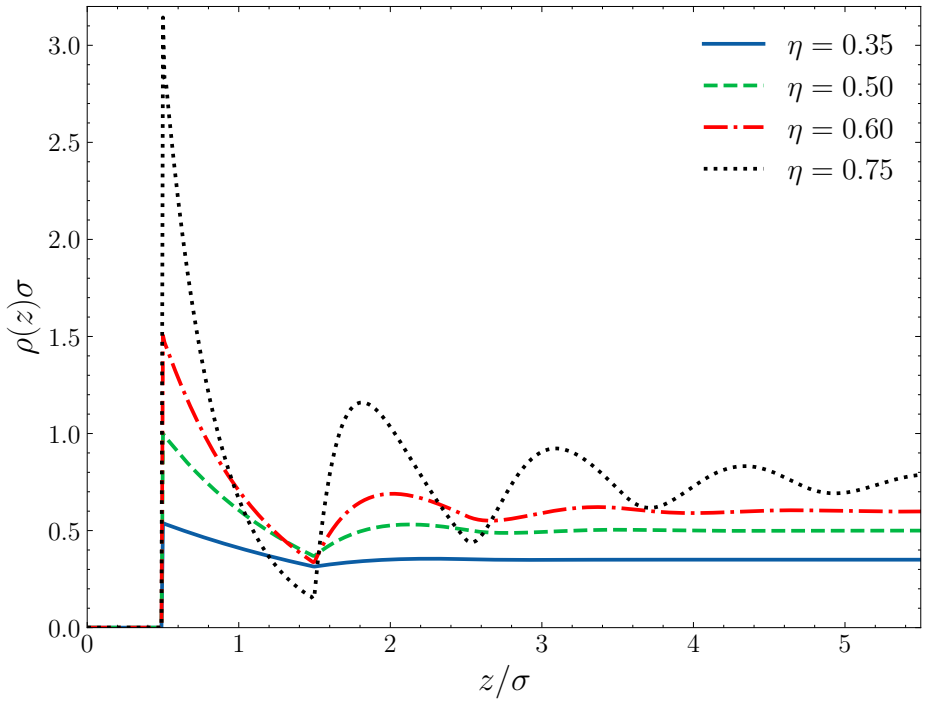

Figure 4.3: Normalized density profiles $\rho(z)/\rho_b$ for several packing fractions $\eta = 0.35$, 0.50, 0.60, and 0.75 near a hard wall located at $z = 0$. Correlations close to the hard wall become more pronounced and prolonged towards the bulk as the density in the system increases.

The one-body correlation function $c^{(1)}(z)$ needed for minimization is given by

$$\begin{aligned} c^{(1)}(z) &= -\beta \frac{\delta \mathcal{F}_{\text{ex}}[\rho]}{\delta \rho(z)} \\ &= -\frac{\delta}{\delta \rho(z)} \int dz' \, \Phi(n_0, n_1) \\ &= -\int dz' \sum_{\alpha=0}^{1} \frac{\partial \Phi}{\partial n_\alpha(z')} \frac{\delta n_\alpha(z')}{\delta \rho(z)} \\ &= -\int dz' \sum_{\alpha=0}^{1} \frac{\partial \Phi}{\partial n_\alpha(z')} \omega_\alpha(z' - z) \end{aligned} \tag{4.31}$$

where we used the definition Eq.(4.2) of the weighted densities n_α in the last line. Hence, the computation of $c^{(1)}(z)$ includes convolutional integrals of the partial derivatives of the free energy density Φ with respect to the weighted densities. An explicit representation of the convolutions for the weighted densities is shown in Sec.B.1.

Finally, the excess chemical potential μ_{ex} is derived from the pressure to give

$$\beta \mu_{\text{ex}} = \frac{\eta}{1 - \eta} - \log(1 - \eta). \tag{4.32}$$

In Fig.4.3 we display several density profiles $\rho(z)$ for several packing fractions. As we expect, for $z < 0.5 \cdot \sigma$ the density profile is zero since the wall is impenetrable. Close to the wall, we observe oscillations that become more pronounced as the packing fraction

η	$\rho_c\sigma$	$\beta P\sigma$	Γ	$-(d\gamma/d\mu)_T$
0.35	0.538462	0.538526	-0.112638	-0.113750
0.50	1.000540	1.000000	-0.123121	-0.125001
0.60	1.502499	1.500000	-0.117364	-0.120004
0.75	3.063320	3.000000	-0.088933	-0.093958

Table 4.1: Listed are values of the sum rules for pressure and adsorption of hard spheres at a hard wall of Fig.4.3. We see good agreement for both relations of Eq.(4.33) and Eq.(4.36).

is increased. Furthermore, the density profiles approach their bulk value, i.e. spatial correlations vanish as the distance to the hard wall increases.

The contact value, i.e. $\rho_c = \rho(R^+)$, is directly related to the bulk pressure βP

$$\rho_c = \beta P \tag{4.33}$$

also termed as contact theorem [7]. This simple relation is insofar interesting as it connects on the one hand microscopic quantities with a thermodynamic one and on the other hand serves as a numerical test of the underlying computation of cDFT therefore also measuring the accuracy of the minimization. The contact theorem Eq.(4.33) is easily generalized to mixtures also including more complicated external potentials. In addition, the Gibbs adsorption Γ is employed as a second measure for accuracy. It is interpreted as the excess amount of particles in the system, i.e. if the dividing Gibbs surface is repulsive or attractive. Keep in mind that cDFT uses the grand-canonical ensemble, thus particles can be added or removed from the surrounding particle reservoir. In the $D = 1$ case, the adsorption is given by

$$\Gamma = \int dz \, (\rho(z) - \rho_b) \tag{4.34}$$

and at the same time also given by a thermodynamic relation

$$\Gamma = -\left(\frac{\partial \gamma}{\partial \mu}\right)_T, \tag{4.35}$$

where γ is the surface tension defined on the Gibbs dividing surface at $z = R$. Note that in principle any dividing surface could be taken, i.e. the definition of γ has an ambiguity. The surface tension γ is obtained from the thermodynamic relation $\Omega = -pV + \gamma A$, i.e. where the grand potential Ω is now expressed for a system of volume V and surface A.

Thus, if our cDFT computation is correct, to a good degree we should satisfy

$$\int_R^\infty dz \, (\rho(z) - \rho_b) = -\left(\frac{\partial \gamma}{\partial \mu}\right)_T \tag{4.36}$$

which is termed as Gibbs adsorption theorem. It should be reminded that $\rho(z)$ and γ in Eq.(4.36) are calculated in cDFT minimizing the grand functional $\Omega[\rho]$. Table4.1 demonstrates the degree of numerical consistency for high packing fractions.

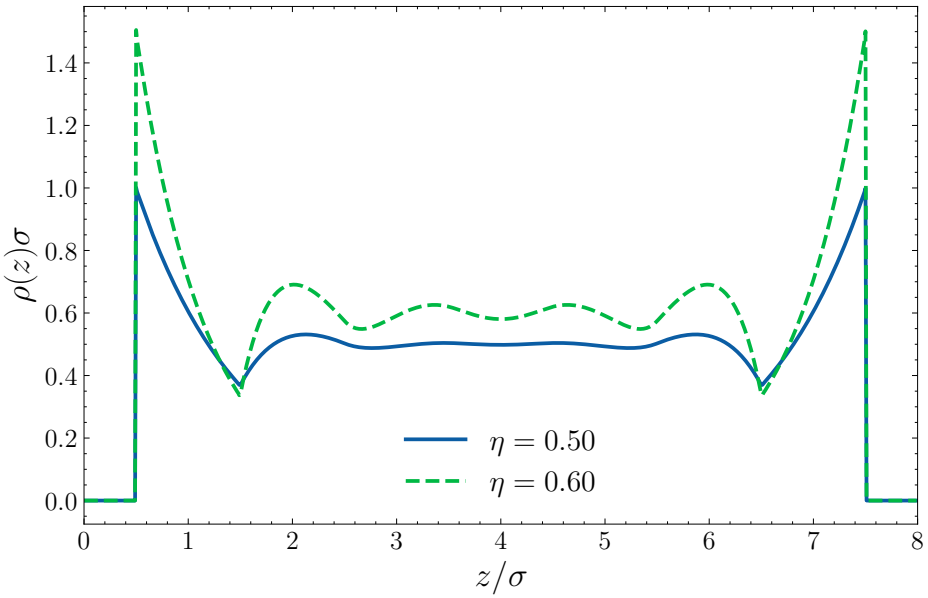

Figure 4.4: Density profiles $\rho(z)$ of hard spheres between two hard walls representing a finite system of length $L = 8\sigma$.

4.1.2 Hard Rods between two Hard Walls

We can put a second wall at $z = L$ where L shall be the finite length of the system. Then, here the external potential has the form

$$V_{\text{ext}}(z) = \begin{cases} \infty, & z < R \quad \text{or} \quad z > L - R \\ 0, & \text{otherwise,} \end{cases} \tag{4.37}$$

so that the density profile is initialized as $\rho^{(0)}(z) = \rho_b\,\Theta(z - R)\Theta(L - R - z)$. Thus, the corresponding grand potential $\Omega[\rho]$ is again minimized where the same convolutions are performed as in Sec.4.1.1. As we now consider a finite system of length L, we should see deviations regarding thermodynamic quantities. This is due to the fact that the thermodynamic limit, i.e. $N, V \to \infty$ with $N/V = \text{const.}$, is not well fulfilled.

Figure4.4 displays two density profiles $\rho(z)$ for high packing fractions. According to our expectation, $\rho(z)$ is symmetric with respect to the middle of the system $z = L/2$ and exhibits oscillations that decay towards the "bulk". This finite system, of course, starts to resemble the case of hard spheres at a hard wall with a well defined bulk, i.e. $\rho(z \to \infty) \to \rho_b$, if the system's size L is made arbitrarily high. Another way to put it is that correlations at the hard walls begin to vanish towards the bulk of the system sufficiently enough. On the other hand, the contact value $\rho(R^+)$ being related to the bulk pressure P, Eq.(4.33), does not hold anymore as it remains true only if the thermodynamic limit is assumed.

The rather simple system of hard rods in a slit can be also described analytically by making the following observation on the corresponding Euler-Lagrange equation [71]

$$\beta\mu = \beta u(x) + \log\rho(x) - \log\left[1 - \int_x^{x+\sigma} dx'\,\rho(x')\right] + \int_x^{x+\sigma} dx'\,\frac{\rho(x')}{1 - \int_x^{x+\sigma} dx''\,\rho(x'')}, \tag{4.38}$$

where μ is the chemical potential and σ the rod length. $u(x)$ is an external potential with

the property

$$e^{-\beta u(x)} = \begin{cases} 0, & \text{if} \quad x < 0, \quad x > L \\ e^{-\beta\phi(x)}, & \text{otherwise.} \end{cases} \tag{4.39}$$

Now, we can introduce the auxiliary function

$$h(x) = \frac{\rho(x)}{1 - \int_x^{x+\sigma} dx'\, \rho(x')} \tag{4.40}$$

to rewrite Eq.(4.38) in the form

$$h(x) = e^{\beta(\mu - u(x))} \exp\left[- \int_{x-\sigma}^{x} dx'\, h(x') \right]. \tag{4.41}$$

The purpose of this approach is to differentiate Eq.(4.40) and Eq.(4.41) and rearrange them to obtain

$$h'(x) + h(x)\left(\beta\phi'(x) + h(x) - h(x-\sigma)\right) = 0 \tag{4.42}$$

and with $\ell(x) = \rho(x)/h(x)$

$$\ell'(x) - h(x)\ell(x) + \ell(x+\sigma)h(x+\sigma) = 0 \tag{4.43}$$

which can be considered as to differential equations for h and ℓ that determine the density profile via $\rho(x) = h(x)\ell(x)$. We have the following boundary conditions

$$h(0) = e^{\beta(\mu - \phi(0))}, \quad \ell(L) = 1. \tag{4.44}$$

In general, given the external potential $\phi(x)$ inside the slit, Eq.(4.42) is solved first as it is completely decoupled from the other auxiliary function $\ell(x)$. Due to the shift $x - \sigma$ being present in Eq.(4.42), there is no known recipe to solve the non-local differential equation. Instead, the solutions $h_j(x)$ can only be found piecewise in the intervals $j\sigma < x < (j+1)\sigma$ using the associated boundary conditions. Consequently, the length L of the slit determines the number of steps necessary in order to fully solve for $h(x)$. The detailed procedure is presented in [72].

4.2 Hard Spheres in $D = 3$

Starting point for the construction of an excess functional for a three-dimensional hard-sphere mixture of m components is the exact low-density limit

$$\beta\mathcal{F}_{\text{ex}}[\{\rho_i\}] = -\frac{1}{2}\sum_{ij} \int\int d\mathbf{r}\, d\mathbf{r}'\, \rho_i(\mathbf{r})\rho_j(\mathbf{r}')f_{ij}(|\mathbf{r} - \mathbf{r}'|) \tag{4.45}$$

with the Mayer function

$$f_{ij}(r) = \begin{cases} -1, & r < R_i + R_j \\ 0, & \text{otherwise} \end{cases} \tag{4.46}$$

which represents the volume being not accessible by, let's say species i, close to species j, i.e. an exclusion sphere of radius $R_i + R_j$. Rosenfeld proposed the following decomposition of the Mayer function in terms of weight functions $\omega_\alpha(\mathbf{r})$ [9]

$$-f_{ij}(r) = \omega_3^i \otimes \omega_0^j + \omega_0^i \otimes \omega_3^j + \omega_2^i \otimes \omega_1^j + \omega_1^i \otimes \omega_2 - \mathbf{w}_2^i \otimes \mathbf{w}_1^j - \mathbf{w}_1^i \otimes \mathbf{w}_2^j, \tag{4.47}$$

where now we have several weight functions

$$\omega_3^i(\mathbf{r}) = \Theta(R_i - |\mathbf{r}|), \quad \omega_2^i(\mathbf{r}) = \delta(R_i - |\mathbf{r}|) \tag{4.48}$$
$$\omega_1^i(\mathbf{r}) = \frac{\omega_2^i(\mathbf{r})}{4\pi R_i}, \quad \omega_0^i(\mathbf{r}) = \frac{\omega_2^i(\mathbf{r})}{4\pi R_i^2}$$
$$\mathbf{w}_2^i(\mathbf{r}) = \delta(R_i - |\mathbf{r}|)\mathbf{e}_r, \quad \mathbf{w}_1^i(\mathbf{r}) = \frac{\mathbf{w}_2^i(\mathbf{r})}{4\pi R_i},$$

with the unit vector $\mathbf{e}_r = \mathbf{r}/r$ and $\otimes$ again abbreviating the now three-dimensional convolution

$$\omega_i^\alpha \otimes \omega_j^\beta(\mathbf{r} = \mathbf{r}_i - \mathbf{r}_j) = \int d\mathbf{r}'\, \omega_i^\alpha(\mathbf{r}' - \mathbf{r}_i)\omega_j^\beta(\mathbf{r}' - \mathbf{r}_j). \tag{4.49}$$

We see that, in contrary to the one-dimensional case, instead of only two weight functions we now have three independent weight functions, ω_3^i, ω_2^i and $\mathbf{w}_2^i$ where latter is a vector. The vectorial weight functions are needed because Rosenfeld [9] had to take into account the jump of the Mayer function at $r = \sigma$ in Eq.(4.47).

The deconvolution of Eq.(4.47) would be too complicated if the one-component system is concerned. However, inspired by the structure for one-dimensional hard rods [69, 70] this representation of the Mayer functions is suggested. Additionally, Kierlik and Rosinberg proposed weight functions that replace the vector-like ones of Eq.(4.48) with weight functions containing first and second derivative of the Dirac Delta [73]. The equivalence of these two approaches was shown in [74].

Analogously to the one-dimensional case in Sec.4.1, we introduce the weighted densities

$$n_\alpha(\mathbf{r}) = \sum_{i=1}^{m} \int d\mathbf{r}'\, \rho_i(\mathbf{r}')\, \omega_\alpha^i(\mathbf{r} - \mathbf{r}'), \tag{4.50}$$

where again we sum over all contributions stemming from the species i with their corresponding weight functions $\omega_\alpha^i(\mathbf{r})$. As was already observed in Sec.4.1, the weighted densities tend to their associated scaled-particle variables ξ_i, Sec.3.9, when the bulk of the system is reached, i.e. where $\rho(\mathbf{r}) = \rho_b$ holds due to the absence of any external potential $V_{\text{ext}}(\mathbf{r})$. Therefore, for a m-component system we have the bulk limits

$$n_3 \to \xi_3 = \frac{4\pi}{3} \sum_{i=1}^{m} \rho_b^i R_i^3, \quad n_2 \to \xi_2 = 4\pi \sum_{i=1}^{m} \rho_b^i R_2^3, \quad n_1 \to \xi_1 = \sum_{i=1}^{m} \rho_b^i R_i \tag{4.51}$$
$$n_0 \to \xi_0 = \sum_{i=1}^{m} \rho_b^i, \quad \mathbf{n}_2 \to 0, \quad \mathbf{n}_1 \to 0$$

in which the vectorial weighted densities $\mathbf{n}_2$ and $\mathbf{n}_1$ vanish in the bulk. Since there is no orientation preferred, antipodal contributions in Eq.(4.50) cancel out each other. From Eq.(4.51) we can infer that n_3 is a measure for the total packing fraction of the hard-sphere mixture.

Given the weighted densities, we can re-express the exact low-density limit Eq.(4.45) as

$$\beta\mathcal{F}_{\text{ex}}[\{\rho_i\}] = \int d\mathbf{r}\ (n_0(\mathbf{r})n_3(\mathbf{r}) + n_1(\mathbf{r})n_2(\mathbf{r}) - \mathbf{n}_1(\mathbf{r}) \cdot \mathbf{n}_2(\mathbf{r})) \tag{4.52}$$

which reduces to Eq.(4.45) again, if we insert the definitions of the weighted densities, Eq.(4.50).

4.2.1 Rosenfeld Functional

We would like to repeat the derivation of the free energy density Φ of Sec.4.1 which was found to be exact, as $D = 1$ does not allow for three-body, four-body etc. interactions. However, here we consider $D = 3$ and thus the higher order corrections to the excess functional must be neglected in order to make the same approach for Φ feasible in $D = 3$. This means, that $\Phi(\{n_\alpha\})$ for three-dimensional hard spheres can only be an approximation fulfilling the exact low-density limit of Eq.(4.45) and any extrapolation to higher densities has to be tested on its accuracy. In particular, for asymmetrical hard-sphere mixtures, i.e. mixtures where the radii R_i severely differ from each other, this turns into a serious problem of FMT [66].

Rosenfeld again proposed the ansatz of the form of Eq.(4.9)

$$\beta\mathcal{F}_{\text{ex}}[\{\rho_i\}] = \int d\mathbf{r}\, \Phi(\{n_\alpha\}) \tag{4.53}$$

and dimensional analysis led Rosenfeld to the following ansatz

$$\Phi(\{n_\alpha\}) = f_1(n_3)n_0 + f_2(n_3)n_1n_2 + f_3(n_3)\mathbf{n}_1\mathbf{n}_2 + f_4(n_3)n_2^3 + f_5(n_3)n_2\mathbf{n}_2\mathbf{n}_2, \tag{4.54}$$

where the dimensionless functions $f_i(n_3)$, $i = 1, \ldots, 5$ are yet to be determined. These functions, in order to obey the low-density limit Eq.(4.52), must behave for low n_3 as

$$\begin{aligned} f_1(n_3) = n_3 + \ldots, \quad f_2(n_3) = 1 + \ldots, \quad f_3(n_3) = -1 + \ldots \\ f_4(n_3) = \frac{1}{24\pi} + \ldots, \quad f_5(n_3) = -\frac{3}{24\pi} + \ldots \end{aligned} \tag{4.55}$$

with the explicitly written leading order terms. To further proceed with the determination of the functions $f_i(n_3)$, we again use the thermodynamic condition as in the original derivation of Rosenfeld [75]

$$\lim_{R_i\to\infty} \frac{\mu^i_{\text{ex}}}{V_i} = P, \tag{4.56}$$

where $V_i = 4\pi R_i^3/3$ is the volume of a particle of radius R_i that is subject to an expansion $R_i \to \infty$, thus performing reversible work against the surrounding hard-sphere fluid of pressure P. We furthermore have

$$\beta\mu^i_{\text{ex}} = \frac{\partial\Phi}{\partial\rho_i} = \sum_\alpha \frac{\partial\Phi}{\partial n_\alpha}\frac{\partial n_\alpha}{\partial\rho_i} = V_i\frac{\partial\Phi}{\partial n_3} + \ldots \tag{4.57}$$

and together with Eq.(4.56) we find the important relation

$$\beta P = \frac{\partial\Phi}{\partial n_3}. \tag{4.58}$$

At the same time, we can employ the thermodynamic relation $\Omega = -pV$ from which $\beta\Omega/V = \Phi + \beta f_{\text{id}} - \sum_i \rho_b^i\beta\mu_i$ follows and with Eq.(4.57)

$$\beta P = -\Phi + \sum_\alpha \frac{\partial\Phi}{\partial n_\alpha}n_\alpha + n_0. \tag{4.59}$$

Finally, combining it with Eq.(4.58) we obtain a differential equation for Φ

$$\frac{\partial\Phi}{\partial n_3} = -\Phi + \sum_\alpha \frac{\partial\Phi}{\partial n_\alpha}n_\alpha + n_0. \tag{4.60}$$

To solve Eq.(4.60), we can first start to collect all terms being proportional to n_0 so

$$\frac{df_1(n_3)}{dn_3}(1-n_3)=1 \tag{4.61}$$

must hold yielding the solution

$$f_1(n_3)=-\log(1-n_3)+C_1, \tag{4.62}$$

where the integration constant C_1 has to vanish in order to fulfill the low-density limit. This goes similarly for the integration constants associated to the remaining functions $f_i(n_3)$. Rosenfeld has found the solutions [9]

$$\begin{aligned} f_1(n_3)=-\log(1-n_3), \quad f_2(n_3)=\frac{1}{1-n_3}, \quad f_3(n_3)=-f_2(n_3) \\ f_4(n_3)=\frac{1}{24\pi(1-n_3)^2}, \quad f_5(n_3)=-3f_4(n_3) \end{aligned} \tag{4.63}$$

which do satisfy the exact low-density limit, Eq.(4.52), as can be shown straightforwardly. The fact that $f_3(n_3)=-f_2(n_3)$ and $f_5(n_3)=-3f_4(n_3)$ is true assumes that Eq.(4.56) is still valid for slightly inhomogeneous systems. Since the vectorial weighted densities vanish in the bulk, there cannot be in principal thermodynamic relations that determine the functions $f_3(n_3)$ and $f_5(n_3)$. It can be only stated that the success of Rosenfeld's approach justifies the findings of Eq.(4.63).

Herewith, we arrive at the so-called Rosenfeld functional

$$\Phi^{\mathrm{RF}}(\{n_\alpha\})=\Phi_1+\Phi_2+\Phi_3^{\mathrm{RF}} \tag{4.64}$$

with the parts reading

$$\begin{aligned} \Phi_1=-n_0\log(1-n_3), \quad \Phi_2=\frac{n_1n_2-\mathbf{n}_1\mathbf{n}_2}{1-n_3} \\ \Phi_3^{\mathrm{RF}}=\frac{n_2^3-3n_2\mathbf{n}_2\mathbf{n}_2}{24\pi(1-n_3)^2}, \end{aligned} \tag{4.65}$$

where the special emphasis on Φ_3^{RF} will be clear later on when we introduce functionals that improve upon Rosenfeld's functional solely differing in the third part.

It should be appreciated that the Rosenfeld functional in Eq.(4.65) possesses the Percus-Yevick equation of state for a hard-sphere mixture and also reproduces the two-body correlation function of Percus-Yevick, see Eq.(3.55) and Eq.(3.57). It is very accurate in describing highly inhomogeneous fluid phases, however fails to describe the fluid to solid phase transition of pure hard-sphere systems. Including certain features of dimensional crossover, Rosenfeld could empirically remedy these shortcomings [61, 76]. For spherical cavities representing extreme confinement it was found that these modifications led to better results [77, 78]. The problem lies in the regularity of the Φ_3^{RF} term of the Rosenfeld functional for systems with highly pronounced peaks of the density profile. It turns out that Φ_3^{RF} is not bounded from below and thus leads to a divergence. Rosenfeld rather proposed the following modification

$$\Phi_3^{\mathrm{RF}}\to\Phi_3^{\mathrm{RF},q_3}=\frac{n_2^3}{24\pi(1-n_3)^2}\left(1-\frac{\mathbf{n}_2\cdot\mathbf{n}_2}{n_2^2}\right)^3 \tag{4.66}$$

being referred as the q_3-correction. Indeed, the new form of Eq.(4.66) is bounded from below, i.e. $\Phi_3^{\mathrm{RF},q_3} \geq 0$ as $|\mathbf{n}_2| \leq n_2$ which is shown from the simple inequality [79]

$$\begin{aligned} 0 &\leq \int d\mathbf{r}'\, \delta(R-|\mathbf{r}'|)\rho(\mathbf{r}-\mathbf{r}') \left(\frac{\mathbf{r}'}{r'} n_2(\mathbf{r}) - \mathbf{n}_2(\mathbf{r})\right)^2 \\ &= \int d\mathbf{r}'\, \delta(R-|\mathbf{r}'|)\rho(\mathbf{r}-\mathbf{r}') \left(n_2^2(\mathbf{r}) + \mathbf{n}_2^2(\mathbf{r}) - 2n_2(\mathbf{r})\frac{\mathbf{r}'}{r'}\cdot\mathbf{n}_2(\mathbf{r})\right) \\ &= n_2(\mathbf{r})\left(n_2^2(\mathbf{r}) + \mathbf{n}_2^2(\mathbf{r}) - 2\mathbf{n}_2^2(\mathbf{r})\right) \\ &= n_2(\mathbf{r})(n_2^2(\mathbf{r}) - \mathbf{n}_2^2(\mathbf{r})), \end{aligned} \tag{4.67}$$

thereby giving in total $\mathbf{n}_2^2(\mathbf{r}) \leq n_2^2(\mathbf{r})$. From the second to the third line in Eq.(4.67) we used the definition of $n_2(\mathbf{r})$ and considered merely the one-component case for simplicity. The power in Eq.(4.66) is chosen to be three as the leading terms reproduce those of the original Rosenfeld functional, Eq.(4.65). Other powers q are also used, but the version $q = 3$ is the most commun.

Another way to regularize Φ_3^{RF} is to introduce a tensorial weighted density $\mathbf{U}(\mathbf{r})$ with its associated weight function defined as

$$\mathbf{w}_{\mathrm{T}}^i(\mathbf{r}) = \left(\mathbf{e}_r \otimes \mathbf{e}_r - \frac{1}{3}\mathbb{I}\right)\delta(R_i - |\mathbf{r}|) \tag{4.68}$$

so $\mathbf{U}(\mathbf{r})$ reads [65]

$$\mathbf{U}(\mathbf{r}) = \sum_{i=1}^{m} \int d\mathbf{r}'\, \rho_i(\mathbf{r}')\mathbf{w}_{\mathrm{T}}^i(\mathbf{r}-\mathbf{r}'). \tag{4.69}$$

Then, the new functional is declared to be

$$\Phi_3^{\mathrm{RF}} \to \Phi_3^{\mathrm{RF,T}} = \Phi_3^{\mathrm{RF}} + \frac{9}{2}\frac{\mathbf{n_2}\mathbf{U}\mathbf{n}_2 - \mathrm{Tr}(\mathbf{U}^3)}{24\pi(1-n_3)^3} \tag{4.70}$$

that has the convenient property that while being successful in the description of hard-sphere crystal, as the q_3 functional of Eq.(4.66), it basically does not affect the already good description of the fluid phase, particularly leaving unchanged the equation of state. Alternatively to the definition of the traceless tensorial weight function of Eq.(4.68), also

$$\mathbf{w}_{\mathrm{T}}^i(\mathbf{r}) = \mathbf{e}_r \otimes \mathbf{e}_r\, \delta(R_i - |\mathbf{r}|) \tag{4.71}$$

is employed with the corresponding tensorial weighted density

$$\mathbf{T}(\mathbf{r}) = \frac{1}{3}n_2(\mathbf{r})\mathbb{I} + \mathbf{U}(\mathbf{r}) \tag{4.72}$$

and the functional now reading

$$\Phi_3^{\mathrm{RF,T}} = \frac{3\left(-n_2\mathbf{n}_2\cdot\mathbf{n}_2 + \mathbf{n}_2\mathbf{T}\mathbf{n}_2 + n_2\mathrm{Tr}(\mathbf{T}^2) - \mathrm{Tr}(\mathbf{T}^3)\right)}{16\pi(1-n_3)^2}. \tag{4.73}$$

The equivalence between Eq.(4.70) and Eq.(4.73) can be shown in first considering the traces

$$\begin{aligned} \mathrm{Tr}(\mathbf{T}) &= \mathrm{Tr}\left(\frac{1}{3}n_2\mathbb{I} + \mathbf{U}\right) = n_2 \\ \mathrm{Tr}(\mathbf{T}^2) &= \mathrm{Tr}\left(\frac{1}{9}n_2^2\mathbb{I} + \frac{2}{3}n_2\mathbf{U} + \mathbf{U}^2\right) = \frac{1}{3}n_2^2 + \mathrm{Tr}(\mathbf{U}^2) \\ \mathrm{Tr}(\mathbf{T}^3) &= \mathrm{Tr}\left(\frac{1}{27}n_2^3\mathbb{I} + \frac{1}{3}n_2^2\mathbf{U} + n_2\mathbf{U}^2 + \mathbf{U}^3\right) = \frac{1}{9}n_2^3 + n_2\mathrm{Tr}(\mathbf{U}^2) + \mathrm{Tr}(\mathbf{U}^3), \end{aligned} \tag{4.74}$$

where we have used $\mathrm{Tr}(\mathbb{I}) = 3$ and by definition $\mathrm{Tr}(\mathbf{U}) = 0$. Then, the parenthesis in the numerator of Eq.(4.73) becomes

$$-n_2\mathbf{n}_2\cdot\mathbf{n}_2 + \mathbf{n}_2\left(\frac{1}{3}n_2\mathbb{I}+\mathbf{U}\right)\mathbf{n}_2 + n_2\left(\frac{1}{3}n_2^2+\mathrm{Tr}(\mathbf{U}^2)\right) - \left(\frac{1}{9}n_2^3+n_2\mathrm{Tr}(\mathbf{U}^2)+\mathrm{Tr}(\mathbf{U}^3)\right) = \tag{4.75}$$

$$\begin{aligned}
&-n_2\mathbf{n}_2\cdot\mathbf{n}_2 + \frac{1}{3}n_2\mathbf{n}_2\cdot\mathbf{n}_2 + \mathbf{n}_2\mathbf{U}\mathbf{n}_2 + \frac{1}{3}n_2^3 + n_2\mathrm{Tr}(\mathbf{U}^2) - \frac{1}{9}n_2^3 - n_2\mathrm{Tr}(\mathbf{U}^2) - \mathrm{Tr}(\mathbf{U}^3) = \\
&-\frac{2}{3}n_2\mathbf{n}_2\cdot\mathbf{n}_2 + \mathbf{n}_2\mathbf{U}\mathbf{n}_2 + \frac{2}{9}n_2^3 - \mathrm{Tr}(\mathbf{U}^3) = \\
&\frac{2}{9}\left(n_2^3 - 3n_2\mathbf{n}_2\cdot\mathbf{n}_2\right) + \mathbf{n}_2\mathbf{U}\mathbf{n}_2 - \mathrm{Tr}(\mathbf{U}^3),
\end{aligned}$$

so inserting into Eq.(4.73) just yields the expression of Eq.(4.70).

4.2.2 White-Bear Functionals

The derivation of the Rosenfeld functional, Eq.(4.65), is based upon the idea of scaled-particle theory in combination with the thermodynamic relationship between the pressure P and the free energy density $\Phi(\{n_\alpha\})$ set to be a function of weighted densities n_α. Rosenfeld thus found a differential equation of Φ and solving for it provided him with the corresponding excess functional for hard spheres in three dimensions. It is noteworthy that in the derivation Rosenfeld did not provide the pressure beforehand but instead obtained it from the theory itself with the remarkable fact that the Percus-Yevick equation of state, directly following from scaled-particle theory, is an output of the excess functional construction. This means in particular, that the Percus-Yevick equation of state is built into the formalism outlined in Sec.4.2.1, i.e. there cannot be any other equation of state, such as the more accurate Carnahan-Starling equation of state, that could arise from the formalism.

However, we could think of providing a more accurate equation of state that, instead of being a direct output of the theory, is inputed from the beginning. Then, we can solve the corresponding differential equation of the type given in Eq.(4.59) and obtain a new functional. The ansatz made before for the Rosenfeld functional should remain the same.

Let's consider the more accurate equation of state of Mansoori-Carnahan-Starling-Leland (MCSL) [80] being a generalization to the m-component hard-sphere fluid of Carnahan-Starling (CS) equation of state [35].

Therefore, the MCSL equation of state reads as

$$\beta P^{\mathrm{MCSL}} = \frac{n_0}{1-n_3} + \frac{n_1 n_2}{(1-n_3)^2} + \frac{n_2^3}{12\pi(1-n_3)^3} - \frac{n_3 n_2^3}{36\pi(1-n_3)^3}, \tag{4.76}$$

where we already replaced the scaled-particle varialbes ξ_i with the corresponding weighted densities in the bulk, n_i. Compared to the scaled-particle equation of state, Eq.(3.94), we see that the last term in Eq.(4.76) is newly added. As before, we make an ansatz for the free energy density already taking into account the fact that $f_3 = -f_2$ and $f_5 = -3f_4$

$$\Phi = f_1(n_3)n_0 + f_2(n_3)(n_1 n_2 - \mathbf{n}_1\cdot\mathbf{n}_2) + f_4(n_3)(n_2^3 - 3n_2\mathbf{n}_2\cdot\mathbf{n}_2). \tag{4.77}$$

Now, in contrast to the derivation of Sec.4.2.1 we take the MCSL equation of state as the thermodynamic pressure

$$\beta P^{\mathrm{MCSL}} = -\Phi + \sum_\alpha \frac{\partial\Phi}{\partial n_\alpha} n_\alpha + n_0, \tag{4.78}$$

where, of course, the sum runs only over the scalar weighted densities. With the differential equation Eq.(4.78) we can again determine the remaining functions f_1, f_2 and f_4 which is done by collecting all the terms proportional to n_0, $n_1 n_2$ and n_2^3. While f_1 and f_2 equal those of Rosenfeld Eq.(4.63), f_4 turns out to be of a more complicated form

$$f_4(n_3) = \frac{n_3 + (1-n_3)^2 \log(1-n_3)}{36\pi n_3^2 (1-n_3)^2} \tag{4.79}$$

leading to the White-Bear functional [62]

$$\Phi^{\mathrm{WB}} = \Phi_1 + \Phi_2 + \Phi_3^{\mathrm{WB}} \tag{4.80}$$

with

$$\Phi_3^{\mathrm{WB}} = (n_2^3 - 3n_2 \mathbf{n}_2 \cdot \mathbf{n}_2) \frac{n_3 + (1-n_3)^2 \log(1-n_3)}{36\pi n_3^2 (1-n_3)^2}. \tag{4.81}$$

Since the function f_4, Eq.(4.79), has the limit $\lim_{n_3 \to 0^+} f_4(n_3) = 1/(24\pi)$ the correct low-density limit of Eq.(4.45) is guaranteed.

However, if we reconsider the scaled-particle relation Eq.(4.58) we see that in the case of the White-Bear functional Eq.(4.80)

$$\frac{\partial \Phi^{\mathrm{WB}}}{\partial n_3} = \frac{n_0}{1-n_3} + \frac{n_1 n_2}{(1-n_3)^2} - \frac{n_2^3 (2 + n_3(n_3-5))}{36\pi n_3^2 (1-n_3)^3} - \frac{n_2^3}{18\pi n_3^3} \log(1-n_3) \tag{4.82}$$

which is seemingly different from the MCSL equation of state, Eq.(4.76). Of course, this difference arises through the fact that we have dropped out the scaled-particle relation Eq.(4.58) leading to the inconsistency. Nonetheless, this inconsistency stays below 2% for the one-component fluid phase, where it should be noted that the Percus-Yevick equation of state overestimates the pressure close to freezing up to 7% [62], see Fig.4.5. In addition, the liquid-solid densities are improved by the White-Bear functional [81].

A new version of the Carnahan-Starling equation of state that improves for binary and higher hard-sphere mixtures in comparison with computer simulations [68], the White-Bear Mark II version was developed [82]. It is grounded on a new equation of state respecting the scaled-particle relation of Eq.(4.58) in the one-component case

$$\beta P^{\mathrm{CSIII}} = \frac{n_0}{1-n_3} + \frac{n_1 n_2}{(1-n_3)^2} \left(1 + \frac{1}{3} n_3^2\right) + \frac{n_2^3}{12\pi (1-n_3)^3} \left(1 - \frac{2}{3} n_3 + \frac{1}{3} n_3^2\right) \tag{4.83}$$

which, with the same analysis as was being done for the White-Bear functional, leads to the mark II version

$$\Phi^{\mathrm{WBII}} = \Phi_1 + \varphi_1(n_3)\Phi_2 + \varphi_2(n_3)\Phi_3^{\mathrm{RF}} \tag{4.84}$$

with the functions

$$\begin{aligned} \varphi_1(n_3) &= 1 + \frac{2n_3 - n_3^2 + 2(1-n_3)\log(1-n_3)}{3n_3} \\ \varphi_2(n_3) &= 1 - \frac{2n_3 - 3n_3^2 + 2n_3^3 + 2(1-n_3)^2 \log(1-n_3)}{3n_3^2}. \end{aligned} \tag{4.85}$$

Therefore, the White-Bear mark II functional is constructed such that in the one-component case it holds

$$\beta P^{\mathrm{CS}} = \frac{\partial \Phi^{\mathrm{WBII}}}{\partial n_3}, \tag{4.86}$$

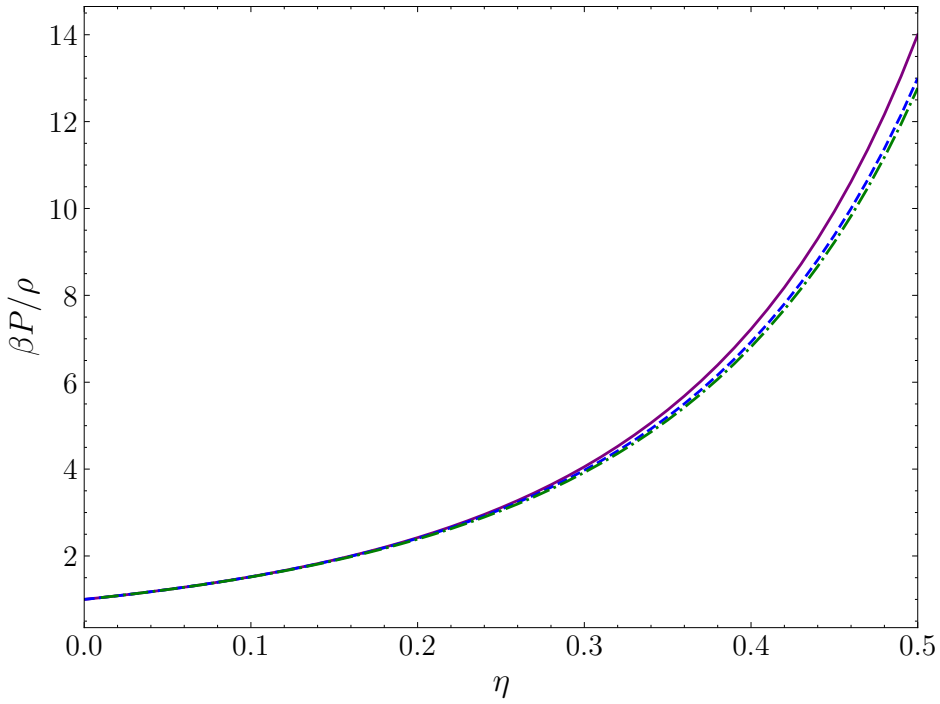

Figure 4.5: Compressibility factor $\beta P/\rho$ plotted as a function of the packing fraction η in the fluid phase. The purple curve represents the Percus-Yevick, the green curve Carnahan-Starling and the blue curve Eq.(4.82). We see that latter two differ only slightly for higher packing fractions.

where P^{CS} is the Carnahan-Starling (CS) pressure, Eq.(2.101).

Since the White-Bear functionals were virtually derived the same way as for the Rosenfeld functional, only the equation of states were imposed onto the differential equations of Eq.(4.59), they pose the same issues when it comes to highly confined systems. These can again be remedied by extending the original versions given in Eq.(4.81) and Eq.(4.84) to the aforementioned q_3 version, Eq.(4.66), as was done for Rosenfeld's functional. Also the tensorial versions can be considered, e.g. in the case of White-Bear

$$\Phi_3^{\mathrm{WB}} \to \Phi_3^{\mathrm{WB,T}} = \left(-n_2 \mathbf{n}_2 \cdot \mathbf{n}_2 + \mathbf{n}_2 \mathbf{T} \mathbf{n}_2 + n_2 \mathrm{Tr}(\mathbf{T}^2) - \mathrm{Tr}(\mathbf{T}^3)\right) \frac{n_3 + (1-n_3)^2 \log(1-n_3)}{36\pi n_3^2 (1-n_3)^2} \tag{4.87}$$

or White-Bear mark II

$$\Phi_3^{\mathrm{WBII}} \to \Phi_3^{\mathrm{WBII,T}} = \varphi_2(n_3) \Phi_3^{\mathrm{RF,T}}, \tag{4.88}$$

where the remaining parts of the functionals stay unchanged. Especially the tensorial White-Bear mark II version proved to be very successful in the description of hard-sphere crystals [83].

4.2.3 Spherical Wall: Test Particle

We can also apply cDFT in the case of a spherical hard wall of radius R_s placed at the origin $r = 0$ of the coordinate system and minimize the grand functional $\Omega[\rho(r)]$ in order to obtain the spherically symmetric equilibrium density profile $\rho(r)$. This system comes with the intriguing insight that the spherical wall can be understood as as solute particle of radius R_s whose interaction with the surrounding particles of the system is described

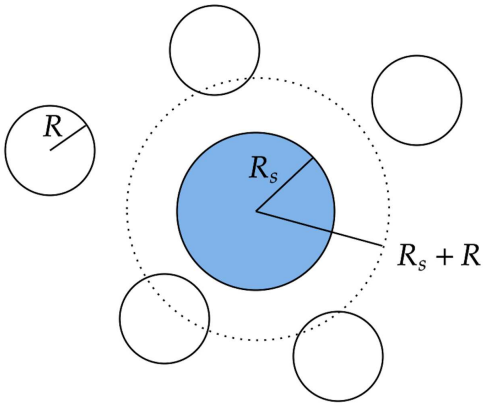

Figure 4.6: A hard sphere of radius R_s (solute particle blue) interacts with neighboring hard spheres of radius R leading to an exclusion sphere of radius (dashed circle) $R_s + R$.

by its interaction potential $\phi(r)$ acting as an external potential $V_{\text{ext}}(r)$. The test particle hence is considered to be co-moving with the other particles resembling a tracer particle that leads to coordination shells of the neighboring particles.

Assuming only hard-sphere interactions, the presence of the solute particle leads to a radially symmetric external potential of the form

$$V_{\text{ext}}(r) = \begin{cases} \infty, & \text{if} \quad r < R_s + R \\ 0, & \text{otherwise,} \end{cases} \tag{4.89}$$

meaning that there cannot be penetration when the test particle overlaps with a hard sphere of the system, which defines the exclusion sphere depicted in Fig.4.6. The external potential in Eq.(4.89) causes the surrounding hard spheres to congregate themselves in shells, i.e. there are correlations between the test particle and the hard-sphere fluid that decays with increasing distance r. Thus, in this geometry we can derive the radial distribution function $g(r) = \rho(r)/\rho_b$ from which other thermodynamic quantities can be inferred [44]. In Fig.4.7 we present the radial distribution functions $g(r)$ calculated for $\eta = 0.40$ employing the state-of-the-art functionals including MC data points near a spherical wall of radius $R_s = R$ centered at $r = 0$. Clearly visible is the first coordination shell located at $r \approx 2\sigma$ with the oscillations decaying as the distance r to the test particle increases. The various functionals displayed in Fig.4.7 describe well the MC data points with slight deviations occurring at the first minimum and maximum. In particular, at the exclusion boundary ($r \approx R_s + R$) we observe that the WB functionals perform better than RF in catching the contact value. The contact theorem, which we presented for the planar geometry in Sec.2.5.1, takes another form when the surface is curved [84, 85]

$$\rho(R_s^+) = \beta P + \frac{1}{4\pi R_s^2} \left(\frac{\beta \Omega_s}{\partial R_s} \right)_{T,\mu}, \tag{4.90}$$

where Ω_s is the surface excess grand potential in the accessible volume. Equation(4.90) can be recast in terms of the surface tension taking the Gibbs dividing surface at $r = R_s$

$$\rho(R_s^+) = \beta P + \frac{2\beta\gamma(R_s)}{R_s} + \left(\frac{\partial \beta\gamma(R_s)}{\partial R_s} \right)_{\mu,T} \tag{4.91}$$

which, of course, reduces to Eq.(4.33) for $R_s \to \infty$. Again, the contact sum rule serves as a numerical check for consistency. For instance, the calculations based on Fig.4.7 for

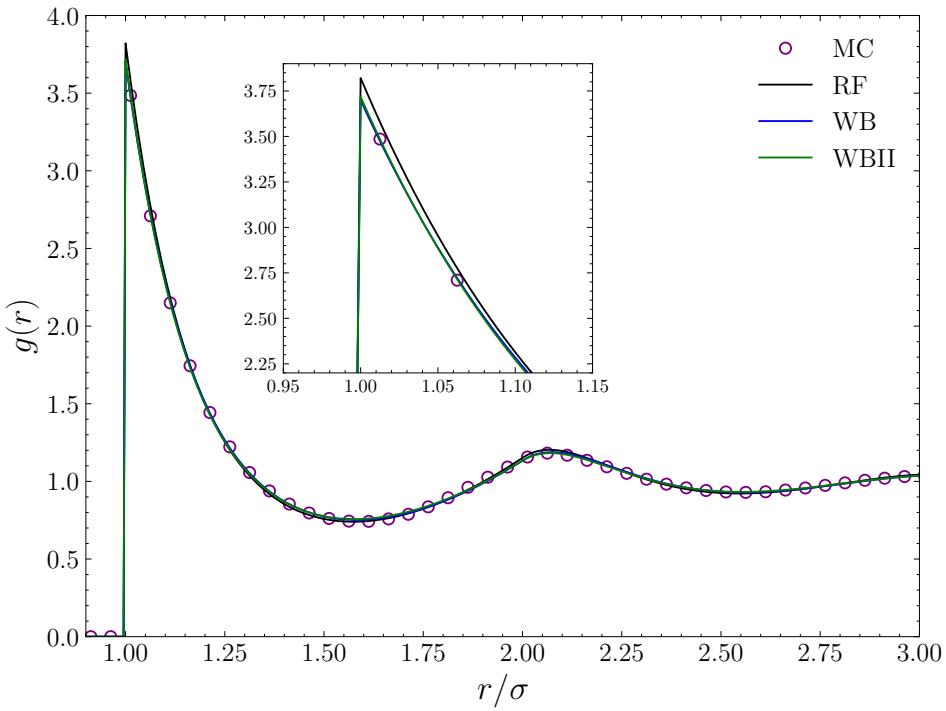

Figure 4.7: Radial distribution function $g(r)$ of the Rosenfeld (RF), White-Bear (WB) and White-Bear mark II (WBII) functionals for a packing fraction $\eta = 0.40$ and $R_s = R$. Also included are data points obtained from MC simulations.

WBII, where we used a resolution of 50 points per diameter σ, yield for the left-hand side of Eq.(4.91) the value $\rho(R_s^+)\sigma^3 = 2.839744$ whereas the right-hand side yields (same units) 2.838832, i.e. a relative error of ca. 0.03%. Furthermore, the Gibbs adsorption theorem

$$-\left(\frac{\partial\Omega_s}{\partial\mu}\right)_T = 4\pi\int_{R_s}^{\infty} dr\, r^2(\rho(r)-\rho_b) \tag{4.92}$$

is an additional check for consistency. Once more, taking the example from above the left-hand side of Eq.(4.92) gives 0.044323 and the right-hand side 0.044337, thus a relative error of 0.03% showing in total that the numerics performed consistently.

4.2.4 Spherical Cavity

The spherical cavity is also an interesting application of DFT for hard spheres. As the name suggests, we consider a spherical volume V of radius R that contains hard spheres of radii R_i where i corresponds to the species. In particular, Zhou and Stell investigated the application of several kinds of integral equation approximations for fluids confined inside of pores possessing different shapes [86]. In addition, the cDFT was also applied to this case [87] where the results were also compared to Monte Carlo simulations showing in total that even for small numbers of particles, the agreement is rather good.

The work [72] further considered the aforementioned integral equation approximations for simple fluids inside spherical containers taking into account grand-canonical Monte Carlo (GCMC) simulations of hard spheres in spherical pores for comparison [88]. They could show that the PY/PY approximation seems to perform best among the integral equation approximations to predict coefficients of the partition. However, it cannot be

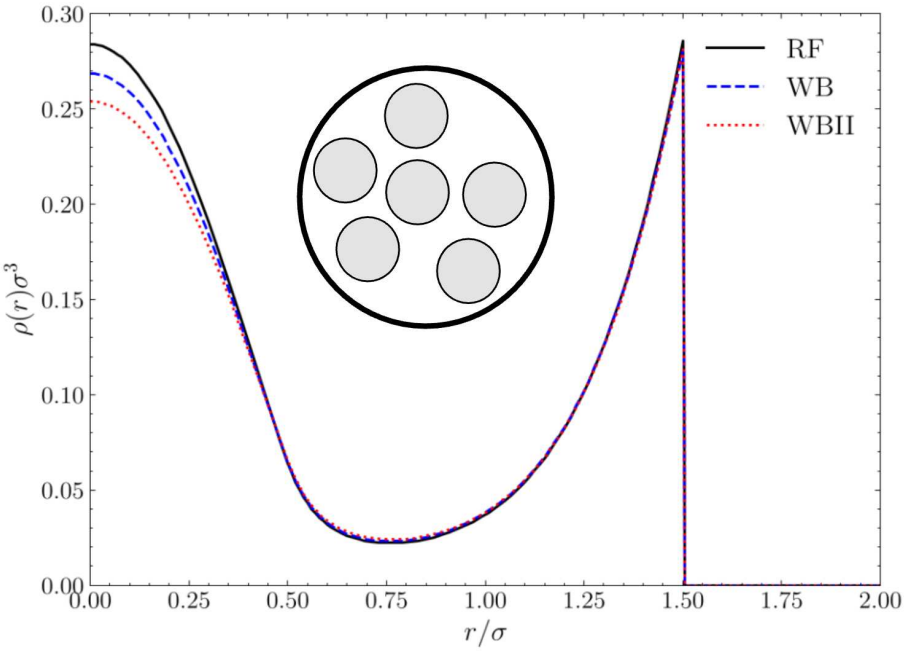

Figure 4.8: Radially symmetric density profiles $\rho(r)$ of the Rosenfeld (RF), White-Bear (WB) and White-Bear mark II (WBII) functional for a spherical cavity of radius $R = 2\sigma$ and packing fraction $\eta = 0.27$. The inset depicts a cross section of the spherical cavity.

stated that any of the approximations is best suited overall for describing density profiles of hard spheres inside spherical pores.

According to the appendix of [72], the grand canonical partition function Z_{GC} of a system of hard spheres inside a spherical cavity must be zero if $R < \sigma/2$ where σ is the diameter of a sphere. Instead, if $R = \sigma$, the cavity can hold just one particle. In the case of $\sigma/2 < R < \sigma$, we find for the partition function

$$Z_{\mathrm{GC}}(V, T, \mu) = 1 + \frac{z}{\lambda_T^3} \int d\mathbf{r} \, \exp(-\beta u_1(\mathbf{r})), \tag{4.93}$$

where $u_1(\mathbf{r})$ is the one-particle potential function that, of course, has to have the form

$$u_1(r) = \begin{cases} 0, & \text{if} \quad 0 \leq r \leq R - \sigma/2 \\ \infty, & \text{otherwise.} \end{cases} \tag{4.94}$$

Hence, the partition function is given as

$$Z_{\mathrm{GC}}(V, T, \mu) = 1 + z\mathcal{V} \tag{4.95}$$

with the available volume inside the pore $\mathcal{V} = (4\pi/3)(R - \sigma/2)^2$. Finally, the corresponding density profile $\rho(r)$ reads

$$\rho(r) = \frac{z \exp(-\beta u_1(r))}{1 + z\mathcal{V}}. \tag{4.96}$$

The devote study of [89] attempted to analytically calculate the canonical partition

function of three hard spheres confined inside a spherical cavity, allowing to derive its thermodynamic properties as a function of cavity radius. By making use of symmetry relations, its dual pendant, where hard spheres surround a spherical hard object, is also analyzed. Latter on top enables to calculate the corresponding partition function and hence the thermodynamic quantities.

We can apply cDFT in order to obtain the density profiles of the corresponding functionals of Rosenfeld and the well-established White-Bear functionals, see Fig.4.8. There we see the apparent contact value at $r = R - \sigma/2$ as the wall is impenetrable. Furthermore we see a maximum at the origin $r = 0$ of the spherical cavity, which is to be expected since the hard spheres otherwise cannot be packed into the cavity for such a rather high packing fraction $\eta = 0.27$. While there are only minor differences between the shapes of the three profiles close to the hard wall, deviations occur in the center of the cavity. The packing fractions in the same time sets the chemical potential of the system, i.e. we can calculate the expectation value of the number of particles, $\langle N \rangle$, inside the cavity. Given the accessible volume $\mathcal{V}$, the maximum number of particles $N_{\max}$ is found to scale as $(2R/\sigma - 1)^3$ which certainly cannot be reached geometrically. Within DFT, we can compute the expected number of particles through the simple relation

$$\langle N \rangle = 4\pi \int_{\mathcal{V}} dr\, r^2 \rho(r) \tag{4.97}$$

which in our example of Fig.4.8 gives approximately 13 while $N_{\max}$ is found to be 27.

It is no coincidence that we have chosen $\eta = 0.27$ for the spherical cavity of Fig.4.8. If we slightly increased the packing fraction, the functional of Rosenfeld, for instance, would not converge towards an equilibrium solution indicating that for this given geometry the stability of the functionals is not guaranteed. This issue can be rectified by using the q_3-versions of the corresponding functionals having the effect of rendering the functional more stable, see Sec.4.2.1 for more details. Finally, it is noteworthy to mention that the Lutsko functionals, see Ch.5, that arise from consideration on stability and accuracy within the framework of dimensional crossover also show a more stable behavior inside of small spherical cavities. Despite its alleged simplicity, highly confined spherical cavities serve as a benchmark for testing the stability of functionals.

4.3 Dimensional Crossover

As we pointed out in the introduction of this chapter, dimensional crossover provides a new insight into the construction of excess functionals for hard spheres. Imposing the condition that any D-dimensional excess functional has to lead to the correct $D = 0$ limit restricts the possible functional dependencies of the free energy density Φ up to a certain accuracy. We can simply start from a setup of a three-dimensional $D = 3$ system with density profile $\rho(\mathbf{r})$ such that the system is held between to very close walls along the z-axis, i.e. we can write $\rho(\mathbf{r}) = \rho_{2D}(x, y)\delta(z)$. The resulting excess free energy density arising from this parametrization of the density profile as a highly confined $D = 3$ system agrees very well with numerical results although the functional differs from that of the scaled-particle approach [90, 91, 92].

If we further confine the system, let's say, along the y-axis we obtain $\rho(\mathbf{r}) = \rho_{1D}(x)\delta(y)\delta(z)$. It is observed that while the first two terms of the Rosenfeld functional, Eq.(4.65), reproduce the exact $D = 1$ free energy density, the third term produces divergencies due to

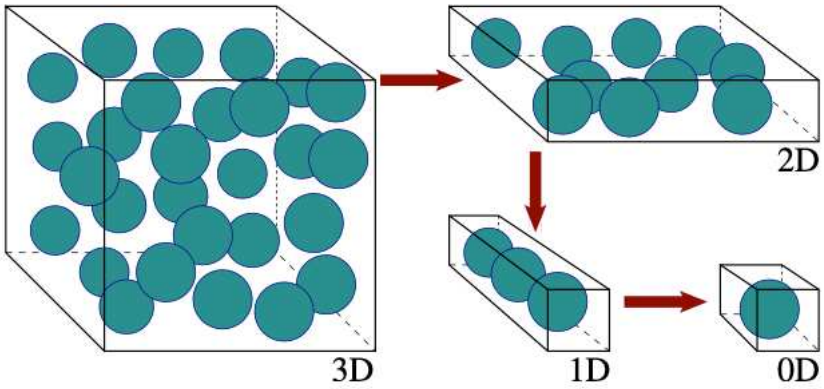

Figure 4.9: An initially $D = 3$ system is further confined up until the $D = 0$ limit, which is exactly known, is reached. Picture taken from [92]

overlapping delta functions. For instance, the weighted density $n_3(\mathbf{r})$ becomes

$$\begin{aligned} n_3(\mathbf{r}) &= \int d\mathbf{r}\, \rho_{1D}(x')\delta(y')\delta(z')\Theta\left(R - \sqrt{(x-x')^2 + (y-y')^2 + (z-z')^2}\right) \\ &= \int dx'\, \rho_{1D}(x')\Theta(R - |x - x'|) \\ &\equiv n_{3,1D}(x), \end{aligned} \tag{4.98}$$

where the integrals of y and z are easily performed at we set $y = z = 0$ for simplicity. Thus, we effectively have a $D = 1$ weighted density $n_{3,1D}(x)$ aligning with the actual $D = 1$ definition of the weighted density, Eq.(4.4). Similarly, we find

$$\begin{aligned} n_2(\mathbf{r}) &= \int d\mathbf{r}\, \rho_{1D}(x')\delta(y')\delta(z')\delta\left(R - \sqrt{(x-x')^2 + (y-y')^2 + (z-z')^2}\right) \\ &= \int dx'\, \rho_{1D}(x')\delta(R - |x - x'|) \\ &\equiv n_{2,1D}(x) \end{aligned} \tag{4.99}$$

and finally

$$\mathbf{n}_2(\mathbf{r}) = \int d\mathbf{r}\, \rho_{1D}(x')\delta(y')\delta(z')\delta\left(R - \sqrt{(x-x')^2 + (y-y')^2 + (z-z')^2}\right) \frac{\mathbf{r} - \mathbf{r}'}{|\mathbf{r} - \mathbf{r}'|} \tag{4.100}$$

$$\begin{aligned} &= \int dx'\, \rho_{1D}(x')\delta(R - |x - x'|)\mathbf{e}_x \\ &\equiv n_{2,1D}(x)\mathbf{e}_x. \end{aligned}$$

We see that $n_2^2 = \mathbf{n}_2^2$ and due to the antisymmetry of Φ_2, the second term of the Rosenfeld free energy density cancels. However, the third term does not have such a property and it follows that $\int d\mathbf{r}\, \Phi_3^{\mathrm{RF}} \to -\infty$ [61]. This idea is also valid in the case of full confinement to $D = 0$ with $\rho(\mathbf{r}) \propto \delta(\mathbf{r})$.

The ultimate confinement, the situation of a $D = 0$ cavity being able to hold at most one particle, has an average particle number $N \leq 1$. For this setup, the grand-canonical partition sum Z_{GC}, Eq.(2.52), has the form [92]

$$Z_{\mathrm{GC}} = 1 + zZ_1, \quad z = \exp(\beta\mu), \tag{4.101}$$

where μ is the chemical potential and Z_1 the canonical partition sum of one particle. The average particle is derived as

$$\begin{aligned} N &= \frac{\partial \log Z_{\mathrm{GC}}}{\partial \beta \mu} \\ &= \frac{Z_1 z}{1 + Z_1 z} \end{aligned} \tag{4.102}$$

which, solving for Z_1, gives an expression in terms of the average particle number N

$$Z_1(N) = \frac{N}{z(1-N)}. \tag{4.103}$$

Herewith, we infer for the grand-canonical partition sum

$$Z_{\mathrm{GC}} = \frac{1}{1-N} \quad \Rightarrow \quad \beta P = \log Z_{\mathrm{GC}} = -\log(1-N) \tag{4.104}$$

with the associated dimensionless pressure of the $D = 0$ cavity. The free energy F therefore is obtained via the thermodynamic relation $F = -P + \mu N$ to give

$$F = \log(1-N) + N \log\left(\frac{N}{Z_1(1-N)}\right) \tag{4.105}$$

and as we are only interested in the excess contribution we have to subtract the ideal-gas part F_{id}. Latter is found to be

$$F_{\mathrm{id}} = -N + N \log\left(\frac{N}{Z_1}\right), \tag{4.106}$$

where it should be noted that in this case there is no restriction on the particle number N as by definition the particle are point-like. Therefore, we obtain for the excess part

$$\Phi_{\mathrm{0D}} = \eta + (1-\eta)\log(1-\eta) \tag{4.107}$$

in which we already made use of the fact that since $N \leq 1$, the particle number is equivalent to the packing fraction η.

One of the key insights of dimensional crossover is that the crystalline state can be understood as a highly confined system, i.e. whose particles are strongly packed by their immediate neighbors. Consequently, a proper functional must reduce to the exactly known $D = 0$ case, Eq.(4.107), with the associated profile $\rho(\mathbf{r}) = \delta(\mathbf{r})$.

The simple observation that the $D = 1$ functional Eq.(4.15) reduces to the exact $D = 0$ functional, gave rise to the following ansatz of a D-dimensional functional

$$\begin{aligned} \beta \mathcal{F}_{\mathrm{ex},1}[\rho] &= -\int d\mathbf{r}\, n_0(\mathbf{r}) \log(1 - n_D(\mathbf{r})) \\ &= -\int d\mathbf{r}\, n_0(\mathbf{r}) \psi_1(n_D(\mathbf{r})), \end{aligned} \tag{4.108}$$

where we have defined

$$\psi_1(\eta) \equiv \frac{\partial \Phi_{\mathrm{0D}}(\eta)}{\partial \eta}. \tag{4.109}$$

It can be easily shown that Eq.(4.108) correctly recovers the case of a single $0D$ cavity. However, if we regard more complicated constellations of two cavities, the proposed functional Eq.(4.108) produces additional terms that should not appear. In order to overcome this issue, adding

$$\beta\mathcal{F}_{\mathrm{ex},2}[\rho] = \int d\mathbf{r}\,(n_1 n_2 - \mathbf{n}_1 \cdot \mathbf{n}_2)\psi_2(n_D(\mathbf{r}))$$

with

$$\psi_2(\eta) \equiv \frac{\partial^2 \Phi_{\mathrm{0D}}(\eta)}{\partial \eta^2} \tag{4.110}$$

comprises the case of two cavities. In particular, the total excess free energy, i.e. $\beta\mathcal{F}_{\mathrm{ex}}[\rho] = \beta\mathcal{F}_{\mathrm{ex},1}[\rho] + \beta\mathcal{F}_{\mathrm{ex},2}[\rho]$ is just the Rosenfeld functional, Eq.(4.65). Going even further, the case of three cavities with pairwise overlap might be still in the scope of the so far constructed functional. As it turns out, these so-called lost cases cannot be captured by FMT, i.e. they do not reduce to the exact $0D$-limit [63, 93]. In Ch.5, we will take another look at dimensional crossover as was outlined by Lutsko[93] leading to a whole class of new functionals.

Chapter 5

Accurate Functionals for Hard Spheres

Current established Helmholtz free energy functionals for hard-sphere mixtures such as the standard Rosenfeld functional and the more accurate White-Bear and White-Bear mark II functionals prove themselves to be very powerful and efficient for obtaining density profiles of confined systems. However, there are several deficiencies which are inherent in these functionals as for example consistency of certain thermodynamic relations that, in principle, should be satisfied if these functionals were exact. Based on Lutsko's work [93] on building a new class of functionals that possess two yet undetermined parameters A and B for hard spheres using key ideas of dimensional crossover, we investigate accuracy, consistency and stability of these functionals by employing two equilibrium sum rules in the test-particle geometry. In addition, we try to give an answer to which specific values of A and B these sum rules are best fulfilled. We further propose new functionals ourselves that grounds on the findings made by Lutsko [93].

5.1 Explicitly Stable Functionals

The following introduction to explicitly stable functionals sticks to the discussion of [93]. The formalism for hard-sphere systems in which exact lower-dimensional functionals are reproduced from higher dimensional ones is termed as dimensional crossover, see Sec.4.3. Besides the one-dimensional hard-sphere system, the excess functional of 0D-systems containing at most one single hard sphere of radius R is also exactly known. Let us consider a cavity of radius $R(1+\epsilon)$ with $\epsilon \to 0$ corresponding to a point. Then, the density takes the form

$$\rho(\mathbf{r}) = N\delta(\mathbf{r}), \tag{5.1}$$

where $N \in [0,1]$ being determined by the chemical potential. One can work out the excess free energy with its functional form given by

$$\mathcal{F}_{\text{ex}}[\rho] = \Phi_0[N[\rho]], \tag{5.2}$$

with the $0D$ free energy density Eq.(4.105)

$$\Phi_0(x) = (1-x)\log(1-x) - (1-x) \tag{5.3}$$

and

$$N[\rho] = \int \rho(\mathbf{r})\, d\mathbf{r}. \tag{5.4}$$

By extending to two or more cavities there arises the possibility of pairwise overlapping between the cavities. By taking two cavities with centers $\mathbf{s}_i$ that can overlap, the density becomes

$$\rho_2(\mathbf{r}) = N_1\delta(\mathbf{r}-\mathbf{s_1}) + N_2\delta(\mathbf{r}-\mathbf{s_2}) \tag{5.5}$$

where it must hold $0 \leq N_1 + N_2 \leq 1$. The excess free energy functional becomes

$$\mathcal{F}_{\text{ex}}[\rho_2] = \Phi_0(N_1+N_2), \tag{5.6}$$

whereas for no overlap we have

$$\mathcal{F}_{\text{ex}}[\rho_2] = \Phi_0(N_1) + \Phi_0(N_2). \tag{5.7}$$

By going to three cavities further complicates and multiplies the number of constellations. It has to be mentioned that not all of these possible constellations can be captured within this formalism, see [93] for a more comprehensive examination of multiple cavities. Rosenfeld and Tarazona [76] proposed the following ansatz for the excess functional

$$\mathcal{F}_{\text{ex}}[\rho] = \mathcal{F}_{\text{ex}}^{(1)}[\rho] + \mathcal{F}_{\text{ex}}^{(2)}[\rho] + \dots, \tag{5.8}$$

where the leading contributions read

$$\begin{aligned}
\mathcal{F}_{\text{ex}}^{(1)}[\rho] &= \int d\mathbf{r}\, \Psi_1[\mathbf{r};[\rho]] \int d\mathbf{r}_1 \rho(\mathbf{r}-\mathbf{r}_1)\delta(R-r_1)\, K_1(\hat{\mathbf{r}}_1), \\
\mathcal{F}_{\text{ex}}^{(2)}[\rho] &= \int d\mathbf{r}\, \Psi_2[\mathbf{r};[\rho]] \int d\mathbf{r}_1 d\mathbf{r}_2 \rho(\mathbf{r}-\mathbf{r}_1)\delta(R-r_1)\delta(R-r_2) K_2(\hat{\mathbf{r}}_1,\hat{\mathbf{r}}_2)
\end{aligned} \tag{5.9}$$

and in the same manner for higher orders. They can be evaluated for several 0D-cavity systems, e.g. a single cavity, two cavities etc. For the single cavity example, it can be easily shown that the second and higher contributions of Eq.(5.9) will be divergent unless the Kernels $K_n(\hat{\mathbf{r}}_1,\dots,\hat{\mathbf{r}})$ vanish whenever two of its arguments become equal. This is an important stability constraint on the construction of these functionals. As the kernels are taken to be scalars they can only depend on scalar products of their arguments, e.g. $K_2(\hat{\mathbf{r}}_1,\hat{\mathbf{r}}_2) = K_2(\hat{\mathbf{r}}_1\cdot\hat{\mathbf{r}}_2;R)$.
For a single cavity one finds using the stability property

$$\mathcal{F}_{\text{ex}}[\rho_1] = \mathcal{F}_{\text{ex}}^{(1)}[\rho_1] = \overline{K}_1\psi_0(N_1)\frac{\partial V_D(R)}{\partial R}, \tag{5.10}$$

where $V_D(R)$ is the volume of a sphere of radius R in D dimensions. Furthermore, $\psi_1(x) \equiv \psi_0'(x)$. The exact result is obtained if $\psi_0(x) = \Phi_0(x)$ and $\overline{K}_1 V_D'(R) = \overline{K}_1 S_D(R) = 1$, where $S_D(R)$ is the surface area of the sphere.
Similarly, the calculation for two cavities, after identifying $\psi_2(x) = \Phi_0''(x)$, yields

$$\begin{aligned}
\mathcal{F}_{\text{ex}}[\rho_2] &= \mathcal{F}_{\text{ex}}^{(1)}[\rho_2] + \mathcal{F}_{\text{ex}}^{(2)}[\rho_2] \\
&= \Phi_0(N_1+N_2) + (\Delta_2(s_{12})-1)\left[\Phi_0(N_1+N_2) - \Phi_0(N_1) - \Phi_0(N_2)\right],
\end{aligned} \tag{5.11}$$

where s_{12} is the distance between the centers of the two cavities. $\Delta_2(s_{12})$ does vanish if the cavities are not intersecting, otherwise in three dimensions it is

$$\Delta_2(s_{12}) = 1 - \frac{s_{12}}{2R} + \frac{4\pi R^2}{s_{12}}\overline{K}_2\left(1-\frac{s_{12}^2}{2R^2};R\right). \tag{5.12}$$

In order to obtain the exact result it must hold $\Delta_2(s_{12}) = 1$ which results in

$$\overline{K}_2\left(1 - \frac{s_{12}^2}{2R^2}; R\right) = \frac{1}{4\pi R}\frac{s_{12}^2}{2R^2} \tag{5.13}$$

or

$$\overline{K}_2(x; R) = \frac{1}{4\pi R}(1 - x). \tag{5.14}$$

Now, we introduce weighted densities η, s $\mathbf{v}$ and $\mathbf{T}$ according to [93] given as follows

$$\begin{aligned}
\eta(\mathbf{r}) &= \int d\mathbf{r}_1\, \Theta(R - r_1)\rho(\mathbf{r} - \mathbf{r}_1), \\
s(\mathbf{r}) &= \int d\mathbf{r}_1\, \delta(R - r_1)\rho(\mathbf{r} - \mathbf{r}_1), \\
\mathbf{v}(\mathbf{r}) &= \int d\mathbf{r}_1\, \frac{\mathbf{r}_1}{|\mathbf{r}_1|}\delta(R - r_1)\rho(\mathbf{r} - \mathbf{r}_1) \\
\mathbf{T}(\mathbf{r}) &= \int d\mathbf{r}_1\, \left(\frac{\mathbf{r}_1}{|\mathbf{r}_1|} \otimes \frac{\mathbf{r}_1}{|\mathbf{r}_1|}\right)\delta(R - r_1)\rho(\mathbf{r} - \mathbf{r}_1),
\end{aligned} \tag{5.15}$$

i.e. η and s are scalars, $\mathbf{v}$ is a vector and $\mathbf{T}$ is a tensor. Contrary to the notation we have used in Ch.4, the measures given in Eq.(5.15) only apply for one-component systems. A corresponding generalization to mixtures enforces a correct replacement with weighted densities n_α commonly employed in FMT.

Taking the two kernels above, up to two cavities the excess functional becomes

$$\mathcal{F}_{\text{ex}}^{(1)}[\rho_2] + \mathcal{F}_{\text{ex}}^{(2)}[\rho_2] = \int d\mathbf{r}\, \left\{-\frac{1}{4\pi R^2}s(\mathbf{r})\log(1 - \eta(\mathbf{r})) + \frac{1}{4\pi R}\frac{s^2(\mathbf{r}) - \mathbf{v}^2(\mathbf{r})}{1 - \eta(\mathbf{r})}\right\}, \tag{5.16}$$

which are just the first two terms of the Rosenfeld functional, Eq.(4.65), in three dimensions. This was possible since we assumed the kernels to be polynomials in $\hat{\mathbf{r}}_i$, see [93]. The polynomial ansatz allows to employ merely measures that are already used in a FMT approach of cDFT. Equivalently, K_3 can be obtained by only including known measures of FMT and making use of full symmetry between $\hat{\mathbf{r}}_1$, $\hat{\mathbf{r}}_2$ and $\hat{\mathbf{r}}_3$. The corresponding functional hence becomes

$$\mathcal{F}_{\text{ex}}^{(3)}[\rho] = \frac{1}{24\pi}\int d\mathbf{r}\, \frac{\mathcal{N}(A, B)}{(1 - \eta(\mathbf{r}))^2}, \tag{5.17}$$

where

$$\begin{aligned}
\mathcal{N}(A, B) = (A + B)s^3(\mathbf{r}) - 3As(\mathbf{r})\mathbf{v}^2(\mathbf{r}) + 3A\mathbf{v}(\mathbf{r})\mathbf{T}(\mathbf{r})\mathbf{v}(\mathbf{r}) \\
-3Bs(\mathbf{r})\mathrm{Tr}\,\mathbf{T}^2(\mathbf{r}) + (2B - A)\mathrm{Tr}\,\mathbf{T}^3(\mathbf{r})
\end{aligned} \tag{5.18}$$

with new constants A and B that yet have to be determined. It is clear that these constants will have an impact on the stability as well as on the quality of the functional. Lutsko has shown that for $A, B > 0$ the functional is explicitly stable, hence referring to explicitly stable functionals or for short esFMT(A, B). A similar conclusion for other cases of A and B on the stability of the associated functional cannot be made, rather it must be clarified in a different way. It is generally possible to construct examples of geometries where the established Rosenfeld and White-Bear functionals are seemingly not bounded from below [79]. From Eq.(5.17) we can already observe that Tarazonas

functional Eq.(4.72) is recovered in the case of $A = -B = 3/2$, apparently not belonging to esFMT(A, B). Put more generally, any pair (A, B) fulfilling the condition $8A+2B = 9$ reproduce the Percus-Yevick equation of state thus with a corresponding functional that is exact for low densities. In the proceeding sections we will investigate the functional proposed by Lutsko, Eq.(5.16) together with Eq.(5.17), under the light of equilibrium sum rules that allow a determination of optimized constants A and B.

5.2 Lutsko Functional

Lutsko insightfully revisited the ideas of dimensional crossover laid out by Tarazona and Rosenfeld in constructing a new class of functionals that are parametrized by two constants A and B, to which we will from now on refer as Lutsko parameters and to the corresponding functional as the Lutsko functional LK(A, B). The free energy density Φ^{LK} of Lutsko then can be recast in the form

$$\Phi^{\mathrm{LK}} = \Phi_1 + \Phi_2 + \Phi_3^{\mathrm{LK}}, \tag{5.19}$$

where Φ_1 and Φ_2 are equal to those of Rosenfeld's functional, Eq.(4.65), whereas Φ_3^{LK} reads

$$\Phi_3^{\mathrm{LK}} = \frac{(A+B)n_2^3 - 3A\; n_2 \mathbf{n}_2 \cdot \mathbf{n}_2 + 3A\; \mathbf{n}_2\; \mathbf{T}\; \mathbf{n}_2 - 3B\; n_2 \mathrm{Tr}\,\mathbf{T}^2 + (2B-A)\mathrm{Tr}\,\mathbf{T}^3}{24\pi(1-n_3)^2}. \tag{5.20}$$

In Eq.(5.20) we rewrote, in contrast to Eq.(5.18), the measures employed in [93] in terms of the weighted densities n_α of FMT. Hereby, we also allow for a straightforward extension to hard-sphere mixtures. The tensorial weighted density $\mathbf{T}(\mathbf{r})$ is given by

$$\mathbf{T}(\mathbf{r}) = \int d\mathbf{r}'\, \rho(\mathbf{r}') w_T(\mathbf{r} - \mathbf{r}') \tag{5.21}$$

with the weight function w_T of Eq.(4.71). Here, it is worth noticing that Eq.(5.20) is a generalization of the corresponding expression for Φ_3 of the tensor version [63] of the Rosenfeld functional, which is recovered for $A = B = -3/2$.

The remaining task is to give some physical motivations on how to determine values for the free Lutsko parameters. Lutsko himself considered the application to stable crystals, focusing on global stability. As was outlined in Sec.5.1, any choice $A, B > 0$ ensures the free energy density to be bounded from below [79]. The bulk pressure $P^{\mathrm{LK}}(A, B)$ following from the free energy density of Eq.(5.19) is given by

$$\frac{\beta P^{\mathrm{LK}}(A,B)}{\rho} = \frac{\beta P^{\mathrm{PY}}}{\rho} + \frac{\eta^2}{3(1-\eta)^3}(8A + 2B - 9) \tag{5.22}$$

which reduced to the PY equation of state (EoS), Eq.(3.95), if $8A+2B = 9$ holds. Therefore, we can see that bulk thermodynamic quantities associated to the Lutsko functional will have a deviation from the PY expressions accounted by the term $8A + 2B - 9$.

5.2.1 Test-Particle Sum Rules

So far two sum rules were encountered, the contact sum rule and the Gibbs adsorption theorem, see Ch.4. These sum rules are standard, in the sense that they are examined for

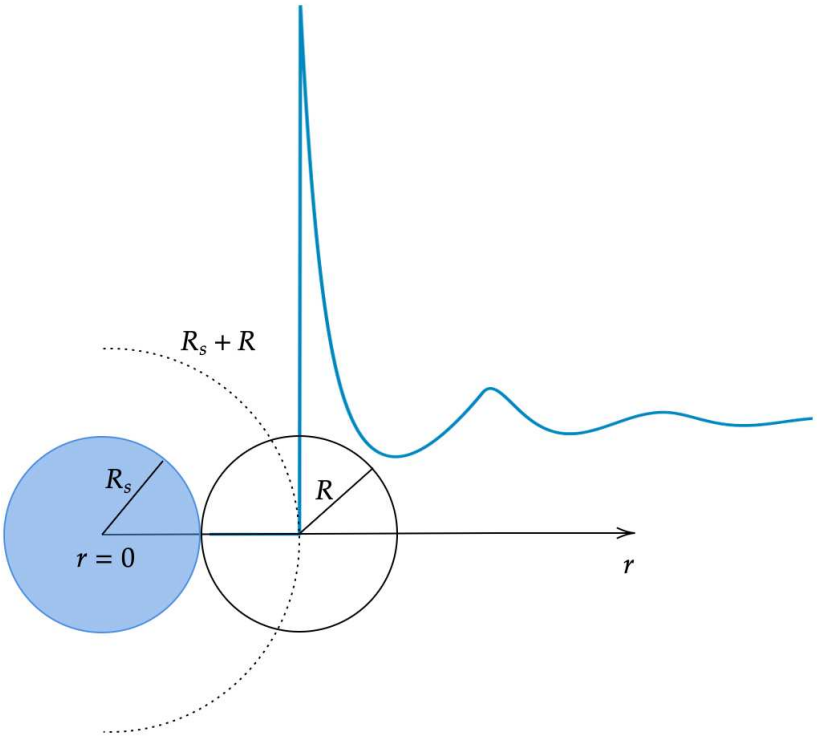

Figure 5.1: Test particle (blue) with radius R_s surrounded by hard spheres with radius R. The dotted circle indicates the exclusion sphere due to hard-sphere repulsion. The blue curve illustrates the radial distribution function $g(r)$.

any DFT calculation and serve as a numerical consistency check. In essence, structural or thermodynamic quantities can be obtained via several routes that must yield the same result. The Gibbs adsorption, for instance, is expressed in spherical geometry as follows

$$\Gamma(R_s, \mu) = 4\pi \int_0^\infty dr\, r^2 (\rho(r) - \rho_b) = -\left(\frac{\partial \Omega_s}{\partial \mu}\right)_T , \tag{5.23}$$

where the adsorption Γ depends on the solute radius R_s and the chemical potential μ. The grand potential Ω_s is obtained by minimizing the grand functional $\Omega[\rho]$ and evaluating it at equilibrium density $\rho(r)$, i.e. $\Omega_s = \Omega[\rho(r)]$. The contact sum rule on the other hand reads

$$\rho(R_s^+) = \beta P(R_s^+) + \frac{1}{4\pi R_s^2}\left(\frac{\partial \beta \Omega_s}{\partial R_s}\right)_{T,\mu} \tag{5.24}$$

with the bulk pressure P of the fluid. As the solute size is set infinitely big, $R_s \to \infty$, the contact sum rule at a hard wall is attained. Thus, any meaningful approximate functional of DFT satisfies Eq.(5.23) and Eq.(5.24) automatically. Then, we need further sum rules that allow for optimization of the Lutsko functional. In the test-particle geometry, see Sec.4.2.3, the insertion of a solute particle of radius R_s induces a change in grand potential, $\Delta\Omega$. Herewith, an exclusion sphere of size $R_s + R$ is created that necessitates a reversible work, given by $\Delta\Omega$, applied onto the system, see Fig.5.1. Before the insertion of the solute, the grand potential is $\Omega_0 = -PV$. In the presence of the solute, we instead have

$$\Omega_s = -P\left(V - \frac{4\pi}{3} R_s^3\right) + 4\pi R_s^2 \gamma(R_s) \tag{5.25}$$

with the surface tension $\gamma(R_s)$ defined on the surface of the solute. Then, the change in grand potential becomes

$$\Delta\Omega = \Omega_s - \Omega_0 = \frac{4\pi}{3} R_s^3 P + 4\pi R_s^2 \gamma(R_s). \tag{5.26}$$

It should be noticed that this idea is formally equivalent to the idea of scaled-particle theory, Sec.3.9. As we can identify $\Delta\Omega$ with the excess chemical potential μ_{ex}, we have

$$\mu_{\text{ex}}^{\text{DFT}} = \frac{4\pi}{3} R_s^3 P + 4\pi R_s^2 \gamma(R_s), \tag{5.27}$$

containing a volume term proportional to P and a surface term proportional to γ. Note that we use a superscript in Eq.(5.27) to indicate that this route is taken in the DFT calculation. The excess chemical potential can be on the other hand computed via the thermodynamic route

$$\beta\mu_{\text{ex}}^{\text{Bulk}} = \left.\frac{\partial\Phi}{\partial\rho}\right|_{\rho=\rho_b} \tag{5.28}$$

which evaluated for the free energy density of Lutsko, Eq.(5.19), yields

$$\beta\mu_{\text{ex}}^{\text{Bulk}}(A,B) = \beta\mu_{\text{ex}}^{\text{RF}} + \frac{\eta^2(3-\eta)}{6(1-\eta)^3}(8A + 2B - 9), \tag{5.29}$$

where $\mu_{\text{ex}}^{\text{RF}}$ is the excess chemical potential of Rosenfeld.

Percus could prove that the density distribution $\rho(r)$ is proportional to the radial distribution function $g(r)$ [44], $\rho(r) = \rho_b g(r)$. We have seen that $g(r)$ accounts for the probability to find a particle in the concentric shell $[r, r+dr]$. In Sec.3.7 we could relate the total correlation function $h(r) = g(r) - 1$ with the structure factor $S(\mathbf{q})$. More specifically, their Fourier transforms satisfy the equation

$$\hat{S}(\mathbf{k}) = 1 + \rho_b \hat{h}(\mathbf{k}) \tag{5.30}$$

which taken at $\mathbf{k} = 0$ can be put in the form

$$\hat{S}(0) = 1 + 4\pi\rho_b \int_0^\infty dr\, r^2 h(r), \tag{5.31}$$

where we explicitly made use of the Fourier representation for $\hat{h}(0)$. Since $\hat{S}(0) = \chi_T$, where $\chi_T = \rho_b k_B T \kappa_T$ is the reduced compressibility, we find

$$\chi_T^{\text{DFT}} = 1 + 4\pi\rho_b \int_0^\infty dr\, r^2 h(r). \tag{5.32}$$

Similar to the case of the excess chemical potential, the reduced isothermal compressibility χ_T is also obtained using the thermodynamic relation

$$\chi_T^{\text{Bulk}} = \left(\left.\frac{\partial\beta P}{\partial\rho}\right|_{\rho=\rho_b} \right)^{-1} \tag{5.33}$$

which becomes for the Lutsko free energy density

$$\chi_T^{\text{Bulk}}(A,B) = \chi_T^{\text{RF}} \left(1 + \frac{(8A + 2B - 9)\eta^2}{(1+2\eta)^2} \right)^{-1}, \tag{5.34}$$

where χ_T^{RF} is the reduced isothermal compressibility of Rosenfeld.

If the corresponding functional were exact, we would expect both Eq.(5.28) and Eq.(5.29) for the excess chemical potential and both Eq.(5.32) and Eq.(5.34) for the isothermal compressibility to be equal. However, as we employ functionals that are approximate, differences that occur in examining those equilibrium sum rules give some hint on the accuracy and consistency of the functional. As was observed for the pressure of Eq.(5.22), the bulk quantities derived in Eq.(5.29) and Eq.(5.34) do also reduce to their respective PY expression if $8A + 2B = 9$ is fulfilled. This is in agreement with the fact that the Rosenfeld functional is exact for low densities, therefore provides exact thermodynamic quantities up to second order in density.

In order to quantify the performance of the Lutsko functional $\mathrm{LK}(A, B)$ with respect to the aforementioned sum rules, we define the relative deviations

$$\delta_\mu = \frac{\mu_{\mathrm{ex}}^{\mathrm{DFT}} - \mu_{\mathrm{ex}}^{\mathrm{Bulk}}}{\mu_{\mathrm{ex}}^{\mathrm{Bulk}}}, \quad \delta_\chi = \frac{\chi_T^{\mathrm{DFT}} - \chi_T^{\mathrm{Bulk}}}{\chi_T^{\mathrm{Bulk}}}, \tag{5.35}$$

where the DFT quantities $\mu_{\mathrm{ex}}^{\mathrm{DFT}}$ and χ_T^{DFT} refer to Eq.(5.27) and Eq.(5.32), respectively as they are employed in the DFT calculations. Hence, given a suitable function $\mathcal{M}(\delta_\mu, \delta_\chi)$ we can optimize the Lutsko parameters A and B with the minimization prescription $\min_{\eta,A,B} \mathcal{M}(\delta_\mu, \delta_\chi)$. One possibility is to choose $\mathcal{M}(\delta_\mu, \delta_\chi) = \frac{1}{2}(|\delta_\mu| + |\delta_\chi|)$, which ensures that both the relative deviations of Eq.(5.35) must be small. Note that we take the absolute values in order to prevent cancellations that stem from differences in sign.

In order to optimize the Lutsko parameters, we have to compute the relative deviations of excess chemical potential and isothermal compressibility, Eq.(5.35), for every density or packing fraction η over a certain region in the parameter plane spanned by A and B. This means that for a fixed η one optimal point (A, B) is found. Hence, in order to provide a single optimal point performing best over a wide range of packing fractions, we have to apply some sort of averaging. We already know from the exactness of the Rosenfeld functional up to second order in density that the optimal point will be close to the line given by $8A + 2B - 9 = 0$, which we call the PY-line. Therefore, the global optimal point is only affected by the high-density data. In summary, the optimization process can be summarized as follows:

1. We fix the regions for packing fraction η and Lutsko parameters A and B for which the optimization is performed. For the former, we choose the fluid phase at high densities, i.e. $\eta \in [0.35, 0.45]$. The Lutsko parameters are considered in the regions $A \in (0.3, 1.5)$ and $B \in (-1.5, 1.5)$.

2. Then, we perform for a given packing fraction η a DFT minimization for Lutsko parameters A and B that respectively run over the values given in the previous step. The corresponding density profile $\rho(r)$ at hand, we compute the relative deviations $\delta_\mu(\eta; A, B)$ and $\delta_\chi(\eta; A, B)$ according to Eq.(5.35).

3. We repeat the second step until all high-density data is collected.

4. Finally, we compute the arithmetic means $\bar{\delta}_{\mu,\chi}(A, B) = \frac{1}{3}\sum_{\eta=0.35,0.40,0.45} |\delta_{\mu,\chi}(\eta; A, B)|$. Averaging is crucial insofar as to provide an optimal point that improves the sum rules not only for one single high-density point. Afterwards, we find the minimum $\min_{A,B} \mathcal{M}(\bar{\delta}_\mu, \bar{\delta}_\chi)$ yielding the optimal point (A, B).

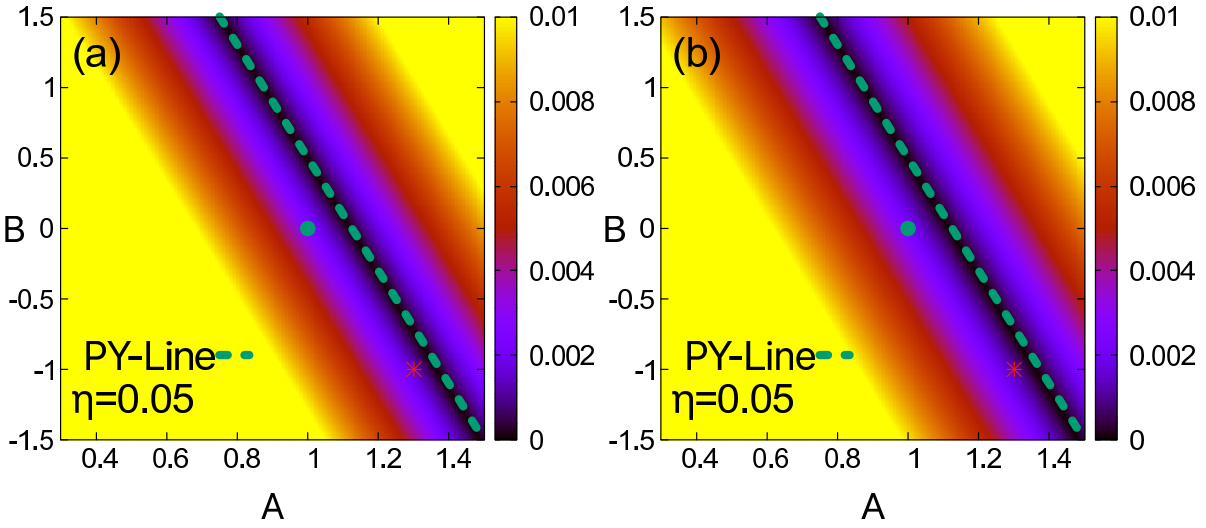

Figure 5.2: Relative deviations (a) $|\delta_\mu|$ and (b) $|\delta_\chi|$, defined in Eq.(5.35), in the parameter plane (A, B) for packing fraction $\eta = 0.05$. The color indicates the magnitude of the deviation. The PY-line is given by $8A + 2B - 9 = 0$. The green circle indicates Lutsko's choice $A = 1.0$, $B = 0.0$ and the red asterisk our optimal point $A = 1.3$, $B = -1.0$

The DFT minimization of the second step requires the computation of the one-body correlation function $c^{(1)}(\mathbf{r}) = -\delta\mathcal{F}_{ex}[\rho]/\delta\rho(\mathbf{r})$ which enters in the Euler-Lagrange equation

$$\rho(r) = \rho_b \exp\left(c^{(1)}(r) + \beta\mu_{\text{ex}} - \beta V_{\text{ext}}(r)\right) \tag{5.36}$$

that we solve using the Picard-iteration, Eq.(3.42).

5.2.2 Optimal Point of LK

For each combination of parameters A and B in Lutsko's functional, we evaluate the excess chemical potential μ_{ex}^{DFT} and the isothermal compressibility χ_T^{DFT}. To visualize their accuracy, we represent the corresponding relative deviations, δ_μ and δ_χ, defined in Eq.(5.35), as heatmaps in Fig.5.2 and Fig.5.3. At each point (A, B) in the parameter plane, the quantities $|\delta_\mu|$ and $|\delta_\chi|$ are shown using a color scale. For reference, we include the PY-line, shown in bright green, defined by $8A+2B-9 = 0$. The displayed parameter range, $A \in [0.3, 1.5]$ and $B \in [-1.5, 1.5]$, is chosen because (i) small deviations are observed near the PY-line, and (ii) the optimal point lies within this region.

At the low packing fraction $\eta = 0.05$, shown in Fig.5.2, the relative deviations for both quantities are small. The regions of minimal deviation are aligned with the PY-line, which is consistent with the fact that the PY approximation is exact up to second order in density. For larger packing fractions, however, the positions of minimal deviation shift away from the PY-line. This effect is visible in Fig.5.3, corresponding to $\eta = 0.35$. In this case, we extend the color scale for δ_χ to improve the visibility of the line of minimum deviation. Furthermore, the region of small deviations in δ_χ is narrower than that of δ_μ. It is also worth noting that, in absolute terms, deviations in the compressibility δ_χ are typically much larger than those in the excess chemical potential δ_μ and increase more rapidly. We thus identify a region, approximately $A \in (1.2, 1.4)$ and $B \in (-1.2, -0.9)$, where both relative deviations remain small.

That we have guaranteed alignment with the PY-line in the low-density regime implies that we do not have to consider low densities in our approach for optimization.

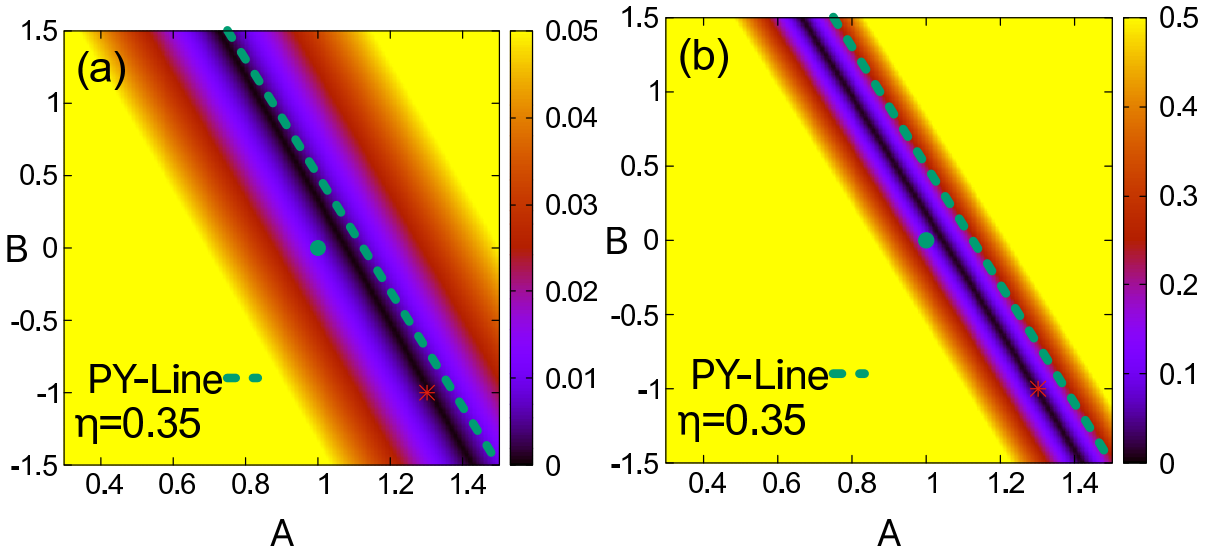

Figure 5.3: Relative deviations (a) $|\delta_\mu|$ and (b) $|\delta_\chi|$, defined in Eq. (5.35), in the parameter plane (A, B) for packing fraction $\eta = 0.35$. The color indicates the magnitude of the deviation; note the distinct scales in (a) and (b). The PY-line is given by $8A+2B-9 = 0$. The green circle marks Lutsko's choice $A = 1.0$, $B = 0.0$, while the red asterisk denotes our optimal parameters $A = 1.3$, $B = -1.0$.

Thus, employing the prescription described in the previous section, we find the following optimal point

$$A = 1.3, \quad B = -1.0, \tag{5.37}$$

which neither lies on the PY-line nor belongs to esFMT(A, B). Lutsko [93] has shown that demanding explicit stability, i.e. $A, B \geq 0$, creates differences from PY in the pair direct correlation function $c^{(2)}(r)$ already at first order in the density, which is unfavorable since PY is exact up to second order. Lutsko proposed a simple choice $A = 1$ and $B = 0$ which still produces a small error at second order in η but improves the virial expansion at higher order [93].

We first present results for the excess chemical potential and isothermal compressibility. In Fig.5.4(a) we see that for μ_{ex}^{DFT} the results from the two Lutsko functionals (LK) lie between the RF and WB results for large η. LK$(1.0, 0.0)$ is closer to WB. The WB results for χ_T^{DFT}, Fig.5.4(b), lie well below RF and both LK results are below WB, with LK$(1.0, 0.0)$ closer to WB. This turns out to be significant when we examine the overall consistency of the underlying functional in Fig.5.5. Here we plot the relative deviations δ_μ and δ_χ versus packing fraction. In Fig.5.5(a) we see that results for δ_μ for our optimal point LK$(1.3, -1.0)$ are generally more consistent than for LK$(1.0, 0.0)$ over the full range of η. As expected, RF performs better than the LK functionals for $\eta \leq 0.2$. WB exhibits the smallest deviations across the range of η . Overall the relative deviations for δ_μ are small for the various functionals even for high densities, typically $< 1\%$.

In Fig.5.5(b), where results for δ_χ are plotted, we first observe that the magnitude of the deviation is generally much larger than for δ_μ; note the vertical scales. WB again exhibits small deviations but these grow as η approaches 0.45. LK$(1.0, 0.0)$ exhibits a large variation with η whereas LK$(1.3, -1.0)$ shows a smoother, monotonic variation and $\delta_\chi < 0.04$ at $\eta = 0.45$. RF performs poorly with $\delta_\chi > 0.13$ for $\eta = 0.3$ and growing for higher values of η.

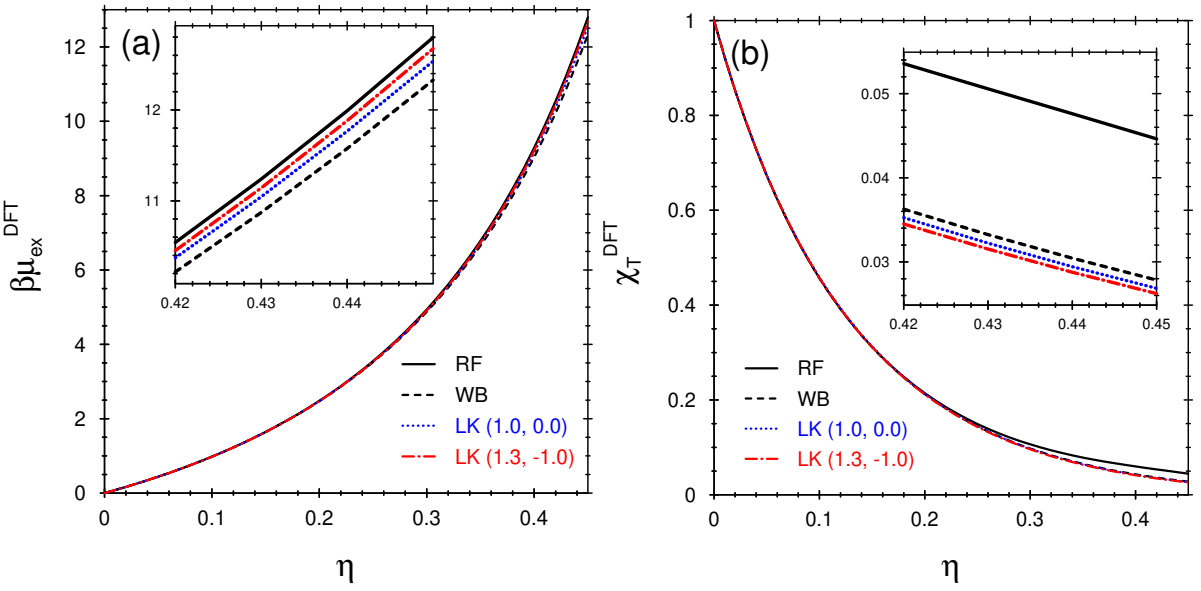

Figure 5.4: Density functional results from test-particle calculations: (a) $\beta\mu_{ex}^{\mathrm{DFT}}$ and (b) χ_T^{DFT} vs. the packing fraction η; the insets show the results on an expanded scale for high densities. We display results for RF, WB, LK$(1.0, 0.0)$ and LK$(1.3, -1.0)$.

Note that from the thermodynamic result, Eq.(5.34), we would expect χ_T for RF to lie below LK(1.3,-1.0), LK(1.0,0.0) and WB. Why this is not the case in the DFT results of Fig.5.4(b) now becomes clear.

Although we have derived our optimal point using large η data the relative deviations remain small for lower densities. This is simply a consequence of the fact that the optimal point is close to the PY-line which represents the correct behaviour at small η. We also note that LK functionals with $8A + 2B \neq 9$ create errors of second order in the density as signalled in Fig.5.5(a) where the relative deviation δ_μ starts to increase rapidly as η increases from zero.

Figure5.6(a) shows the pressure as a function of the packing fraction η. At high densities the deviations between the different functionals become evident. Both LK$(1.3, -1.0)$ and LK$(1.0, 0.0)$ satisfy $8A + 2B < 9$. Thus, according to Eq.(5.22), the corresponding pressure will be lower than PY. LK$(1.0, 0.0)$ is closer to WB which corresponds to the Carnahan-Starling (CS) EoS, known to be very close to that from computer simulations [7]. Adjusting A and B such that the CS result is obtained does not work since the latter corrects the PY result, Eq.(3.95), by subtracting a term proportional to η^3 whereas the additonal term stemming from Lutsko's functional, Eq.(5.22), is proportional to η^2. However, provided $8A + 2B < 9$ the corresponding correction lowers the PY pressure thereby coming closer to the accurate CS result.

In this context it is instructive to examine the virial coefficients. B_n^{esFMT} from the Lutsko functional, given in Table I of [93], deviate from the PY virial coefficients by an amount proportional to $C = \frac{1}{3}(8A + 2B - 9)$ for $n > 2$. While PY is exact for $n = 2$ and $n = 3$, it overestimates the higher order coefficients B_n^{exact}. Since we have $C < 0$ for the Lutsko functionals considered here, the corresponding virial coefficients improve upon those of PY. For LK$(1.3, -1.0)$, with $C = -0.2$, B_4 is closer to the exact result than that from LK$(1.0, 0.0)$, with $C = -0.33333$. For larger n, however, LK$(1.0, 0.0)$ yields results that are closer, in keeping with observations above regarding EoS. Recall that $B_3 = 10 + C$ is not exact since $C < 0$.

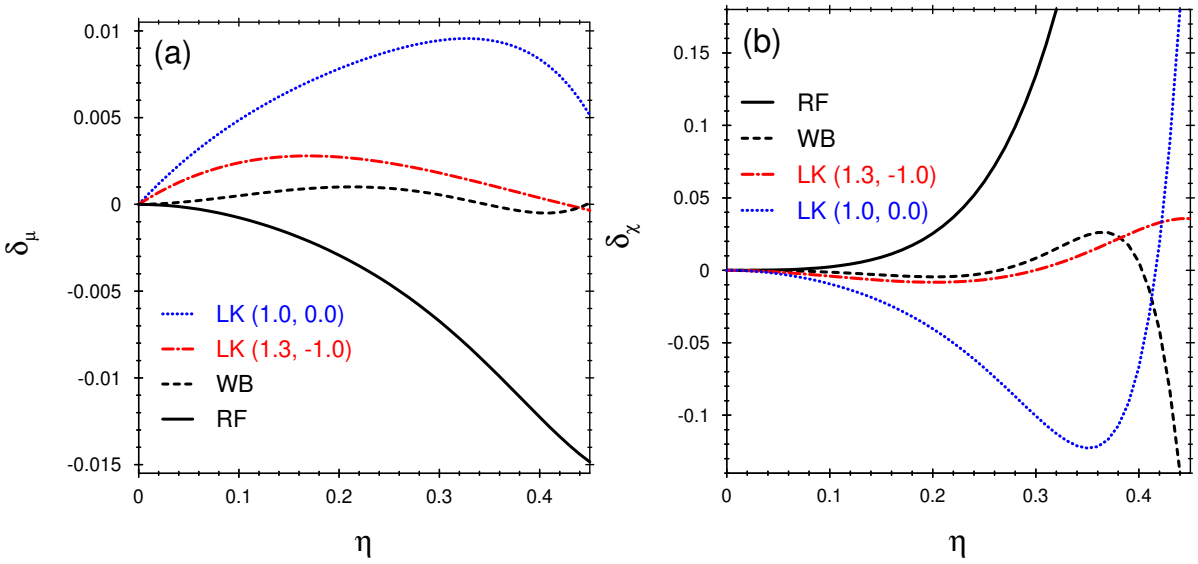

Figure 5.5: Relative deviations (a) δ_μ and (b) δ_χ, defined in Eq.(5.35), vs.the packing fraction η. Note that for the Rosenfeld functional (RF) and the (original) White Bear version of FMT (WB) the deviations are fixed from the underlying theory. By contrast for the Lutsko functional, deviations depend on the parameters A and B which can be tuned. We display results for RF, WB, LK$(1.0, 0.0)$ and LK$(1.3, -1.0)$.

In Fig.5.6(b), we compare the pair direct correlation function $c^{(2)}(r)$ obtained from different functionals with Monte Carlo (MC) simulation results [94] at packing fraction $\eta = 0.4189$. An explicit expression for $c^{(2)}(r)$ derived from Lutsko's functional is provided in App.C.2. Over the full range of r/σ, the WB functional shows the best overall agreement with simulation data, whereas LK$(1.0, 0.0)$ performs slightly better than WB at small values of r/σ.

For r very close to σ, we observe that LK$(1.3, -1.0)$ reproduces the MC data more accurately than LK$(1.0, 0.0)$, yielding a fit comparable to that of the WB functional. Examining $c^{(2)}(r)$ in this way suggests an additional route for optimizing the parameters A and B. By fixing $\eta = 0.4189$, as in Fig.5.6(b), and minimizing the quadratic deviation between $c^{(2)}(r)$ and the simulation results, we obtain $A = 1.44$ and $B = -1.90$. These values differ considerably from those determined via the test-particle sum rules. Alternatively, one may fix A and B by requiring that $c^{(2)}(r)$ at $r = 0$ and $r = \sigma$ match the corresponding simulation values, leading to $A = 1.32$ and $B = -1.33$, which are closer to the optimal parameters obtained from the sum rule analysis. We provide further discussion on this issue in App.C.6.

We thus note that LK functionals lying outside the esFMT class appear to achieve the most consistent performance across the different optimization schemes.

Finally, we examine the overall accuracy of the various functionals we have considered by comparing results, with MC simulation, for density profiles $\rho(r)$, for several high values of η, at a hard spherical test particle Fig.5.7 and a hard planar wall, Fig.5.8. Note that the density profile at the spherical test particle is plotted with contact at $r = \sigma$ whereas for the planar hard wall contact is at $z = 0.5 \times \sigma$.

From Fig.5.7 we observe that for the four functionals we consider the agreement with our own simulation data is good with slight differences near the first maximum of the density profile, i.e. $r/\sigma \approx 2$. Only in the vicinity of contact with the test particle do

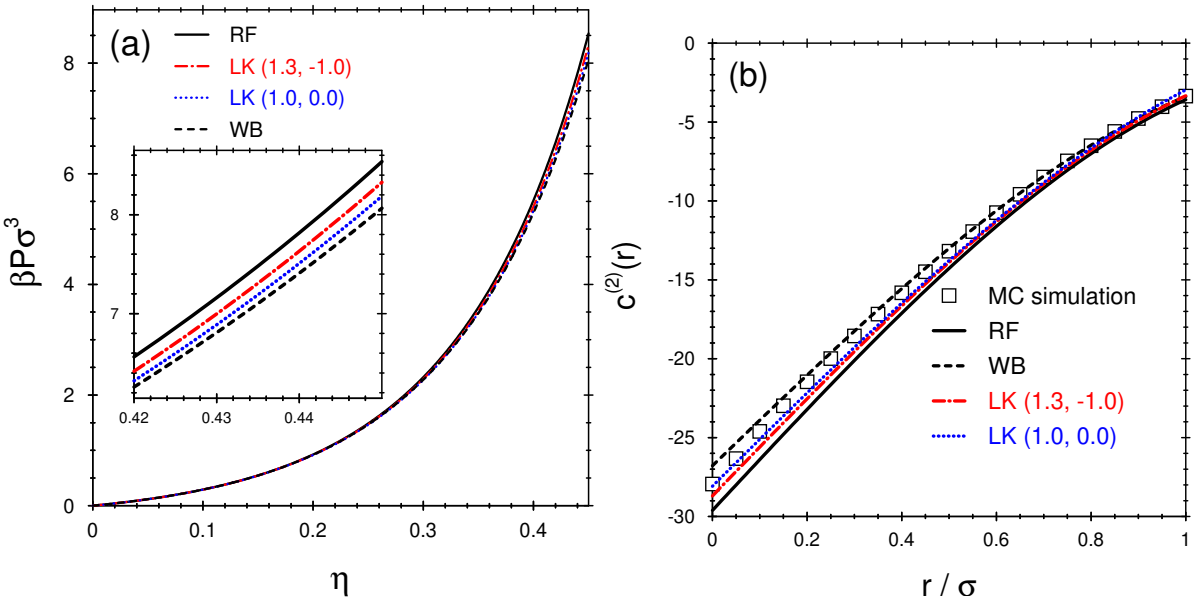

Figure 5.6: (a) Reduced pressure $\beta P\sigma^3$ vs. the packing fraction η; the inset shows the results on an expanded scale for high densities. Recall that the WB results are equivalent to those of CS which are very close to simulation. (b) Pair direct correlation function $c^{(2)}(r)$ as a function of r/σ for $\eta = 0.4189$. DFT results are compared with MC simulation data [94]. Recall $\sigma = 2R$ is the HS diameter. In all these theories $c^{(2)}(r) = 0$, for $r > \sigma$.

deviations become relevant. The density profile from the RF-functional lies above the MC data points whereas results corresponding to LK-functionals stay between RF and WB. As expected, WB captures best the MC data points near the test particle. LK$(1.0, 0.0)$ and LK$(1.3, -1.0)$ both perform better than RF. Of course, this reflects the accuracy of the underlying EoS and the contact value theorem Eq.(5.24).

For the planar hard wall, Fig.5.8, we see that deviations from MC are pronounced at the first maximum of the density profile near $z/\sigma \approx 1.5$, especially for $\eta = 0.4911$, see Fig.5.8(b). Deviations also occur close to the wall. Again WB fits the MC data points best, reflecting the fact that it incorporates the CS EoS. It is important to note that there is no reason that LK$(1.3, -1.0)$ should provide an accurate description at the planar wall. Recall this was derived in the test-particle geometry. Figure5.8 clearly shows that the corresponding planar profile is very close to those from other functionals. Differences of the density profiles occur only close to the wall.

5.2.3 Conclusion

Current FMT functionals are powerful tools to describe hard-sphere mixtures. Building on RF, the WB versions make more accurate predictions for structure and thermodynamics compared to simulations. Motivated by improving accuracy, we investigated statistical mechanical sum rules, namely the Gibbs-adsorption theorem, Eq.(5.23) and contact theorem, Eq.(5.24), which are satisfied by FMT and serve as numerical checks only.

We introduced new sum rules for the excess chemical potential $\mu_{\rm ex}$, Eq.(5.27), and isothermal compressibility χ_T, Eq.(5.32), in test-particle geometry using Percus' ideas. FMT does not generally satisfy these sum rules, allowing us to assess its internal consistency via relative deviations δ_μ and δ_χ, Eq.(5.35). Results for RF and WB are shown in

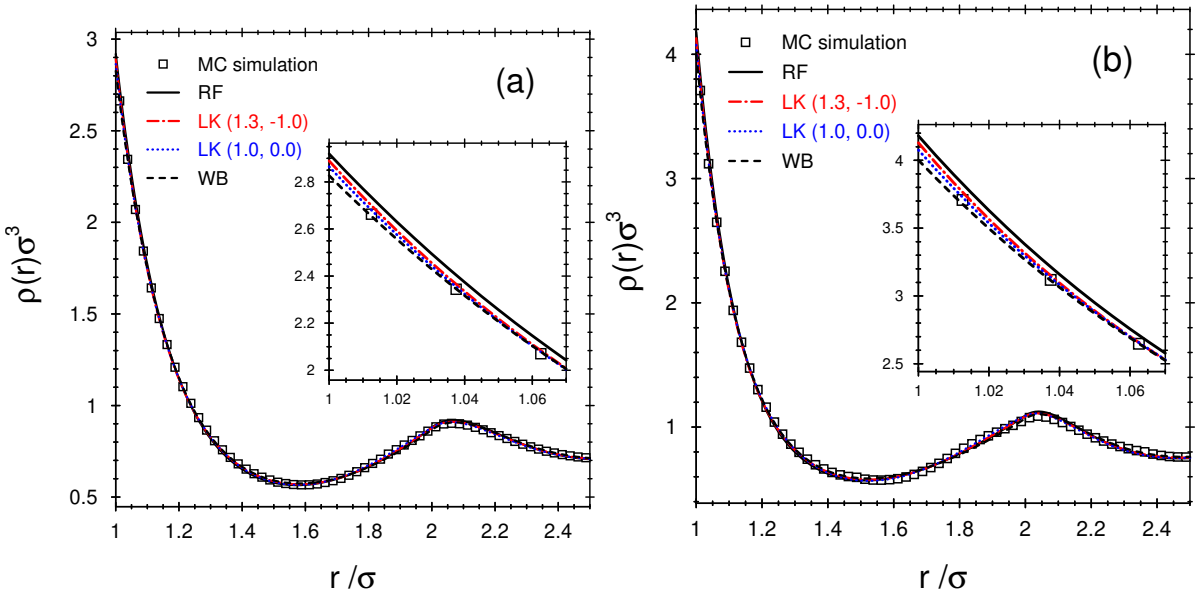

Figure 5.7: Density profile $\rho(r)$ at a spherical test particle of diameter σ for (bulk) packing fractions (a) $\eta = 0.40$ and (b) $\eta = 0.45$; the inset shows results close to contact on an expanded scale.

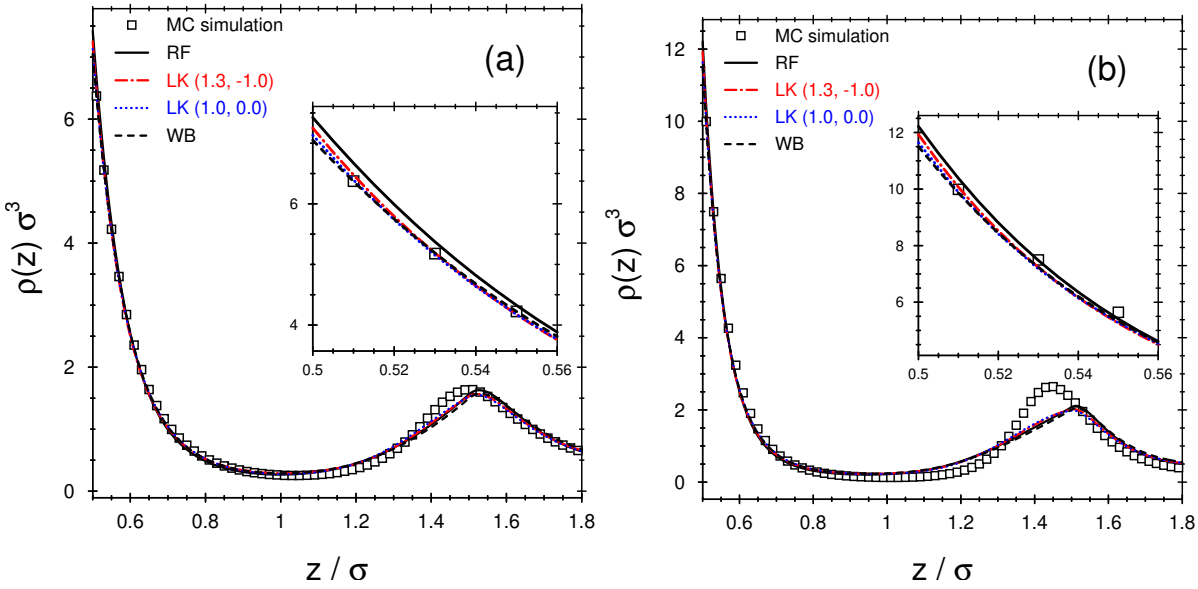

Figure 5.8: Density profile $\rho(z)$ at a planar hard wall for (bulk) packing fractions (a) $\eta = 0.4341$ and (b) $\eta = 0.4911$; the inset shows results close to the wall on an expanded scale. The MC data are taken from [95].

Fig.5.5, where WB performs well except, unless high packing fractions are reached.

These sum rules help fix the free parameters A and B in the Lutsko functional, Eq.(5.20). We defined a target function $\mathcal{M}(\delta_\mu, \delta_\chi) = \frac{1}{2}(|\delta_\mu| + |\delta_\chi|)$ and minimized it over three packing fractions $\eta \in 0.35, 0.40, 0.45$. The optimal parameters for fluid states are $A = 1.3$, $B = -1.0$, denoted as LK$(1.3, -1.0)$. These differ from Lutsko's original choice LK$(1.0, 0.0)$ [93], selected under stability constraints $(A, B \geq 0)$ and for crystals. Our negative B violates these, but does not directly imply instability. LK$(1.3, -1.0)$ does not lie on the PY line $(8A + 2B = 9)$. It yields a pressure closer to CS, while LK$(1.0, 0.0)$ matches CS even better, see Fig.5.6(a). Similar trends hold for $c^{(2)}(r)$, see Fig.5.6(b).

Overall, LK$(1.3, -1.0)$ performs well. The deviation in μ, Fig.5.5(a), is smaller than RF and LK$(1.0, 0.0)$, and comparable to WB. The compressibility deviation, Fig.5.5(b), is smaller than in all other cases, especially at high η.

The Lutsko functional, Eq.(5.19), represents an extension of the tensorial version [61] of Rosenfeld's original functional [9], discussed in Sec.4.2. In many subsequent developments of FMT, modifications have primarily targeted the Φ_3 term, often by introducing additional dependencies on the weighted density n_3, with the goal of improving the resulting EoS [66, 62, 67]. From the broader perspective of the FMT toolbox approach [10], Lutsko's generalization [93] can be viewed as a systematic framework that can also be applied to existing functionals such as WB [62, 67] or WBII [68]. In this way, one can construct modified versions of these models that potentially achieve an even higher degree of internal consistency and thermodynamic accuracy. In the next section we introduce and discuss these new set of functionals in more detail. The sum rules we introduced apply to any pair potential. We focused on hard spheres due to the accuracy of existing functionals. A major challenge in classical DFT remains the accurate inclusion of attractive forces, often treated by mean-field methods [60]. Recent approaches include a correlated treatment via Barker-Henderson theory [96, 97], which could be tested with our sum rules. Similarly, machine learning DFT methods, which learn functionals from one-body profiles for hard spheres [98] and Lennard-Jones fluids [99], and others [100], can also be assessed for internal consistency using our framework.

5.3 Lutsko-WB Functionals

In the previous section, we investigated the Lutsko functional under the scope of two equilibrium sum rules, namely excess chemical potential μ_{ex} and isothermal compressibility χ_T for the test-particle geometry that we presented in Sec.5.2.1. This allowed us to optimize the free parameters A and B of the Lutsko functional by minimizing the errors between thermodynamic and DFT route. For that, we have calculated the errors for a given region in the parameter plane spanned by A and B in order to apply an optimization scheme that only included data from high densities as these notably affect the result. We found that for low densities values of A and B being on the PY-line, i.e. $8A + 2B = 9$, minimize these errors, in accordance with our expectation that the PY approximation is exact up to second order in the density. By going to higher densities, it turned out that the line of minimal errors is somehow shifted to the PY-line. Thus, the optimal point we derived only from high densities is slightly off the PY-line leading to errors already at second order.

Now we want to extend Lutsko's idea for a functional incorporating the structure of Φ_3^{LK} of the original proposal, but now for the WB and WBII functionals of Sec.4.2.2

[62, 67, 68]. By doing so, we try to further improve upon the sum rules of excess chemical potential and isothermal compressibility for functionals being somewhat more precise than the RF functional. We showed in the previous section, Sec.5.2, that due to the Lutsko parameters A and B the thermodynamic quantities are modified such that for $8A+2B=9$ the RF expressions are reproduced. Therefore, by constructing the corresponding WB and WBII versions of the Lutsko functional we expect a similar observation, but now the quantities reducing to the expressions derived from the WB free energy density where we only consider one-component systems. As was discussed in Sec.4.2.2, the WB functional is inconsistent with respect to pressure, i.e. there is a (slight) difference between the inputted Carnahan-Starling (CS) pressure [80, 35] in the derivation and the pressure obtained through the scaled-particle relation $\partial\Phi^{\mathrm{WB}}/\partial n_3$ [75]. In the case of the WBII version, this problem is remedied by using a different expression for the pressure [68]. Hence, by introducing the Lutsko parameters A and B in the corresponding version of the Lutsko functional, these inconsistencies will be affected accordingly offering the possibility of further minimizing the error in the case of WB.

Recalling that the WB functionals are somewhat more consistent than the RF functional, it is compelling to extend the form of the Lutsko functional, Eq.(5.19), such that the tensorial version of WB and WBII can be recovered. Hence, we expect a higher degree of self-consistency for these type of functionals. As the WB functional merely differs in its n_3-dependence in Φ_3 of the RF functional, it is obvious to apply the same reasoning also to Φ_3^{LK}, Eq.(5.20), of the Lutsko functional. The same approach we also apply to WBII.

Regarding the WB version of the Lutsko functional we therefore write

$$\Phi_3^{\text{LK-WB}} = f(n_3)\left[(A+B)n_2^3 - 3A\; n_2\mathbf{n}_2\cdot\mathbf{n}_2 + 3A\;\mathbf{n}_2\;\mathbf{T}\;\mathbf{n}_2 - 3B\;n_2\mathrm{Tr}\,\mathbf{T}^2 + (2B-A)\mathrm{Tr}\,\mathbf{T}^3\right], \tag{5.38}$$

where $f(n_3)$ reads

$$f(n_3) = \frac{n_3 + (1-n_3)^2\log(1-n_3)}{36\pi n_3^2(1-n_3)^2}, \tag{5.39}$$

so in total we have the Lutsko-WB functional

$$\Phi^{\text{LK-WB}} = \Phi_1 + \Phi_2 + \Phi_3^{\text{LK-WB}}. \tag{5.40}$$

Similarly, the WBII version of the Lutsko functional shall take the form

$$\Phi^{\text{LK-WBII}} = \Phi_1 + \varphi_1(n_3)\Phi_2 + \varphi_2(n_3)\Phi_3^{\text{LK}}, \tag{5.41}$$

where

$$\begin{aligned}\varphi_1(n_3) &= 1 + \frac{2n_3 - n_3^2 + 2(1-n_3)\log(1-n_3)}{3n_3}\\ \varphi_2(n_3) &= 1 - \frac{2n_3 - 3n_3^2 + 2n_3^3 + 2(1-n_3)^2\log(1-n_3)}{3n_3^2}.\end{aligned} \tag{5.42}$$

are the functions of the original derivation in the WBII construction[68].

Therefore, we generalize the original Lutsko functional to its WB and WBII version by replacing the numerator of the corresponding Φ_3 of WB or WBII with the numerator given in Lutsko's functional, Eq.(5.20), containing the parameters A and B [93]. By construction of these new functionals, the tensorial versions of WB and WBII are again recovered for $A=-B=3/2$ and therefore the thermodynamic quantities of CS.

n	B_n^{exact}	B_n^{LK}	$B_n^{\text{LK-WB}}$	$B_n^{\text{LK-WBII}}$
2	4	4	4	4
3	10	$10+C$	$10+C$	$10+C$
4	18.36	$19+3C$	$18+\frac{8}{3}C$	$18+\frac{7}{3}C$
5	28.22	$31+6C$	$28+5C$	$28+\frac{13}{3}C$
6	39.82	$46+10C$	$40+8C$	$40+7C$
7	53.34	$64+15C$	$54+\frac{35}{3}C$	$54+\frac{31}{3}C$

Table 5.1: Virial coefficients B_n of the Lutsko functionals together with the exact values B_n^{exact} and $C = \frac{1}{3}(8A + 2B - 9)$.

Certainly, the condition for explicit stability, as was outlined in [93], is not affected by these novel functionals. Indeed, Lutsko has shown [79] that introducing the White-Bear and White-Bear mark II functionals do not qualitatively change the stability condition on the Rosenfeld functional including its tensorial version. It will be convenient to abbreviate the Lutsko-WB functional as LK-WB(A, B) and analogously LK-WBII(A, B) for the mark II version.

The corresponding EoS via the thermodynamic route $\beta P = -\Phi + \rho\partial\Phi/\partial\rho$ are given by

$$\frac{\beta P^{\text{LK-WB}}(A,B)}{\rho} = \frac{\beta P^{\text{CS}}}{\rho} + (8A + 2B - 9)\frac{\eta^2(3-\eta)}{9(1-\eta)^3} \tag{5.43}$$

and

$$\frac{\beta P^{\text{LK-WBII}}(A,B)}{\rho} = \frac{\beta P^{\text{CS}}}{\rho} + (8A + 2B - 9)\frac{\eta^2(3-2\eta+\eta^2)}{9(1-\eta)^3}, \tag{5.44}$$

where P^{CS} is the CS EoS. Again, we see that for $8A + 2B = 9$ both EoS, Eq.(5.43) and Eq.(5.44), reduce to the CS EoS. Note that $P^{\text{LK-WBII}}$ is modified differently compared to $P^{\text{LK-WB}}$. Tabular5.1 shows the first six Virial coefficients of the Lutsko-WB functionals. Deviations due to the Lutsko parameters first occur at $n = 3$. Here, it is important to note that the self-consistency of the LK-WB functional with respect to the pressure, namely

$$\beta P^{\text{SP}} = \frac{\partial\Phi}{\partial n_3}, \tag{5.45}$$

is violated, in accordance with the original discussion, given in [62]. The associated deviation between the bulk pressure and the scaled-particle pressure obtained in Eq.(5.45) however will depend on the free Lutsko parameters A and B. This implies that full consistency with respect to the pressure can be realized by choosing the Lutsko parameters accordingly. Due to its construction, the same relation, Eq.(5.45), is automatically fulfilled in the case of LK-WBII, as long as $8A + 2B = 9$ is satisfied. Note that in the case of the Lutsko functional in Sec.5.2 the self-consistency is automatically fulfilled.

5.3.1 Optimal Points of LK-WB and LK-WBII

Similar to the analysis we have made in Sec.5.2.2, we optimize the Lutsko-WB functionals Eq.(5.40) and Eq.(5.41) by minimizing the relative error between the bulk and DFT route of Eq.(5.35) with respect to the parameters A and B hence providing the optimal point (A, B) of the corresponding functional. We again chose $M(\delta_\mu, \delta_\chi) = \frac{1}{2}(|\delta_\mu| + |\delta_\chi|)$ for

minimization. We compute $\mu_{\text{ex}}^{\text{DFT}}$ and χ_T^{DFT} according to Eq.(5.27) and Eq.(5.32) in the test-particle geometry for spherically symmetric equilibrium density profile $\rho(r)$. The bulk values $\mu_{\text{ex}}^{\text{Bulk}}$ and χ_T^{Bulk} are calculated according Eq.(5.28) and Eq.(5.33) giving in total for Lutsko-WB

$$\beta\mu_{\text{ex}}^{\text{LK-WB}}(A,B) = \beta\mu_{\text{ex}}^{\text{CS}} + (8A+2B-9)\frac{\eta(1+2\eta-\eta^2)+(1-\eta)^3\log(1-\eta)}{9(1-\eta)^3}, \tag{5.46}$$

$$\chi_T^{\text{LK-WB}}(A,B) = \chi_T^{\text{CS}}\left(1+(8A+2B-9)\frac{\eta^2}{9}\frac{9-4\eta+\eta^2}{1+4\eta+4\eta^2-4\eta^3+\eta^4}\right)^{-1}$$

and for Lutsko-WBII

$$\beta\mu_{\text{ex}}^{\text{LK-WBII}}(A,B) = \beta\mu_{\text{ex}}^{\text{CS}} - (8A+2B-9)\frac{\eta(1-7\eta+6\eta^2-2\eta^3)+(1-\eta)^3\log(1-\eta)}{9(1-\eta)^3} \tag{5.47}$$

$$\chi_T^{\text{LK-WBII}}(A,B) = \chi_T^{\text{CS}}\left(1+(8A+2B-9)\frac{\eta^2}{9}\frac{9-8\eta+7\eta^2-2\eta^3}{1+4\eta+4\eta^2-4\eta^3+\eta^4}\right)^{-1}.$$

As we expect, these quantities reduce to the CS expressions for μ_{ex} and χ_T when $8A+2B-9=0$ is satisfied.

Here we want to emphasize once more that the analysis takes into account only high densities as for these values considerable deviations occur, i.e. we apply the same strategy as in Sec.5.2.2. This, of course, assumes that the optimal points will lie close to the now CS-line $8A+2B=9$ so that even for low densities the associated deviations will remain small. This argument follows directly from the fact that the functionals are exact up to second order in density therefore producing small errors at low densities. This further implies that we perform an average relative deviation for δ_μ and δ_χ at high densities in order to derive the optimal point. The averaging is done for packing fractions $\eta = 0.35, 0.40$ and 0.45 which are weighted equally. Herewith, we guarantee that instead of optimizing solely for one high packing fraction we rather want to find an optimal point that possesses small relative deviations throughout high densities.

With the same ranges of A and B as given in Sec.5.2.2, the following optimal points are found

$$\begin{aligned} \text{LK-WB}: &\quad A=1.35, \quad B=-0.85 \\ \text{LK-WBII}: &\quad A=1.25, \quad B=-0.2, \end{aligned} \tag{5.48}$$

where it is interesting to note that the A values are similar to that of the optimal point found for LK in Sec.5.2.2. The deviations caused by $8A+2B-9$ show that the optimal point of LK-WB is relatively close to the CS-line ($8A+2B-9=0.1$) whereas that of LK-WBII is much more distant ($8A+2B-9=0.6$). Similarly to Fig.5.2 and Fig.5.3, there is a region in the (A,B)-plane where the line of smallest deviations intersect, being close to the CS-line. The latter observation causes some inconsistency with respect to the pressure.

We start with presenting the relative deviations δ_μ and δ_χ, Eq.(5.35), as a function of the packing fraction η, see Fig.5.9. For comparison, we again display the curve of LK$(1.3,-1.0)$. We observe that the relative deviations in the case of WBII increase most rapidly, well above the others for $\eta > 0.35$. What we can also infer for lower packing fractions is that LK$(1.3,-1.0)$ and LK-WBII$(1.25,-0.20)$ already have high relative

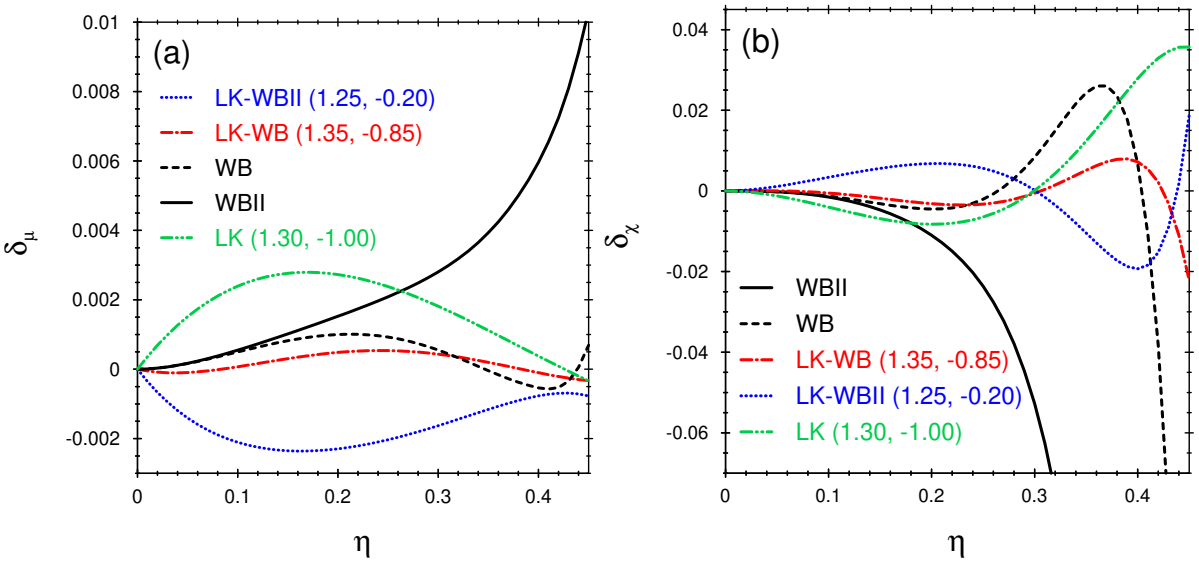

Figure 5.9: Relative deviations (a) δ_μ and (b) δ_χ vs.the packing fraction η.

deviations since they are most distant to the PY- and CS-line, respectively. It is worth noticing that the relative deviations for both seem to be mirrored with respect to the zero-line. For LK-WB$(1.35, -0.85)$ we find that the relative deviations remain small over the whole range we consider here. Especially for $\eta > 0.35$ the relative deviations are smaller than those of WB, in particular smaller than LK$(1.30, -1.00)$ and LK-WBII$(1.25, -0.20)$. Due to its proximity to the CS-line, the relative deviations of LK-WB$(1.35, -0.85)$ are small for low densities and only increase slowly for higher densities. Especially the excess chemical potential μ_{ex} is very accurately described by LK-WB$(1.35, -0.85)$.

Overall, we can conclude that the sum rules for μ_{ex} and χ_T can be improved, achieving slightly higher accuracy than LK$(1.3, -1.0)$ at high densities. In particular, for the WBII functional, introducing its Lutsko form, Eq.(5.42), leads to a significant improvement in the fulfillment of the sum rules, although its overall accuracy across the full range of liquid packing fractions remains somewhat lower than that of LK-WB$(1.35, -0.85)$.

Figure5.10(a) displays the relative deviations of the various Lutsko functionals with respect to the CS EoS. While LK$(1.30, -1.00)$ and LK-WBII$(1.25, -0.20)$ deviate from P^{CS} at high densities, LK-WB$(1.35, -0.85)$ remains close, as expected, since its parameters lie near the CS-line. Recall that, unlike WBII, which exactly reproduces the CS EoS for the one-component fluid, the Lutsko-modified version LK-WBII$(1.25, -0.20)$ exhibits deviations due to its altered parameterization. In Fig.5.10(b), we show the pressure inconsistencies of the corresponding functionals, comparing results obtained via the thermodynamic route with those computed from the scaled-particle relation $\partial\Phi/\partial n_3$ [59]. The inconsistencies for WB and LK-WB$(1.35, -0.85)$ are nearly identical, remaining below 2% and diverging only slightly at high densities. LK-WBII$(1.25, -0.20)$ shows inconsistencies of similar magnitude, though with a different shape. While the original WBII functional is fully consistent, the Lutsko-modified form LK-WBII(A, B) becomes inconsistent whenever $8A + 2B - 9 \neq 0$. Nevertheless, the overall degree of consistency remains high.

The virial coefficients B_n of the Lutsko functionals are obtained from their respective EoS by expansion in powers of the density. For the optimized parameters, these coefficients are shown in Fig.5.11 for $n = 2, \ldots, 7$. Since all Lutsko functionals are exact up to

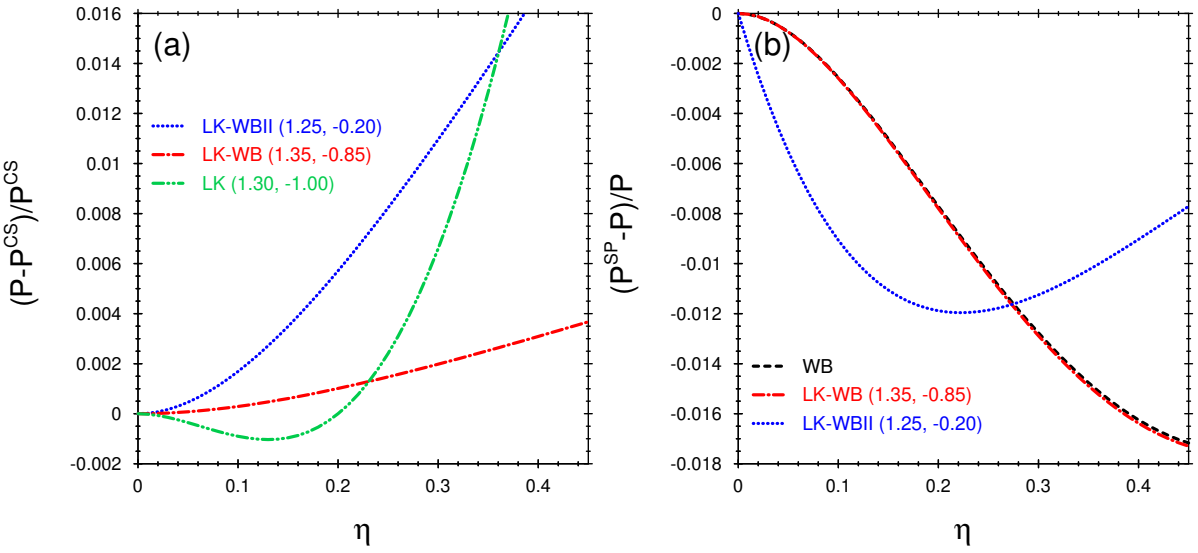

Figure 5.10: (a) displays relative deviations of the corresponding pressures of the Lutsko functionals with respect to the CS pressure P^{CS}. (b) shows the inconsistency $(P^{\mathrm{SP}}-P)/P$ between βP obtained via Eq.(5.43), Eq.(5.44) and $\beta P^{\mathrm{SP}} = \partial\Phi/\partial n_3$ for the LK-WB functionals. We see that errors stay below 2%, showing high self-consistency.

second order, they yield identical values for $n = 2$ and begin to differ for $n > 2$. Starting from $n = 3$, small deviations appear among the functionals. LK-WB$(1.35, -0.85)$ and LK-WBII$(1.25, -0.20)$ remain close to the exact values, with LK-WB showing slightly better accuracy, especially at higher orders. This observation is consistent with the fact that the optimal point of LK-WB lies near the CS-line. In contrast, LK$(1.30, -1.00)$ tends to overestimate the exact coefficients for $n \geq 5$. Tabular5.1 contains the virial coefficients of the Lutsko functionals up to $n = 7$.

Furthermore, we examine the pair direct correlation functions $c^{(2)}(r)$ of the selected functionals for two high packing fractions η, as shown in Fig.5.12. For $r \approx 0$, the WB, WBII and LK-WB$(1.35, -0.85)$ functionals slightly overestimate the Monte Carlo (MC) simulation data, whereas LK$(1.3, -1.0)$ and LK-WBII$(1.25, -0.20)$ provide a more accurate description. Once again, the Lutsko parameters A and B can be optimized using the correlation function at packing fraction $\eta = 0.419$. By constraining $c^{(2)}(r = 0)$ and $c^{(2)}(r = \sigma)$ to match the MC results, we obtain for LK-WB the values $A = 1.48$ and $B = -0.94$, which are close to the optimal parameters previously determined from the sum rules. Similarly, for LK-WBII we find $A = 1.60$ and $B = -1.61$, which deviate more substantially from the corresponding sum-rule optimum. Alternatively, minimizing the overall deviation between the DFT prediction and the MC simulation yields $A = 1.73$, $B = -2.12$ for LK-WB and $A = 1.72$, $B = -2.21$ for LK-WBII. In App.C.6 we refer to the corresponding improvements.

In summary, all functionals presented in Fig.5.12 reproduce the direct correlation function $c^{(2)}(r)$ with good accuracy, with noticeable deviations appearing only near $r \approx 0$. In this regime, a modest improvement over WB is achieved with LK-WB$(1.35, -0.85)$, and an even greater one with LK-WBII$(1.25, -0.20)$. For $r \approx \sigma$, the differences between the various functionals are minimal, and all yield an excellent agreement with the MC data.

We now draw some conclusions regarding the stability of the Lutsko functionals considered in this work. Figure5.13 displays the density profiles for LK$(1.3, -1.0)$, LK-

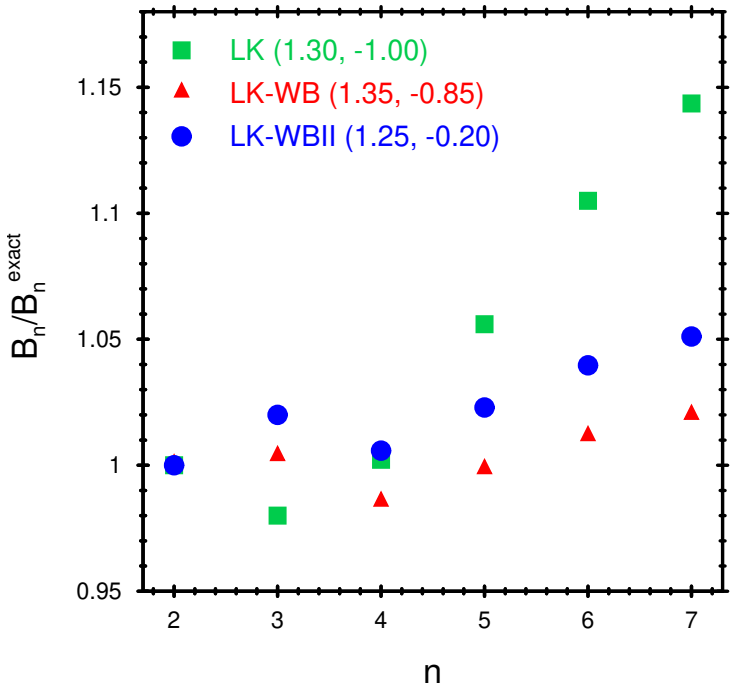

Figure 5.11: Virial coefficients B_n of the optimized Lutsko functionals normalized to the exact values B_n^{exact} taken from [31].

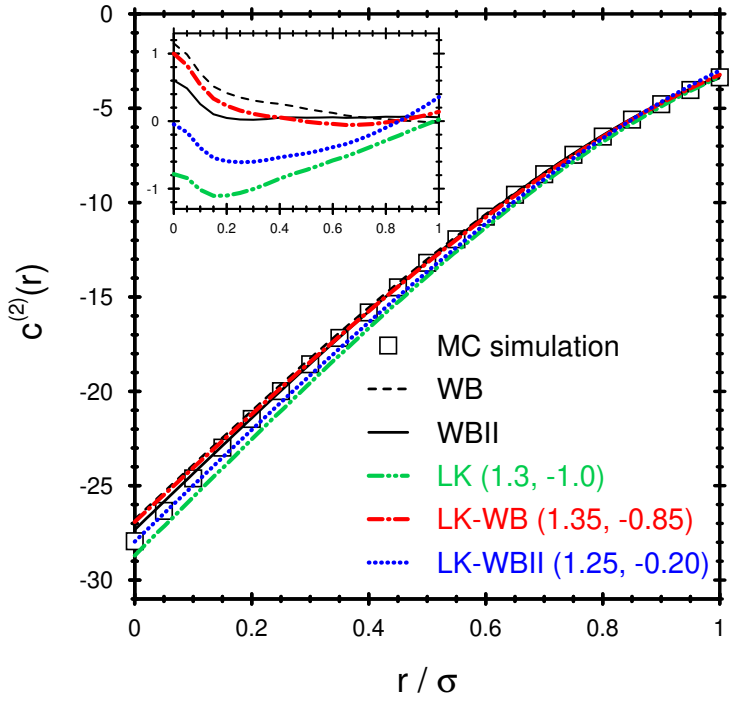

Figure 5.12: The direct correlation function $c^{(2)}(r)$ is shown at a packing fraction $\eta = 0.419$ for WB, WBII, LK$(1.3, -1.0)$, LK-WB$(1.35, -0.85)$ and LK-WBII$(1.25, -0.20)$ together with MC simulation data taken from [94]. The inset shows the difference to MC data.

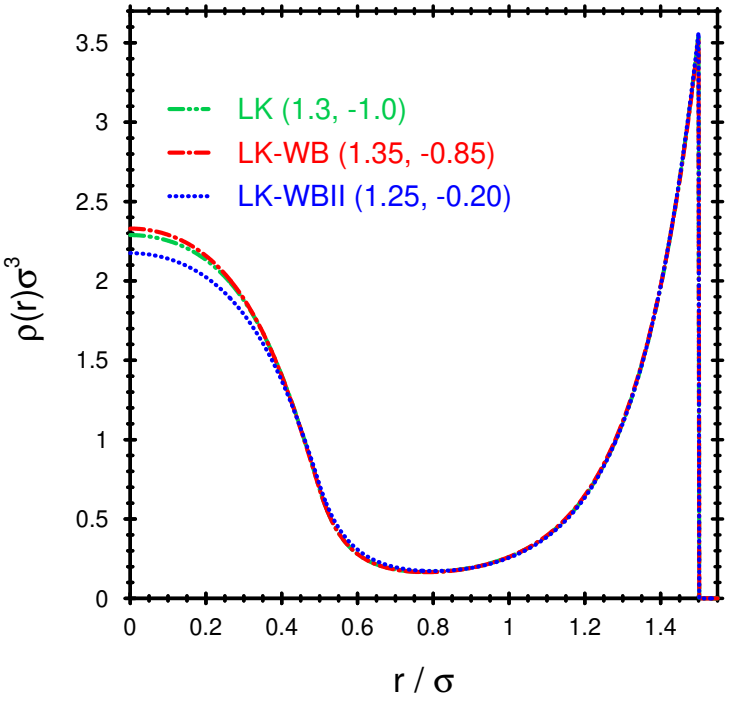

Figure 5.13: The density profile $\rho(r)$ is shown at a packing fraction $\eta = 0.419$ for WB, WBII, LK$(1.3, -1.0)$, LK-WB$(1.35, -0.85)$ and LK-WBII$(1.25, -0.20)$.

WB$(1.35, -0.85)$, and LK-WBII$(1.25, -0.20)$ inside a spherical cavity of radius $R = 2\sigma$ at a packing fraction $\eta = 0.32$. The contact value appears at $r = 3/2\,\sigma$, corresponding to the location of the hard wall. Notably, differences between the density profiles produced by the various functionals are most pronounced near the center of the cavity. Despite the strong confinement and relatively high packing fraction, the Lutsko functionals do not exhibit any signs of instability when minimizing the grand potential. In contrast, both the original Rosenfeld and White-Bear functionals fail under these conditions. However, their q_3-modified versions remain stable [76, 61], see also Sec.4.2.1 and Sec.4.2.2. This empirical modification was originally introduced to address unphysical behavior namely, the lack of a lower bound in Φ_3^{RF} observed for highly structured density profiles in crystals [9, 90]. Lutsko later demonstrated that stability is explicitly ensured when the parameters A and B are positive, although the behavior outside this regime remains unclear [93]. Using this simple test case of a spherical cavity, we find that the Lutsko functionals examined here, although not belonging to the explicitly stable class, exhibit greater numerical stability than the original Rosenfeld and White-Bear functionals.

5.3.2 Conclusion

We investigated the novel functionals for hard spheres based on the idea of Lutsko's paper [93] regarding their consistency and accuracy in the light of two equilibrium sum rules, namely excess chemical potential and isothermal compressibility. These new versions outlined in Sec.5.3 are motivated by the more accurate functionals of hard spheres of WB and WBII [62, 67, 68] in the framework of FMT [9]. The construction of these novel functionals in Eq.(5.40) and Eq.(5.41) is achieved in such a way that the tensorial versions of WB and WBII are recovered for $8A + 2B = 9$, akin to the property of Eq.(5.19). Although there are no a-priori reasons to propose these functionals, the concept of incor-

porating the structure of Eq.(5.20) into WB and WBII is compelling, given the fact that latter serve as more accurate descriptions of hard-sphere mixtures. Again, the additional parameters of Lutsko, A and B, allowed us to optimize the corresponding functionals such that the aforementioned sum rules are fulfilled best. The optimization scheme is equal to the scheme employed in Sec.5.2, i.e. after having calculated all deviations δ_μ and δ_χ for each point (A, B) at fixed packing fraction η, we calculate averaged values for high densities.

Similarly to the optimal point obtained in Sec.5.2 in the case of the Rosenfeld based functional of Lutsko, the optimal points of Lutsko-WB and Lutsko-WBII have the property $A > 0$ and $B < 0$, given in Eq.(5.48). However, as can be inferred from Fig.5.9, the consistency of the White-Bear versions of the Lutsko functional are improved, especially in the case of WBII. Latter exhibits rather high deviations with respect to the sum rules which are corrected extensively when employing the associated optimal point $(A, B) = (1.25, -0.20)$. These improvements furthermore are better performing than LK$(1.3, -1.0)$, particularly for LK-WB$(1.35, -0.85)$. LK-WBII$(1.25, -0.20)$ is somehow reflected with respect to zero-line compared to LK$(1.30, -1.00)$ with slightly smaller magnitude in deviation.

The introduction of the Lutsko parameters, in addition, affects the consistency of the functionals in Eq.(5.40) and Eq.(5.41) with respect to pressure, P. While in the case of the Rosenfeld version, Eq.(5.19), consistency is automatically satisfied, deviations are induced for Lutsko-WB, see Fig.5.10. In particular, the LK-WBII functional possesses deviations as long as $8A + 2B \neq 9$. For the optimal points considered here, the corresponding deviations in pressure stay below 2%. The direct correlation functions of Fig.5.12 show in total that extending Lutsko's idea to the White-Bear functional improves upon the accuracy when compared to MC results. The Lutsko-WBII functional, in contrast, only improves close to $r \approx 0$, becoming less accurate than WBII as r approaches σ. Still, the Lutsko-WB functionals show good agreement with MC data over the whole range $0 \leq r \leq \sigma$ and even outperforming LK$(1.30, -1.00)$.

Chapter 6

Effective Square-Well Interactions

In Sec.2.5 we introduced the square-well (SW) interaction that is widely use for intermolecular forces in classical fluids. Despite its simplicity, the SW model captures rich fluid behavior and serves as a benchmark for testing approximations in density functional theory (DFT). Of course, the assumed simplicity entails a lack of understanding or describing fully correlations in dense or critical regimes. One key feature of the SW model is the ability of giving rise to phase coexistence between a liquid and a vapor phase with a corresponding critical point being determined by rather simple model parameters, such as interaction range λ and strength ϵ. Rendering the interaction range to be of finite size comes along undoubtably with restrictions on the quality of the model. However, DFT calculations can be performed in a straightforward manner, with convolutions that are similar to those being done within FMT, see Ch.4.

Making use of the SW interaction within the framework of DFT enables a first simplistic study of inhomogeneous fluids on their thermodynamics and properties. Typically, the underlying free-energy or Helmholtz functional $\mathcal{F}_{\text{ex}}$, see Sec.3.8, is decomposed into a repulsive, hard-core part $\mathcal{F}_{\text{hs}}$ and an attractive part $\mathcal{F}_{\text{sw}}$ accounting for SW interactions. Latter is often taken in a mean-field treatment, i.e. there is a background field $n_{\text{sw}}(\mathbf{r})$ acting on a reference particle at position $\mathbf{r}$. This is a crude description insofar as only two-body interactions are taken into account and important correlational effects are not captured. Nonetheless, as far as low densities and high temperatures are concerned, the mean-field approach is sufficiently descriptive in order to predict interesting features of SW interactions.

6.1 Square-Well in DFT

The square-well (SW) fluid is a fairly simple model to describe systems with attractive forces like argon. The pair-interaction potential is given by

$$\phi(r) = \begin{cases} \infty, & r < \sigma, \\ -\epsilon, & \sigma \leq r \leq \lambda\sigma, \\ 0, & \text{otherwise}, \end{cases} \tag{6.1}$$

where σ is the hard-core diameter, ϵ the strength and λ the range of the interaction. Within classical density functional theory (cDFT) as a powerful framework to access structure and thermodynamics of a fluid, the grand functional

$$\Omega[\rho] = \mathcal{F}[\rho] + \int d\mathbf{r}\, \rho(\mathbf{r})\, (V_{\text{ext}}(\mathbf{r}) - \mu) \tag{6.2}$$

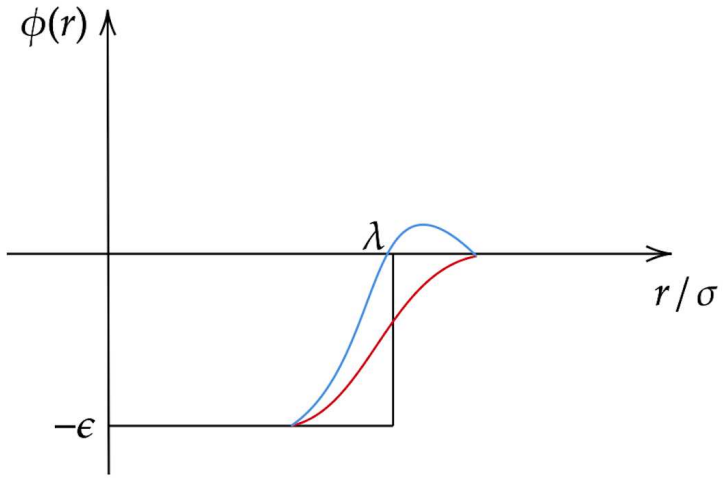

Figure 6.1: The SW interaction potential $\phi_{\rm sw}(r)$ is parametrized as a box of depth ϵ and width $\lambda\sigma$. The blue and red curves represent modifications of $\phi_{\rm sw}(r)$ such that the free-energy density of Eq.(6.8) is preserved. While the red curve is somehow a smoothened version of $\phi_{\rm sw}(r)$, the blue curve has a repulsive region at $r \approx \lambda\sigma$.

is minimized with respect to the one-body density $\rho(\mathbf{r})$

$$\left.\frac{\delta\Omega[\rho]}{\delta\rho(\mathbf{r})}\right|_{\rho(\mathbf{r})=\rho_{\rm eq}(\mathbf{r})} = 0 \tag{6.3}$$

in order to obtain the equilibrium density distribution $\rho_{\rm eq}(\mathbf{r})$. $V_{\rm ext}(\mathbf{r})$ is the external potential acting on the fluid, μ is the chemical potential and $\mathcal{F}[\rho] = \mathcal{F}_{\rm id}[\rho] + \mathcal{F}_{\rm ex}[\rho]$ the intrinsic Helmholtz free-energy functional that can be split into an exactly known ideal-gas part

$$\mathcal{F}_{\rm id}[\rho] = \frac{1}{\beta}\int d\mathbf{r}\,\rho(\mathbf{r})\left(\log\left(\lambda_T^3\rho(\mathbf{r})\right) - 1\right), \tag{6.4}$$

where Λ is the thermal wavelength of the particles, and an excess part containing all the information of the particle interactions. We consider the mean-field functional to describe the SW fluid

$$\mathcal{F}_{\rm ex}[\rho] = \mathcal{F}_{\rm hs}[\rho] + \frac{1}{2}\int\int d\mathbf{r}\,d\mathbf{r}'\rho(\mathbf{r})\rho(\mathbf{r}')\phi_{\rm sw}(|\mathbf{r}-\mathbf{r}'|), \tag{6.5}$$

where $\mathcal{F}_{\rm hs}[\rho]$ accounts for the hard-sphere repulsion well described by the White-Bear (WB) functional and $\phi_{\rm sw}(\mathbf{r})$ for the SW attraction. By extending the attractive part to the inside of the core, i.e. $\phi_{\rm sw}(r) = -\epsilon\Theta(\lambda\sigma - r)$, we can compensate the underestimation of correlations. The SW one-body correlation function $c^{(1)}_{\rm sw}(\mathbf{r})$ is found to be

$$-c^{(1)}_{\rm sw}(\mathbf{r}) = \int d\mathbf{r}'\,\rho(\mathbf{r}')\phi_{\rm sw}(|\mathbf{r}-\mathbf{r}'|) \equiv n_{\rm sw}(\mathbf{r}), \tag{6.6}$$

i.e. being essentially the background field $n_{\rm sw}(\mathbf{r})$ of the mean-field approach, Eq.(3.67). Therefore, the calculation of $c^{(1)}_{\rm sw}(\mathbf{r})$ is rather simple as the density $\rho(\mathbf{r})$ has to be convoluted with the kernel $\phi_{\rm sw}(\mathbf{r}-\mathbf{r}')$. For constant density $\rho(\mathbf{r}) = \rho_b$, the SW contribution of the Helmholtz functional in Eq.(6.5) attains the form

$$\mathcal{F}_{\rm sw}[\rho_b] = \frac{\rho_b^2}{2}\int d\mathbf{r}\int d\mathbf{r}'\,\phi_{\rm sw}(\mathbf{r}) \tag{6.7}$$

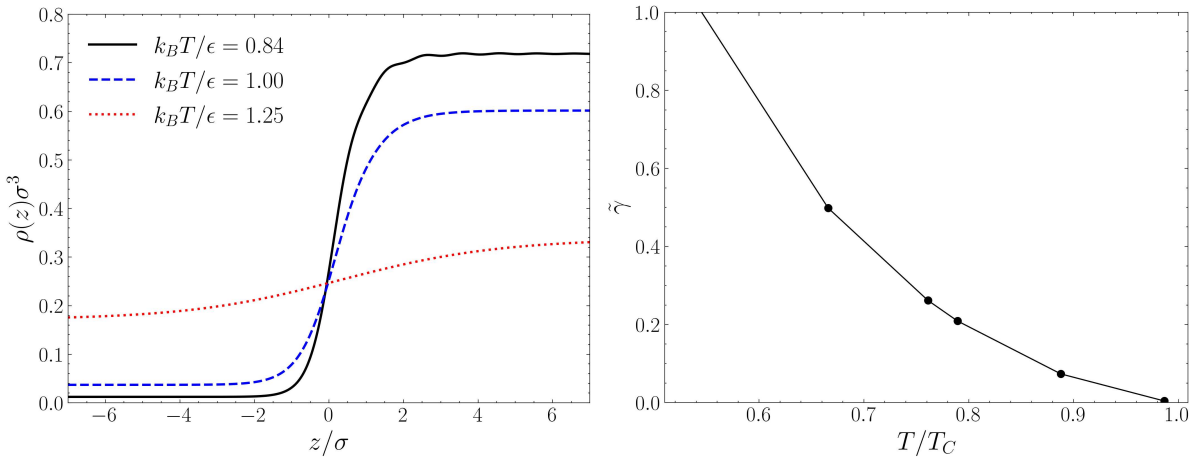

Figure 6.2: (Left) Density profiles $\rho(z)$ of the liquid-vapor interface for several temperatures T. (Right) Interfacial surface tension γ as plotted against the temperature T in units of the critical temperature T_C.

from which we obtain the free-energy density

$$f_{\text{sw}} = \frac{\rho_b^2}{2} \int d\mathbf{r}\, \phi_{\text{sw}}(\mathbf{r}), \tag{6.8}$$

so we are left with a volume integral over a sphere of radius $\lambda\sigma$. From Eq.(6.8) it is clear that as long as the integral remains unchanged, the thermodynamics is not affected. This allows us to modify the SW potential in a way, that for example the cut-off being put at $r = \lambda\sigma$ is replaced by a smooth transition. Or, we could even append a slightly repulsive region around $\lambda\sigma$ which could lead to a different structure of the fluid compared to the original SW potential. Fig.6.1 displays two possible modified interaction potentials that provide a smooth transition from the attractive region to outwards. The construction of such a potential is achieved by the following ansatz

$$\phi(r) = \begin{cases} -\epsilon, & \text{for} \quad 0 \le r \le \lambda\sigma - \delta \\ p(r), & \text{for} \quad \lambda\sigma - \delta < r < \lambda\sigma + \delta \\ 0, & \text{otherwise} \end{cases} \tag{6.9}$$

where δ is a parameter controlling the width of the associated transition. Of course, for $\delta = 0$ we should recover the original SW potential. Here, $p(r)$ can be a polynomial function whose coefficients are determined by imposing boundary conditions. One condition we want to be realized is the fact that the volume integral in Eq.(6.8) has the same value also for the modified potentials. Thus, assuming that $p(r)$ be a polynomial of degree three, we have the conditions

$$\begin{aligned} p(\lambda\sigma - \delta) &= -\epsilon \\ p(\lambda\sigma + \delta) &= 0 \\ p'(\lambda\sigma - \delta) &= 0 \\ \int_{\lambda\sigma-\delta}^{\lambda\sigma+\delta} dr\, p(r) r^2 &= \epsilon \left(-\lambda^2\sigma^2\delta + \lambda\sigma\delta^2 - \frac{\delta^3}{3} \right), \end{aligned} \tag{6.10}$$

where the last condition ensures that f_{ex} remains unchanged. The other three conditions merely render the modified potential continuous at the locations $r = \lambda\sigma - \delta$ and $r = \lambda\sigma + \delta$.

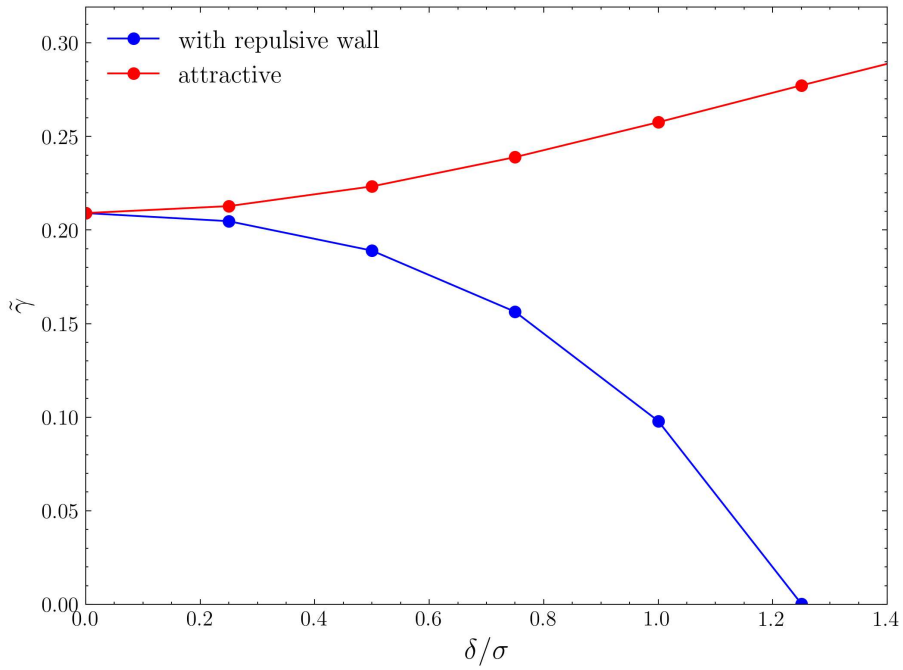

Figure 6.3: Interfacial surface tension γ evaluated for several width parameter δ of the modified SW interaction potential, Eq.(6.9).

The resulting interaction potential is represented by the blue curve in Fig.6.1, which has particularly the property of being repulsive at $r \approx \lambda\sigma + \delta$. Finally, assuming a polynomial of degree four with the additional condition $p'(\lambda\sigma + \delta) = 0$, results in the red curve of Fig.6.1 that is solely attractive.

For a (uniform) bulk fluid with bulk density ρ_b and corresponding packing fraction $\eta = \pi\rho_b\sigma^3/6$ Eq.(6.5) gives the excess free-energy density

$$\beta f_{\text{ex}} = \frac{\beta\mathcal{F}_{\text{ex}}[\rho_b]}{V} = \rho_b \frac{4\eta - 3\eta^2}{(1-\eta)^2} - 4\beta\epsilon\rho_b\eta\lambda^3 \tag{6.11}$$

with the corresponding equation of state (EoS)

$$\beta P = \rho_b \frac{1 + \eta + \eta^2 - \eta^3}{(1-\eta)^3} - 4\beta\epsilon\rho_b\eta\lambda^3. \tag{6.12}$$

and chemical potential

$$\beta\mu = \text{const.} + \log(\eta) + \frac{\eta(8 - 9\eta + 3\eta^2)}{(1-\eta)^3} - 8\beta\epsilon\lambda^3\eta. \tag{6.13}$$

The SW fluid gives rise to gas-liquid phase separation, i.e. for given gas and liquid density, ρ_v and ρ_l we have phase coexistence

$$\begin{aligned} P(\rho_v) &= P(\rho_l) \\ \mu(\rho_v) &= \mu(\rho_l). \end{aligned} \tag{6.14}$$

as long as we are below the critical temperature T_c. For instance, we can use values for the one-component SW fluid $\beta\epsilon = 1.0$ and $\lambda = 1.5$ with the corresponding liquid and vapor packing fractions

$$\eta_l = 0.315, \quad \eta_v = 0.0019 \tag{6.15}$$

and an interfacial, reduced surface tension $\tilde{\gamma} = \beta\gamma\sigma^2 = 0.209057$. Latter is derived by making use of the grand potential at equilibrium $\Omega = -pV + \gamma A$ so that

$$\gamma A = \Omega + pV, \tag{6.16}$$

where it should be noted that $\Omega = \Omega[\rho_{\text{eq}}]$ is the grand potential evaluated for the equilibrium density profile ρ_{eq}. Figure6.2 shows three density profiles $\rho(z)$ each with an associated energy ϵ. The critical temperature is reached for $k_B T_C/\epsilon \approx 1.267$, so that the red profile of Fig.6.2 has coexisting densities of liquid and vapor that are smaller in magnitude and closer to each other, which is typical for being close to the critical point. This also comes along with a small interfacial surface tension, as can be read off from Fig.6.2. Below a certain threshold of the temperature T, the corresponding density profile, being well described by a sigmoidal function, possesses oscillations at the liquid side of the interface, see the black profile of Fig.6.2. The reason is given by the fact that correlations become oscillatory for a specific region in the phase space of the SW liquid. The Fisher-Widom line separates those regions of oscillatory and monotonic decay [7, 101]. The blue curve of Fig.6.2 for instance lies in a region of monotonic decay of correlations.

As was pointed out above, the modified potentials of Eq.(6.9) do not alter the free-energy density so that the solutions for phase coexistence to Eq.(6.14) are equal. However, the modified form of the potentials will somehow change the interfacial surface tension due to further attractions or repulsions of the particle of liquid and vapor. Figure6.3 displays the change in surface tension γ by changing the width parameter δ of the modified SW interaction potential. By increasing δ, the effect of the modified potential becomes noticeable. While the smoothed version of the SW potential slightly enhances the surface tension γ, appending a repulsive wall at $r \simeq \lambda\sigma + \delta$ reduces it severely when $\delta > 0.5\sigma$.

6.1.1 Applications of the Square-Well Interaction

The square-well interaction already provides some interesting examples for rather simple geometries, such as at a hard wall or a spherical wall (test-particle geometry). We add the SW interaction by making use of the mean-field functional (see Eq.(6.5))

$$\beta\mathcal{F}_{\text{sw}}[\rho] = \frac{1}{2}\int d\mathbf{r}\int d\mathbf{r}'\rho(\mathbf{r})\rho(\mathbf{r}')\phi_{\text{sw}}(\mathbf{r}-\mathbf{r}') \tag{6.17}$$

which performs well as long as low densities and high temperatures are concerned. It is convenient to introduce the mean field $n_{\text{sw}}(\mathbf{r})$ given in Eq.(6.6) which, at the same time, is the one-body correlation function $c^{(1)}_{\text{sw}}$ of the SW interaction. As we extend the SW potential $\phi_{\text{sw}}(\mathbf{r})$ inside the hard core, we can write

$$\phi_{\text{sw}}(\mathbf{r}) = -\epsilon\Theta(\lambda\sigma - |\mathbf{r}|), \tag{6.18}$$

i.e. we have a kernel of the SW interaction that is similar to the weight function $\omega_3(\mathbf{r})$ of FMT, see Eq.(4.48). Let us consider the case of a SW fluid close to a hard wall, i.e. the corresponding density profile possesses azimuthal symmetry, $\rho(\mathbf{r}) = \rho(z)$. Then, as is proven in Sec.B.2 the mean-field weighted density $n_{\text{sw}}(z)$ reduces to the following effectively one-dimensional convolution integral

$$n_{\text{sw}}(z) = -\epsilon\int_{z-\lambda\sigma}^{z+\lambda\sigma} dz'\rho(z')\left((\lambda\sigma)^2 - (z-z')^2\right), \tag{6.19}$$

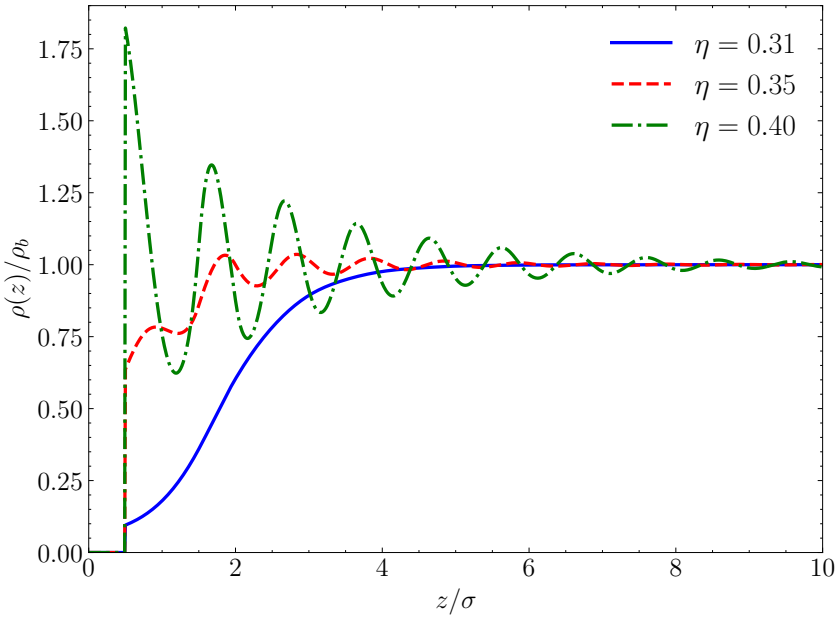

Figure 6.4: Normalized density profiles $\rho(z)$ of a SW fluid with interaction parameters $\beta\epsilon = 1$ and $\lambda = 1.5$ for three different packing fractions close to coexistence.

hence only the replacement $R \to \lambda\sigma$ together with the prefactor ϵ must be adjusted when going from $n_3(z)$ to $n_{\text{sw}}(z)$. In Fig.6.4 we present three density profiles, minimized with the RF functional, of a SW fluid where we have chosen the parameters to be $\beta\epsilon = 1$ and $\lambda = 1.5$. Furthermore, we have normalized the profiles with respect to their bulk densities in order to better visualize the qualitatively different structure close to the hard wall. While for the high packing fraction of $\eta = 0.40$ there are oscillations close to the hard wall smearing out towards the bulk, by coming closer to the coexisting liquid density of roughly $\eta_l \approx 0.306$ we see first that the oscillations become weaker and eventually there arises a region of the vapor at the vicinity of the hard wall. This effect, termed as complete drying, is even more pronounced when the coexisting density is further approached. The reason behind this observation is that the pressure βP of the SW fluid becomes less than the bulk density ρ_b due to the van der Waals loop which, in turn, means according to the contact theorem that the contact value $\rho(R^+)$ is lower than the liquid bulk density. A simple measure of the corresponding thickness of the gas film at the hard wall is provided by the excess adsorption

$$\Gamma = \int dz \, (\rho(z) - \rho_b) \tag{6.20}$$

that, sufficiently close to coexistence, behaves as $\Gamma \propto \log \Delta\mu$ where $\Delta\mu = \mu - \mu_{\text{coex}}$ is the difference of the chemical potential μ to its coexistence value. Now, we can further confine the system by putting a second hard wall to the right, i.e. a SW fluid contained in a slit of length L. Again, we consider the SW fluid close to its liquid density at coexistence, let's say $\eta = 0.32$, and minimize with DFT for several lengths L of the system keeping the density constant. In Fig.6.5 we show the associated density profiles within the slit. We find for $L = 10\sigma$ that the liquid is present in the middle of the slit with a rather small gas film at the boundaries. As we decrease the size L of the system, the liquid phase becomes metastable compared to the vapor phase leading to capillary evaporation. The mechanism behind this transition from liquid to gas can be understood by considering the grand potential per unit area $\Omega(L)/A \approx -PL + 2\gamma$ of this one-dimensional system.

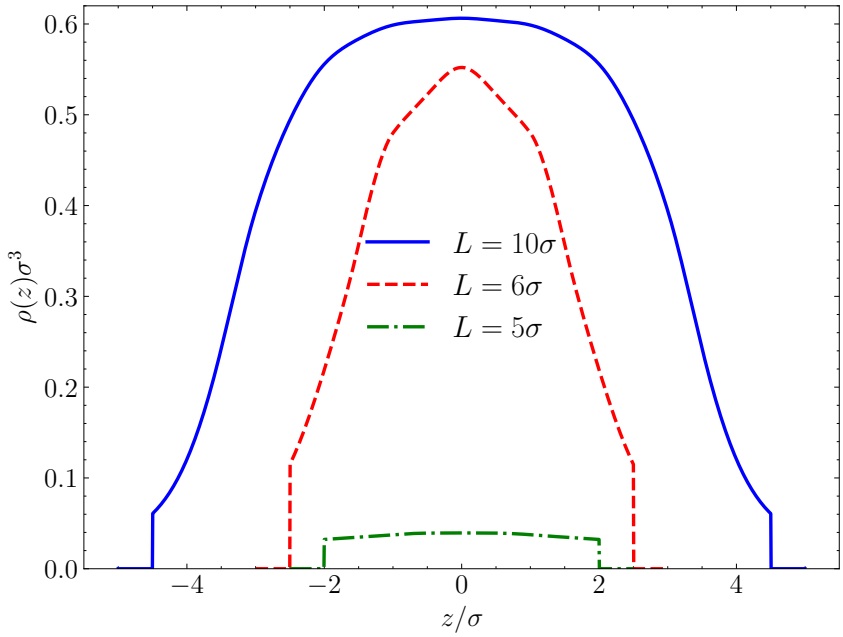

Figure 6.5: Density profiles $\rho(z)$ of a SW fluid with interaction parameters $\beta\epsilon = 1$ and $\lambda = 1.5$ confined in a slit of length $L = 10\sigma$, 6σ and 5σ.

Thus, the competition between the volume and surface term in $\Omega(L)$ can explain the transition from liquid to vapor via shrinking of the system. Finally, we can minimize the spherically symmetric density profile $\rho(r)$ of a SW fluid around a spherical wall of radius R_b that is attractive with SW parameters $\beta\epsilon = 1$ and $\lambda = 1.5$ as for the SW fluid. Suppose that latter is close to its vapor phase with density $\rho\sigma^3 \approx 0.038$ and the spherical wall being five times the size of the surrounding particles of the SW fluid, $R_b = 5R$. The attractive spherical wall has the effect of producing a layer of a liquid close to the wall with increasing thickness as the density of the vapor approaches its coexistence value at that temperature. In Fig.6.6 we present three cases of vapor with densities that are relatively close to the coexistence value, $\eta \approx 0.0019$, even with one example slightly above. If the density of the vapor is too small, $\eta = 0.005$ in Fig.6.6, the attractions of the spherical wall are not strong enough to create a liquid layer around it. However, if we slightly increase the density, $\eta = 0.010$, wetting starts to occur with the property that the liquid density is roughly its coexistence value, $\rho\sigma^3 \approx 0.76$. By further increasing the vapor density, $\eta = 0.0193$, we see first stronger correlations of the liquid and a higher thickness of the layer although the liquid density retains its value. The insets of Fig.6.6 visualize the wetting of the surrounding SW fluid in a heatmap. Lastly, we can define the thickness ξ of the adsorbed liquid film through the reduced adsorption [7]

$$\Gamma = 4\pi \int_{R_b}^{\infty} dr\, r^2(\rho(r) - \rho_v) \tag{6.21}$$

given by

$$\xi = \frac{\Gamma}{\rho_v}, \tag{6.22}$$

where ρ_v is the vapor density. If we generally approach the liquid-vapor coexistence curve from the unsaturated vapor side for temperatures T below a wetting temperature T_w, the adsorption stays finite, which is termed as partial wetting, see Fig.6.6. However, if the

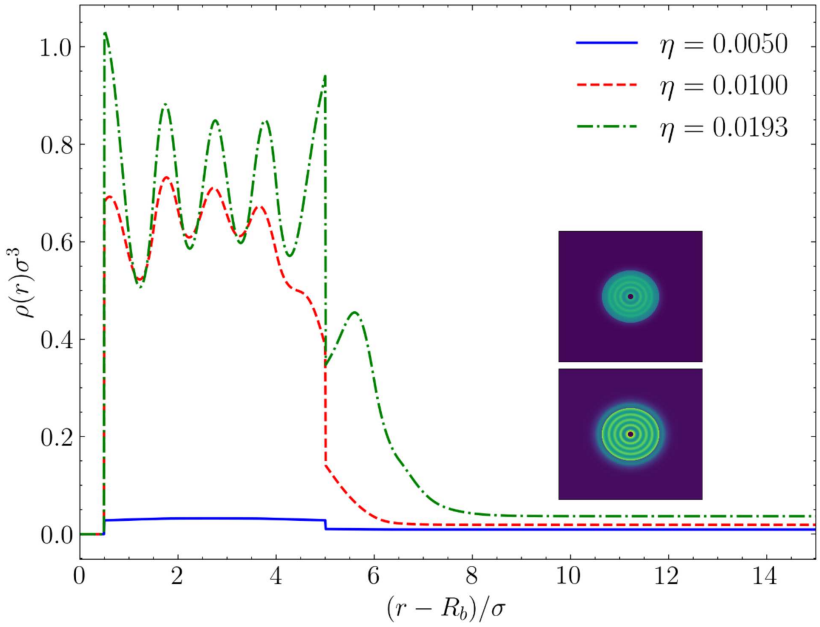

Figure 6.6: Wetting of around a spherical wall of radius $R_b = 5R$ for several densities of surrounding SW fluid close to its coexisting vapor density.

coexistence curve is reached for values $T > T_w$ the adsorption diverges. For a more detailed discussion see [7].

In general, wetting refers to the spreading of liquids on a solid surface describing a balance between adhesive and cohesive forces. The contact angle θ measures the degree of wetting on a surface as it is defined as the angle between liquid-vapor interface and the solid surface at contact line. Therefore, complete wetting is given for $\theta = 0$, partial wetting for $\theta \in (0, \pi)$ and non-wetting for $\theta > \pi$. Young's relation [102, 103, 104]

$$\gamma_{\text{sg}} = \gamma_{\text{sl}} + \gamma_{\text{lg}} \cos\theta \tag{6.23}$$

describes a force balance driven by surface tensions γ_{sg}, γ_{sl} and γ_{lg} between solid-gas, solid-liquid and liquid-gas, respectively. From Eq.(6.23) we can define the spreading coefficient

$$S = \gamma_{\text{sg}} - \gamma_{\text{ls}} - \gamma_{\text{lg}} \tag{6.24}$$

which must be negative. If $S = 0$, we have complete wetting, i.e. the liquid forms a macroscopically thick film. In this case the surface excess free energy of the solid-gas interface is just the sum of those associated with liquid-solid and liquid-gas. For $S < 0$ we have partial wetting as here there is no thermodynamic driving force for the liquid to spread [105].

6.2 SW Binary Mixture and Effective Interactions

In fluid mixtures with particles of differing sizes, it is often advantageous to reduce the system to an effective one-component description by integrating out the degrees of freedom

of the remaining species [106, 107, 108, 109, 10, 82]. This leads to effective interactions between the retained particles [110], which can yield complex behavior. A classic example is the Asakura-Oosawa (AO) depletion attraction in ideal colloid-polymer mixtures [111, 112, 113], where purely repulsive bare interactions result in an effective attraction. For small size ratios $\sigma_c/\sigma_p < 0.1547$, the AO potential becomes pairwise [114]; otherwise, many-body effects arise. In hard-sphere mixtures [115, 116], correlations among the smaller spheres further complicate the effective potential, often requiring the inclusion of higher-body terms beyond the dominant two-body interaction.

While AO-type interactions can be derived geometrically, calculating effective interactions in hard-sphere mixtures is more involved [117, 116]. A general approach relies on Widom's insertion theorem [118, 84], which relates changes in the grand potential to the insertion of a particle into an inhomogeneous system. Within classical density functional theory (cDFT) [8, 60, 119], and specifically fundamental measure theory (FMT) [9, 10], this framework accurately describes hard-sphere mixtures and serves as a reference for perturbative treatments of more complex interactions.

Effective pair potentials are extracted in the dilute limit of the retained species to avoid overcounting their mutual influence. The procedure involves two steps: (i) computing the depletant density profile around a fixed test particle (test-particle geometry), and (ii) applying Widom's insertion theorem to calculate the grand potential change from inserting a second particle at finite distance from the test particle [118, 84, 115]. Subtracting the potential at infinite separation ensures proper normalization. This can be interpreted as removing a particle from the bulk and inserting it near another, fixed particle [115].

In this section, we consider a related but distinct scenario: the effective interaction between solute particles induced by a liquid-vapor interface of the solvent. Here, the inhomogeneity stems from the interface rather than a fixed particle. Using Widom's theorem [118, 84], we calculate the change in the grand potential when transferring a solute particle from the bulk (far from the interface) into the interfacial region, thus defining the effective solute-interface interaction [115].

Phase separation and interfacial phenomena crucially affect solute behavior. Solubility enhancements near interfaces have been observed in simulations with Lennard-Jones and water-like solvents [120], and interpreted in terms of entropic and energetic contributions [121]. Density functional studies using weighted density approximations (WDA) [122, 123] have reproduced interfacial adsorption and surface tension variations in mixtures. Bubble nucleation studies [124] and DFT-based treatments of dilute mixtures [125] further support enhanced solute adsorption at interfaces.

To analyze these effects, we employ a square-well fluid mixture model, which captures the essential features of phase separation and inter-particle interactions via adjustable diameter, interaction strength, and range. This simple yet versatile system provides a suitable framework for studying interface-induced effective interactions in nanoscale solute systems.

6.2.1 Multi-Component Systems in DFT

We start by introducing the grand functional $\Omega[\{\rho_i\}]$ of a m-component system allowing non-trivial interactions (beyond ideal gas) encoded in $\mathcal{F}_{\text{ex}}[\{\rho_i\}]$ and external potentials

$V^i_{\rm ext}(\mathbf{r})$

$$\Omega[\{\rho_i(\mathbf{r})\}] = \mathcal{F}_{\rm id}[\{\rho_i(\mathbf{r})\}] + \mathcal{F}_{\rm ex}[\{\rho_i(\mathbf{r})\}] + \sum_{i=1}^{m} \int d\mathbf{r}\, \rho_i(\mathbf{r}) \left(V^i_{\rm ext}(\mathbf{r}) - \mu^i\right), \tag{6.25}$$

where $\mathcal{F}_{\rm id}$ is the exactly known free energy of the ideal gas

$$\beta\mathcal{F}_{\rm id}[\{\rho_i(\mathbf{r})\}] = \sum_{i=1}^{m} \int d\mathbf{r}\, \rho_i(\mathbf{r}) \left(\log(\lambda^3_{T,i}\rho_i(\mathbf{r})) - 1\right), \tag{6.26}$$

with $\lambda_{T,i}$ the thermal wave length of species i. This a straightforward generalization to Eq.(3.37) of the one-component case. The chemical potential μ^i corresponds to the i-th component. The external potential $V^i_{\rm ext}$ will be not considered in our study and is set to zero. The functional of the excess free energy can be split

$$\mathcal{F}_{\rm ex}[\{\rho_i(\mathbf{r})\}] = \mathcal{F}_{\rm hs}[\{\rho_i(\mathbf{r})\}] + \mathcal{F}_{\rm sw}[\{\rho_i(\mathbf{r})\}] \tag{6.27}$$

into a hard-sphere reference part $\mathcal{F}_{\rm hs}$, that we treat within the framework of fundamental measure theory (FMT) [9, 10], and a perturbation contribution $\mathcal{F}_{\rm sw}$ that here shall account for the square-well attraction within the random phase approximation [68, 126], see Sec.3.8.

We have demonstrated in Sec.3.5 that the functional of the grand potential, Eq.(6.25), is minimized by the equilibrium density profiles $\rho_{i,0}(\mathbf{r})$

$$\left.\frac{\delta\Omega[\{\rho_i\}]}{\delta\rho_i(\mathbf{r})}\right|_{\rho_i(\mathbf{r})=\rho_{i,0}(\mathbf{r})} = 0, \tag{6.28}$$

and its value at the minimum reduces to the grand potential of the system.

The reference system of a hard-sphere mixture can be accurately described by the White-Bear version of FMT [62, 67] which has the form

$$\beta\mathcal{F}_{\rm hs}[\{\rho_i(\mathbf{r})\}] = \int d\mathbf{r}\, \Phi_{\rm hs}(\{n_\alpha\}), \tag{6.29}$$

where the free energy density $\Phi_{\rm hs}$ is a function of weighted densities

$$n_\alpha(\mathbf{r}) = \sum_{i=1}^{m} \int d\mathbf{r}'\, \rho_i(\mathbf{r}') w^i_\alpha(\mathbf{r} - \mathbf{r}'), \tag{6.30}$$

with the sum running over all m components of the hard-sphere mixture. The weight functions $w^i_\alpha(\mathbf{r})$ characterize the size and shape of the hard spheres.

From Eq.(6.28) we obtain an implicit equation for the equilibrium density profile

$$\rho_i(\mathbf{r}) = \rho_i \exp\left(c^{(1)}_i(\mathbf{r}) + \beta\mu^i_{\rm ex} - \beta V^i_{\rm ext}(\mathbf{r})\right). \tag{6.31}$$

Here, ρ_i is the bulk density, $c^{(1)}_i(\mathbf{r})$ is the one-body correlation function and μ^i_{ex} is the excess chemical potential of component i which in this case is given by the sum of hard-sphere and SW contributions $\mu^i_{\rm ex} = \mu^i_{\rm hs} + \mu^i_{\rm sw}$. Equation(6.31) cannot be solved analytically since the density profile $\rho(\mathbf{r})$ also appears on the right-hand side, contributing to the one-body correlation function $c^{(1)}_i(z)$.

The remaining part of the functional is the perturbation treatment of the square-well interaction, which we will discuss in some details, assuming additive mixtures.

6.2.2 Square-Well Mixture

The square-well interaction (SW) is a commonly used model to realize liquid-vapor coexistence with a simple interaction potential that possesses both a hard-core repulsion at short distances preventing particle to overlap, and a short-ranged attraction. The interaction potential takes the form

$$\phi^{(i,j)}(r) = \begin{cases} \infty, & r \leq \sigma_{ij} \\ -\epsilon_{ij}, & \sigma_{ij} < r < \lambda_{ij}\sigma_{ij}, \\ 0, & \text{otherwise}, \end{cases} \tag{6.32}$$

where $\sigma_{ij} = (\sigma_i + \sigma_j)/2$ are the distances of closest approach. Here σ_i is the hard core diameter of species i, ϵ_{ij} is the interaction strength and λ_{ij} is the interaction range. The hard core repulsion is taken into account by the hard-sphere reference system, and the attractive square-well part is treated within the well-known random-phase approximation (RPA) [68, 126]

$$\beta\mathcal{F}_{\text{sw}}[\{\rho_i(\mathbf{r})\}] = \sum_{i,j}^{m} \frac{1}{2} \int d\mathbf{r} \int d\mathbf{r}'\, \rho_i(\mathbf{r})\rho_j(\mathbf{r}')\beta\phi_{\text{sw}}^{(i,j)}(\mathbf{r}-\mathbf{r}'), \tag{6.33}$$

where the SW potential $\phi_{\text{sw}}^{(i,j)}(\mathbf{r})$ is extended inside the hard core

$$\phi_{\text{sw}}^{(i,j)}(\mathbf{r}) = \begin{cases} -\epsilon_{ij}, & 0 < r < \lambda_{ij}\sigma_{ij} \\ 0, & \text{otherwise}. \end{cases} , \tag{6.34}$$

in order to compensate the lack of correlations in the interaction term.

The total bulk free energy density f is obtained by evaluating at bulk densities $\rho_i(\mathbf{r}) \to \rho_i$, in particular for the SW expression we find

$$f_{\text{sw}} = \frac{\mathcal{F}_{\text{sw}}[\{\rho_i\}]}{V} = -\frac{2\pi}{3} \sum_{i,j}^{m} \rho_i\rho_j(\lambda_{ij}\sigma_{ij})^3\epsilon_{ij}. \tag{6.35}$$

From Eq.(6.35) we can derive the square-well contributions to the chemical potential μ_{sw}^i and the pressure P_{sw} as

$$\mu_{\text{sw}}^i = \frac{\partial f_{\text{sw}}}{\partial \rho_i} = -\frac{4\pi}{3} \sum_{j=1}^{m} \rho_j(\lambda_{ij}\sigma_{ij})^3\epsilon_{ij}, \tag{6.36}$$

and

$$P_{\text{sw}} = -f_{\text{sw}} + \sum_{i=1}^{m} \rho_i\mu_{\text{sw}}^i = -\frac{2\pi}{3} \sum_{i,j}^{m} \rho_i\rho_j(\lambda_{ij}\sigma_{ij})^3\epsilon_{ij}. \tag{6.37}$$

6.2.3 FMT-like Functional for SW Mixtures

Besides the usual expression Eq.(6.33), which can be cumbersome if a mixture of several components is considered, we want to make use of the geometrical structure of the square-well interaction. We recall from Sec.4.2 the exact low-density expression for a hard-sphere system in Eq.(4.45)

$$\lim_{\rho_i \to 0} \beta\mathcal{F}_{\text{hs}}[\{\rho_i(\mathbf{r})\}] = \int d\mathbf{r}\, \left(n_0(\mathbf{r})n_3(\mathbf{r}) + n_1(\mathbf{r})n_2(\mathbf{r}) - \mathbf{n}_1(\mathbf{r}) \cdot \mathbf{n}_2(\mathbf{r})\right), \tag{6.38}$$

where the right-hand side is written in terms of weighted densities of FMT, see Sec.4.2. Since the square-well perturbation term within RPA has the same geometrical structure as the hard-sphere low-density limit, it is possible to define weight functions w_α^ϵ of the SW fluid in such a way that we get a functional equivalent to Eq.(6.33). By defining

$$w_3^{\epsilon,i}(\mathbf{r}) = \sqrt{\epsilon_i}\,\Theta(\lambda_i R_i - |\mathbf{r}|), \quad w_2^{\epsilon,i}(\mathbf{r}) = \sqrt{\epsilon_i}\,\delta(\lambda_i R_i - |\mathbf{r}|), \quad \mathbf{w}_2^{\epsilon,i}(\mathbf{r}) = w_2^{\epsilon,i}(\mathbf{r})\frac{\mathbf{r}}{r} \tag{6.39}$$
$$w_1^{\epsilon,i}(\mathbf{r}) = -\frac{w_2^{\epsilon,i}(\mathbf{r})}{4\pi\lambda_i R_i}, \quad w_0^{\epsilon,i}(\mathbf{r}) = -\frac{w_2^{\epsilon,i}(\mathbf{r})}{4\pi(\lambda_i R_i)^2}, \quad \mathbf{w}_1^{\epsilon,i}(\mathbf{r}) = -\frac{\mathbf{w}_2^{\epsilon,i}(\mathbf{r})}{4\pi\lambda_i R_i}$$

we obtain

$$\beta\mathcal{F}_{\rm sw}[\{\rho_i(\mathbf{r})\}] = \int d\mathbf{r}\,\beta\left(n_0^\epsilon(\mathbf{r})n_3^\epsilon(\mathbf{r}) + n_1^\epsilon(\mathbf{r})n_2^\epsilon(\mathbf{r}) - \mathbf{n}_1^\epsilon(\mathbf{r})\cdot\mathbf{n}_2^\epsilon(\mathbf{r})\right) \tag{6.40}$$

which is the RPA of the SW fluid, now in the fashion of FMT. It should be noticed that in order to produce the correct sign in the case of SW interaction, the weight functions $w_2^{\epsilon,i}(\mathbf{r})$, $w_1^{\epsilon,i}(\mathbf{r})$ and $\mathbf{w}_1^{\epsilon,i}(\mathbf{r})$ must have a minus sign. For square-shoulder interactions, these minus signs would be absent.

Similar to the weighted densities of Sec.4.2, the new weighted densities $n_\alpha^\epsilon(\mathbf{r})$ are given by

$$n_\alpha^\epsilon(\mathbf{r}) = \sum_{i=1}^m \int d\mathbf{r}'\,\rho_i(\mathbf{r}')w_\alpha^{\epsilon,i}(\mathbf{r}-\mathbf{r}') \tag{6.41}$$

which attain, similar to the limits for hard spheres of Eq.(4.51), the following values in the bulk

$$n_3^\epsilon(\mathbf{r}) \to \frac{4\pi}{3}\sum_{i=1}^m(\lambda_i R_i)^3\rho_i\sqrt{\epsilon_i}, \quad n_2^\epsilon(\mathbf{r}) \to 4\pi\sum_{i=1}^m(\lambda_i R_i)^2\rho_i\sqrt{\epsilon_i}, \tag{6.42}$$
$$n_1^\epsilon(\mathbf{r}) \to -\sum_{i=1}^m\lambda_i R_i\rho_i\sqrt{\epsilon_i}, \quad n_0^\epsilon(\mathbf{r}) \to -\sum_{i=1}^m\rho_i\sqrt{\epsilon_i},$$
$$\mathbf{n}_2^\epsilon(\mathbf{r}) \to 0, \quad \mathbf{n}_1^\epsilon(\mathbf{r}) \to 0.$$

Then, the excess free energy density $f_{\rm sw}$ of the SW mixture is found to be

$$f_{\rm sw} = -\frac{2\pi}{3}\sum_{i=1}^m\rho_i^2(\lambda_i\sigma_i)^3\epsilon_i - \frac{\pi}{6}\sum_{(i,j)}^m\rho_i\rho_j\left(\lambda_i\sigma_i + \lambda_j\sigma_j\right)^3\sqrt{\epsilon_i\epsilon_j}, \tag{6.43}$$

where the first term on the r.h.s. refers to SW interaction of component i with itself and equals those of Eq.(6.35). The second term of Eq.(6.43), which it is summed over all possible pairs (i,j) with $i \neq j$, accounts for inter-component SW interactions wherein the energies and ranges are predefined by the energies and ranges of the components, respectively. For a one-component SW fluid this FMT inspired approach seems to be more complicated, however, by considering a multi-component mixture the simplicity of Eq.(6.40) becomes apparent. As for the multi-component hard-sphere mixture, also here the concise description of the excess SW functional is advantageous. We want to emphasize also that the mixing rule according to Lorentz-Berthelot is already inherent in this description, i.e. given the SW energies ϵ_i and ranges λ_i, the inter-component energies and ranges are fixed. For example, the energy ϵ_{ij} between component i and j is given by

$$\epsilon_{ij} = \sqrt{\epsilon_i\epsilon_j} \tag{6.44}$$

with the range

$$\lambda_{ij} = \frac{\lambda_i \sigma_i + \lambda_j \sigma_j}{\sigma_i + \sigma_j}. \tag{6.45}$$

Imposing these mixing rules, Eq.(6.44) and Eq.(6.45), onto the SW free energy density Eq.(6.35) in the most general case, shows the equivalence to Eq.(6.43) hence describing the same thermodynamics.

6.2.4 Interface of Binary Mixture

Here we focus on the case $m = 2$ where we study the phase coexistence of the binary SW mixture using the free energy density in Eq.(6.43). Therefore, we have three contributions to f_{sw}

$$f_{\text{sw}}(\rho_1, \rho_2) = -\frac{2\pi}{3}\lambda_1^3\sigma_1^3\rho_1^2\epsilon_1 - \frac{2\pi}{3}\lambda_2^3\sigma_2^3\rho_2^2\epsilon_2 - \frac{\pi}{6}(\lambda_1\sigma_1 + \lambda_2\sigma_2)^3\rho_1\rho_2\sqrt{\epsilon_1\epsilon_2}. \tag{6.46}$$

Here, the first two contributions are assigned to SW interactions of the two components, and the third contribution to the SW interaction between the first and the second component.

The total pressure $P(\rho_1, \rho_2)$ of the binary SW mixture reads as

$$P(\rho_1, \rho_2) = P_{\text{BMCSL}}(\rho_1, \rho_2) + P_{\text{sw}}(\rho_1, \rho_2) \tag{6.47}$$

in which P_{BMCSL} refers to the Boublik-Mansoori-Carnahan-Starling-Leland (BMCSL) [80] pressure, a generalization to hard-sphere mixtures of the Carnahan-Starling expression for pure fluids [35], expressed in terms of scaled-particle variables [58], see Sec.3.9, which are identified by the bulk limits of the weighted densities, Eq.(6.30). The pressure P_{sw}, Eq.(6.37), due to SW interactions is derived from the free energy density Eq.(6.46). The chemical potentials $\mu_1(\rho_1, \rho_2)$ and $\mu_2(\rho_1, \rho_2)$ are obtained in a similar way and are given in Eq.(6.36).

Since we are interested in the effective interaction of a liquid-vapor interface of a solvent (component 1) on dissolved nano particles (component 2), we first have to establish equilibrium conditions for a binary mixture. The conditions for phase coexistence are given by

$$\begin{aligned} P(\rho_1^l, \rho_2^l) &= P(\rho_1^v, \rho_2^v) \\ \mu_1(\rho_1^l, \rho_2^l) &= \mu_1(\rho_1^v, \rho_2^v) \\ \mu_2(\rho_1^l, \rho_2^l) &= \mu_2(\rho_1^v, \rho_2^v) \end{aligned} \tag{6.48}$$

which are fulfilled at a given temperature T. The densities ρ_i^l and ρ_i^v refer to the liquid (l) and the vapor (v) density of component i, respectively.

We see that Eq.(6.48) provides us with three equations for four unknowns ρ_i^l and ρ_i^v with $i = 1, 2$. Hence, we further provide a fixed low value for the liquid density $\rho_2^l = \rho_{2,0} = 10^{-6} \times 6/(\pi\sigma_2^3)$ and solve Eq.(6.48) for the remaining densities given the SW parameters ϵ_i and λ_i.

We regard the first component as solvent with fixed SW parameters $\beta\epsilon_1 = 1$ and $\lambda_1 = 1.5$, and the second component as dilute solute composed of nano particles, i.e. $\rho_2 \ll \rho_1$ has to be satisfied. Then, we expect the solute not to considerably change the

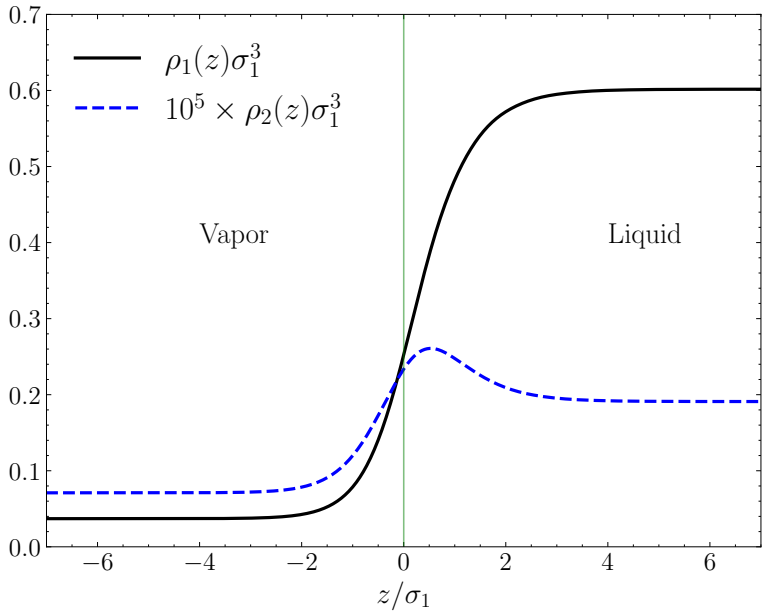

Figure 6.7: Liquid-vapor phase separation of the SW binary mixture with corresponding interface (green vertical line) located at $z = 0$ and density profiles of the first component (black solid) and the second component (dashed blue) which we magnified for visualization. The SW parameters of the second component are chosen to be $\beta\epsilon_2 = 0.6$ and $\lambda_2 = 1.5$ with $\sigma_2/\sigma_1 = 1$.

phase behavior of the solvent, which specifically means that the coexisting densities ρ_1^l and ρ_1^v of the pure one-component SW fluid remain virtually unchanged with values

$$\rho_1^l\sigma_1^3 = 0.6016, \quad \rho_1^v\sigma_1^3 = 0.0370 \tag{6.49}$$

and a reduced interfacial surface tension

$$\beta\gamma\sigma_1^2 = 0.20906. \tag{6.50}$$

We solve Eq.(6.48) numerically for several values of the interaction parameter ϵ_2 and size ratio σ_2/σ_1. We further perform a minimization with cDFT according to Eq.(6.31) employing the functional proposed in Eq.(6.40) in order to obtain density profiles $\rho_1(z)$ and $\rho_2(z)$ for the planar free interface between the liquid and vapor phases. The interaction range λ_2 of the solute is set such that the corresponding width $\sigma_2(\lambda_2 - 1)$ is equal to the width $\sigma_1(\lambda_1 - 1)$ of the first component, i.e. we have $\lambda_2 = 1 + (\lambda_1 - 1)\sigma_1/\sigma_2$. Particularly, the symmetric case where $\rho_2^l = \rho_2^v$ is of interest and is realized for a specific interaction energy ϵ_2 of the second component.

The qualitative behavior of the solubility can be well understood considering the equilibrium condition of the grand canonical potential density $\omega(\rho_1, \rho_2) = \Omega(\rho_1, \rho_2)/V = f(\rho_1, \rho_2) - \mu_1\rho_1 - \mu_2\rho_2$ in the dilute limit $\rho_2 \to 0$. Hence, the equilibrium distribution of the solvent $\rho_1(z)$ is assumed to be unaffected by the nano particles and can be described in a good approximation as a sigmoidal of the form

$$\rho_1(z) = \rho_1^v + \frac{\rho_1^l - \rho_1^v}{1 + \exp(-az)}, \tag{6.51}$$

where $a \approx 1.79/\sigma_1$ is obtained from a fit using the SW values of the solvent, $\beta\epsilon_1 = 1.0$ and $\lambda_1 = 1.5$. At equilibrium, we have $\partial\omega/\partial\rho_2 = 0$ from which in leading order

$$\log\left(\frac{\rho_2(z)}{\rho_{2,0}}\right) + \beta V_{\text{eff}}(\rho_1(z), \epsilon_{12}, \lambda_{12}) = 0 \tag{6.52}$$

follows, with an effective potential

$$V_{\text{eff}}(\rho_1(z), \epsilon_{12}, \lambda_{12}) = \left.\frac{\partial \Delta f(\rho_1, \rho_2)}{\partial \rho_2}\right|_{\rho_2=0}. \tag{6.53}$$

Here $\Delta f(\rho_1, \rho_2)$ is the change in free energy due to the insertion of solutes. Note that due to the linearization with respect to ρ_2, only the inter-component interaction parameters ϵ_{12} and λ_{12} contribute in Eq.(6.53). In [120], an equivalent investigation to Eq.(6.52) was done by applying the potential distribution theorem providing a description of the excess adsorption of solute particles at the liquid-vapor interface. The solubility thus is connected to the local excess chemical potential of the solute particle. Abe and Koga showed that varying the interaction energy leads to different shapes of solubility that can exhibit local maxima at the interface. Finally, Eq.(6.52) provides an effective description of a system only being comprised of solute particles, see Sec.6.2.5.

In Fig.6.7 we present one scenario of the binary SW mixture where both components prefer to stay together (good solvent) and we divide the system after phase separation into vapor ($z < 0$) and liquid ($z > 0$). We see that the solvent assumes its coexisting densities of vapor and liquid sufficiently far away from the interface located at $z = 0$ where it makes a transition, that is well described by a sigmoidal function. According to our assumption that $\rho_2 \ll \rho_1$, the coexisting densities and the shape of the density profile are only slightly affected by the presence of the solute. We observe an adsorption of nano particles at the interface with a pronounced maximum.

We can alter the behavior of the solute with respect to the solvent by changing the energy ϵ_2. By doing that we change the interaction energy ϵ_{12} according to Eq.(6.44). Figure7.3 displays some density profiles of the nano particles normalized by $\rho_{2,0}$ and for energies ϵ_2 located slightly below and above the energy $\beta\epsilon_2 = 0.4235$ for which the coexisting densities ρ_2^l and ρ_2^v are equal. The particles prefer neither the liquid nor the vapor phase thus gather at the interface. For reasons of clarity we do not plot the interface profile of the solvent. All three density profiles show a maximum close to the interface. The nano particles are attracted to the interface in the presence of (slightly) solvophobic and (slightly) solvophilic nano particles. The maximum at the interface becomes more pronounced as we lower the value of ϵ_2. In addition, as we include $\rho_2(z \to \infty) = \rho_{2,0}$ as a fourth equation to Eq.(6.48), the normalized density profiles approach unity for $z \to \infty$.

Now, we extend our discussion to size ratios $\sigma_2/\sigma_1 > 1$ as shown in Fig.6.9. We again consider the density profile $\rho_2(z)$ for values of ϵ_2 below and above the symmetric case. Even in the slightly asymmetric mixture shown in Fig.6.9(b), we observe a more pronounced density maximum in $\rho_2(z)$ at the liquid-vapor interface, compared to the symmetric mixture shown in Fig.7.3. Furthermore, the energy ϵ_2 required for the symmetric solution is roughly doubled. By further increasing the size ratio the accumulation of nano particles at the interface becomes stronger, reaching around three orders of magnitude in Fig.6.9(c) and up to five orders of magnitude in Fig.6.9(d). Therefore, the resulting energy ϵ_2 has to increase in order to keep the particles at the interface. By going to the highest asymmetric mixture $\sigma_2/\sigma_1 = 3$ considered here, Fig.6.9(d), we see some additional structure of the density profile $\rho_2(z)$ for $\beta\epsilon_2 = 2$ towards the vapor phase.

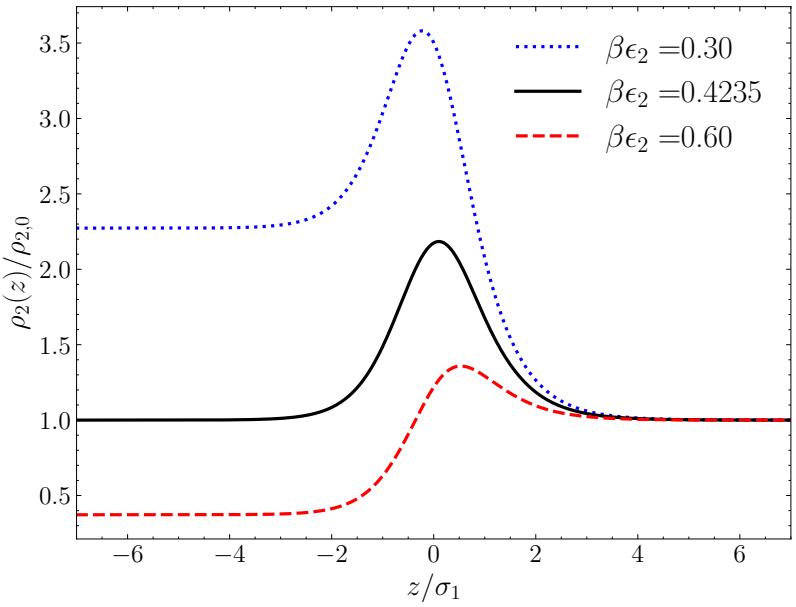

Figure 6.8: Normalized density profile $\rho_2(z)/\rho_{2,0}$ of the second component at the interface $z = 0$ for three energies ϵ_2 with range $\lambda_2 = 1.5$ and size ratio $\sigma_2/\sigma_1 = 1$. For reasons of clarity we do not show the density profile of the solvent. The lowest value of ϵ_2 corresponds to the case of (slightly) solvophobic nano particles, that prefer the vapor phase, while the highest value of ϵ_2 corresponds to case of (slightly) solvophilic nano particles, which prefer the liquid phase. In this case neither the liquid nor the vapor phase is preferred by the nano particles.

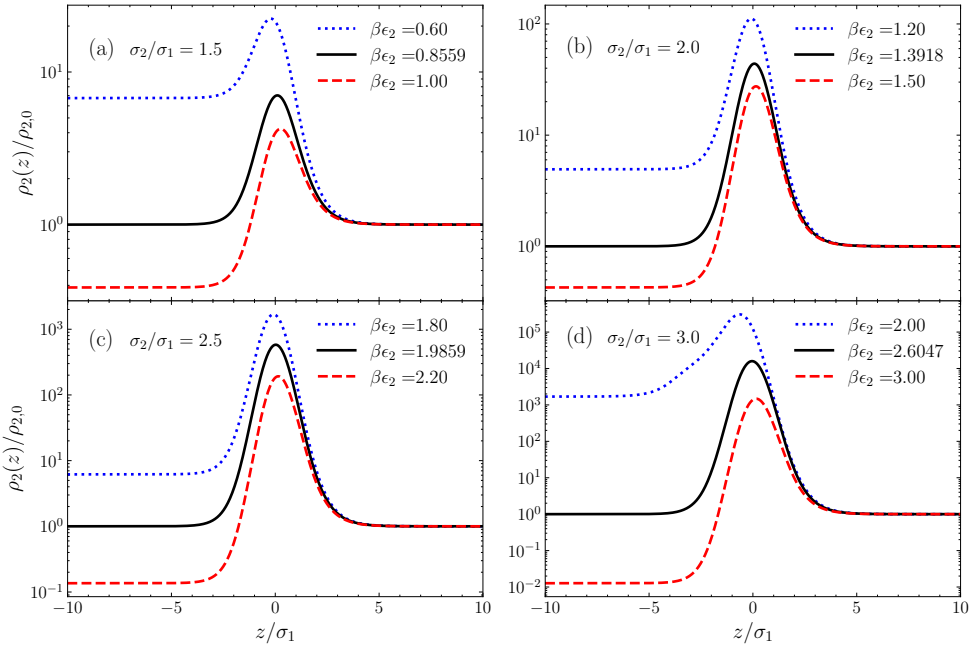

Figure 6.9: Normalized density profiles $\rho_2(z)/\rho_{2,0}$ for several size ratios $\sigma_2/\sigma_1 = 1.5, 2.0, 2.5, 3.0$ and energies ϵ_2 slightly below (dotted blue) and above (dashed red) the symmetric solutions (solid black). By increasing the size ratio the adsorption at the interface becomes stronger and enhances the density by several orders of magnitude. Note the logarithmic scaling of the ordinates.

σ_2/σ_1	1	1.5	2.0	2.5	3.0
DFT	$-9.0 \cdot 10^{-6}$	$-1.0 \cdot 10^{-5}$	$-2.0 \cdot 10^{-5}$	$-9.3 \cdot 10^{-5}$	$-1.2 \cdot 10^{-3}$
Gibbs	$-1.3 \cdot 10^{-6}$	$-1.7 \cdot 10^{-6}$	$-4.0 \cdot 10^{-6}$	$-2.2 \cdot 10^{-5}$	$-3.0 \cdot 10^{-4}$

Table 6.1: Reduction $\tilde{\gamma} - \tilde{\gamma}_0$ in the surface tension $\tilde{\gamma} = \beta\gamma\sigma_1^2$ of the binary SW mixture calculated for the symmetric solution $\rho_2^l = \rho_2^v$ for different size ratios σ_2/σ_1 using DFT and from the Gibbs adsorption theorem, Eq.(6.57). Due to our assumption $\rho_2 \ll \rho_1$, only a small deviation from the surface tension of the one-component system, Eq.(6.50), is observed.

The addition of nano particles reduces the surface tension γ of the liquid-vapor interface as they accumulate at the interface which is significantly enhanced in the case of highly asymmetric mixtures, see Fig.6.9(c) and Fig.6.9(d). This adsorption of particles lowers the free energy associated with the interface and consequently leads to a reduction of the surface tension. In Tab.6.1 we present values of the reduced surface tension $\beta\gamma\sigma_1^2$ for several size ratios σ_2/σ_1. Since we only allow for a very low density reservoir ρ_2 of the second component, the expected reduction of the surface tension is very small, around 0.6%. The change of the surface tension as we increase the size ratio σ_2/σ_1 from 2.5 to 3, that can be seen in Tab.6.1, can be explained by the fact, that the chemical potential μ_2 and the excess adsorption Γ_2 increase with the size ratio. For a binary mixture the Gibbs adsorption theorem reads

$$d\gamma = -\Gamma_1 d\mu_1 - \Gamma_2 d\mu_2, \tag{6.54}$$

where Γ_i, $i = 1, 2$ is the excess adsorption of component i that depends on the location z^* of the Gibbs dividing surface $A = \sigma_1^2$. We choose z^* such that $\Gamma_1 = 0$, i.e.

$$0 = \Gamma_1 = \frac{1}{A}\left(\int_{-\infty}^{z^*} dz\,(\rho_1(z) - \rho_1^v) + \int_{z^*}^{\infty} dz\,(\rho_1(z) - \rho_1^l)\right) \tag{6.55}$$

is fulfilled by z^*. In the same manner, the excess adsorption Γ_2 is obtained

$$\Gamma_2 = \frac{\rho_{2,0}}{A}\int_{-\infty}^{\infty} dz\,\left(e^{-\beta V_{\text{eff}}(z)} - 1\right), \tag{6.56}$$

where we used Eq.(6.52) and the symmetric case $\rho_2^l = \rho_2^v = \rho_{2,0}$. Then, from Eq.(6.54) we obtain as a first approximation in the dilute limit

$$\beta\gamma \approx \beta\gamma_0 - \Gamma_2, \tag{6.57}$$

where γ_0 is the reference surface tension, Eq.(6.50), of the one-component case. At this point we can already infer from Eq.(6.56) that the excess adsorption Γ_2 must be positive, since the integrand is positive due to $\beta V_{\text{eff}}(z) < 0$. Thus, the surface tension γ, according to Eq.(6.57), is reduced, in agreement with our expectation. We can therefore compare Eq.(6.57) to those obtained from our DFT minimization, see Tab.6.1, showing good agreement between both routes of calculating the reduced surface tension where slight differences occur for larger size ratios. As can be inferred from Fig.6.9, the excess adsorption Γ_2 increases when the size ratio becomes larger. This has in total the effect of lowering the surface tension according to Eq.(6.57).

6.2.5 Effective Interactions

Finally, the binary SW mixture can also be treated as an effectively one-component system of nano particles by integrating out the degrees of freedom of the solvent species [106, 107, 108, 109, 117]. This mapping introduces effective interactions [115, 110] in the remaining species of nano particles. In contrast to the models mentioned in Sec.6.2, the ideal colloid-polymer mixture [111, 112, 113] or the hard sphere mixture [115, 116], where the leading order contribution of the mapping from a mixture onto an effective one-component system was an effective two-body interaction, i.e. a pair potential, between particles, here the presence of the liquid-vapor interface introduces an important and strong one-body term. While two- and higher order terms are also a consequence of the mapping [106, 107, 108, 109, 117], we will not consider them here. The effective one-body term takes the form of a potential $V_{\text{eff}}(z)$ and is caused by the solvent. In the dilute limit of nano particles, the density profile $\rho_2(z)$ of the nano particles can be written as $\rho_2(z) = \rho_{2,0} \exp(-\beta V_{\text{eff}}(z))$, which in turn implies that given the density profile $\rho_2(z)$ stemming from the binary mixture the corresponding effective potential has to be

$$\beta V_{\text{eff}}(z) = -\lim_{\rho_{2,0}\to 0} \log\left(\frac{\rho_2(z)}{\rho_{2,0}}\right). \tag{6.58}$$

If we start from a true binary mixture, this limit can be obtained *numerically* by choosing a sufficiently small value of $\rho_{2,0}$.

On the other hand, we can also make use of Widom's insertion theorem [118, 84, 115], stating that the change in grand potential due to inserting a particle is related to the excess chemical potential of that particle. Here, we consider the displacement of a particle from the bulk ($z \to \pm\infty$) towards the proximity of the interface, at position z, and interpret the associated change in grand potential as the effective potential $V_{\text{eff}}(z)$. In more detail, the effective potential $V_{\text{eff}}(z)$ according to the Widom insertion theorem is given by

$$\beta V_{\text{eff}}(z) = \lim_{\rho_{2,0}\to 0} \left(c_2^{(1)}(\pm\infty) - c_2^{(1)}(z)\right), \tag{6.59}$$

where we take the dilute limit of vanishing density of the nano particles. It is interesting to note, that the dilute limit can be taken explicitly in this route, so that only the density profile of the interface of the solvent, without the presence of any nano particles, is required. Still, for the calculation of $c_2^{(1)}$, the one-body direct correlation function of the nano particles, a theory for a mixture is necessary. Note that $c_2^{(1)}(\pm\infty) = -\beta\mu_{2,\text{ex}}$ as the correct bulk limit of the one-body direct correlation function $c_2^{(1)}(z)$ at phase coexistence.

We can compare these two routes to calculate the effective potential, as displayed in Fig.6.10 for one example in the case $\sigma_2/\sigma_1 = 2$ with the symmetric solution $\beta\epsilon_2 = 1.3918$, Fig.6.10(a), and the solvophilic solution $\beta\epsilon_2 = 1.50$, Fig.6.10(b). Since in the former case the particles do not prefer the liquid to the vapor and vice versa, the effective potential $V_{\text{eff}}(z)$ must tend to 0 when the bulk either to the left or to the right is reached, which is clearly observable in Fig.6.10(a). Furthermore, we see a minimum at the interface which implies that latter is highly attractive for nano particles. By slightly increasing the energy ϵ_2 as in Fig.6.10(b), the nano particles become more solvophilic, i.e. they prefer the liquid to the vapor which in Fig.6.10(b) is reflected by the fact, that the effective potential becomes positive for $z \to -\infty$.

We observe an excellent agreement between the two routes of calculating the effective potential which also holds for other size ratios that we have considered here.

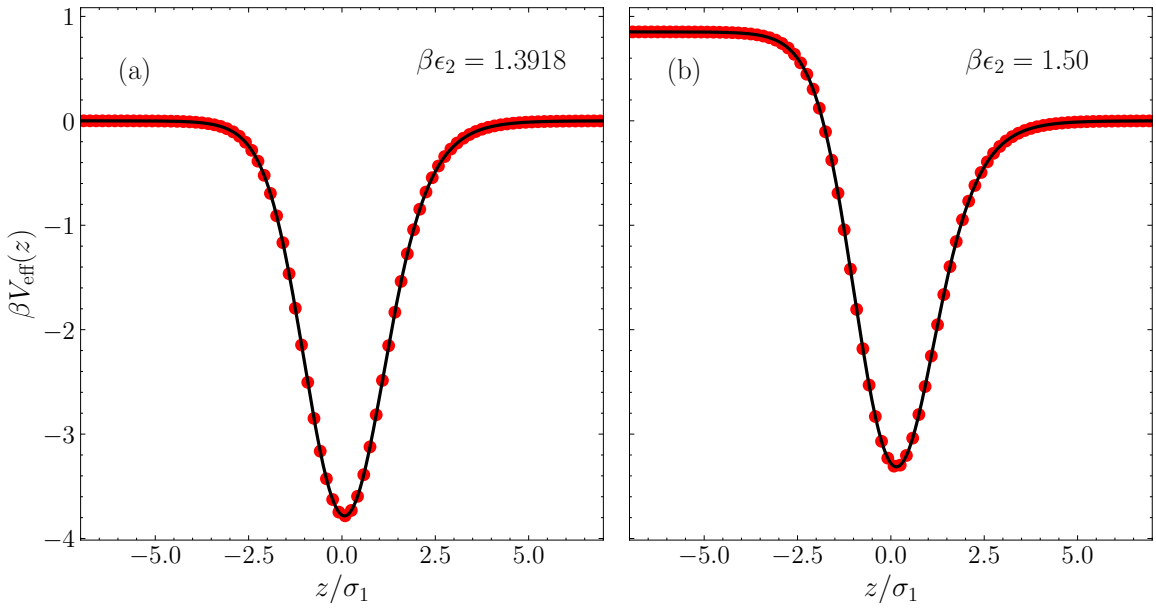

Figure 6.10: Effective potential $V_{\text{eff}}(z)$ near the interface at $z = 0$ once obtained via Eq.(6.58) (red dots) and Eq.(6.59) (solid black) of the asymmetric mixture $\sigma_2/\sigma_1 = 2$ evaluated for the symmetric case $\beta\epsilon_2 = 1.3918$ (a) and the case $\beta\epsilon_2 = 1.50$ (b) where the nano particles prefer the liquid. The agreement between both routes is very good.

6.2.6 Conclusion

In this section, we investigated a binary square-well (SW) mixture using classical density functional theory (DFT). We extended the (optimized) random phase approximation [68, 126] for the SW perturbation to additive mixtures by reformulating it in terms of weighted densities, reminiscent of fundamental measure theory (FMT) [9, 10]. This reformulation exploits the geometric structure of SW interactions, allowing efficient predictions of inhomogeneous structures and thermodynamic properties in multicomponent systems.

A key result is the reduction of surface tension at liquid-vapor interfaces due to nanoparticle accumulation, especially in mixtures with large size asymmetry. This enhanced interfacial adsorption aligns with previous studies using WDA and RPA [123, 122, 124, 125]. Closely related work by [120] also reports solute enrichment at interfaces as a function of interaction strength. In the dilute limit, solubility can be understood through Widom's insertion theorem, where the local excess chemical potential reflects the averaged solute-solvent interaction. This adsorption behavior parallels the coffee-stain effect [127], where particles accumulate non-uniformly due to evaporation dynamics. In our case, a similar segregation emerges from size and interaction disparities, minimizing the interfacial free energy. These findings suggest several directions for future research. One is to analyze higher-order effective interactions in the presence of wetting or drying phenomena [128, 129]. Another is to extend the framework to include confinement or external fields. Finally, the analogy to the coffee-stain effect [127] hints at potential applications in nanotechnology, such as designing functional coatings by controlling particle distributions at interfaces.

Chapter 7

Laden Droplet

The spread of diseases like SARS-CoV-2 led to controversial critics and argument in the last few years with the beginning of the pandemic. Experiments of recent times found out that viruses can remain infectious in aerosols for a long period of time [130, 131, 132]. The duration of infectious droplets in air is controlled by several factors, such as droplet size. According to experiments of [133], small droplets completely evaporate before reaching the ground whereas bigger droplets directly fall to the ground. The associated sedimentation time, i.e. the time for a droplet to reach the ground, is dependent on evaporation cooling and solute induced effects. Investigations of analytical nature [134] prove that evaporation induced cooling of droplets does have noticeable effect on the evaporation process. The presence of solutes in water droplets, for instance, also slows down the evaporation speed and hence the evaporation cooling compared to pure water droplets [135]. Not only does the reduction of pressure inside the solute-containing droplet slow down the evaporation process, but also drying processes due to water concentration gradients [136]. In addition, the presence of solutes in water droplets decreases the evaporation time by producing a lower limit in the density of water. On top, water diffusivity is affected in liquid droplets. However, the analysis presented in [136] show that these effects are negligible.

We mentioned that droplet size has an impact on evaporation time. Besides that, the volume fraction of solutes, ambient temperature and humidity and non-ideal effects of solute interactions inside the droplet determine the overall evaporation process. Especially the relative humidity and initial size of the droplet, for example produced inside the mouth of a coughing person, play a key role. This more specifically means that with increasing volume fraction of solutes or relative humidity of ambient air, the final droplet radius increases.

The constellation of solute particles in liquid droplets can be considered as a binary mixture in the light of classical density functional theory (cDFT) where these solute particles are able to prevent the droplet from complete evaporation. Particularly the effect of size disparity between the liquid (solvent) and solute particles can be captured within the framework of fundamental measure theory (FMT). Attractive forces between solvents and solutes can be modeled by square-well (SW) interactions, for which analytical and numerical calculations are feasible. The aforementioned observations on droplet stability, especially taking into account the influence of solute volume fraction and relative humidity of air, can be tested. On the one hand, a corresponding equilibrium state of a droplet containing (much larger) solute particles can be described using a rather simple thermodynamic model that encompasses all relevant SW interaction parameters and is thus capable of predicting a stable droplet. On the other hand, making use of

the powerful framework of FMT enables us to perform numerical calculations of binary hard-sphere mixtures with additional, attractive SW interactions. Of course, employing a model based on SW interactions cannot be considered as being realistic. Latter is reliable only for systems of low density and high temperature. In addition, the large size disparity between a typical virus particle and a water molecule (ca. 10000) is out of scope for any resourceful and stable computation within DFT. Furthermore, we disregard any associative interactions that are needed if we aimed to capture a water droplet to a good degree. This, however, does not alter our claim that the presence of nanoparticles stabilizes the droplet, irrespective of the specific properties of water. Still, essential parts of such a binary mixture can be studied and compared to the findings of [134, 136].

While the on-lattice calculations of [137] do not possess any information about the detailed shape of the equilibrium droplet, our continuum DFT calculations are able to give more insight into the transition of the interior of the droplet to its environment, e.g. adsorption of solute particles close to the surface. It is also to be expected that solvent and solutes particles tend to coordinate themselves in concentric shells which would lead to oscillatory shapes of the density distributions. Furthermore, the accumulation of liquid and nanoparticles can be captured by this approach also including the influence of size disparity between the components [138, 139, 140, 141, 142]. Indeed, we allow for a size ratio between the liquid and nanoparticles, rendering the latter two to ten times the size of the former. While non-volatile particles suspended in water droplets have a much larger size ratio of roughly 10,000, our choice is limited by numerical feasibility and accuracy of FMT. The work of [143] investigates the properties of very small droplets of a Lennard-Jones fluid in a super saturated environment leading to vapor-liquid nucleation. They could find a good prediction by DFT for microscopic structure, size and free-energy barrier of critical nuclei. Finally, molecular dynamics (MD) simulations can capture the time evolution of laden droplets by incorporating certain important evaporation mechanisms with which morphological structure and diameter shrinkage of these droplets can be understood [144, 145, 146, 147].

7.1 Model for Droplets in Equilibrium

A single-component, spherically shaped liquid droplet undergoes evaporation due to the mechanical imbalance introduced by the Laplace pressure, which depends on the droplet radius R. Even at liquid–vapor coexistence, where mechanical and chemical equilibrium would ordinarily be satisfied, a convex structure such as a droplet does not fulfill mechanical equilibrium. Instead, the pressure difference across the interface is given by

$$P_{\text{in}} - P_{\text{out}} = \frac{2\gamma}{R}, \tag{7.1}$$

where γ denotes the surface tension, and P_{in} and P_{out} are the pressures inside and outside the droplet, respectively. Clearly, mechanical equilibrium is violated in general, and only in the limit of large droplets do the pressures become approximately equal. Consequently, the droplet evaporates, with the process accelerating as the radius R decreases due to the increasing Laplace pressure. Put differently, the saturation vapor pressure $P(R)$ of the droplet is increased with respect to that of a flat surface, P_{sat}

$$H_r = \exp\left(\frac{2\gamma v_m}{k_B T R}\right), \tag{7.2}$$

where we have introduced the saturation or relative humidity $H_r = P(R)/P_{\text{sat}}$ and the molar volume v_m. Note that $P_{\text{sat}} = P(R \to \infty)$, i.e. that of a flat surface. From Eq.(7.2) we easily deduce that $H_r > 1$, i.e. supersaturation is necessary to allow for equilibrium of the pure droplet. Indeed, only in the latter case does an equilibrium radius exist which, however, is merely an unstable state; slight perturbations lead either to complete evaporation or further condensation of the droplet.

In contrast, droplets laden with nanoparticles may achieve mechanical equilibrium through compensation of the Laplace pressure. The attractive interactions between nanoparticles and the surrounding liquid can reduce the saturation vapor pressure, allowing equilibrium to be restored. More specifically, the presence of nanoparticles in the droplet gives rise to a change ΔP in the pressure inside the droplet with contributions stemming from the attractive SW interaction and repulsive hard-sphere interaction due to finite size of the nanoparticles. Compared to the pure solvent case, adding solute particles increases internal pressure P_{in}, accounting for the surface term of Eq.(7.1). Hence, due to the presence of nanoparticles Eq.(7.2) is changed to

$$H_r = a_l \exp\left(\frac{2\gamma v_m}{k_B T R}\right), \tag{7.3}$$

where a_l is the solvent's activity. Typically, $a_l < 1$ and additional attractive interactions between liquid and nanoparticles pushes a_l further down. Latter is connected to the fact that not only mixing entropy is included, but also attractive forces. As a consequence, there can exist a stable equilibrium state of the droplet for $H_r < 1$, i.e. for undersaturated vapor. Finally, at this stage we would like to add that considering a canonical setup of the droplet a stable equilibrium of a pure water droplet exists. As the number of liquid particles is conserved (no open atmosphere), an evaporation would increase vapor pressure eventually stopping further evaporation, followed by condensation and therefore back to the equilibrium state. In case of first condensation, the argument is similar.

We now consider a spherical system of radius R_m containing a droplet of radius $R < R_m$, where the liquid and vapor phases have packing fractions η_l and η_v, respectively. A total of N_n nanoparticles are present, of which a fraction ξ resides within the droplet, while the remaining $1-\xi$ are dispersed in the vapor phase, see Fig.7.1. From this setup, the nanoparticle packing fractions inside and outside the droplet are given by

$$\eta_n^{(\text{in})} = \frac{\xi N_n}{8q^3\tilde{R}^3}, \quad \eta_n^{(\text{out})} = \frac{(1-\xi)N_n}{8q^3(\tilde{R}_m^3 - \tilde{R}^3)}, \tag{7.4}$$

where we use the dimensionless radii $\tilde{R} = R/\sigma_l$ and $\tilde{R}_m = R_m/\sigma_l$.

Mechanical equilibrium is established when the following condition is satisfied:

$$\tilde{P}(\eta_l^{(\text{in})}, \eta_n^{(\text{in})}) = \tilde{P}(\eta_l^{(\text{out})}, \eta_n^{(\text{out})}) + \frac{\pi\tilde{\gamma}}{3\tilde{R}}, \tag{7.5}$$

where $\tilde{\gamma}$ is defined as the interfacial surface tension of the pure liquid at phase coexistence, and $\tilde{P} = \beta\frac{\pi}{6}\sigma_l^3 P$ denotes the reduced pressure of the binary mixture, which is a sum Boublik-Mansoori-Carnahan-Starling-Leland pressure P_{BMCSL} [80, 35] of a hard-sphere mixture and the SW contribution P_{sw}. It is worth noting that the presence of nanoparticles affects the surface tension, resulting in a value different from that of the pure liquid system. However, for sufficiently large droplets ($R \gg \sigma_l$), the surface term in Eq.(7.5) becomes negligible. It is only for droplets with radii 10 times or higher the liquid particle diameter that the surface contribution becomes significant.

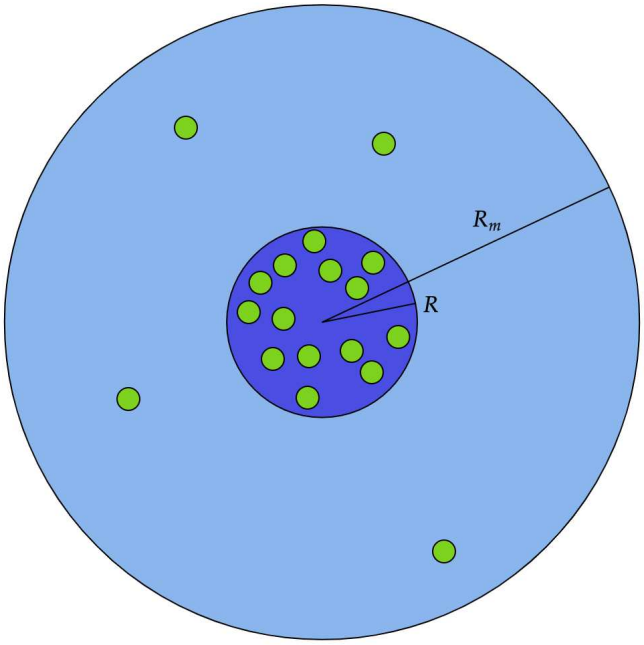

Figure 7.1: Schematic picture of a nanoparticle-laden droplet in a spherical system of radius R_m containing a droplet (dark blue) of radius R in equilibrium surrounded by vapor (light blue). A fraction ξ of the nanoparticles (green) is inside the droplet.

In addition to mechanical equilibrium, we must also enforce chemical equilibrium for both the liquid and nanoparticle components. For the liquid, we prescribe a chemical potential μ_0 that is below the coexistence value μ_c, corresponding to a relative humidity $H_r < 100\%$. Thus, we require

$$\begin{aligned} \mu_0 &= \mu_l(\eta_l^{(\mathrm{in})}, \eta_n^{(\mathrm{in})}) \\ \mu_n(\eta_l^{(\mathrm{in})}, \eta_n^{(\mathrm{in})}) &= \mu_n(\eta_l^{(\mathrm{out})}, \eta_n^{(\mathrm{out})}). \end{aligned} \tag{7.6}$$

The first equation ensures that the chemical potential of the liquid inside the droplet matches the prescribed external value. Furthermore, the second line of Eq.(7.6) makes sure that the rates of nanoparticles leaving and entering the droplet are equal. Importantly, the equilibrium droplet size depends on the system size R_m as long as $\xi < 1$. To understand this, consider a droplet stabilized with a given fraction $\xi < 1$ of nanoparticles inside. Due to chemical equilibrium, a fixed amount $1 - \xi$ of nanoparticles must remain in the vapor phase. Increasing the system size (with fixed N_n) provides more external volume, diluting the vapor-phase nanoparticle density. As a result, fewer nanoparticles are available for stabilization inside the droplet, which must then shrink. Only in the limit $\xi \approx 1$, where nearly all nanoparticles reside in the droplet, does the configuration become independent of system size.

We emphasize that the above description is equivalent to the capillarity model proposed in [137]. For a system of volume V filled with pure vapor at pressure P_v, the change in grand potential due to inserting a droplet of radius R and internal pressure P_d is given by

$$\Delta\Omega(\rho_l, R) = -\frac{4\pi}{3} R^3 \left(P_d(\rho_l, R) - P_v\right) + 4\pi R^2 \gamma, \tag{7.7}$$

and the equilibrium droplet radius follows from the stationarity condition

$$\frac{\partial \Delta\Omega(\rho_l, R)}{\partial R} = 0. \tag{7.8}$$

By prescribing a chemical potential μ near the coexistence value, we can determine both the equilibrium radius R and the corresponding liquid density ρ_l of the droplet. Notably, Eq.(7.5) coincides with the equilibrium condition in Eq.(7.8), thus linking the two frameworks.

With Eq.(7.5) and Eq.(7.6), we can predict stable droplet configurations. Given the system size R_m, a droplet radius R, and the relative humidity H_r (via μ_0), we solve for the total number of nanoparticles N_n, the liquid packing fraction η_l, and the fraction ξ of nanoparticles inside the droplet. Alternatively, we may fix ξ and determine the required interaction strength ϵ_{ln} to achieve that configuration particularly useful when targeting system-size-independent droplets.

We then use these thermodynamic quantities to initialize a droplet minimization for a square-well (SW) binary mixture. This is particularly relevant in strongly asymmetric mixtures, where a good initial guess is essential for stable convergence. For instance, we compute the equilibrium droplet radius R based on a set of SW parameters, and initialize the density profiles ρ_l and ρ_n, along with the corresponding N_n, accordingly. If instead we started with an off-equilibrium radius, the minimization would not only require more iterations to equilibrate but also be significantly more prone to instability. Thus, by providing accurate initial conditions and employing multi-stage minimization, we render the full procedure robust and computationally efficient.

7.2 Computational Approach

We want to describe a nanoparticle-laden droplet as a square-well (SW) binary mixture within Density Functional Theory (DFT) by employing spherical symmetry. Furthermore, we will refer to the first component as the liquid or solvent with density $\rho_l(\mathbf{r})$ and the second component as the "nanoparticle" with density $\rho_n(\mathbf{r})$.

The excess functional of the corresponding binary mixture reads

$$\begin{aligned}\mathcal{F}_{\text{ex}}[\rho_l, \rho_n] = \mathcal{F}_{\text{hs}}[\rho_l, \rho_n] + \frac{1}{2}\int\int d\mathbf{r}\, d\mathbf{r}'\, \rho_l(\mathbf{r})\rho_l(\mathbf{r}')\phi_{\text{sw}}^{(ll)}(|\mathbf{r}-\mathbf{r}'|) + \\ + \frac{1}{2}\int\int d\mathbf{r}\, d\mathbf{r}'\, \rho_n(\mathbf{r})\rho_n(\mathbf{r}')\phi_{\text{sw}}^{(nn)}(|\mathbf{r}-\mathbf{r}'|) + \int\int d\mathbf{r}\, d\mathbf{r}'\, \rho_l(\mathbf{r})\rho_n(\mathbf{r}')\phi_{\text{sw}}^{(ln)}(|\mathbf{r}-\mathbf{r}'|),\end{aligned} \tag{7.9}$$

where we now distinguish between the SW interactions liquid-liquid $\phi_{\text{sw}}^{(ll)}$, nano-nano $\phi_{\text{sw}}^{(nn)}$ and inter-component liquid-nano $\phi_{\text{sw}}^{(ln)}$ with energies ϵ_{ll}, ϵ_{nn}, ϵ_{ln} and ranges λ_{ll}, λ_{nn}, λ_{ln}, respectively. These SW parameters can be chosen independently in general; however, certain mixing rules such as Lorentz-Berthelot prescribe the inter-component interactions of a SW mixture [148, 149]. By respecting the Lorentz-Berthelot mixing rules, we can also employ the functional of Eq.(6.40) à la FMT.

We minimize the grand functional $\Omega[\rho_l, \rho_n]$ with respect to ρ_l and ρ_n:

$$\begin{aligned}\frac{\delta\Omega[\rho_l, \rho_n]}{\delta\rho_l(\mathbf{r})} &= 0, \\ \frac{\delta\Omega[\rho_l, \rho_n]}{\delta\rho_n(\mathbf{r})} &= 0, \quad N_n = \text{const.},\end{aligned} \tag{7.10}$$

where we use the restriction on ρ_n that the number of nanoparticles $N_n = \int d\mathbf{r}, \rho_n(\mathbf{r})$ is constant. This means that we are describing the binary mixture in the semi-grand canonical ensemble, i.e., the liquid grand canonically and the non-volatile nanoparticles canonically.

From Eq.(7.10) we obtain, in the absence of any external potentials ($V_{\text{ext}}(\mathbf{r}) = 0$), the implicit equations for ρ_l and ρ_n:

$$\begin{aligned} \rho_l(\mathbf{r}) &= \rho_l^{(0)} \exp\left(c_l^{(1)}(\mathbf{r}) + \beta\mu_l\right), \\ \rho_n(\mathbf{r}) &= \rho_n^{(0)} \exp\left(c_n^{(1)}(\mathbf{r})\right), \end{aligned} \tag{7.11}$$

with the one-body correlation functions $c_i^{(1)}(\mathbf{r}) \equiv -\delta\beta\mathcal{F}_{\text{ex}}[\rho_l, \rho_n]/\delta\rho_i(\mathbf{r})$ for $i = l, n$, and the excess chemical potential of the liquid μ_l. We want to emphasize that since the nanoparticles are treated canonically, there is no chemical potential in the exponential of Eq.(7.11) for ρ_n.

The reason for utilizing a canonical ensemble for the nanoparticles is that these cannot be placed anywhere in the system as would be the case if we used the grand canonical ensemble. Furthermore, by applying the grand canonical ensemble for the liquid, we can easily impose humidity onto the system and investigate nanoparticle-laden droplets in different environments. We expect that the relative humidity will have an impact on the equilibrium size and density of such droplets.

We solve Eq.(7.11) iteratively using the Picard iteration scheme, where we mix the solution of the k-th step $\rho_i^{(k)}$ with the right-hand side (rhs) of Eq.(7.11), $\rho_i^{(\text{rhs},k)}$:

$$\rho_{l,n}^{(k+1)}(\mathbf{r}) = (1-\alpha_i)\rho_{l,n}^{(k)}(\mathbf{r}) + \alpha_i\rho_{l,n}^{(\text{rhs},k)}(\mathbf{r}). \tag{7.12}$$

Here, α_i are mixing parameters that can be chosen independently from each other. Indeed, it will be typical for α_n to be many magnitudes smaller than α_l. Equation(7.12) is repeated until the densities ρ_i have converged sufficiently.

As it turns out, the Picard scheme given in Eq.(7.12) reaches its limit of applicability for a binary mixture of high size ratio, i.e. one component being much bigger than the other. The reason lies in the fact that the exponential in Eq.(7.11), $\exp\left(c_n^{(1)}(\mathbf{r})\right)$, becomes very large in this scenario of a highly asymmetric binary mixture, hence leading to numerical instabilities. Therefore, it is necessary to employ a different kind of minimization scheme where we also make use of several stages of pre-minimization. This allows us to come closer to the real solutions $\rho_l(\mathbf{r})$ and $\rho_n(\mathbf{r})$, thus improving numerical stability. Hence, the following four stages are successively performed:

1. We first consider the second component of nanoparticles with initial density $\rho_n(r) = \rho_n^{(0)}\Theta(R-r)$, where R is the equilibrium droplet radius and $\rho_n^{(0)}$ the uniform nanoparticle density inside the droplet. Then, to confine these nanoparticles, we impose an effective external potential $V_{\text{ext}}(r)$ of the form:

$$V_{\text{ext}}(r) = V_{\text{in}} + \frac{V_{\text{out}} - V_{\text{in}}}{1 + \exp\left(-a(r-R)\right)}, \quad V_{\text{in}} = -\epsilon_{ln}\left(\lambda_{ll}q + \lambda_{nn}\right)^3 \eta_l^{(0)}\eta_n^{(0)} \tag{7.13}$$

with a and V_{out} being positive constants chosen appropriately. V_{in} ensures that nanoparticles prefer to stay inside the droplet. The effective potential is sigmoidal, attractive inside the droplet, and repulsive outside, see Fig.7.2. Here, $\eta_l^{(0)}$ and $\eta_n^(0)$ are the uniform packing fractions of the liquid and nanoparticles, respectively, and

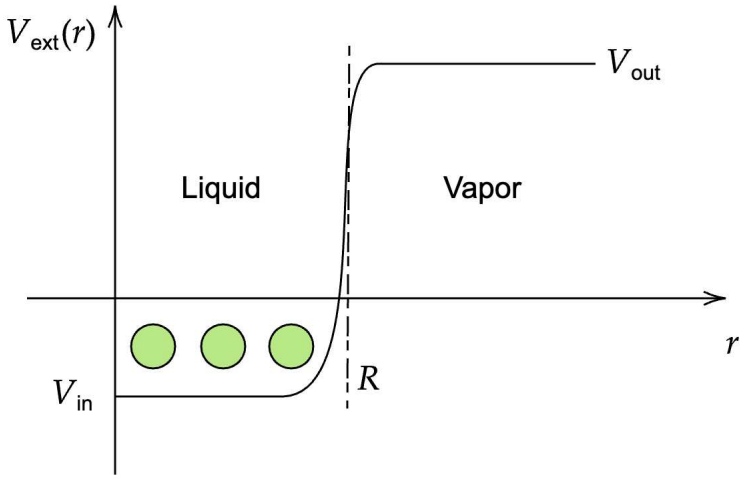

Figure 7.2: The effective external potential $V_{\text{ext}}(r)$ confines the nanoparticles (green) in a spherical region of radius R resembling the droplet.

$q = \sigma_l/\sigma_n$ is the size ratio. With this potential, we apply the Picard scheme, see Eq.(7.12), for $\rho_n(r)$:

$$\rho_n^{(k)}(r) = (1-\alpha)\rho_n^{(k-1)}(r) + \alpha\rho_n^{(0)} \exp\left(c_n^{(1)}(r) - \beta V_{\text{ext}}(r)\right), \quad N_n = \text{const.}, \tag{7.14}$$

with $\alpha = 0.1$. At this stage, we neglect the liquid density $\rho_l(r)$.

2. Now, we Picard iterate the liquid density profile $\rho_l(r)$, initialized as $\rho_l(r) = \rho_l\Theta(R-r) + \rho_v\Theta(r-R)$, while keeping the nanoparticle density profile fixed

$$\rho_l^{(k)}(r) = (1-\alpha)\rho_l^{(k-1)}(r) + \alpha\rho_l^{(0)} \exp\left(c_l^{(1)}(r) + \beta\mu_l\right), \quad \rho_n(r) = \text{const.} \tag{7.15}$$

with $\alpha = 0.1$. The fixed $\rho_n(r)$ enters through $c_l^{(1)}(r)$.

3. Having obtained both density profiles, several thousand Picard iterations are performed via Eq.(7.12). The mixing parameter α_n is now chosen as

$$\alpha_n = \tilde{\alpha}_n \exp\left(-||c_n^{(1)}||_{\max}\right), \tag{7.16}$$

which avoids instabilities from large exponentials in Eq.(7.11). Here, $||c_n^{(1)}||_{\max}$ is the maximum of the correlation function $c_n^{(1)}(r)$ in the corresponding domain of r. Typically, $\tilde{\alpha}_n \in [0.01, 0.1]$. It should be noted that choosing the mixing parameter α_n in this way mimics a Picard iteration in the grand-canonical fashion.

4. Finally, we use the Ng algorithm of [150], outlined in App.D, to greatly improve minimization accuracy. Several intermediate steps are combined via optimal mixing to construct the new iteration step.

Therefore, several previous steps are necessary in order to successfully minimize the asymmetric binary mixture. The purpose of these pre-minimization procedures lies in the fact that it is very challenging to find the right minimum of the grand potential fuctional, $\Omega[\{\rho_i\}]$. The challenge becomes more severe as the size disparity, $q = \sigma_l/\sigma_n$, is increased. Applying the pre-minimizations allows us to come closer to the minimum, with the effect of enabling the common minimization schemes such as Picard to be useful.

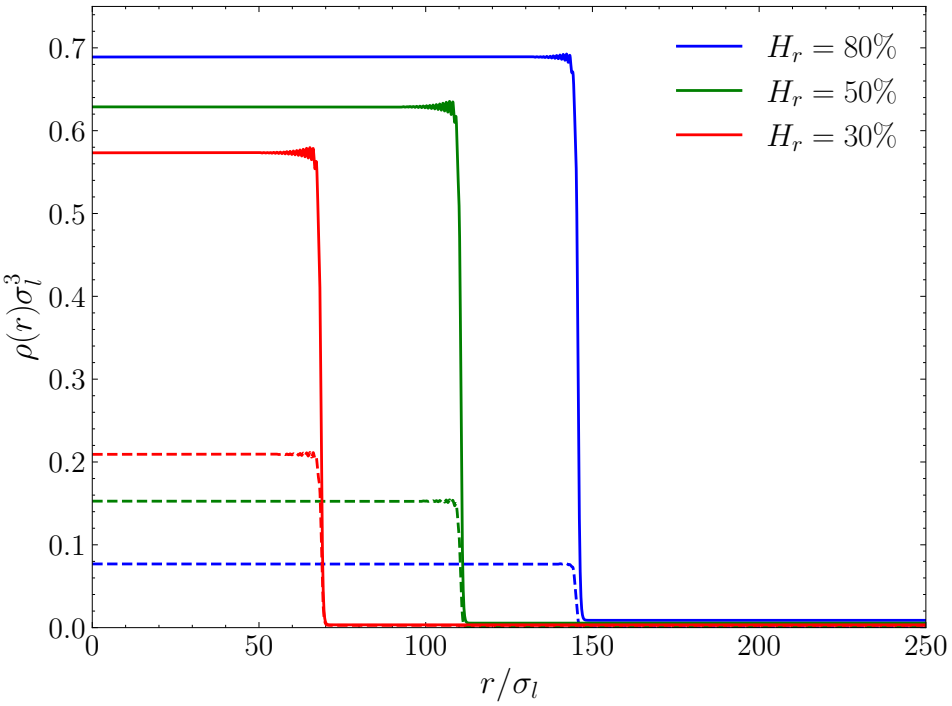

Figure 7.3: Spherically symmetric density profiles $\rho(r)$ of solvent (solid) and solute particles (dashed) for three humidity values $H_r = 80\%$, 50% and 30% resembling an environment of moist air, air of temperate zones and arid climate, respectively.

7.3 Symmetric Mixture $q = 1$

Before we come to the more interesting application of DFT for asymmetric binary mixtures, it is worth mentioning some results on the symmetric case of a 1:1 droplet, i.e. equally sized solvent and solute particles. Not only can it be captured well by FMT, but also from a numerical point of view this case is much more stable in the minimization. We assume the interaction parameters of the solvent to be $\beta\epsilon_{ll} = 1.2$ and $\lambda_{ll} = 1.5$. We further suppose that there is no interaction between the solute particles with themselves, i.e. $\beta\epsilon_{nn} = 0$, but we, of course, allow for interactions between solvent and solute particles by choosing $\beta\epsilon_{ln} = 1.725$ whose range is given by the interaction ranges of the solvent and the solute, where for the latter we choose $\lambda_{nn} = 1.5$. The number of solute particles is taken as $N_n = 992513$, i.e. roughly one million. There is no specific reason why we choose these values, however, given numerical feasibility and computation time those chosen by us here are sufficient. In principle, we could also introduce solute-solute interactions but this is not necessary for droplet stabilization. Our system or container filled with the vapor of the solvent and the droplet laden with solute or nanoparticles shall have a diameter of $R_m = 200\sigma_l$. According to our thermodynamic model of Sec.7.1, for the given interaction parameters above we expect a stable droplet at humidity of $H_r = 80\%$ of ca. $R = 146\sigma_l$. In Fig.7.3 we depict density profiles of solvent and solute particles for three different environments prescribed by humidity H_r. Since we are close to the pure-liquid phase equilibrium for $H_r = 80\%$, the corresponding density inside the droplet is almost the magnitude of the coexisting liquid density, roughly $\rho\sigma_l^3 \approx 0.76$. Furthermore, we can observe some structures of the solvent density profile close to the boundary of the droplet while the inside remains at a constant value.

As we diminish the humidity of the environment, the droplet shrinks to a new equi-

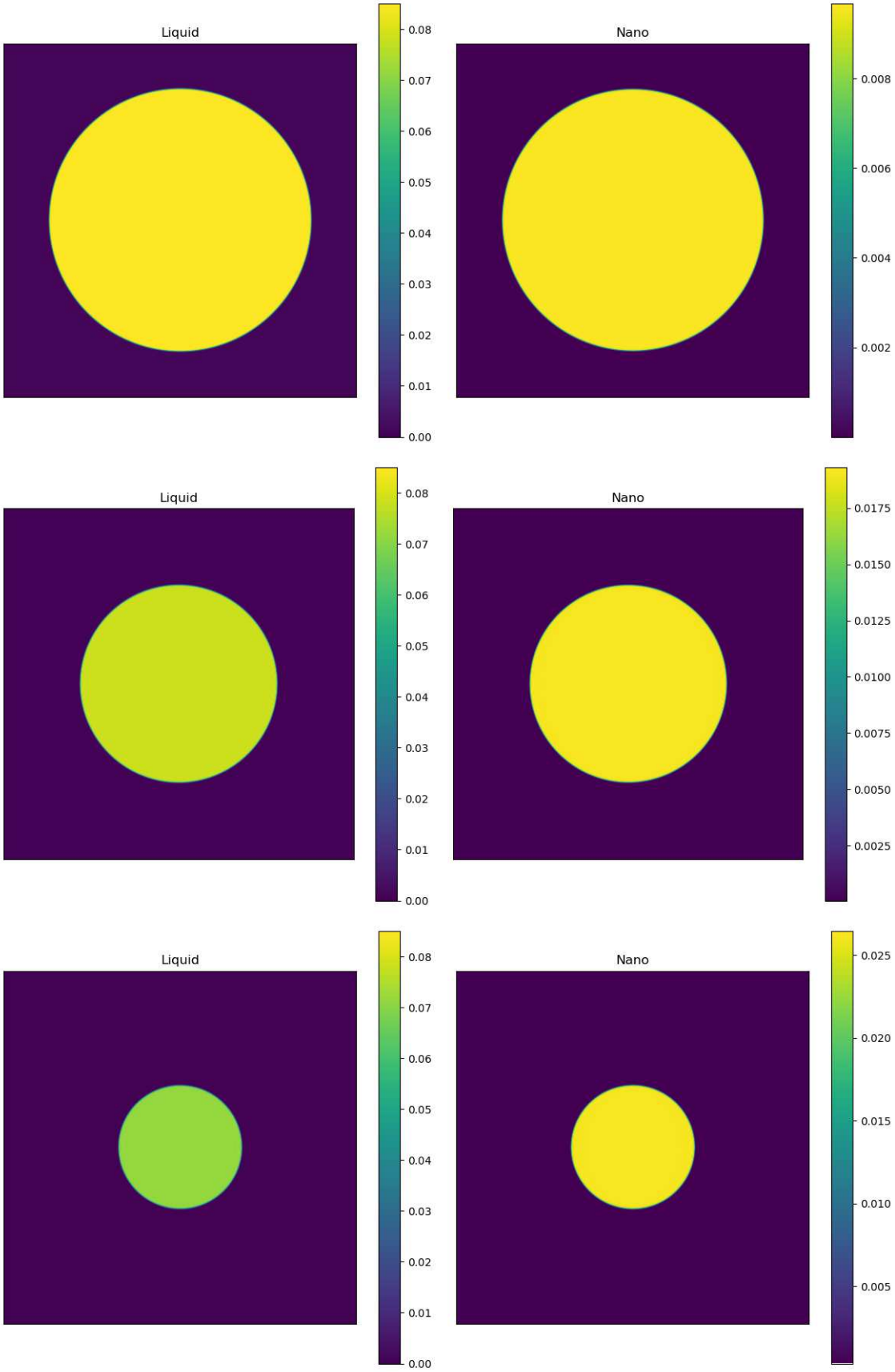

Figure 7.4: Heatmpas of the 1:1 droplet discussed in the text. Top $H_r = 80\%$, middle 50% and bottom 30%.

librium radius and loses a part of its initial solute particles to its environment. This is explained through the fact that for lower humidity the droplet has less solvent or liquid particles available to retain the droplet and consequently loses nanoparticles until it reaches a new and hence smaller radius. But still, as there is less volume for the solute particles to fill their density increases correspondingly, as can be inferred from Fig.7.3. Through the shrinking process, the solute particles become more densely packed and the solvent-solute interactions lead to first signs of oscillations close to the boundary or surface of the droplet. For completeness, we present the corresponding heatmaps to Fig.7.3 in Fig.7.4.

Although this simple example of a symmetric 1:1 droplet is by far not close to what is observed in water droplets suspended with viruses, we nonetheless could show that there is a solution to a stable droplet and that in particular this droplet can be minimized within the framework of DFT.

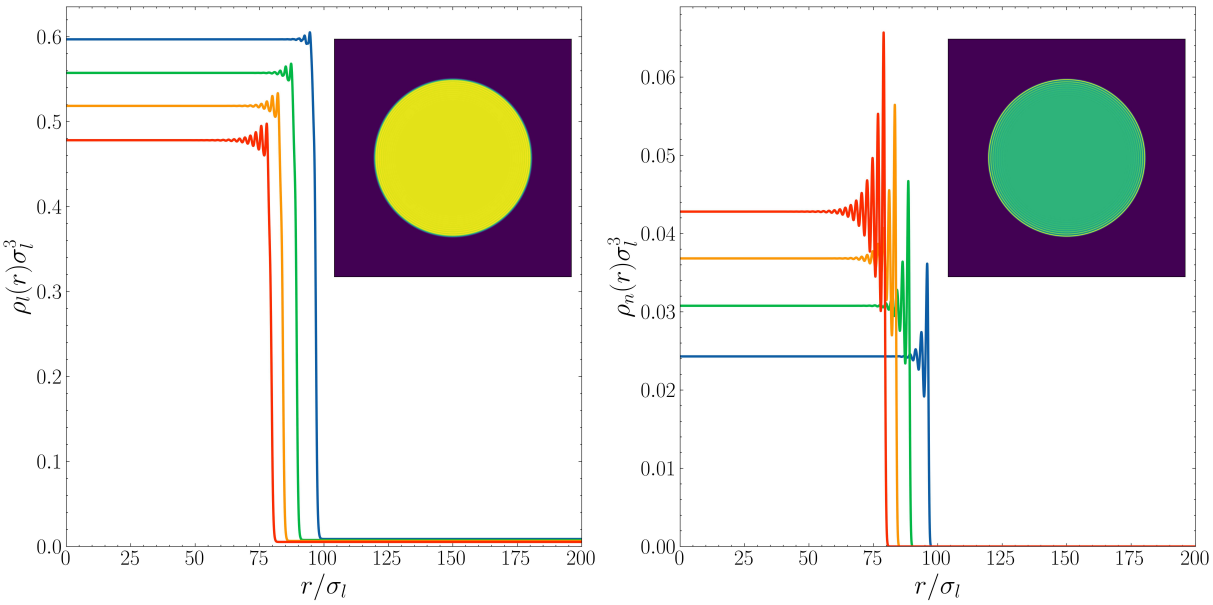

Figure 7.5: Density profiles $\rho_l(r)$ (left) and $\rho_n(r)$ (right) of a 2:1 droplet with $\epsilon_{nn} = 0$, $\epsilon_{ln} = 3.78$, $\lambda_{nn} = 1.01$ and $N_n = 92281$. For $H_r = 50\%$ (red) the droplet has a radius $\tilde{R} = 80$ which increases as the humidity is raised to $H_r = 60\%$ (green), $H_r = 70\%$ (orange) and $H_r = 80\%$ (blue). The insets show a heatmap of the 2:1 droplet for $H_r = 50\%$.

7.4 Stable Droplets

Having outlined the model for nanoparticle-laden droplets in equilibrium in Sec.7.1, we now apply the numerical scheme described in Sec.7.2 to obtain radially symmetric equilibrium density profiles, $\rho_l(r)$ and $\rho_n(r)$, corresponding to the liquid and nanoparticle species, respectively. For the liquid component, we fix the square-well (SW) interaction parameters to $\beta\epsilon_{ll} = 1.2$ and $\lambda_{ll} = 1.5$, which yield the coexistence densities of Eq.(2.111) resembling those of water. Introducing nanoparticles into the system allows for the stabilization of a droplet of a given radius under an external environment characterized by its relative humidity. Unlike a more realistic situation, in which a nanoparticle is roughly ten thousand times larger than a liquid particle, we restrict ourselves to the numerically more tractable case where the nanoparticle diameter is ten times that of the liquid particles. This simplification avoids the substantial computational challenges that arise when minimizing a highly asymmetric binary functional. Droplets can thus be generated under different environmental conditions, i.e. for various values of the humidity H_r. The latter is formally defined as $H_r = 100 \times P(\mu_0)/P(\mu_c)$, where $\mu_0 \leq \mu_c$ denotes the chemical potential imposed in the calculation. For example, setting $H_r = 50\%$ corresponds to a typical room-humidity level at a temperature of approximately 20 °C.

Once the interaction parameters ϵ_{nn}, ϵ_{ln}, λ_{nn}, and λ_{ln} are specified, together with the fraction of nanoparticles remaining inside the droplet, $\xi \approx 1$, we can determine both the dimensionless equilibrium radius $\tilde{R} = R/\sigma_l$ and the number of nanoparticles N_n required to stabilize the droplet. The size ratio $q = \sigma_l/\sigma_n$ quantifies the degree of asymmetry in the binary mixture. For instance, a value of $q = 1/2$ corresponds to what we refer to as a 2:1 droplet. We present scenarios where we set $\epsilon_{nn} = 0$ while $\epsilon_{ln} < 0$ and also scenarios where the mixing rule of the energy, i.e. $\epsilon_{ln} = \sqrt{\epsilon_{ll}\epsilon_{nn}}$ is satisfied. The corresponding mixing rule for the interaction range, i.e. $\lambda_{ln} = (\lambda_{ll}\sigma_l + \lambda_{nn}\sigma_n)/(\sigma_l + \sigma_n)$ is obeyed

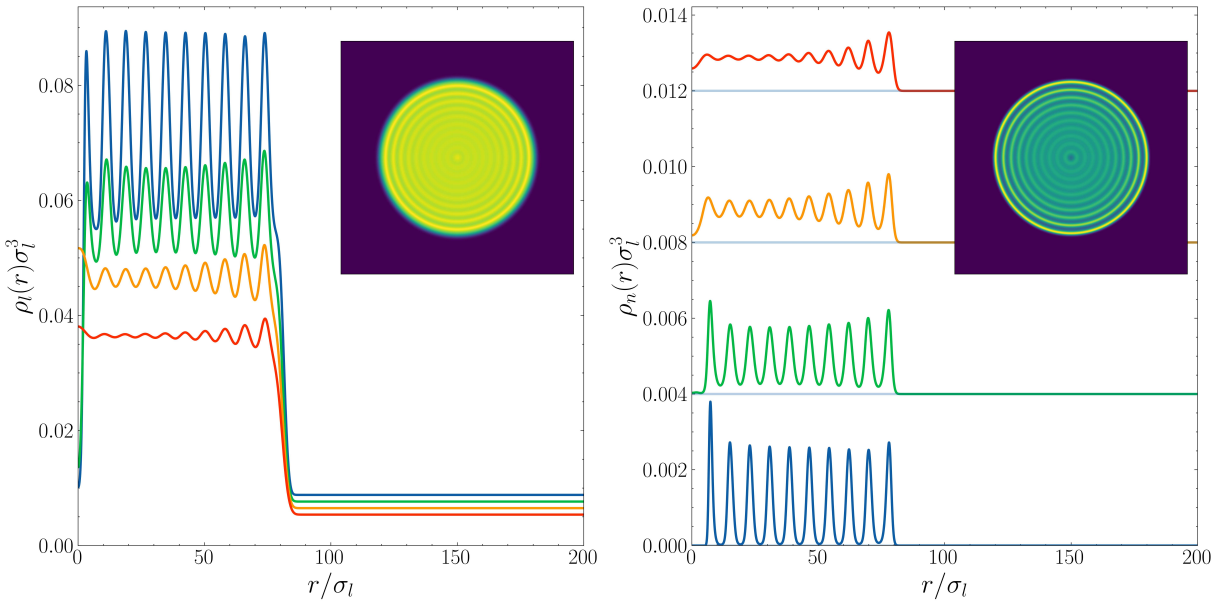

Figure 7.6: Density profiles $\rho_l(r)$ (left) and $\rho_n(r)$ (right) of a 10:1 droplet with $\epsilon_{nn} = 0$, $\epsilon_{ln} = 3.69$, $\lambda_{nn} = 1.01$ and $N_n = 1983$ with an offset represented by blue lines. For $H_r = 50\%$ (red) the droplet has a radius $\tilde{R} = 80$ which increases as the humidity is raised to $H_r = 60\%$ (green), $H_r = 70\%$ (orange) and $H_r = 80\%$ (blue). The insets show a heatmap of the 10:1 droplet for $H_r = 50\%$.

throughout the discussion. We expect the interaction parameter ϵ_{ln} to have the most impact on droplet stabilization as it describes the solubility of nanoparticles inside the liquid while the interaction energy between the nanoparticles ϵ_{nn} becomes important only for sufficiently high nanoparticle densities, when nanoparticles start to interact with each other. The ranges for ϵ_{ln} and ϵ_{nn} are prescribed by the following arguments: First, we are not seeking configurations of nanoparticles inside the droplet that clump together, i.e. the values for ϵ_{ln} and ϵ_{nn} must not be too large. The solubility of the nanoparticles, on the other hand, is merely controlled by the inter-component interaction strength ϵ_{ln} that must be large enough such that the nanoparticles prefer to assemble themselves within the droplet. In total, these restrictions on ϵ_{ln} and ϵ_{nn} are fulfilled by those values we consider here in our discussion.

Before presenting the case of 10:1 size ratio, it is also interesting to first regard the case of a less asymmetric case of 2:1. In Fig.7.5 we show density profiles of a droplet having a radius $\tilde{R} = 80$ at a humidity $H_r = 50\%$ with the corresponding SW interaction parameters given in the figure caption. We observe that inside the droplet the density profiles of liquid and nanoparticles are constant, exhibiting oscillations only close to the surface of the droplet. These oscillations become more pronounced as humidity is diminished. The oscillatory behavior is explained generally by the Fisher-Widom line separating pure exponential decay from exponentially damped decay for density distributions [151, 152]. Further we see that the liquid density $\rho_l(r)$ decreases as the humidity is decreased while the nanoparticle density $\rho_n(r)$ increases. This is, of course, due to the fact that as the droplet shrinks the nanoparticles have less space available.

Figure7.6 shows a 10:1 droplet with the same radius as the 2:1 droplet in Fig.7.5. As the size ratio now is increased, the amount of nanoparticles needed for stabilization is much less. Furthermore, we observe much stronger oscillations not only Close to the

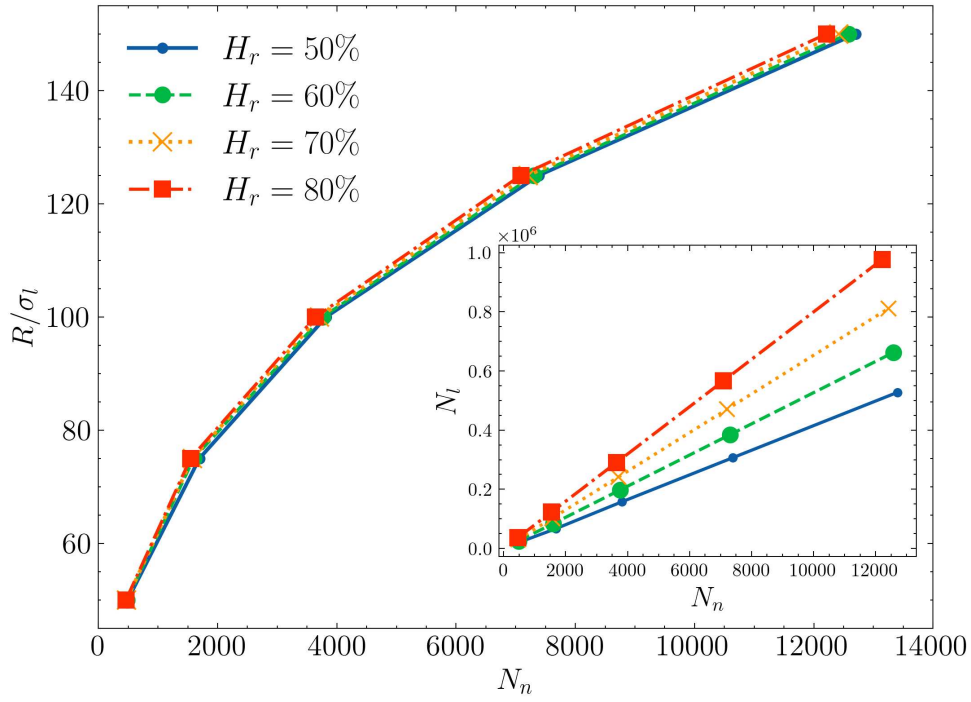

Figure 7.7: The droplet radius R is plotted as a function of nanoparticle number N_n with a fixed interaction strength $\epsilon_{ln} = 3.69$ of Fig.7.6 for several humidity values considered here. The inset displays the dependence of liquid particles on the nanoparticle number N_n.

surface but also inside the droplet, especially for high humidity. What we can also observe is that the droplet radius is almost unchanged , in contrast to the 2:1 droplet demonstrated in Fig.7.5. The oscillations, clearly visible in the insets of Fig.7.6, have a pattern of concentric circles for both the liquid and nanoparticles in such a way that a maximum of the former meets a minimum of the latter. Hence, the particles have a tendency to align themselves in shells which becomes stronger as the humidity is increased, i.e. there are more liquid particles in the droplet thus enforcing the nanoparticles to congregate in shells. In Fig.7.7 we present the model predictions on the droplet radius R and number of liquid particles inside the droplet N_l as a function of the number of nanoparticles N_n. For that, we take into account several values of humidity H_r. By adding nanoparticles into the droplet, the corresponding droplet radius increases according to the expected law $R \propto N_n^{1/3}$. Matching to the observation made on Fig.7.6, the droplet radius barely varies by changing humidity. However, as can be inferred from the inset of Fig.7.7, the amount of liquid particles N_l inside the droplet is susceptible to humidity, changing in a linear fashion with respect to N_n. Note that a similar observation was also made in [137], where the slope is increased for high humidity values. Discrepancies between the lattice DFT calculation and the model output is believed to be caused by the usage of a value for the interfacial surface tension γ that is taken from the pure liquid system.

We can also realize a numerically challenging droplet with 10:1 size ration that respects the mixing rule of energy, i.e. $\epsilon_{ln} = \sqrt{\epsilon_{ll}\epsilon_{nn}}$, as is shown in Fig.7.8. Thus, we need slightly more nanoparticles in order to keep the droplet of the same size stable compared to the case of Fig.7.6 where we set $\epsilon_{nn} = 0$. We also notice that oscillations are less pronounced throughout the droplet both for the liquid and nanoparticles. In addition, the density profiles of the nanoparticles have almost the same magnitude and shape

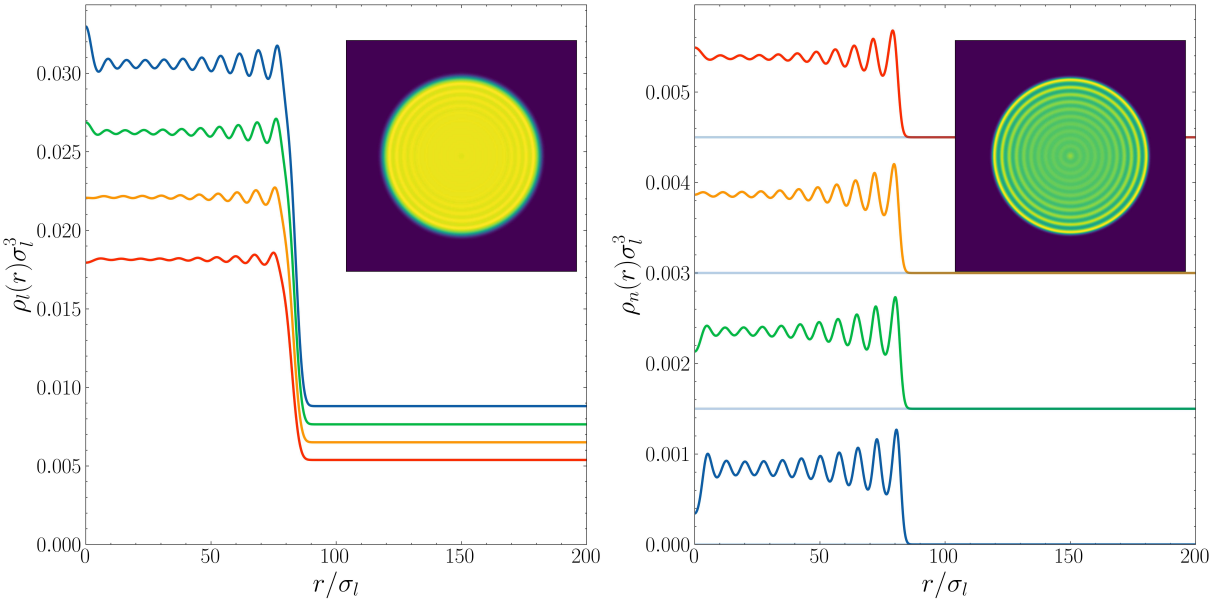

Figure 7.8: Density profiles $\rho_l(r)$ (left) and $\rho_n(r)$ (right) of a 10:1 droplet with $\epsilon_{nn} = 6.96$, $\epsilon_{ln} = \sqrt{\epsilon_{ll}\epsilon_{nn}}$, $\lambda_{nn} = 1.01$ and $N_n = 2063$ with an offset represented by blue lines. For $H_r = 50\%$ (red) the droplet has a radius $\tilde{R} = 80$ which increases as the humidity is raised to $H_r = 60\%$ (green), $H_r = 70\%$ (orange) and $H_r = 80\%$ (blue). The insets show a heatmap of the 10:1 droplet for $H_r = 50\%$.

between each other only showing differences in the center of the droplet. Comparing the overall magnitudes of the liquid densities inside the droplet of Fig.7.6 and Fig.7.8 we see that with the mixing rule for the energy the liquid densities inside the droplet are much lower. This is because with the mixing rule we obtain $\epsilon_{ln} \approx 2.89$ which is lower than the value found in Fig.7.6 therefore weaker attraction between liquid and nanoparticles. Latter simply do not need as many of liquid particles as of Fig.7.6 due to the additional attraction between the nanoparticles necessary to keep the droplet stable. Furthermore, as is observed for the droplet of Fig.7.6, the radius of the droplet of Fig.7.8 varies just a little. We conclude that it is possible to minimize a SW binary mixture within the framework of DFT in order to obtain structural information. The main feature of these density profiles is the appearance of oscillations close to the surface of the droplet. These become more pronounced as we increase the size ratio, q, of the SW binary mixture, see Fig.7.5 and Fig.7.6. For the 2:1 droplet, these oscillations solely appear close to the surface, becoming stronger as the humidity is decreased. Here, it is important to note that the liquid density inside the droplet is close to the density at coexistence of the pure liquid. However, considering the 10:1 droplet the corresponding liquid density inside the droplet is lowered, especially in the case of respecting the energy mixing rule, $\epsilon_{ln} = \sqrt{\epsilon_{ll}\epsilon_{nn}}$. Furthermore, we observe oscillations throughout the droplet which become stronger in an humid environment where the droplet radius remains constant. The aforementioned MD techniques of [144], for instance, study diameter and structural properties of droplets being initially contained with nanoparticles. The evaporation process is then determined by the Peclet-number that encodes dynamic and density properties of the droplet. Crust formation, as is found in [144], resembles our findings in Fig.7.11 and Fig.7.8 with similar oscillatory behavior near the surface of the droplet. It should be emphasized that what we present here are mere equilibrium profiles whereas the MD studies capture the full

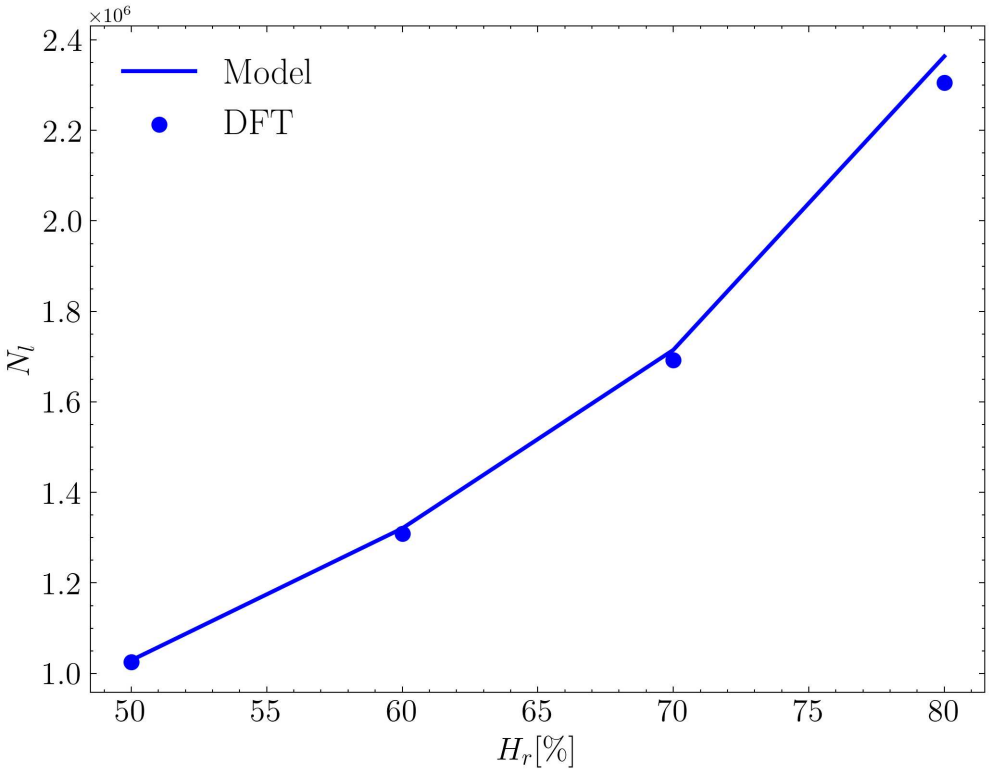

Figure 7.9: The number of liquid particles $N_l = 4\pi/3R^3\rho_l$ inside the droplet of the 2:1 system of Fig.7.5 plotted against humidity H_r.

dynamical evolution.

Similarly to the discussion in [137] where the amount of liquid particles inside the corresponding droplet was compared to the prediction of the capillarity model, we want to consider the change of liquid particles by altering humidity. Here, our model of Sec.7.1 predicts the uniform liquid packing fraction $\eta_l^{(\mathrm{in})}$ inside the droplet of radius R. Therefore, the amount of liquid particles N_l is given by

$$N_l = 8\eta_l^{(\mathrm{in})}\tilde{R}^3 \tag{7.17}$$

where again $\tilde{R}$ is the droplet radius in units of liquid diameter σ_l. On the other hand, the corresponding DFT calculations provide spherically symmetric equilibrium density profiles $\rho_l(r)$ from which we can obtain the number of liquid particles inside the droplet

$$N_l = 4\pi \int_0^R dr\, r^2 \rho_l(r). \tag{7.18}$$

Thus, the model prediction given in Eq.(7.17) can be directly compared with the DFT calculation of Eq.(7.18) for the number of liquid particles N_l in several droplet configurations. Figure7.9 presents the values of N_l for the 2:1 system shown in Fig.7.5 across different humidity levels H_r. We observe that the DFT predictions are slightly lower than those obtained from the model, with the discrepancy becoming more pronounced at higher humidity values.

This difference can be attributed to the fact that the DFT evaluation of Eq.(7.18) requires specifying the droplet radius R, which must be inferred from the density profile. One common approach is to define R as the position where the liquid-to-vapor transition

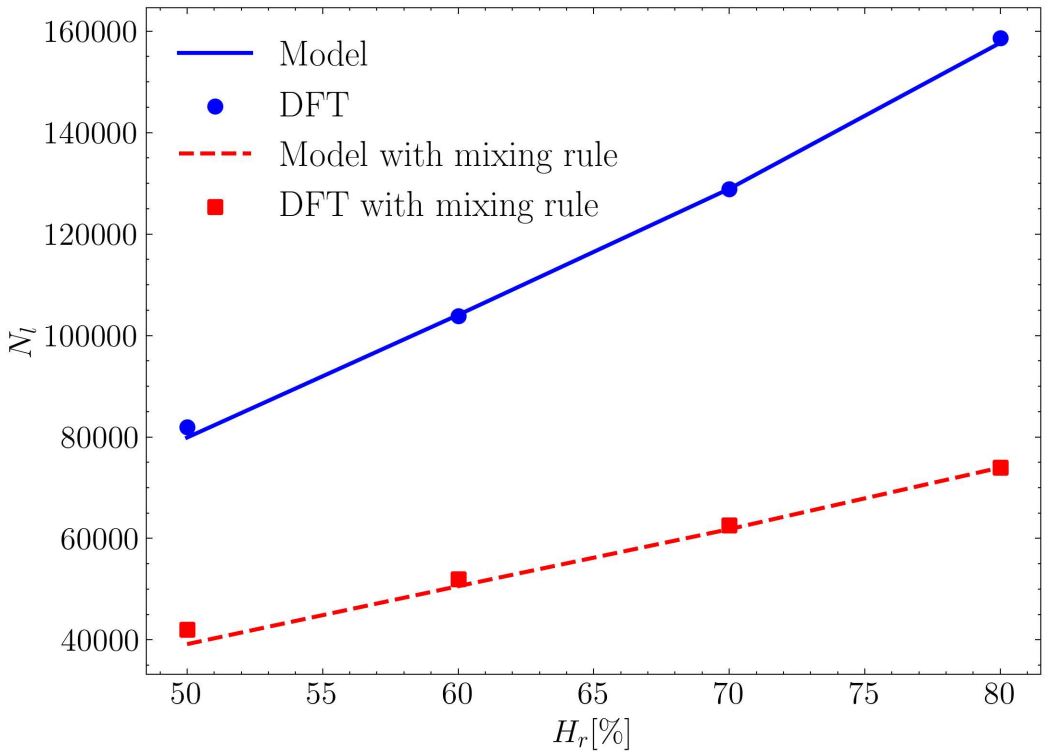

Figure 7.10: The number of liquid particles $N_l = 4\pi/3R^3\rho_l$ inside the droplet of the 10:1 system of Fig.7.6 and Fig.7.8 plotted against humidity H_r.

occurs within a certain density threshold. For an uncertainty δr in the determination of R, the corresponding relative error in the droplet volume scales as $3\delta r/R$. In our calculations, we typically find $|\delta r| \leq 2\sigma_l$, leading to a relative volume error of approximately 8%. The largest deviation observed in Fig.7.9 is about 4.4%, which thus falls well within the uncertainty of the DFT calculation.

Finally, it should be noted that we have used the surface tension $\tilde{\gamma} = 0.25$ corresponding to the pure liquid system. In the presence of solute species, however, the effective surface tension is modified, which in turn affects the equilibrium density profiles of both liquid and nanoparticles and may slightly alter the droplet radius.

As expected, the number of liquid particles within the droplet increases with rising humidity. The magnitude of N_l is on the order of 10^6, consistent with the large values of the liquid density in Fig.7.5. Similarly, Fig.7.10 shows the number of liquid particles N_l for the 10:1 system under the two scenarios presented in Fig.7.6 and Fig.7.8. In this case, we again find good agreement between the model and DFT results, with a maximum deviation of about 6.8%. Moreover, the scale of N_l is roughly an order of magnitude smaller than that of the 2:1 system. Finally, the dependence of N_l on humidity appears nearly linear in Fig.7.10, in contrast to the more parabolic trend observed in Fig.7.9.

For completeness, we present heatmaps of a 10:1 droplet in Fig.7.11 further illuminating the structure of the corresponding densities of liquid and nanoparticles. Contrary to the example shown in Fig.7.4 of a symmetric mixture, we see a much richer structure inside droplet with a droplet radius that remains more or less constant. As is discussed above, there are concentric shells of liquid and nanoparticles arranged in such a way that the distance between two adjacent shells is roughly the diameter of the nanoparticle. In addition, we observe an enhancement of nanoparticle density at the surface of the droplet.

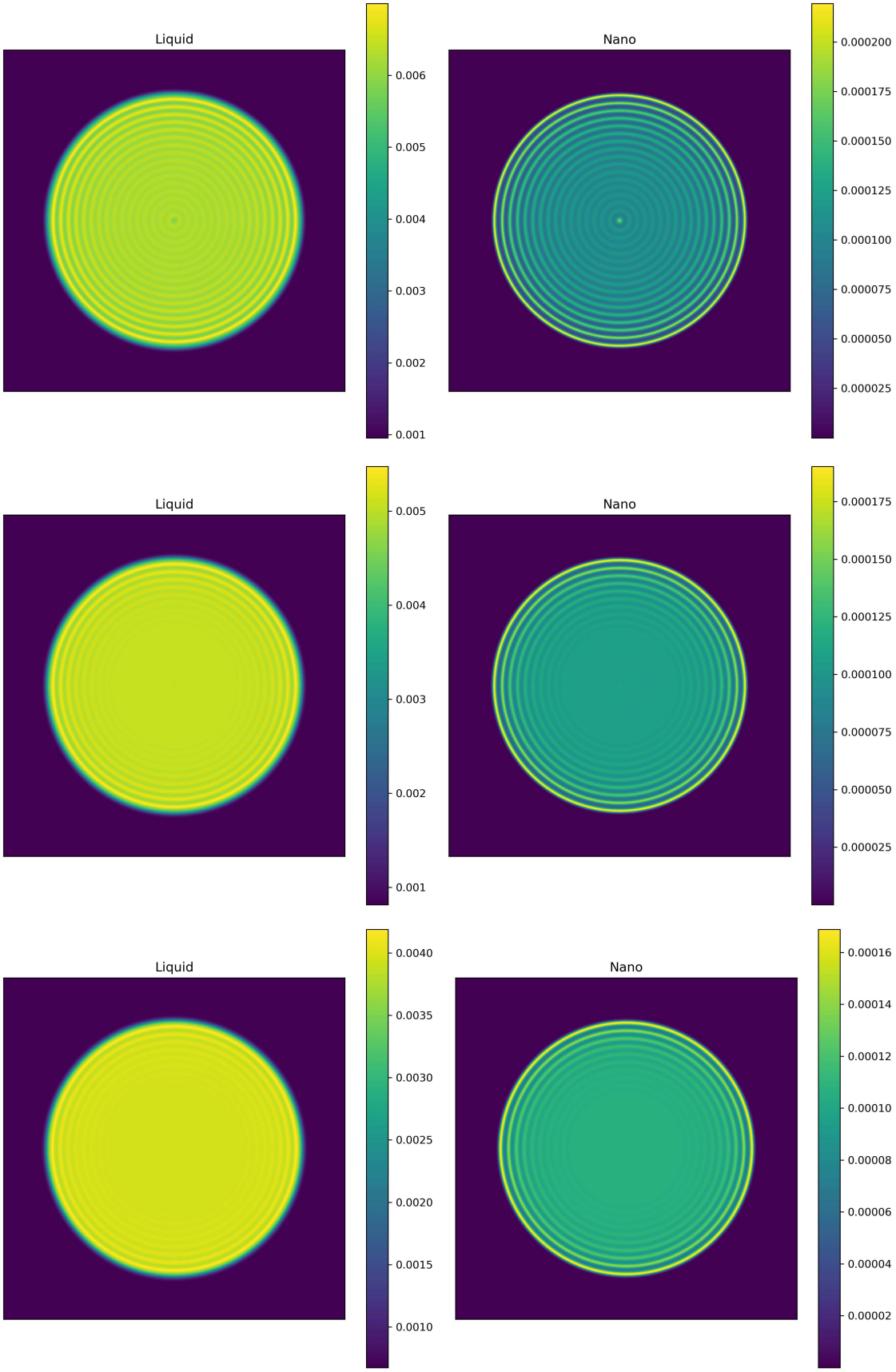

Figure 7.11: Heatmpas of a 10:1 droplet with SW model parameters $\epsilon_{nl} = 3.57$ and $\lambda_{nn} = 1.01$. The number of nanoparticles is $N_n = 8187$ with a droplet radius $\tilde{R} \approx 133$. Top H_r =70%, middle 60% and bottom 50%.

The example of $H_r = 70\%$ of Fig.7.11 also shows a constellation of nanoparticles with high density in the center of the droplet where the liquid particle must be therefore more absent.

Of course, our study does not provide any information about the time evolution of the nanoparticle laden droplet but instead describes its state in thermodynamic equilibrium. Hence, the density profiles we obtained and presented in Sec.7.4 must be understood as ensemble averages, i.e. averages that arise through constellations of solvent and solute particles preferred by the system. Since an ensemble average is equivalent to its time averaged pendant, former is attained when many constellations of the droplet constituents, compatible with the macro variables such as liquid density inside the droplet and droplet radius, are averaged over time. In turn, this also means that after a sufficiently long time the system will have evolved into one of these preferred states of the droplet through diffusion processes. The work of [137] has also applied dynamical density functional theory (DDFT) to capture the time evolution of droplet coalescence. It is finally also interesting to note that the Picard iteration performed in order to obtain equilibrium density profiles sort of provide quasi-dynamics. It is observed that both routes towards the equilibrium distribution display different intermediate stages where, of course, the quasi-dynamics of Picard iteration are considered to be a rough approximation of the true dynamics described by DDFT.

7.5 Conclusion

The section presented here demonstrates that a simple thermodynamic model of a droplet containing solute particles of varying sizes can serve as a theoretical framework to determine the equilibrium droplet size at a given humidity, see Sec.7.1. In addition, we employed continuum DFT calculations in Sec.7.4, which provide density profiles for solvent and solute particles, revealing intriguing internal structures within the droplet. For a smaller size ratio of 2:1 between solute and solvent particles, the profiles show structure primarily near the droplet surface. In contrast, for a 10:1 size ratio, density oscillations are observed throughout the droplet's interior, as illustrated in Fig.7.6 and Fig.7.8. Moreover, the liquid density required to stabilize the droplet is significantly lower in the 10:1 case compared to the 2:1 case, see Fig.7.5. This is because larger solute particles require fewer solvent particles to achieve equilibrium. When attractive interactions between solute particles are also present, even fewer solvent particles are needed, as evidenced in Fig.7.8, which also corresponds to a scenario where the Lorentz-Berthelot mixing rules are fulfilled.

Given the DFT-calculated density profiles, we can compare the predicted liquid density within the droplet or equivalently, the number of liquid particles it contains with the result from the minimized density profile. Fig.7.9 and Fig.7.10 show the number of liquid particles as a function of humidity. The agreement between the thermodynamic model discussed in Sec. 7.1 and the DFT results is compelling, particularly since the DFT analysis is essential to capturing the internal density structures.

The stability of nanoparticle-laden droplets can be effectively captured using classical density functional theory (DFT), provided that more sophisticated minimization algorithms are applied than those typically used. Given the known limitations of Fundamental Measure Theory (FMT) in treating strongly asymmetric hard-sphere mixtures with attractive forces, our investigation focused on a solute-solvent size ratio of 10:1. While

the DFT-derived density profiles exhibit pronounced inhomogeneities that contrast with the uniform assumption made in the thermodynamic model, the overall consistency between both approaches remains remarkably good. Notably, the observed nanoparticle enrichment near the interface of the droplet supports the hypothesis that such structures could facilitate the transmission of virus-laden aerosols, such as those containing SARS-CoV-2. This surface localization arises from interfacial free energy contributions between the droplet's interior, its surrounding vapor, and the embedded nanoparticles.

Our findings demonstrate that nanoparticles embedded within the droplet play a key role in preventing complete evaporation. The mutual attraction between the liquid constituents and the solutes, modeled via square-well potentials, enhances the internal pressure, allowing the droplet to achieve mechanical balance with the ambient gas. As a consequence, these stabilized structures can persist in air for extended periods, with their sedimentation timescales exceeding those of evaporation. This effect is particularly pronounced for droplets of moderate size containing an optimal concentration of nanoparticles. In conclusion, the mechanism we describe provides a plausible explanation for the unexpectedly long airborne survival of virus-containing droplets, offering insight into the high transmissibility of diseases like COVID-19 even in spaces unoccupied by infected individuals for several days.

Chapter 8

Final Remarks

This thesis outlined the machinery of classical density functional theory (cDFT) that is applied to problems in statistical physics of classical fluids. The system of hard spheres serves as a crucial reference system for interactions that include attractive forces, hence being able to describe a liquid and vapor state. Fundamental measure theory (FMT) is a powerful and practical framework to provide excess functionals for hard-sphere mixtures by using size and shape of the impenetrable constituents. State-of-the-art functionals such as White-Bear and White-Bear mark II yield accurate predictions on hard-sphere thermodynamic quantities merely depending on density compared to computer simulations, such as Monte-Carlo simulations.

One specific model for attractions we have employed is the square-well (SW) interaction that, due to its simplicity in terms of modeling and computational efficiency, is widely used to study classical fluids. In this thesis we applied the SW model to understand the interfacial properties between liquid and vapor and, in addition, interfaces of a binary SW mixture. The recent pandemic of SARS-Cov-2 raised the question how water droplets laden with viruses remain airborne for a very long time. Surprisingly, considering a SW binary mixture with spherical symmetry already enables us to study and predict stabilized droplets by making use of cDFT.

We begin in Ch.2 with the fundamental concepts in thermodynamics and statistical physics. Former must be understood as a consequence of the latter in regards of the fundamentally statistical nature of thermodynamical laws. Only in the thermodynamic limit do equilibrium properties of a system become valid. Thermal fluctuations caused by erratic motions of particles are negligible when it comes to macroscopic systems. This eminent observation of macroscopic systems is key in the development and comprehension of many-particle systems that can also undergo mutual interactions. In particular, it is intriguing to comprehend the emergence of macroscopic behavior and thermodynamic equilibrium given the fact that the microscopic properties are time reversible. This issue, also termed as Loschmidt's paradox, discusses how it is possible that time reversible, microscopic laws like Newton's equation of motion can lead to irreversible phenomena on a macroscopic scale, particularly the second law of thermodynamics, namely entropy.

In Sec.2.2 we introduce essential notions of statistical physics, such as the concept of phase space spanned by microscopic degrees of freedom of particles. It inevitably raises the question how a microscopic approach can be connected to quantities that are considered to be macroscopic, i.e. quantities which do not provide any information about a specific microscopic state of the system but instead resemble measures of the whole system, e.g. pressure P, temperature T or volume V. With the assumption of quasi-

ergodic behavior of macroscopic systems, at least for most under consideration, we are able to relate time-averaged observables to so-called ensemble-averaged observables. Latter, discussed in Sec.2.3, provide a powerful description of systems that are subject to an environment, considered to be much larger than the system of interest, prescribed by fixed thermodynamic quantities. The main object is the partition sum or partition function that contains all information of the system, i.e. in principle any thermodynamic quantity can be derived at equilibrium. We address three ensembles often used in statistical physics, the microcanonical, canonical and grand-canonical ensembles. They differ in the setup of the surrounding, macroscopic environment or heat bath that controls the system. We further attempt to relate the entropy notion of Shannon from information theory to entropy of statistical physics in Sec.2.4. By maximizing the entropy of information theory with imposed conditions connected to average values, the correct probability distributions of the classical ensembles are reproduced. We conclude this chapter by presenting models for simple liquids in Sec.2.5. The hard-sphere model is the simplest, non-trivial interaction and is purely of geometric nature. There are accurate equation of states for hard-sphere fluids on which attractive potentials such as the SW potential can be appended, i.e. we treat SW interactions as a perturbation around the hard-core repulsion. The Lennard-Jones potential is another widely used candidate for liquids where the hard-core repulsion on longer-ranged attraction is given by a power-law potential.

In Ch.3 we present the main concern of this thesis. Formerly developed and used for quantum mechanical systems such as an electron gas, classical density functional theory was also introduced for classical gases or liquids. Instead of taking into account all degrees of freedom, for instance coordinates of particles, cDFT is grounded on the uniqueness of the phase-space probability distribution with respect to an external potential imposed onto the system. Herewith, the one-body density distribution or density profile is obtained which encapsulates the thermodynamics of the system at equilibrium. However, calculating the density profiles requires knowing the excess functional containing all the information of non-trivial interactions when minimizing the grand functional. There are several ways to construct excess functionals which we present in Sec.3.8. For hard-sphere fluids, excess functionals are well-known and developed, see Sec.4.2.1. When it comes to other, more sophisticated interactions we are restricted to rather crude and approximative excess functionals, for example excess functionals given by the random-phase approximation which makes use of a mean-field ansatz. Latter only includes pairwise interactions which often times do not suffice to capture all correlations in dense fluids. Correlation functions play a crucial role by attempting to describe the structure of a fluid. In Sec.3.7 we show an important relationship between the correlation functions termed after Leonard Ornstein and Frits Zernike. Together with a so-called closure relation it enables to compute the structure factor which can, at the same time, be easily derived from scattering experiments. At last, we present key ideas of scaled-particle theory, Sec.3.9, that also provide important insights into hard-sphere mixtures.

Latter are well described within the framework of fundamental measure theory (FMT), Ch.4. The basic ingredients are weight functions that measure size and shape of the constituents. Especially, in the case of mixtures of hard spheres FMT serves as an effective tool to obtain the corresponding density profiles. Weighted densities as measures of how hard-sphere particles are distributed in a given volume with specific boundaries give rise to an excess free energy of hard spheres. Originally, the Rosenfeld functional is regarded as a benchmark functional for hard-sphere mixtures whose derivation is based on the ideas of scaled-particle theory and dimensional analysis. The one-dimensional system of hard

rods, for instance, can be exactly described by FMT using fundamental measures, see Sec.4.1. Surprisingly, the Rosenfeld functional yields the well-established Percus-Yevick correlation function and equation of state for a uniform fluid as we have presented in Sec.4.2.1. Further improvements on the equation of states of hard-sphere fluids allowed the construction of somewhat more accurate functionals, namely White-Bear and White-Bear mark II, see Sec.4.2.2. Secs.4.2.3 and 4.2.4 are two examples where the application of cDFT for hard spheres. The test-particle geometry is particularly of interest as it connects important thermodynamic quantities with the correlation functions obtained via cDFT. Especially, so-called equilibrium sum rules do provide valuable checks on accuracy and consistency of hard-sphere functionals.

In Ch.5 we first introduce the key ideas of Lutsko [93] to construct a new class of functionals by making use of dimensional crossover. Latter is an exact, limiting case of a single spherical cavity that can at most hold one particle. Thus, this limiting case can be imposed on hard-sphere functionals expressed in higher dimensions that, in principle, should reduce to the $D = 0$ case being termed dimensional crossover, see Sec.4.3. It is also possible to consider a system of two or three spherical cavities that can overlap with each other. With these constellations of spherical cavities, it is possible to reproduce the excess free energy functional of Rosenfeld only using weight functions common in FMT. The construction, however, deploys two free parameters A and B that determine whether the associated functional possesses stability and do alter the equation of state. It turns out that as long as $8A + 4B = 9$ is fulfilled the Percus-Yevick equation of state is recovered. In the case of $A, B > 0$ we know that explicit stability of the functional is guaranteed. Hence, the question can be raised if there is any way of choosing somehow optimal values for A and B. One possibility we have made use of is presented in Sec.5.2. By applying two equilibrium sum rules in the test-particle geometry, Sec.5.2.1, we can seek for values A and B such that the relative error between what is found in bulk thermodynamics and in DFT is minimal. Our main finding of Sec.5.2.2 is that the optimal point derived from these sum rules do not belong to the explicit class. More specifically, for the Lutsko functional proposed in [93] we find $A = 1.3$ and $B = -1.0$.

Inspired by the form of the Lutsko functional, we have next extended the underlying idea to the cases of White-Bear and White-Bear mark II in Sec.5.3. As these functionals are somewhat more accurate than the original Rosenfeld functional, it is tempting to incorporate the structure of the Lutsko functional for Φ_3 to White-Bear and White-Bear mark II. The stability conditions being discussed in [79] show that the stability of the Lutsko versions of the White-Bear functionals is not affected with respect to Lutsko's original proposal. Again, by employing the same sum rules of the test-particle geometry, we find $A = 1.35$ and $B = -0.85$ in the case of White-Bear, and $A = 1.25$ and $B = -0.20$ in the case of White-Bear mark II, see Sec.5.3.1. Note that these optimal points do also not allow for explicit stability again. In addition, not only are the equations of state changed, but also the consistency with respect to pressure is altered for values of A and B with $8A+4B \neq 9$. Especially for White-Bear mark II this has the effect of spoiling the consistency with respect to pressure that in the original version is satisfied for the one-component case. Nonetheless, we could improve upon the sum rules, most significantly in the case of White-Bear mark II. As it remains unclear to assess stability of the Lutsko functionals not belonging to the explicitly stable class, it is noteworthy to mention a specific system that can, at least, give some insights into stability, namely a small spherical cavity. It is found that for sufficiently high packing fractions, the Rosenfeld, White-Bear and White-Bear mark II functionals fail to remain stable when a minimization is

performed. Rather, using the empirical q_3-correction render these functionals applicable for highly confined spherical cavities. In contrary, when we attempt to minimize for the aforementioned optimized Lutsko functionals, no such instabilities occur.

Finally, in Ch.6 interesting applications of the simple SW model are discussed. We start with the main properties of a one-component SW fluid, e.g. liquid-vapor coexistence and its interface in Sec.6.1. We also plot the interfacial surface tension as a function of temperature and show that close to the critical point, the surface tension becomes vanishingly small. Furthermore, we present possible, smooth modifications to the SW potential by rendering its boundary at $r = \lambda\sigma$ continuous without overall changing the total free energy of the SW contribution. This retains the phase behavior of the SW fluid, however, changes its structure at the interface and the associated surface tension. Afterwards, we demonstrate several intriguing applications of a SW fluid within DFT in Sec.6.1.1, among others wetting at a spherical, attractive wall.

In Sec.6.2 we investigate binary SW mixtures on their interfacial properties. While the first component is regarded as a solvent, the second component (solute) is assumed to be very diluted. At phase coexistence, there are different ways how the solute accumulates around the interface. In particular, we can respect the mixing rules according to Berthelot and Lorentz which are motivated by dipole-dipole like interactions. The main observation is that the solubility attains its maximum at the interface, which becomes even more pronounced when an asymmetric mixture is considered. As we consider the dilute limit of the second component in our analysis, the solubility behavior can be also described by an effective potential solely acting on the solute particles, see Sec.6.2.5. This effective potential is, at the same time, closely related to the Widom insertion theorem by making use of the one-body correlation function. It turns out that the effective potential possesses a minimum close to the interface and assumes asymptotic values far inside the liquid and vapor regions of the solvent. This feature nicely illuminates the behavior of dilute solute particles close to an interface of a solvent.

We close the thesis in Ch.7 with a discussion and analysis of droplets suspended with solute particles. The recent pandemic caused by widely spreading infections of the Corona virus has ignited several scientific questions on contagious droplets. Especially the surprisingly long lifetime of such droplets, e.g. produced by breathing of infected persons, is addressed by our work stable droplets. Normally a pure liquid droplet is expected to completely evaporate due to its saturation vapor pressure which is higher than the pressure of surrounding vapor. This excess of pressure inside the droplet is caused by the curvature being prescribed by the Laplace-Young equation, connected to the Kelvin effect. However, inserting the right amount of attractive solute particles into the droplet reduces its saturation vapor pressure, allowing in principle for mechanical equilibrium. This reduction of saturation vapor pressure is explained by Raoult's law, stating that the solvent activity is lowered in the presence of solute particles. Entropic mixing (ideal mixing) alone already lowers the solvent's activity, and additional attractive forces between solvent and solutes augment this behavior even further. On-lattice calculations were performed by [137] where they could show that indeed droplets can be stabilized by the presence of solute particles. Our more precise study of Ch.7 in terms of quality of equation of state and also including structure of the droplet using continuum DFT shows the existence of such nanoparticle-laden droplets and, particularly, good agreement with the capillary approximation model underpinning our DFT calculations. For that, the amount of liquid particles of the interior of the droplet is calculated on the one hand using the model output of the capillary approximation and on the other hand what is

found by DFT. One main drawback of our study is the fact that we could only investigate a size ration of maximally 10:1 which is certainly not given in the real world. Actually, typical size rations between viruses and liquid particles is of the order 10,000. Given the deficiencies of FMT for highly or even extremely asymmetric mixtures our study is just in terms of computational feasibility and accuracy restricted to the cases we have analyzed so far.

To sum up the thesis, we have investigated the Lutsko functionals in Ch.5 together with the White-Bear versions by employing two equilibrium sum rules in the test-particle geometry. As these functionals contain two parameters, we could ask the question for which pairs of these parameters the sum rules are best fulfilled. In particular, we achieved improvements of these functionals with respect to the established functionals of Rosenfeld, White-Bear and White-Bear mark II in terms of equation of state, direct correlation function and stability property in confined geometries. In addition, we also considered an optimization scheme that employs the direct correlation function. Using exact Monte-Carlo data, we found new pairs of optimized parameters that differ from those obtained from the aforementioned sum rules. Further tasks regarding this branch of research might be an analysis of the optimal point for hard-sphere mixtures and, for instance, SW interactions. Certainly, other sum rules could provide valuable perspective on the optimized parameters. We then considered binary square-well mixtures in Ch.6 with the inclusion of the Lorentz-Berthelot mixing rule. Instead of employing the random-phase excess functional for attractive interactions, we used a novel functional for SW mixtures. This functional resembles the exact low-density limit for hard-spheres of FMT with corresponding weighted densities containing the interaction parameters of the SW interactions between the components. Although such an approach seems not to be necessary in the one-component or binary system case, due to the straightforward generalization to multi-component systems of FMT the novel functional we propose can be easily extended to SW mixtures respecting also the mixing rule mentioned before. We could show applications of this novel functional for a binary mixture with an interface of the solvent and a second, diluted component as solute that accumulates at the liquid-vapor interface. Finally, in Ch.7 we considered again a SW binary mixture, but now in spherical geometry. More specifically, we modeled and minimized a system within DFT that tries to understand the solution of nanoparticles inside a water droplet, with the effect of preventing the droplet to evaporate completely. Our DFT calculations were able to capture radially symmetric density distributions for solvent and solute particles by taking into account, among other parameters, the size ratio of solvent particle to solute particle. This is insofar important as in reality nanoparticles are roughly ten thousand times larger than water molecules. Our findings of DFT calculations show that the presence of solute particles is able to render it stable and, especially, do stay in agreement with the thermodynamic model of stable droplets. In future, it might be interesting to investigate also the dynamics of such droplets using powerful tools of DDFT. Taking into account orientational degrees of freedom into the interactions, as is the case for water, could even further improve the quality of such DFT calculations.

Appendix A

Functional Derivatives

In this chapter we provide various derivatives $\partial\Phi(\{n_\alpha\})/\partial n_\alpha$ of the Rosenfeld, White-Bear and White-Bear mark II functionals that are necessary in the calculation of $c^{(1)}(\mathbf{r})$. We furthermore include the tensorial derivatives of the Lutsko functional which also encapsulate the tensorial versions of Rosenfeld and White-Bear for $A = -B = 3/2$.

A.1 Rosenfeld

$$\Phi^{\mathrm{RF}} = -n_0 \log(1-n_3) + \frac{n_1 n_2 - \mathbf{n}_1\mathbf{n}_2}{1-n_3} + \frac{n_2^3 - 3n_2\mathbf{n}_2\mathbf{n}_2}{24\pi(1-n_3)^2} \tag{A.1}$$

$$\begin{aligned}
\frac{\partial\Phi^{\mathrm{RF}}}{\partial n_0} &= -\log(1-n_3) \\
\frac{\partial\Phi^{\mathrm{RF}}}{\partial n_1} &= \frac{n_2}{1-n_3} \\
\frac{\partial\Phi^{\mathrm{RF}}}{\partial n_2} &= \frac{n_1}{1-n_3} + \frac{n_2^2 - \mathbf{n_2}\mathbf{n_2}}{8\pi(1-n_3)^2} \\
\frac{\partial\Phi^{\mathrm{RF}}}{\partial n_3} &= \frac{n_0}{1-n_3} + \frac{n_1 n_2 - \mathbf{n}_1\mathbf{n}_2}{(1-n_3)^2} + \frac{n_2^3 - 3n_2\mathbf{n}_2\mathbf{n}_2}{12\pi(1-n_3)^3} \\
\frac{\partial\Phi^{\mathrm{RF}}}{\partial \mathbf{n}_1} &= -\frac{\mathbf{n}_2}{1-n_3} \\
\frac{\partial\Phi^{\mathrm{RF}}}{\partial \mathbf{n}_2} &= -\frac{\mathbf{n}_1}{1-n_3} - \frac{n_2\mathbf{n}_2}{4\pi(1-n_3)^2}
\end{aligned} \tag{A.2}$$

A.2 White-Bear

$$\Phi^{\mathrm{WB}} = -n_0 \log(1-n_3) + \frac{n_1 n_2 - \mathbf{n}_1\mathbf{n}_2}{1-n_3} + f(n_3)(n_2^3 - 3n_2\mathbf{n}_2\mathbf{n}_2) \tag{A.3}$$

$$f(n_3) = \frac{n_3 + (1-n_3)^2\log(1-n_3)}{36\pi n_3^2(1-n_3)^2}$$

$$
\begin{aligned}
\frac{\partial \Phi^{\mathrm{WB}}}{\partial n_0} &= -\log(1-n_3) \\
\frac{\partial \Phi^{\mathrm{WB}}}{\partial n_1} &= \frac{n_2}{1-n_3} \\
\frac{\partial \Phi^{\mathrm{WB}}}{\partial n_2} &= \frac{n_1}{1-n_3} + 3f(n_3)(n_2^2 - \mathbf{n_2}\mathbf{n_2}) \\
\frac{\partial \Phi^{\mathrm{WB}}}{\partial n_3} &= \frac{n_0}{1-n_3} + \frac{n_1 n_2 - \mathbf{n}_1\mathbf{n}_2}{(1-n_3)^2} + \frac{df(n_3)}{dn_3}(n_2^3 - 3n_2\mathbf{n}_2\mathbf{n}_2) \\
\frac{\partial \Phi^{\mathrm{WB}}}{\partial \mathbf{n}_1} &= -\frac{\mathbf{n}_2}{1-n_3} \\
\frac{\partial \Phi^{\mathrm{WB}}}{\partial \mathbf{n}_2} &= -\frac{\mathbf{n}_1}{1-n_3} - 6f(n_3)n_2\mathbf{n}_2 \\
\frac{df(n_3)}{dn_3} &= -\frac{n_3(2-5n_3+n_3^2) + 2(1-n_3)^3\log(1-n_3)}{36\pi(1-n_3)^3 n_3^3}
\end{aligned}
\tag{A.4}
$$

A.3 White-Bear Mark II

$$
\begin{aligned}
\Phi^{\mathrm{WBII}} &= -n_0\log(1-n_3) + \varphi_1(n_3)\frac{n_1n_2 - \mathbf{n}_1\mathbf{n}_2}{1-n_3} + \varphi_2(n_3)(n_2^3 - 3n_2\mathbf{n}_2\mathbf{n}_2) \\
\varphi_1(n_3) &= 1 + \frac{2n_3 - n_3^2 + 2(1-n_3)\log(1-n_3)}{3n_3} \\
\varphi_2(n_3) &= 1 - \frac{2n_3 - 3n_3^2 + 2n_3^3 + 2(1-n_3)^2\log(1-n_3)}{3n_3^2}
\end{aligned}
\tag{A.5}
$$

$$
\begin{aligned}
\frac{\partial \Phi^{\mathrm{WBII}}}{\partial n_0} &= -\log(1-n_3) \\
\frac{\partial \Phi^{\mathrm{WBII}}}{\partial n_1} &= \varphi_1(n_3)\frac{n_2}{1-n_3} \\
\frac{\partial \Phi^{\mathrm{WBII}}}{\partial n_2} &= \varphi_1(n_3)\frac{n_1}{1-n_3} + 3\varphi_2(n_3)(n_2^2 - \mathbf{n_2}\mathbf{n_2}) \\
\frac{\partial \Phi^{\mathrm{WBII}}}{\partial n_3} &= \frac{n_0}{1-n_3} + (n_1n_2 - \mathbf{n}_1\mathbf{n}_2)\left(\frac{\varphi_1(n_3)}{(1-n_3)^2} + \frac{1}{1-n_3}\frac{d\varphi_1(n_3)}{dn_3}\right) + \frac{d\varphi_2(n_3)}{dn_3}(n_2^3 - 3n_2\mathbf{n}_2\mathbf{n}_2) \\
\frac{\partial \Phi^{\mathrm{WBII}}}{\partial \mathbf{n}_1} &= -\varphi_1(n_3)\frac{\mathbf{n}_2}{1-n_3} \\
\frac{\partial \Phi^{\mathrm{WBII}}}{\partial \mathbf{n}_2} &= -\varphi_1(n_3)\frac{\mathbf{n}_1}{1-n_3} - 6\varphi_2(n_3)n_2\mathbf{n}_2 \\
\frac{d\varphi_1(n_3)}{dn_3} &= -\frac{n_3(2+n_3) + 2\log(1-n_3)}{3n_3^2} \\
\frac{d\varphi_2(n_3)}{dn_3} &= \frac{2(1-n_3)(n_3(2+n_3) + 2\log(1-n_3))}{3n_3^3}
\end{aligned}
\tag{A.6}
$$

A.4 Lutsko

Finally, we provide functional derivatives of the Lutsko functionals also including the White-Bear and White-Bear mark II versions by introducing two functions $\phi_1(n_3)$ and

$\phi_2(n_3)$. Hence, we obtain the original version of Lutsko's proposal by setting $\phi_1 = 1$ and $\phi_2 = 1/(24\pi(1-n_3)^2)$, the White-Bear extension by $\phi_1 = 1$ and $\phi_2 = f(n_3)$ and the White-Bear mark II extension by $\phi_1 = \varphi_1$ and $\phi_2 = \varphi_2$.

$$\Phi^{\mathrm{LK}} = -n_0 \log(1-n_3) + \phi_1(n_3)\frac{n_1 n_2 - \mathbf{n}_1\mathbf{n}_2}{1-n_3} + \phi_2(n_3)\mathcal{N}(A,B) \tag{A.7}$$

$$\mathcal{N}(A,B) = (A+B)n_2^3 - 3A\; n_2\mathbf{n}_2\cdot\mathbf{n}_2 + 3A\;\mathbf{n}_2\;\mathbf{T}\;\mathbf{n}_2 - 3B\; n_2 \mathrm{Tr}\,\mathbf{T}^2 + (2B-A)\mathrm{Tr}\,\mathbf{T}^3$$

$$\begin{aligned}
\frac{\partial \Phi^{\mathrm{LK}}}{\partial n_0} &= -\log(1-n_3) \\
\frac{\partial \Phi^{\mathrm{LK}}}{\partial n_1} &= \phi_1(n_3)\frac{n_2}{1-n_3} \\
\frac{\partial \Phi^{\mathrm{LK}}}{\partial n_2} &= \phi_1(n_3)\frac{n_1}{1-n_3} + 3\phi_2(n_3)((A+B)n_2^2 - A\mathbf{n_2}\mathbf{n_2} - B\mathrm{Tr}\,\mathbf{T}^2) \\
\frac{\partial \Phi^{\mathrm{LK}}}{\partial n_3} &= \frac{n_0}{1-n_3} + (n_1 n_2 - \mathbf{n}_1\mathbf{n}_2)\left(\frac{\phi_1(n_3)}{(1-n_3)^2} + \frac{1}{1-n_3}\frac{d\phi_1(n_3)}{dn_3}\right) + \frac{d\phi_2(n_3)}{dn_3}\mathcal{N}(A,B) \\
\frac{\partial \Phi^{\mathrm{LK}}}{\partial \mathbf{n}_1} &= -\phi_1(n_3)\frac{\mathbf{n}_2}{1-n_3} \\
\frac{\partial \Phi^{\mathrm{LK}}}{\partial \mathbf{n}_2} &= -\phi_1(n_3)\frac{\mathbf{n}_1}{1-n_3} - 6A\phi_2(n_3)(n_2\mathbf{n}_2 - \mathbf{T}\mathbf{n}_2) \\
\frac{\partial \Phi^{\mathrm{LK}}}{\partial \mathbf{T}} &= 3\phi_2(n_3)(A\mathbf{n}_2\otimes\mathbf{n}_2 - 2Bn_2\mathbf{T} + (2B-A)\mathbf{T}^2)
\end{aligned} \tag{A.8}$$

Appendix B

Weigthed Densities

Here, we provide calculations of the weighted densities n_α of FMT as convolutional integrals in real space. However, due to the convolution theorem a convolution in real space is a simple product of the corresponding Fourier transforms in Fourier space coming along with numerical efficiency. Nonetheless, it is also valuable to see detailed steps that are needed to perform these convolutions in real space for different geometrical setups.

B.1 Hard Rods

The computation of weighted densities in the case of one-dimensional hard spheres or hard rods is straightforward as only two of them have to be calculated with a rather simple functional form.

The first weighted density $n_0(z)$ is given by

$$n_0(z) = \int dz'\, \rho(z')\omega_0(z - z'), \tag{B.1}$$

where $\omega_0(z)$ is the weight function given in Eq.(4.3). Thus, we find

$$\begin{aligned} n_0(z) &= \frac{1}{2}\int dz'\, \rho(z')\left(\delta(R - z + z') + \delta(R + z - z')\right) \\ &= \frac{1}{2}\left(\rho(z - R) + \rho(z + R)\right). \end{aligned} \tag{B.2}$$

In the same way, by using the weight function $\omega_1(z)$ in Eq.(4.4) we have

$$\begin{aligned} n_1(z) &= \int dz'\, \rho(z')\Theta(R - |z - z'|) \\ &= \int^{z} dz'\, \rho(z')\Theta(R - z + z') + \int_{z} dz'\, \rho(z')\Theta(R + z - z') \\ &= \int_{z-R}^{z} dz'\, \rho(z') + \int_{z}^{z+R} dz'\, \rho(z') \\ &= \int_{z-R}^{z+R} dz'\, \rho(z'), \end{aligned} \tag{B.3}$$

where on the second line we separated the integration region in to two parts $z' < z$ and $z' > z$, and made use of the definition of the Heaviside-function on the third line. In total,

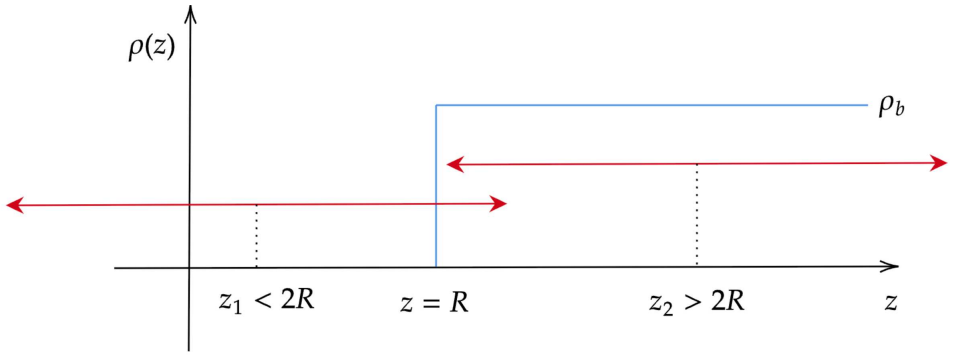

Figure B.1: Two convolutions of the staircase density profile evaluated at points z_1 and z_2 with partial and total overlapping, respectively.

$n_1(z)$ is a convolution of the density profile $\rho(z)$ with a constant kernel of length $2R$. To illuminate the convolutional computation, let us introduce a simple staircase-like density profile of the form $\rho(z) = \rho_b\Theta(z-R)$ which is often employed as an initialization for hard rods minimization at a hard wall. In Fig.B.1 we display two convolutions of Eq.(B.3) for two points z_1 and z_2. Due to the Heaviside-function in the definition of $\rho(z)$, latter attains the value ρ_b for points $z > R$. The red lines of Fig.B.1 indicate the corresponding integration regions of the points z_1 and z_2 with the property that for the former point only a partial overlap with the blue rectangle occurs whereas for the latter point a full overlap is given.

Therefore, we find for the weighted density $n_0(z)$ of Eq.(B.2)

$$n_0(z) = \begin{cases} 0, & \text{if} \quad z < 0 \\ \frac{1}{2}\rho_b, & \text{if} \quad z < 2R \\ \rho_b, & \text{otherwise.} \end{cases} \tag{B.4}$$

For $n_1(z)$, again, we have to take care of the regions of integration. Starting with the simplest case of $z < 0$ we see that there is no contribution to $n_1(z)$ at all as the upper integration boundary $z + R$ is smaller than R, i.e. the associated red integration line of Fig.B.1 would not overlap with the bulk region. If we have $0 < z < 2R$, then only the overlap from R to $z + R$ contributes to the integral, i.e.

$$\int_R^{z+R} dz'\, \rho_b = z\rho_b. \tag{B.5}$$

Finally, for points z with $z > 2R$ we have full overlap and the corresponding integral becomes

$$\int_{z-R}^{z+R} dz'\rho_b = 2R\rho_b = \text{const.} \tag{B.6}$$

Hence, the weighted density $n_1(z)$ reads in total

$$n_1(z) = \begin{cases} 0, & \text{if} \quad z < 0 \\ z\rho_b, & \text{if} \quad 0 < z < 2R \\ 2R\rho_b, & \text{otherwise.} \end{cases} \tag{B.7}$$

If we took an initial point z with the corresponding integration line partially overlapping with the bulk region and shift it from left to right we would increase the overlap such that the area beneath the bulk region, which is just $n_1(z)$, would also increase linearly.

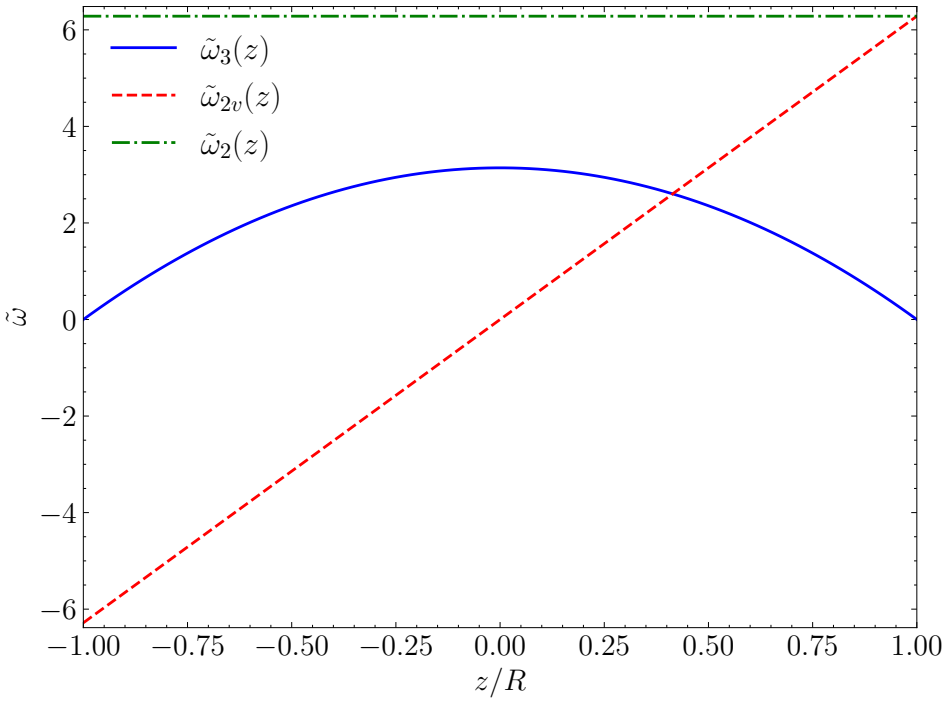

Figure B.2: The three kernels $\tilde{\omega}_3(z)$, $\tilde{\omega}_{2v}(z)$ and $\tilde{\omega}_2(z)$ of the planar geometry depicted in the range $-R \leq x \leq R$.

B.2 Planar Geometry

The planar geometry possesses a symmetry along the z-axis, i.e. an interface, spanned by the x and y coordinates, is only subject to changes when the perpendicular distance to that interface is varied. This fact simplifies the calculation of the weighted densities $n_\alpha(z)$ tremendously. It turns out that due to the underlying symmetry the previously three dimensional convolution can be reduced to an effectively one dimensional one, i.e.

$$n_\alpha(\mathbf{r}) = \sum_i \int d\mathbf{r}\, \rho_i(\mathbf{r}')\omega_\alpha^i(\mathbf{r}-\mathbf{r}') \longrightarrow \sum_i \int dz'\, \rho_i(z')\tilde{\omega}_\alpha^i(z-z'). \tag{B.8}$$

Thus, additional degrees of freedom are integrated out and we are left with effective weight functions $\tilde{\omega_\alpha^i}(z)$. We start with the weighted density $n_3(\mathbf{r})$ assuming that $\rho(\mathbf{r}) = \rho(z)$ and $\mathbf{r} = r\mathbf{e}_z$

$$\begin{aligned} n_3(\mathbf{r}) &= \int d\mathbf{r}'\, \rho(\mathbf{r}')\Theta(R - |\mathbf{r}-\mathbf{r}'|) \\ &= \int_0^\infty dr' r' \int_0^{2\pi} d\varphi' \int_{-\infty}^{\infty} dz'\, \rho(z')\Theta(R - \sqrt{r'^2 + (z-z')^2}) \\ &= 2\pi \int_{R\geq|z-z'|} dz' \rho(z') \int_0^{\sqrt{R^2-(z-z')^2}} dr'\, r' \\ &= \pi \int_{z-R}^{z+R} dz'\, \rho(z')(R^2 - (z-z')^2) \end{aligned} \tag{B.9}$$

from which we can read off the effectively one-dimensional kernel

$$\tilde{\omega}_3(z) = \pi(R^2 - z^2) \tag{B.10}$$

and can conclude that n_3 also only depends on z. The vectorial weighted density $\mathbf{n}_2(z)$ can be easily computed through the simple relation $\mathbf{n}_2(z) = -\partial_z n_3(z)\mathbf{e}_z$ giving

$$\mathbf{n}_2(z) = 2\pi \int_{z-R}^{z+R} dz'\, \rho(z')(z - z')\mathbf{e}_z \tag{B.11}$$

and with the kernel

$$\tilde{\omega}_{2v}(z) = 2\pi z. \tag{B.12}$$

It should be noted that in the derivative $\partial_z n_3(z)$ we obtain a contribution from the integration boundaries of Eq.(B.9). However, since the kernel $\tilde{\omega}_3(z)$ is symmetric with respect to z this term vanishes.

Finally, the calculation of the last independent weighted density $n_2(z)$ goes along with that of $n_3(z)$, however, the Heaviside-function now replaced with the Dirac-Delta

$$\begin{aligned} n_2(z) &= \int_0^\infty dr' r' \int_0^{2\pi} d\varphi' \int_{-\infty}^{\infty} dz'\, \rho(z')\delta(R - \sqrt{r'^2 + (z - z')^2}) \\ &= 2\pi \int_{R\geq|z-z'|} dz'\, \rho(z') \int_0^\infty dr' r' \,\frac{R}{r'}\delta(r' - \sqrt{R^2 - (z - z')^2}) \\ &= 2\pi R \int_{z-R}^{z+R} dz'\, \rho(z') \end{aligned} \tag{B.13}$$

and thus

$$\tilde{\omega}_2(z) = 2\pi R. \tag{B.14}$$

In Fig.B.2 we show the effective kernels in the interval $x \in [-R, R]$. While $\tilde{\omega}_3(z)$ and $\tilde{\omega}_2(z)$ are even functions of z, $\tilde{\omega}_{2v}(z)$ is odd which is expected as the vectorial weighted density $\mathbf{n}_2(z)$ must be zero when the bulk of the system is reached, i.e. $\rho(z) \to \rho_b$ becomes constant.

At last, it remains to provide an expression for the tensorial weighted density $\mathbf{T}$ with the weight function $w_T = \mathbf{e}_r \otimes \mathbf{e}_r\, \delta(R - |\mathbf{r}|)$. Again, making use of axial symmetry, i.e. $\mathbf{r} = r\mathbf{e}_z$, off-diagonal elements of w_T vanish due to the φ'-integrations, so we are left with

$$\mathbf{T}(z) = \int_{-\infty}^{\infty} dz'\rho(z') \int_0^\infty dr' r' \int_0^{2\pi} d\varphi' \frac{\mathrm{diag}(r'^2\cos^2\varphi', r'^2\sin^2\varphi', (z - z')^2)}{r'^2 + (z - z')^2} \delta\left(R - \sqrt{r'^2 + (z - z')^2}\right) \tag{B.15}$$

$$\begin{aligned} &= \int_{R\geq|z-z'|} dz'\rho(z') \int_0^\infty dr' r' \frac{\mathrm{diag}(\pi r'^2, \pi r'^2, 2\pi(z - z')^2)}{r'^2 + (z - z')^2} \frac{R}{r'} \delta\left(r' - \sqrt{R^2 - (z - z')^2}\right) \\ &= \frac{1}{R} \int_{z-R}^{z+R} dz'\rho(z')\, \mathrm{diag}(\pi(R^2 - (z - z')^2), \pi(R^2 - (z - z')^2), 2\pi(z - z')^2) \\ &= \mathrm{diag}(\frac{n_3(z)}{R}, \frac{n_3(z)}{R}, n_2(z) - \frac{2n_3(z)}{R}). \end{aligned}$$

Thus, the tensorial weighted density $\mathbf{T}(z)$ reduces to its diagonal components represented by the weighted densities $n_3(z)$ and $n_2(z)$ in the planar geometry.

B.3 Spherical Geometry

Similar to the planar case, the weighted densities in spherical geometry such as those arising from a spherical boundary or a test particle fixed at the origin can be reformu-

lated using effectively one-dimensional weight functions $\tilde{\omega}_\alpha(r)$, which, due to spherical symmetry, depend solely on the radial coordinate r.

We begin with the definition of the scalar weighted density $n_2(\mathbf{r})$:

$$n_2(\mathbf{r}) = \int d\mathbf{r}'\, \rho(\mathbf{r}')\omega_2(\mathbf{r}-\mathbf{r}'), \tag{B.16}$$

with the weight function $\omega_2(\mathbf{r}) = \delta(R-|\mathbf{r}|)$. Exploiting the spherical symmetry, we can fix $\mathbf{r} = r\hat{e}z$, and parametrize $\mathbf{r}'$ in spherical coordinates as

$$\mathbf{r}' = \left(r'\cos\phi'\sin\theta'\ \ r'\sin\phi'\sin\theta'\ \ r'\cos\theta'\right). \tag{B.17}$$

The Euclidean distance between $\mathbf{r}$ and $\mathbf{r}'$ is then given by

$$|\mathbf{r}-\mathbf{r}'| = \sqrt{r^2+r'^2-2rr'\cos\theta'}. \tag{B.18}$$

Substituting into Eq.(B.16), we obtain

$$n_2(\mathbf{r}) = 2\pi\int_0^\infty dr'\, r'^2\rho(r')\int_{-1}^1 d\cos\theta'\,\delta\left(R-\sqrt{r^2+r'^2-2rr'\cos\theta'}\right). \tag{B.19}$$

The θ'-integration can be carried out using the identity

$$\delta(f(x)) = \sum_i \frac{\delta(x-x_i)}{|f'(x_i)|}, \tag{B.20}$$

where x_i are the simple roots of $f(x)$ with $f'(x_i)\neq 0$.

The root of the argument of the delta function in Eq.(B.19) is given by

$$\cos\theta_0 = \frac{r^2+r'^2-R^2}{2rr'}, \tag{B.21}$$

which imposes a constraint on the integration range of r'. Since $\cos\theta_0 \in [-1,1]$, Eq.(B.21) implies:

$$|r-R| \le r' \le r+R. \tag{B.22}$$

Evaluating the delta function yields

$$n_2(\mathbf{r}) = 2\pi\int_{|r-R|}^{r+R} dr'\, r'^2\rho(r')\int_{-1}^1 d\cos\theta'\,\frac{R}{rr'}\delta(\cos\theta'-\cos\theta_0), \tag{B.23}$$

so the final expression for n_2 becomes

$$n_2(\mathbf{r}) = \frac{2\pi R}{r}\int_{|r-R|}^{r+R} dr'\, r'\rho(r'). \tag{B.24}$$

The weighted density $n_3(\mathbf{r})$ is defined analogously via the Heaviside step function:

$$n_3(\mathbf{r}) = \int d\mathbf{r}'\,\rho(\mathbf{r}')\omega_3(\mathbf{r}-\mathbf{r}'), \quad \text{with} \quad \omega_3(\mathbf{r}) = \theta(R-|\mathbf{r}|). \tag{B.25}$$

This leads to

$$n_3(\mathbf{r}) = \frac{\pi}{r}\int_{|r-R|}^{r+R} dr'\, r'\rho(r')\left(R^2-(r-r')^2\right). \tag{B.26}$$

The vectorial weighted density $\mathbf{n}_2(\mathbf{r})$ follows from the gradient of $n_3(\mathbf{r})$ as

$$\begin{aligned}\mathbf{n}_2(\mathbf{r})\cdot\mathbf{e}_r &= -\partial_r n_3(\mathbf{r}) \\ &= \frac{n_3(\mathbf{r})}{r} - \frac{\pi}{r}\partial_r \int_{|r-R|}^{r+R} dr'\, r'\rho(r')\left(R^2-(r-r')^2\right) \\ &= \frac{n_3(\mathbf{r})}{r} + \frac{2\pi}{r}\int_{|r-R|}^{r+R} dr'\, r'\rho(r')(r-r'),\end{aligned} \tag{B.27}$$

where, in going to the third line, we used that the integrand vanishes at the integration boundaries.

The tensorial weighted density follows a similar derivation to that of $n_2(\mathbf{r})$, with the added complexity of including the tensor product $\mathbf{e}_r\otimes\mathbf{e}_r$. Using the above parametrization, we obtain:

$$\mathbf{T} = \int_0^\infty dr'\, r'^2 \int_{-1}^1 d\cos\theta' \, \frac{\operatorname{diag}\left(\pi r'^2\sin^2\theta',\, \pi r'^2\sin^2\theta',\, 2\pi(r'\cos\theta'-r)^2\right)}{r^2+r'^2-2rr'\cos\theta'}\,\rho(r')\delta(R-|\mathbf{r}-\mathbf{r}'|). \tag{B.28}$$

Due to spherical symmetry, all off-diagonal components vanish after ϕ' integration, so the tensor becomes diagonal:

$$\mathbf{T} = \operatorname{diag}(t_1(r),\, t_1(r),\, t_2(r)), \tag{B.29}$$

with components

$$t_1(r) = \pi\int_0^\infty dr'\, r'^2\int_{-1}^1 d\cos\theta' \frac{r'^2\sin^2\theta'}{r^2+r'^2-2rr'\cos\theta'}\rho(r')\delta(R-|\mathbf{r}-\mathbf{r}'|), \tag{B.30}$$

$$t_2(r) = 2\pi\int_0^\infty dr'\, r'^2\int_{-1}^1 d\cos\theta' \frac{(r'\cos\theta'-r)^2}{r^2+r'^2-2rr'\cos\theta'}\rho(r')\delta(R-|\mathbf{r}-\mathbf{r}'|). \tag{B.31}$$

After performing the $\cos\theta'$ integration, the final expressions read:

$$t_1(r) = \frac{\pi}{R}\int_{|r-R|}^{r+R} dr'\, r'\rho(r')\left[\frac{r'}{r^2}\left(R^2-(r-r')^2\right) - \frac{1}{4r^3}\left((r-r')^2-R^2\right)^2\right], \tag{B.32}$$

$$t_2(r) = \frac{2\pi}{R}\int_{|r-R|}^{r+R} dr'\, r'\rho(r')\left[\frac{1}{4r^3}\left((r-r')^2-R^2\right)^2 - \frac{1}{r^2}(r-r')\left((r-r')^2-R^2\right) + \frac{1}{r}(r-r')^2\right]. \tag{B.33}$$

Finally, we note that the components are related through the scalar weighted density $n_2(r)$:

$$t_1(r) = \frac{1}{2}\left(n_2(r) - t_2(r)\right), \tag{B.34}$$

so only $t_2(r)$ needs to be explicitly evaluated.

Appendix C

Correlation functions of Lutsko Functionals

C.1 Convolution of Weight Functions

We want to evaluate the convolutions of the weight-functions ω_α given by

$$\omega_\alpha \otimes \omega_\beta(\mathbf{r}-\mathbf{r}') = \int d\mathbf{r}''\, \omega_\alpha(\mathbf{r}-\mathbf{r}'')\omega_\beta(\mathbf{r}'-\mathbf{r}''). \tag{C.1}$$

Note that Eq.(C.1) is strictly speaking not a proper convolution insofar as the order of the argument of one of the integrands must be reversed. Without loss of generality we can choose both $\mathbf{r}$ and $\mathbf{r}'$ being aligned on the z-axis

$$\mathbf{r} = 0, \quad \mathbf{r}' = d\,\mathbf{e}_z, \tag{C.2}$$

so d is the distance of the two particles.

- $\omega_3 \otimes \omega_3$

  The convolution of ω_3 with itself can be visualized as two spheres of radii R having a distance d to each other. For $d \leq 2R$ there is an intersection of both and hence we expect the convolution to give the volume of it. If $d > 2R$ there is no intersection and therefore a vanishing convolution. We have

  $$\int d\mathbf{r}\, \Theta(R-|\mathbf{r}|)\Theta(R-|\mathbf{r}-\mathbf{d}|),$$

  i.e. we only get a contribution if both step-functions are 1 at the same time. This restricts the integration regions of the volume integral. From the first step-function we get the condition

  $$r \leq R$$

  and from the second

  $$r^2 + d^2 - 2rd\cos\theta \leq R^2.$$

  From the latter inequality we obtain a lower boundary for $\cos\theta$

  $$\cos\theta \geq \frac{r^2+d^2-R^2}{2rd}.$$

But, it must also hold

$$\frac{r^2+d^2-R^2}{2rd} \leq 1 \quad \leftrightarrow \quad R^2 \geq (r-d)^2,$$

giving in total the boundaries for r

$$d-R \leq r \leq R.$$

Therefore, we have

$$\begin{aligned}\omega_3 \otimes \omega_3 &= 2\pi \int_{d-R}^{R} dr\, r^2 \int_{\frac{r^2+d^2-R^2}{2rd}}^{1} d\cos\theta \\ &= \frac{\pi}{d}\int_{d-R}^{R} dr\, r(R^2-(r-d)^2) \\ &= \frac{4\pi}{3}R^3 - \pi R^2 d + \frac{\pi}{12}d^3.\end{aligned}$$

As we expect, if $d=0$ we obtain the volume of a sphere of radius R and for $d \geq 2R$ (no overlap) 0.

- $\omega_3 \otimes \omega_2$

Here we have

$$\int d\mathbf{r}\, \Theta(R-|\mathbf{r}|)\delta(R-|\mathbf{r}-\mathbf{d}|),$$

or being written explicitly

$$2\pi \int_0^\infty dr\, r^2 \int_{-1}^{1} d\cos\theta\, \Theta(R-r)\delta\left(R-(r^2+d^2-2rd\cos\theta)^{1/2}\right).$$

Again, we have $r \leq R$ and the δ-function can be rewritten as

$$\delta\left(R-(r^2+d^2-2rd\cos\theta)^{1/2}\right) = \frac{R}{rd}\delta(\cos\theta_0-\cos\theta),$$

where

$$\cos\theta_0 = \frac{r^2+d^2-R^2}{2rd} \leq 1.$$

Hence, similarly to $\omega_3 \otimes \omega_3$ we have the boundaries $d-R \leq r \leq R$ so it follows

$$\begin{aligned}\omega_3 \otimes \omega_2 &= 2\pi \int_{d-R}^{R} dr\, r \int_{-1}^{1} d\cos\theta\, \frac{R}{d}\delta(\cos\theta_0-\cos\theta) \\ &= \frac{2\pi R}{d}\int_{d-R}^{R} dr\, r \\ &= 2\pi R^2\left(1-\left(\frac{d}{2R}\right)^2\right).\end{aligned}$$

- $\omega_2 \otimes \omega_2$

Here we have to convolute two δ-functions

$$\int d\mathbf{r}\, \delta(R-|\mathbf{r}|)\delta(R-|\mathbf{r}-\mathbf{d}|).$$

The first δ-function fixes $r = R$, i.e. we can set r to R in the integrand. The second is evaluated similarly to the $\omega_3 \otimes \omega_2$ case

$$\begin{aligned}\omega_2 \otimes \omega_2 &= 2\pi \int_0^\infty dr\, r^2 \int_{-1}^1 d\cos\theta\, \delta(R-r)\delta\left(R - (r^2+d^2-2rd\cos\theta)^{1/2}\right) \\ &= 2\pi R^2 \frac{R}{Rd} \\ &= \frac{2\pi R^2}{d}.\end{aligned}$$

C.2 Direct Correlation Function of Lutsko Functionals

Within the framework of FMT, the direct correlation function (DCF) is given by convolutions of the weight-functions ω_α

$$\begin{aligned}c^{(2)}(\mathbf{r}-\mathbf{r}') &\equiv -\left.\frac{\delta^2\beta\mathcal{F}_{ex}[\rho]}{\delta\rho(\mathbf{r})\delta\rho(\mathbf{r}')}\right|_{bulk} \\ &= -\sum_{\alpha,\beta} \frac{\partial^2\Phi(\{n_\alpha\})}{\partial n_\alpha \partial n_\beta}\, \omega_\alpha \otimes \omega_\beta(\mathbf{r}-\mathbf{r}'),\end{aligned} \tag{C.3}$$

where we use the notation

$$\omega_\alpha \otimes \omega_\beta(\mathbf{r}-\mathbf{r}') = \int d\mathbf{r}''\, \omega_\alpha(\mathbf{r}-\mathbf{r}'')\omega_\beta(\mathbf{r}'-\mathbf{r}''). \tag{C.4}$$

It is easiest to perform these convolutions between the weight-functions in Fourier-space as they become simple products.
The sum in Eq.(C.3) has many contributions which can be drastically simplified when considering a mono-component system. We consider the free energy density proposed by Lutsko, Eq.(5.19)

$$\begin{aligned}\Phi^{\mathrm{LK}} = -n_0\log(1-n_3) + \frac{n_1n_2 - \mathbf{n}_1\mathbf{n}_2}{1-n_3} + \\ f(n_3)\left((A+B)n_2^3 - 3An_2\mathbf{n}_2^2 + 3A\mathbf{n}_2\mathbf{T}\mathbf{n}_2 - 3Bn_2\,\mathrm{tr}(\mathbf{T}^2) + (2B-A)\mathrm{tr}(\mathbf{T}^3)\right),\end{aligned} \tag{C.5}$$

where we have introduced the function $f(n_3)$ for convenience. For the Lutsko functional we of course have

$$f(n_3) = \frac{1}{24\pi(1-n_3)^2}. \tag{C.6}$$

In contrast to Lutsko's writing, we have already introduced the more common weighed densities n_α. We would like to rearrange Eq.(C.5) such that tensor contributions are separated

$$\begin{aligned}\Phi^{\mathrm{LK}} &= \Phi_{\mathrm{nt}} + \Phi_{\mathrm{t}}, \\ \Phi_{\mathrm{nt}} &= -n_0\log(1-n_3) + \frac{n_1n_2 - \mathbf{n}_1\mathbf{n}_2}{1-n_3} + f(n_3)\left((A+B)n_2^3 - 3An_2\mathbf{n}_2^2\right) \\ \Phi_{\mathrm{t}} &= f(n_3)\left(3A\mathbf{n}_2\mathbf{T}\mathbf{n}_2 - 3Bn_2\,\mathrm{tr}(\mathbf{T}^2) + (2B-A)\mathrm{tr}(\mathbf{T}^3)\right).\end{aligned} \tag{C.7}$$

Using the short-hand notation

$$\chi^{(ij)} \equiv \frac{\partial^2 \Phi}{\partial n_i \partial n_j} \tag{C.8}$$

the DCF related to Φ_{nt} can be computed employing the result of [62]

$$\begin{aligned} -c_{\mathrm{nt}}^{(2)}(r) = \chi^{(33)}\,\omega_3 \otimes \omega_3 + 2\chi^{(23)}\,\omega_3 \otimes \omega_2 + 2\chi^{(13)}\,\omega_3 \otimes \omega_1 + \\ \chi^{(22)}\,\omega_2 \otimes \omega_2 + \chi^{(2v2v)}\,\underline{\omega}_2 \otimes \underline{\omega}_2 + 2\chi^{(03)}\,\left(\omega_3 \otimes \omega_0 + \omega_2 \otimes \omega_1 - \underline{\omega}_2 \otimes \underline{\omega}_1\right), \end{aligned} \tag{C.9}$$

where it has been used that $\omega_\alpha \otimes \omega_\beta = \omega_\beta \otimes \omega_\alpha$ for mono-component systems. Notice that due to the appearance of A and B in Φ_{nt} it does not hold $\chi^{(22)} = -\chi^{(2v2v)}$ anymore. The contribution to the DCF regarding the tensor parts reads as follows

$$\begin{aligned} -c_{\mathrm{t}}^{(2)}(r) = \chi^{(33)}\,\omega_3 \otimes \omega_3 + \chi^{(2v2v)}\,\underline{\omega}_2 \otimes \underline{\omega}_2 + \chi^{(TT)}\,\omega_T \otimes \omega_T + 2\chi^{(23)}\,\omega_3 \otimes \omega_2 + \\ 2\chi^{(T3)}\,\omega_T \otimes \omega_3 + 2\chi^{(T2)}\,\omega_T \otimes \omega_2. \end{aligned} \tag{C.10}$$

To be more precise, the tensor-tensor term in Eq.(C.10) for instance is written as

$$\frac{\partial^2 \Phi_{\mathrm{t}}}{\partial T_{ij} \partial T_{kl}}\,(\omega_T)_{ij} \otimes (\omega_T)_{kl}, \tag{C.11}$$

where Einstein's sum convention is used. Hence, the vector- and tensor-like derivatives can be evaluated

$$\begin{aligned} \frac{\partial^2 \Phi_{\mathrm{t}}}{\partial \underline{n}_{2i} \underline{n}_{2j}} &= 3Af(\eta) \frac{\partial^2}{\partial \underline{n}_{2i} \underline{n}_{2j}} \underline{n}_{2k} T_{kl} \underline{n}_{2l} \\ &= 3Af(\eta) \frac{\partial}{\partial \underline{n}_{2i}} \left(\delta_{jk} T_{kl} \underline{n}_{2l} + \underline{n}_{2k} T_{kl} \delta_{jl}\right) \\ &= 3Af(\eta) \left(\delta_{jk}\delta_{il} + \delta_{jl}\delta_{ik}\right) T_{kl} \\ &= 6Af(\eta) T_{ij}, \end{aligned} \tag{C.12}$$

which together with $T_{ij} = \eta/R\,\delta_{ij}$ in the bulk simplifies to

$$\frac{\partial^2 \Phi_{\mathrm{t}}}{\partial \underline{n}_{2i} \underline{n}_{2j}} = 6Af(\eta) \frac{\eta}{R} \delta_{ij}. \tag{C.13}$$

Then, we have

$$\begin{aligned} \frac{\partial^2 \Phi_{\mathrm{t}}}{\partial n_2 \partial T_{ij}} &= -3Bf(\eta) \frac{\partial^2}{\partial n_2 \partial T_{ij}} n_2 T_{kl} T_{lk} \\ &= -3Bf(\eta) \frac{\partial}{\partial T_{ij}} T_{kl} T_{lk} \\ &= -3Bf(\eta) \left(\delta_{ik}\delta_{jl} T_{lk} + \delta_{il}\delta_{jk} T_{kl}\right) \\ &= -6Bf(\eta) T_{ij}, \end{aligned} \tag{C.14}$$

thus

$$\frac{\partial^2 \Phi_{\mathrm{t}}}{\partial n_2 \partial T_{ij}} = -6Bf(\eta) \frac{\eta}{R} \delta_{ij}. \tag{C.15}$$

Using

$$\frac{\partial}{\partial T_{ij}} \operatorname{tr} \mathbf{T}^3 = 3\, T_{im} T_{mj} \to 3 \left(\frac{\eta}{R}\right)^2 \delta_{ij} \tag{C.16}$$
$$\frac{\partial^2}{\partial T_{ij} \partial T_{kl}} \operatorname{tr} \mathbf{T}^3 = 3\, \left(\delta_{ik} T_{lj} + T_{ik} \delta_{lj}\right) \to 6 \frac{\eta}{R} \delta_{ik} \delta_{jl}$$

the remaining tensor contributions become

$$\frac{\partial^2 \Phi_{\mathrm{t}}}{\partial n_3 \partial T_{ij}} = -3(A + 4B) f'(\eta) \left(\frac{\eta}{R}\right)^2 \delta_{ij} \tag{C.17}$$
$$\frac{\partial^2 \Phi_{\mathrm{t}}}{\partial T_{ij} \partial T_{kl}} = -6(A + B) f(\eta) \frac{\eta}{R} \delta_{ik} \delta_{jl}.$$

Finally, we have

$$\frac{\partial^2 \Phi_{\mathrm{t}}}{\partial n_3 \partial n_3} = -3(A + 7B) f''(\eta) \left(\frac{\eta}{R}\right)^3 \tag{C.18}$$
$$\frac{\partial^2 \Phi_{\mathrm{t}}}{\partial n_3 \partial n_2} = -9B f'(\eta) \left(\frac{\eta}{R}\right)^2.$$

Collecting all terms and contracting the indices we obtain

$$\begin{aligned} -c_{\mathrm{t}}^{(2)}(r) = {} & 3(A + 7B) f''(\eta) \left(\frac{\eta}{R}\right)^3 \omega_3 \otimes \omega_3 - 6A f(\eta) \frac{\eta}{R} \underline{\omega}_2 \otimes \underline{\omega}_2 + \\ & 6(A + B) f(\eta) \frac{\eta}{R} \operatorname{tr} \left(\omega_T \otimes \omega_T\right) + 18B f'(\eta) \left(\frac{\eta}{R}\right)^2 \omega_3 \otimes \omega_2 + \\ & 12B f(\eta) \frac{\eta}{R} \operatorname{tr}(\omega_T) \otimes \omega_2 + 6(A + 4B) f'(\eta) \left(\frac{\eta}{R}\right)^2 \operatorname{tr}(\omega_T) \otimes \omega_3. \end{aligned} \tag{C.19}$$

Therefore, all what remains is to perform the convolutions between the weight-functions. ω_T has the nice property that when traces are taken the associated convolutions simplify drastically. Making use of the Fourier representation of the weight-functions one can easily show that

$$\operatorname{tr} \omega_T = \omega_2 \tag{C.20}$$
$$\operatorname{tr} \left(\omega_T \otimes \omega_T\right) = \frac{6}{R^2} \omega_3 \otimes \omega_3 - \frac{4}{R} \omega_3 \otimes \omega_2 + \omega_2 \otimes \omega_2.$$

Hence, we conclude that all convolutions that appear, especially those associated to the tensor contributions, can be reduced to the simple ones between ω_3, ω_2 and themselves.

C.3 Lutsko-DCF

In the case of the original proposal of Lutsko's functional, Eq.(5.20), we set

$$f(n_3) = \frac{1}{24\pi(1 - n_3)^2} \tag{C.21}$$

so that both parts of the corresponding DCF read ($x = r/\sigma$)

$$c_{\mathrm{nt}}^{(2)}(x) = \frac{a_{-1}(\eta)}{x} + a_0(\eta) + a_1(\eta) x + a_3(\eta) x^3 \tag{C.22}$$
$$c_{\mathrm{t}}^{(2)}(x) = \frac{b_{-1}(\eta)}{x} + b_0(\eta) + b_1(\eta) x + b_3(\eta) x^3,$$

with the corresponding coefficients depending on the packing fraction η and Lutsko parameters A and B

$$\begin{aligned} a_{-1}(\eta) &= -\frac{3B\eta}{4(1-\eta)^2} \\ a_0(\eta) &= -\frac{1+4\eta+(-5+9(A+B))\eta^2}{(1-\eta)^4} \\ a_1(\eta) &= \frac{3\eta(5+(-4+6B)\eta+(-1+3B)\eta^2+A(-1+8\eta+2\eta^2))}{2(1-\eta)^4} \\ a_3(\eta) &= -\frac{\eta(1+4\eta+(-5+9(A+B))\eta^2)}{2(1-\eta)^4} \end{aligned} \tag{C.23}$$

and

$$\begin{aligned} b_{-1}(\eta) &= \frac{3B\eta}{4(1-\eta)^2} \\ b_0(\eta) &= \frac{(A+7B)\eta^2}{(1-\eta)^4} \\ b_1(\eta) &= -\frac{\eta(A(1+2\eta^2)+B(2+10\eta+9\eta^2))}{2(1-\eta)^4} \\ b_3(\eta) &= \frac{\eta(A(2-4\eta+3\eta^2)+B(2-4\eta+9\eta^2))}{2(1-\eta)^4}. \end{aligned} \tag{C.24}$$

One should notice that $a_{-1} = -b_{-1}$ so in total there is no term proportional to $1/x$ after all. Together with the PY direct correlation function, Eq.(3.55),

$$c^{(2)}_{\mathrm{PY}}(x) = -\frac{(1+2\eta)^2}{(1-\eta)^4} + \frac{3\eta(2+\eta)^2}{2(1-\eta)^4}x - \frac{\eta(1+2\eta)^2}{2(1-\eta)^4}x^3 \tag{C.25}$$

we obtain the DCF of Lutsko

$$c^{(2),\mathrm{LK}}(x) = c^{(2)}_{\mathrm{nt}}(x) + c^{(2)}_{\mathrm{t}}(x) \tag{C.26}$$

$$= c^{(2)}_{\mathrm{PY}}(x) +$$

$$\{\frac{\eta}{2(1-\eta)^2}x\left[2(A+B)x^2+3-2B-4A\right] - \tag{C.27}$$

$$(8A+2B-9)\frac{\eta^2}{(1-\eta)^3}(1-x)\left[1+\frac{\eta}{2(1-\eta)}(1-x)(2+x)\right]\}\Theta(1-x).$$

C.4 Lutsko-WB-DCF

Here, we set

$$f(n_3) = \frac{n_3+(1-n_3)^2\log(1-n_3)}{36\pi n_3^2(1-n_3)^2} \tag{C.28}$$

and directly give the final result

$$c^{(2),\text{LK-WB}}(x) = \left[a_0(\eta)+a_1(\eta)x+a_3(\eta)x^3\right]\Theta(1-x), \tag{C.29}$$

with

$$a_0(\eta) = \frac{-9+\eta(-36+\eta(45+16A(-4+\eta)+4B(-4+\eta)))}{9(1-\eta)^4} \tag{C.30}$$
$$a_1(\eta) = \frac{1}{18}\left(\frac{24A\log(1-\eta)}{\eta} - 3\frac{N_1(\eta)}{(1-\eta)^4}\right)$$
$$a_3(\eta) = \frac{1}{18}\left(-\frac{36A\log(1-\eta)}{\eta} + \frac{N_2(\eta)}{(1-\eta)^4}\right),$$

where we have introduced the numerators

$$N_1(\eta) = -9(1-\eta)\eta(5+\eta) + 6B\eta(1+(-4+\eta)\eta) + 8A(-1+\eta(5+\eta(-13+3\eta))) \tag{C.31}$$
$$N_2(\eta) = 4A(-9+(-4+\eta)\eta(-9+10\eta)) + \eta(-9(1-\eta)(1+5\eta) + 2B(9+5(-4+\eta)\eta))$$

for abbreviation.

C.5 Lutsko-WBII-DCF

Similarly, we provide the expression for the LK-WBII case

$$c^{(2),\text{LK-WBII}}(r) = \left[b_0(\eta) + b_1(\eta)x + b_3(\eta)x^3\right]\Theta(1-x) \tag{C.32}$$

with

$$b_0(\eta) = -\frac{9+36\eta+(-27+56A+14B)\eta^2 - 2(9+8A+2B)\eta^3 + 2(4A+B)\eta^4}{9(1-\eta)^4} \tag{C.33}$$
$$b_1(\eta) = \frac{(6-4A)\log(1-\eta)}{3\eta} + \frac{N_3(\eta)}{6(1-\eta)^4}$$
$$b_3(\eta) = \frac{2(A-1)\log(1-\eta)}{\eta} + \frac{N_4(\eta)}{18(1-\eta)^4},$$

where we have now defined the fourth degree polynomials

$$N_3(\eta) = 12-8A+(3+16A-6B)\eta+(32A+30+24B)\eta^2-5(9+2B)\eta^3+(8A+4B)\eta^4 \tag{C.34}$$

and

$$N_4(\eta) = -36+36A+(-108A+117+18B)\eta+(112A-198-44B)\eta^2+ \tag{C.35}$$
$$(117-92A+22B)\eta^3+(4A-8B)\eta^4.$$

C.6 Optimization of Lutsko Functionals by DCF

As we discussed in Ch.5, the optimization of the Lutsko functionals with respect to its two free parameters A and B was performed by minimizing the relative errors of the two equilibrium sum rules of chemical potential μ and isothermal compressibility χ_T in test-particle geometry. However, regarding the direct correlation functions $c^{(2)}(r;A,B)$ of Lutsko, which parametrically depend on A and B, these need not be optimized by the sum rules. Therefore, it is intriguing to investigate the optimization with respect to the direct correlation functions $c^{(2)}(r;A,B)$ using data that are obtained by accurate Monte-Carlo (MC) simulations on hard spheres [94]. There are two methods we employ for optimization:

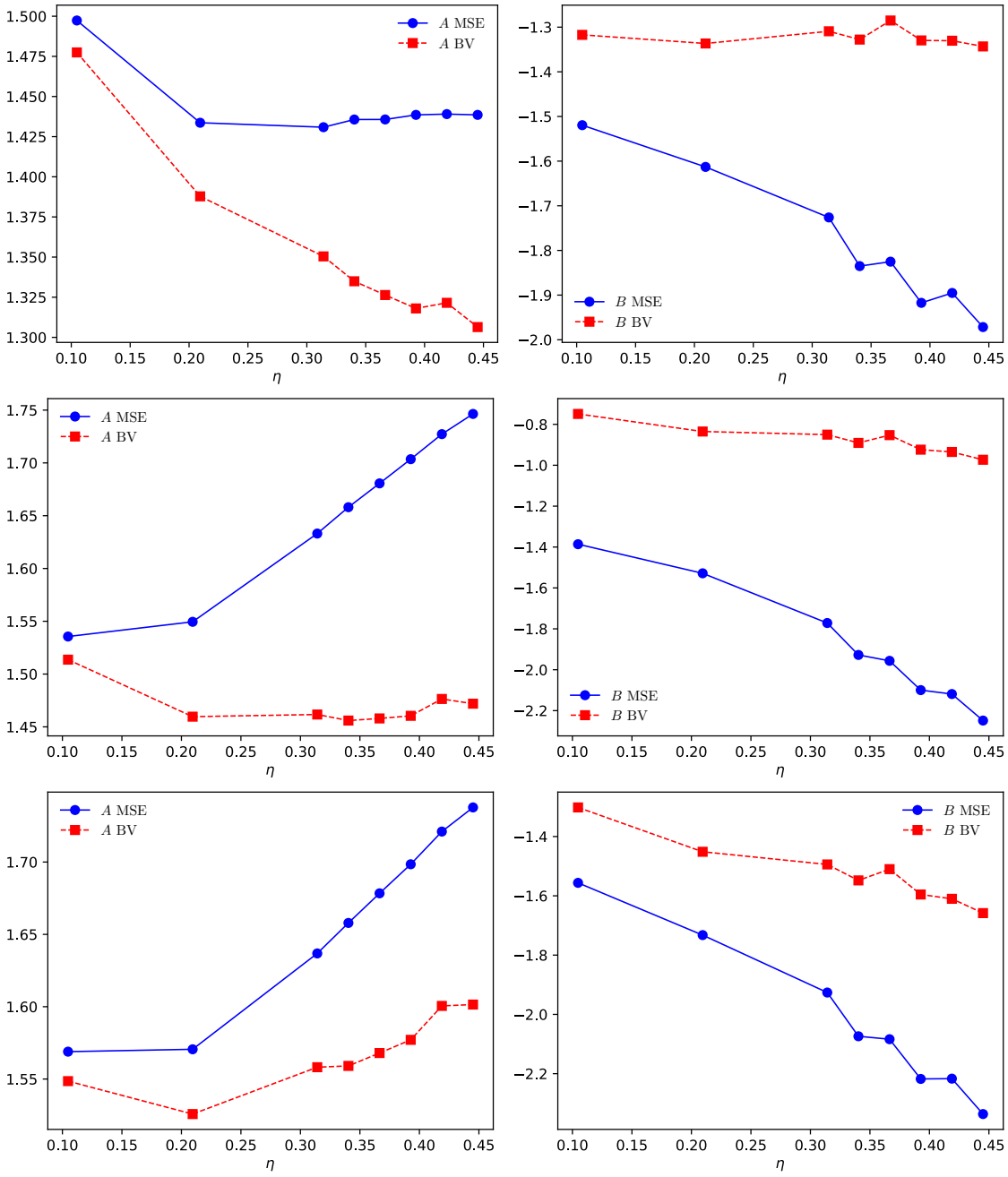

Figure C.1: Lutsko parameters A and B obtained from the optimization procedures mean-squared error (MSE) and boundary value (BV) of the direct correlation function $c^{(2)}(\eta, x; A, B)$ for LK (top), LK-WB (middle) and LK-WBII (bottom).

1. Mean-squared error (MSE): We demand the mean-squared error $\sum_i (c^{(2)}_{\mathrm{MC}}(x_i) - c^{(2)}(x_i; A, B))^2$ to be minimal for specific points $x_i = r_i/\sigma \in [0, 1]$ where data of MC simulations is available. Thus, we fit with respect to A and B that minimize the corresponding MSE for each packing fraction η.

2. Fix the boundary values (BV) $c^{(2)}(x = 0; A, B) = c^{(2)}_{\mathrm{MC}}(x = 0)$ and $c^{(2)}(x = 1; A, B) = c^{(2)}_{\mathrm{MC}}(x = 1)$ by those of the MC data. These two conditions provide two equations for two unknowns A and B for each packing fraction η.

Both procedures hence allow us to determine the optimal parameters $A(\eta)$ and $B(\eta)$ as a function of packing fraction η.

In Fig.C.1 we display the optimized parameters A and B as a function of packing fraction η. We first see that both A and B start at a value of ca. 1.5 and -1.5 (LK-WB somehow starts at $B = -0.8$) respectively and remain there for higher packing fractions $\eta > 0.35$ for all three Lutsko functionals, LK, LK-WB and LK-WBII. This is not surprising as the point $(A, B) = (1.5, -1.5)$ only has the correct low-density limit for $c^{(2)}(r)$. In agreement with our findings of Ch.5, if we restrict the optimization procedures to high densities then A is positive while B is negative. However, we observe first of all that the respective values are only approximately constant and differ significantly in the case of B compared to the optimal points derived from the equilibrium sum rules. For instance, we have found the optimal point $(A, B) = (1.25, -0.20)$ from the sum rules for LK-WBII whereas according to the $c^{(2)}$-optimization we find $(1.74, -2.34)$ from MSE and $(1.60, -1.66)$ from BV. Nonetheless, the results obtained from different optimization procedures show that the optimized functionals do not belong to the explicitly stable class $A, B > 0$.

Finally, we show the direct correlation functions $c^{(2)}(\eta, x; A, B)$ of LK-WBII optimized by the aforementioned procedures for high packing fraction $\eta = 0.419$ in Fig.C.2. Overall we see very good agreement between the optimized correlation functions with noticeable deviations occurring at the boundary $r/\sigma = 1$. Of course, the optimal point $(1.25, -0.20)$ derived from the sum rules exhibits the highest deviation at $r/\sigma = 1$ as there is generally no reason for this point to be optimal with respect to $c^{(2)}$.

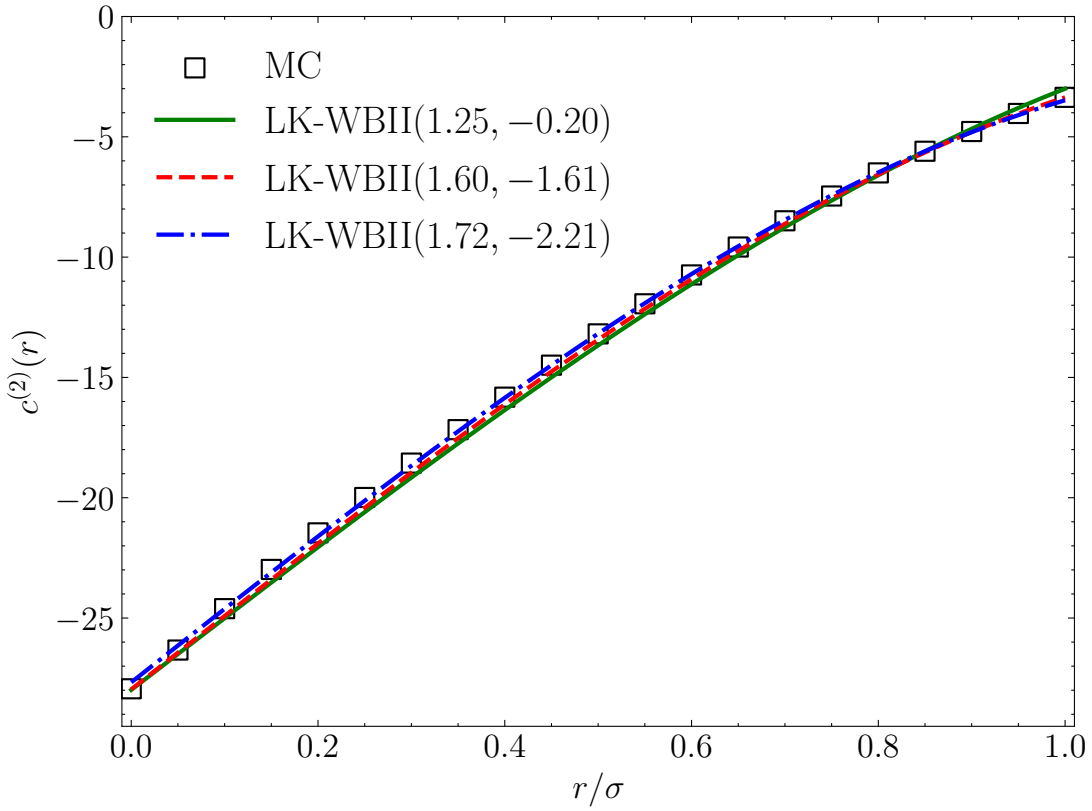

Figure C.2: Direct correlation function $c^{(2)}(r)$ of LK-WBII for three choices of Lutsko parameters obtained via equilibrium sum rules (green solid), BV (red dashed) and MSE (blue dash-dotted) at a packing fraction $\eta = 0.419$. The squares represent MC data [94].

Appendix D

Ng-Algorithm

We dedicate this section to a powerful numerical scheme introduced in [150]. This iterative method was essential in finding our results of stabilized droplets of Ch.7.

The minimizations we perform for numerical calculations in DFT make use of algorithms that can generically be written in the form

$$Af = f, \tag{D.1}$$

where f is a real function and A an operator. A first iterative method to solve Eq.(D.1) is

$$f_{n+1} = Af_n, \quad n = 1, 2, 3, \ldots. \tag{D.2}$$

Therefore, starting with an initial guess f_1, via Eq.(D.2) the next solutions f_i, $i > 1$ are found. However, not always is the convergence of the sequence in Eq.(D.2) guaranteed, instead, it can oscillate or even diverge. We can severely improve upon stability by writing

$$f_{n+1} = (1 - \alpha)f_n + \alpha Af_n \tag{D.3}$$

with a mixing parameter $\alpha \in (0, 1)$. Eq.(D.3) is just the Picard iteration scheme we have introduced in Sec.3.5.1 which is a standard method to obtain density profiles in DFT. As was pointed out before, the choice of α is merely specified on empirical grounds. Now, we want to present an extension to Eq.(D.3) that can be considered to usually converge faster. We define

$$g_n = Af_n, \quad d_n = g_n - f_n = (A - 1)f_n \tag{D.4}$$

with the input function f_n and output function g_n of the n-th iteration. Suppose that we are at step $n \geq 3$. Then, we know at this stage the functions f_{n-2}, g_{n-2}, f_{n-1} and g_{n-1} as well as f_n and g_n. A key part of this iteration is to extract as much information as possible from the preceding functions in order to accelerate the convergence. We further define

$$\bar{f} = (1 - c_1 - c_2)f_n + c_1 f_{n-1} + c_2 f_{n-2}, \tag{D.5}$$

where we want to choose values for c_1 and c_2 such that $\bar{f}$ comes closest to the true solution of Eq.(D.1). If we assume that A is a linear operator, we find

$$\begin{aligned} A\bar{f} &= (1 - c_1 - c_2)g_n + c_1 g_{n-1} + c_2 g_{n-2}, \\ \Delta &= ||A\bar{f} - \bar{f}|| = ||d_n - c_1 d_{01} - c_2 d_{02}||. \end{aligned} \tag{D.6}$$

Here, $||\cdot||$ represents a measure in function space that can be chosen arbitrarily. We also have defined the auxiliary functions

$$d_{01} = d_n - d_{n-1}, \quad d_{02} = d_n - d_{n-2}. \tag{D.7}$$

Hence, we optimize for c_1 and c_2 by minimizing Δ^2 which leads to two equations

$$\begin{aligned}(d_{01}, d_{01})c_1 + (d_{01}, d_{02})c_2 &= (d_n, d_{01}) \\ (d_{01}, d_{02})c_1 + (d_{02}, d_{02})c_2 &= (d_n, d_{02}),\end{aligned} \tag{D.8}$$

where $(,)$ is a suitable scalar product in function space. In total, we can provide a good input for the $n+1$-th iteration step

$$f_{n+1} = (1 - c_1 - c_2)g_n + c_1 g_{n-1} + c_2 g_{n-2} \tag{D.9}$$

wherein c_1 and c_2 are obtained from Eq.(D.8).

Acknowledgements

I would like to thank Prof. Dr. Roland Roth and Prof. Dr. Martin Oettel for offering me the opportunity to conduct my PhD in the field of classical density functional theory. I have learned a lot from Prof. Dr. Roland Roth during this period and have made many valuable experiences where his contributions were important in my scientific development. I would also like to thank Prof. Dr. Robert Evans for having collaborated with me over these years and for his insightful advices on my work. I am also very grateful for having known many wonderful colleagues such as Furio, Hadra, Alessandro, Frank, Jens and Michael who accompanied me during my PhD. Especially to Furio I would like to thank as a really good friend who supported me a lot in this time. I really enjoyed our scientific discussions and miscellaneous conversations embedded in plenty Moka sessions. I am also happy for having met other good friends like Matthias, Tabea and Elaheh. I devote much appreciations to my family for having believed in me all this time and having shown me gratitude and care. Without their invaluable support it would have been virtually impossible for me to reach my goals. Last but not least, I want to mention my brother, Selim, as someone giving me often times different perspectives and opinions on life.

I want to conclude with a section of Voltaire's work *Discours en vers sur l'homme – De la liberté*

Ferme en tes sentiments et simple dans ton coeur;
Aime la vérité, mais pardonne à l'erreur;
Fuis les emportements d'un zèle atrabilaire;
Ce mortel qui s'égare est un homme, est ton frère;
Sois sage pour toi seul, et compatissant pour lui;
Fais ton bonheur enfin par le bonheur d'autrui.

Bibliography

[1] David Chandler. From 50 years ago, the birth of modern liquid-state science. *Annual Review of Physical Chemistry*, 68(1):19–38, May 2017.

[2] K Trachenko and V V Brazhkin. Collective modes and thermodynamics of the liquid state. *Reports on Progress in Physics*, 79(1):016502, December 2015.

[3] Ralph C. Dougherty. Molecular theory of water and aqueous solutions, part i: Understanding water. *Journal of the American Chemical Society*, 132(1):428–428, 2010. PMID: 20014836.

[4] Szilvia Pothoczki, László Temleitner, and László Pusztai. Structure of neat liquids consisting of (perfect and nearly) tetrahedral molecules. *Chemical Reviews*, 115(24):13308–13361, 2015. PMID: 26624528.

[5] G. Maitland, M. Rigby, E. Smith, W. Wakeham, and Douglas Henderson. Intermolecular forces: Their origin and determination. *Physics Today*, 36(4):57–58, 04 1983.

[6] Paola Gallo and Mauro Rovere. *Physics of Liquid Matter*. 01 2021.

[7] Jean-Pierre Hansen and Ian R. McDonald. *Theory of Simple Liquids: With Applications to Soft Matter*. Academic Press, Amsterdam, 3rd edition, 2006.

[8] R. Evans. The nature of the liquid-vapour interface and other topics in the statistical mechanics of non-uniform, classical fluids. *Advances in Physics*, 28(2):143–200, 1979.

[9] Yaakov Rosenfeld. Free-energy model for the inhomogeneous hard-sphere fluid mixture and density-functional theory of freezing. *Phys. Rev. Lett.*, 63:980–983, Aug 1989.

[10] Roland Roth. Fundamental measure theory for hard-sphere mixtures: a review. *J. Phys. Condens. Matter*, 22(6):063102, jan 2010.

[11] Daniel Stopper, Frank Hirschmann, Martin Oettel, and Roland Roth. Bulk structural information from density functionals for patchy particles. *The Journal of Chemical Physics*, 149(22), December 2018.

[12] W. Langel. Introduction to neutron scattering. *ChemTexts 9*, Aug 2023.

[13] Wolfgang Nolting. *Theoretical Physics 6: Statistical Physics*. Springer, Berlin, Germany, 2018.

[14] Franz Schwabl. *Statistische Mechanik*. Springer, 3 edition, 2006.

[15] Linda E. Reichl. *A Modern Course in Statistical Physics*. Wiley, 2nd edition, 1998.

[16] C. E. Shannon. A mathematical theory of communication. *The Bell System Technical Journal*, 27(3):379–423, 1948.

[17] C. E. Shannon. A mathematical theory of communication. *The Bell System Technical Journal*, 27(4):623–656, 1948.

[18] Amar B. Pawar and Ilona Kretzschmar. Fabrication, assembly, and application of patchy particles. *Macromolecular Rapid Communications*, 31(2):150–168, 2010.

[19] J. Russo, J. M. Tavares, P. I. C. Teixeira, M. M. Telo da Gama, and F. Sciortino. Re-entrant phase behaviour of network fluids: A patchy particle model with temperature-dependent valence. *The Journal of Chemical Physics*, 135(3):034501, 07 2011.

[20] Frank Smallenburg, Ludwik Leibler, and Francesco Sciortino. Patchy particle model for vitrimers. *Phys. Rev. Lett.*, 111:188002, Oct 2013.

[21] M. S. Wertheim. Fluids with highly directional attractive forces. I. Statistical thermodynamics. *Journal of Statistical Physics*, 35(1-2):19, April 1984.

[22] M. S. Wertheim. Fluids with highly directional attractive forces. I. Statistical thermodynamics. *Journal of Statistical Physics*, 35(1-2):35, April 1984.

[23] Stephen Whitelam and Robert L. Jack. The statistical mechanics of dynamic pathways to self-assembly. *Annual Review of Physical Chemistry*, 66(Volume 66, 2015):143–163, 2015.

[24] Antonio Moro. Shock dynamics of phase diagrams. *Annals of Physics*, 343, 07 2013.

[25] Edward Armand Guggenheim. The principle of corresponding states. *Journal of Chemical Physics*, 13:253–261, 1945.

[26] Furio Surfaro, Ralph Maier, Kai-Florian Pastryk, Fajun Zhang, Frank Schreiber, and Roland Roth. An alternative approach to the osmotic second virial coefficient of protein solutions and its application to liquid–liquid phase separation. *The Journal of Chemical Physics*, 158(16):164902, 04 2023.

[27] Andrés Santos. *A Concise Course on the Theory of Classical Liquids: Basics and Selected Topics*, volume 990 of *Lecture Notes in Physics*. Springer, 2023.

[28] Barry M. McCoy. *Advanced Statistical Mechanics*. Oxford University Press, Oxford, 2010.

[29] E J Janse van Rensburg. Virial coefficients for hard discs and hard spheres. *Journal of Physics A: Mathematical and General*, 26(19):4805, oct 1993.

[30] Francis H. Ree and William G. Hoover. Fifth and sixth virial coefficients for hard spheres and hard disks. *The Journal of Chemical Physics*, 40(4):939–950, 02 1964.

[31] Stanislav Labík, Ji ří Kolafa, and Anatol Malijevský. Virial coefficients of hard spheres and hard disks up to the ninth. *Phys. Rev. E*, 71:021105, Feb 2005.

[32] Nathan Clisby and Barry M. McCoy. Ninth and tenth order virial coefficients for hard spheres in d dimensions. *Journal of Statistical Physics*, 122(1):15–57, December 2005.

[33] Richard J. Wheatley. Calculation of high-order virial coefficients with applications to hard and soft spheres. *Phys. Rev. Lett.*, 110:200601, May 2013.

[34] Jiří Kolafa, Stanislav Labík, and Anatol Malijevský. Accurate equation of state of the hard sphere fluid in stable and metastable regions. *Phys. Chem. Chem. Phys.*, 6:2335–2340, 2004.

[35] Norman F. Carnahan and Kenneth E. Starling. Equation of state for nonattracting rigid spheres. *The Journal of Chemical Physics*, 51(2):635–636, 07 1969.

[36] P. Hohenberg and W. Kohn. Inhomogeneous electron gas. *Phys. Rev.*, 136:B864–B871, Nov 1964.

[37] W. Kohn and L. J. Sham. Self-consistent equations including exchange and correlation effects. *Phys. Rev.*, 140:A1133–A1138, Nov 1965.

[38] N. David Mermin. Thermal properties of the inhomogeneous electron gas. *Phys. Rev.*, 137:A1441–A1443, Mar 1965.

[39] C. Ebner, W. F. Saam, and D. Stroud. Density-functional theory of simple classical fluids. i. surfaces. *Phys. Rev. A*, 14:2264–2273, Dec 1976.

[40] Roland Roth. *Introduction to Density Functional Theory of Classical Systems: Theory and Applications*. 2006.

[41] Émile Picard. Mémoire sur la théorie des équations aux dérivées partielles et la méthode des approximations successives. *Journal de Mathématiques Pures et Appliquées*, 6:145–210, 1890.

[42] Richard L. Burden and J. Douglas Faires. *Numerical Analysis*. Brooks/Cole, 9th edition, 2010.

[43] Diederik P. Kingma and Jimmy Ba. Adam: A method for stochastic optimization. *International Conference on Learning Representations (ICLR)*, 2015.

[44] J. K. Percus. Approximation methods in classical statistical mechanics. *Phys. Rev. Lett.*, 8:462–463, Jun 1962.

[45] Michael P. Allen and Dominic J. Tildesley. *Computer Simulation of Liquids*. Oxford University Press, 06 2017.

[46] Daan Frenkel and Berend Smit. Preface to the second edition. In *Understanding Molecular Simulation (Second Edition)*, pages xiii–xiv. Academic Press, San Diego, second edition edition, 2002.

[47] Antonio Brasiello, Nino Grizzuti, Pier Luca Maffettone, and Giuseppe Milano. Molecular dynamics of triglycerides: atomistic and coarse-grained approaches. 01 2006.

[48] Accidental deviations of density and opalescence at the critical point of a single substance. *Koninklijke Nederlandse Akademie van Wetenschappen Proceedings Series B Physical Sciences*, 17:793–806, January 1914.

[49] Jerome K. Percus and George J. Yevick. Analysis of classical statistical mechanics by means of collective coordinates. *Phys. Rev.*, 110:1–13, Apr 1958.

[50] M. S. Wertheim. Exact solution of the percus-yevick integral equation for hard spheres. *Phys. Rev. Lett.*, 10:321–323, Apr 1963.

[51] T. V. Ramakrishnan and M. Yussouff. First-principles order-parameter theory of freezing. *Phys. Rev. B*, 19:2775–2794, Mar 1979.

[52] Paul Hopkins, Andrea Fortini, Andrew J. Archer, and Matthias Schmidt. The van hove distribution function for brownian hard spheres: Dynamical test particle theory and computer simulations for bulk dynamics. *The Journal of Chemical Physics*, 133(22):224505, 12 2010.

[53] M. Oettel, S. Dorosz, M. Berghoff, B. Nestler, and T. Schilling. Description of hard-sphere crystals and crystal-fluid interfaces: A comparison between density functional approaches and a phase-field crystal model. *Phys. Rev. E*, 86:021404, Aug 2012.

[54] P. Tarazona and R. Evans. A simple density functional theory for inhomogeneous liquids. *Molecular Physics*, 52(4):847–857, 1984.

[55] G.P. Brenan and R. Evans. Free energy functionals and the structure of the uniform hard-sphere fluid. *Molecular Physics*, 73(4):789–803, 1991.

[56] P. Tarazona. Free-energy density functional for hard spheres. *Phys. Rev. A*, 31:2672–2679, Apr 1985.

[57] Soon-Chul Kim, M Calleja, and G Rickayzen. Density profiles of hard-sphere fluids restricted by hard and permeable walls. *Journal of Physics: Condensed Matter*, 7(42):8053, oct 1995.

[58] H. Reiss, H. L. Frisch, and J. L. Lebowitz. Statistical mechanics of rigid spheres. *The Journal of Chemical Physics*, 31(2):369–380, 08 1959.

[59] J. L. Lebowitz, E. Helfand, and E. Praestgaard. Scaled particle theory of fluid mixtures. *The Journal of Chemical Physics*, 43(3):774–779, 08 1965.

[60] Robert Evans. Density functionals in the theory of nonuniform fluids. *Fundamentals of inhomogeneous fluids*, 1:85–176, 1992.

[61] Y. Rosenfeld, M. Schmidt, H. Löwen, and P. Tarazona. Fundamental-measure free-energy density functional for hard spheres: Dimensional crossover and freezing. *Phys. Rev. E*, 55:4245–4263, Apr 1997.

[62] R Roth, R Evans, A Lang, and G Kahl. Fundamental measure theory for hard-sphere mixtures revisited: the white bear version. *Journal of Physics: Condensed Matter*, 14(46):12063, nov 2002.

[63] P. Tarazona and Y. Rosenfeld. From zero-dimension cavities to free-energy functionals for hard disks and hard spheres. *Phys. Rev. E*, 55:R4873–R4876, May 1997.

[64] P. Tarazona and Y. Rosenfeld. *New Approaches to Problems in Liquid State Theory.* Dordrecht: Kluwer Academic, 1999.

[65] P. Tarazona. Density functional for hard sphere crystals: A fundamental measure approach. *Phys. Rev. Lett.*, 84:694–697, Jan 2000.

[66] Jose Cuesta, Yuri Martínez-Ratón, and Pedro Tarazona. Close to the edge of fundamental measure theory: density functional for hard sphere mixtures. *Journal of Physics Condensed Matter*, 14:11965, 05 2002.

[67] Yang-Xin Yu and Jianzhong Wu. Structures of hard-sphere fluids from a modified fundamental-measure theory. *The Journal of Chemical Physics*, 117(22):10156–10164, 12 2002.

[68] Hendrik Hansen-Goos and Roland Roth. Density functional theory for hard-sphere mixtures: the white bear version mark ii. *Journal of Physics: Condensed Matter*, 18(37):8413, aug 2006.

[69] JK Percus. Equilibrium state of a classical fluid of hard rods in an external field. *Journal of Statistical Physics*, 15:505–511, 1976.

[70] T. K. Vanderlick, H. T. Davis, and J. K. Percus. The statistical mechanics of inhomogeneous hard rod mixtures. *The Journal of Chemical Physics*, 91(11):7136–7145, 12 1989.

[71] T. K. Vanderlick, L. E. Scriven, and H. T. Davis. Solution of percus's equation for the density of hard rods in an external field. *Phys. Rev. A*, 34:5130–5131, Dec 1986.

[72] Peter Sloth. Hard-sphere fluids inside spherical, hard pores. grand canonical ensemble monte carlo calculations and integral equation approximations. *Journal of Chemical Physics*, 93(2):1292–1298, 1990. Copyright (1990) American Institute of Physics. This article may be downloaded for personal use only. Any other use requires prior permission of the author and the American Institute of Physics.

[73] E. Kierlik and M. L. Rosinberg. Free-energy density functional for the inhomogeneous hard-sphere fluid: Application to interfacial adsorption. *Phys. Rev. A*, 42:3382–3387, Sep 1990.

[74] S. Phan, E. Kierlik, M. L. Rosinberg, B. Bildstein, and G. Kahl. Equivalence of two free-energy models for the inhomogeneous hard-sphere fluid. *Phys. Rev. E*, 48:618–620, Jul 1993.

[75] E. Helfand, H. Reiss, H. L. Frisch, and J. L. Lebowitz. Scaled particle theory of fluids. *The Journal of Chemical Physics*, 33(5):1379–1385, 11 1960.

[76] Y Rosenfeld, M Schmidt, H Löwen, and P Tarazona. Dimensional crossover and the freezing transition in density functional theory. *Journal of Physics: Condensed Matter*, 8(40):L577, sep 1996.

[77] A. González, J. A. White, F. L. Román, and Robert Evans. How the structure of a confined fluid depends on the ensemble: Hard spheres in a spherical cavity. *Journal of Chemical Physics*, 109:3637–3650, 1998.

[78] J. White. Equivalence of two approaches for the inhomogeneous density in the canonical ensemble. *Physical Review E*, 62:4427–30, 10 2000.

[79] James F. Lutsko and Julien Lam. Classical density functional theory, unconstrained crystallization, and polymorphic behavior. *Phys. Rev. E*, 98:012604, Jul 2018.

[80] G. A. Mansoori, N. F. Carnahan, K. E. Starling, and Jr. Leland, T. W. Equilibrium thermodynamic properties of the mixture of hard spheres. *The Journal of Chemical Physics*, 54(4):1523–1525, 02 1971.

[81] M. Oettel, S. Görig, A. Härtel, H. Löwen, M. Radu, and T. Schilling. Free energies, vacancy concentrations, and density distribution anisotropies in hard-sphere crystals: A combined density functional and simulation study. *Phys. Rev. E*, 82:051404, Nov 2010.

[82] Hendrik Hansen-Goos and Roland Roth. A new generalization of the carnahan-starling equation of state to additive mixtures of hard spheres. *The Journal of Chemical Physics*, 124(15):154506, 04 2006.

[83] Martin Oettel. Mode expansion for the density profile of crystal-fluid interfaces: Hard spheres as a test case. *Journal of physics. Condensed matter : an Institute of Physics journal*, 24:464124, 10 2012.

[84] J.R. Henderson and. Statistical mechanics of fluids at spherical structureless walls. *Molecular Physics*, 50(4):741–761, 1983.

[85] P. Bryk, R. Roth, K. R. Mecke, and S. Dietrich. Hard-sphere fluids in contact with curved substrates. *Phys. Rev. E*, 68:031602, Sep 2003.

[86] Yaoqi Zhou and George Stell. Fluids inside a pore—an integral-equation approach. *Molecular Physics*, 66(4):767–789, 1989.

[87] A. González, J. A. White, F. L. Román, S. Velasco, and R. Evans. Density functional theory for small systems: Hard spheres in a closed spherical cavity. *Phys. Rev. Lett.*, 79:2466–2469, Sep 1997.

[88] D.J. Adams. Chemical potential of hard-sphere fluids by monte carlo methods. *Molecular Physics*, 28(5):1241–1252, 1974.

[89] Ignacio Urrutia. Three hard spheres in a spherical cavity. *The Journal of Chemical Physics*, 135(2):024511, 07 2011.

[90] Yaakov Rosenfeld. Free energy model for inhomogeneous fluid mixtures: Yukawa-charged hard spheres, general interactions, and plasmas. *The Journal of Chemical Physics*, 98(10):8126–8148, 05 1993.

[91] E. Kierlik and M. L. Rosinberg. Density-functional theory for inhomogeneous fluids: Adsorption of binary mixtures. *Phys. Rev. A*, 44:5025–5037, Oct 1991.

[92] Mostafa Mortazavifar. *Equilibrium properties of crystals in the Hard-sphere and the Asakura-Oosawa model*. PhD thesis, Eberhard-Karls-Universität Tübingen, 2016.

[93] James F. Lutsko. Explicitly stable fundamental-measure-theory models for classical density functional theory. *Phys. Rev. E*, 102:062137, Dec 2020.

[94] R. D. Groot, J. P. van der Eerden, and N. M. Faber. The direct correlation function in hard sphere fluids. *The Journal of Chemical Physics*, 87(4):2263–2270, 08 1987.

[95] Ruslan L. Davidchack, Brian B. Laird, and Roland Roth. *Condens. Mat. Phys.*, 19:23001, 2016.

[96] S. M. Tschopp, H. D. Vuijk, A. Sharma, and J. M. Brader. *Phys. Rev. E*, 102:042140, 2020.

[97] J. A. Barker and D. Henderson. *Rev. Mod. Phys.*, 48:587, 1976.

[98] F. Sammüller, S. Hermann, D. de las Heras, and M. Schmidt. *Proc. Natl. Acad. Sci. U.S.A.*, 120:e2312484120, 2023.

[99] F. Sammüller and M. Schmidt. *arXiv:2406.03327*, 2024.

[100] J. Dijkman, M Dijkstra, R van Roij, M. Welling, J.-W. van de Meent, and B. Ensing. *arXiv:2403.15007*, 2024.

[101] Daniel Stopper, Hendrik Hansen-Goos, Roland Roth, and Robert Evans. On the decay of the pair correlation function and the line of vanishing excess isothermal compressibility in simple fluids. *The Journal of Chemical Physics*, 151(1):014501, 07 2019.

[102] R Evans, J Charvolin, JF Joanny, and J Zinn-Justin. Liquides aux interfaces/liquids at interfaces: Les houches, session xlviii 1988, 1989.

[103] M Schick. Introduction to wetting phenomena. *Liquids at interfaces*, 48, 1990.

[104] Siegfried Dietrich. *Wetting phenomena*. Sekt. Physik der Ludwig-Maximilians-Univ., 1987.

[105] Joris Kuipers and Edgar M. Blokhuis. Wetting and drying transitions in mean-field theory: Describing the surface parameters for the theory of nakanishi and fisher in terms of a microscopic model. *The Journal of Chemical Physics*, 131(4):044702, 07 2009.

[106] Jr. McMillan, William G. and Joseph E. Mayer. The statistical thermodynamics of multicomponent systems. *The Journal of Chemical Physics*, 13(7):276–305, 07 1945.

[107] Marjolein Dijkstra, René van Roij, and Robert Evans. Phase behavior and structure of binary hard-sphere mixtures. *Phys. Rev. Lett.*, 81:2268–2271, Sep 1998.

[108] Marjolein Dijkstra, René van Roij, and Robert Evans. Direct simulation of the phase behavior of binary hard-sphere mixtures: Test of the depletion potential description. *Phys. Rev. Lett.*, 82:117–120, Jan 1999.

[109] Marjolein Dijkstra, René van Roij, and Robert Evans. Phase diagram of highly asymmetric binary hard-sphere mixtures. *Phys. Rev. E*, 59:5744–5771, May 1999.

[110] Christos N. Likos. Effective interactions in soft condensed matter physics. *Physics Reports*, 348(4):267–439, 2001.

[111] Sho Asakura and Fumio Oosawa. On interaction between two bodies immersed in a solution of macromolecules. *The Journal of Chemical Physics*, 22(7):1255–1256, 07 1954.

[112] Sho Asakura and Fumio Oosawa. Interaction between particles suspended in solutions of macromolecules. *Journal of Polymer Science*, 33(126):183–192, 1958.

[113] H.N.W. Lekkerkerker and R. Tuinier. *Colloids and the Depletion Interaction*. Lecture Notes in Physics. Springer Netherlands, 2011.

[114] Marjolein Dijkstra, Joseph M Brader, and Robert Evans. Phase behaviour and structure of model colloid-polymer mixtures. *Journal of Physics: Condensed Matter*, 11(50):10079, dec 1999.

[115] R. Roth, R. Evans, and S. Dietrich. Depletion potential in hard-sphere mixtures: Theory and applications. *Phys. Rev. E*, 62:5360–5377, Oct 2000.

[116] Douglas J. Ashton, Nigel B. Wilding, Roland Roth, and Robert Evans. Depletion potentials in highly size-asymmetric binary hard-sphere mixtures: Comparison of simulation results with theory. *Phys. Rev. E*, 84:061136, Dec 2011.

[117] R. Roth, R. Evans, and A. A. Louis. Theory of asymmetric nonadditive binary hard-sphere mixtures. *Phys. Rev. E*, 64:051202, Oct 2001.

[118] B. Widom. Some topics in the theory of fluids. *The Journal of Chemical Physics*, 39(11):2808–2812, 12 1963.

[119] Robert Evans, Martin Oettel, Roland Roth, and Gerhard Kahl. New developments in classical density functional theory. *Journal of Physics: Condensed Matter*, 28(24):240401, apr 2016.

[120] K. Abe and K. Koga. Local solubility of nonpolar molecules in the liquid–vapor interfaces of water and simple liquids. *Journal of Molecular Liquids*, 200:7–11, 2014. Proceedings of the 7th Mini-Symposium on Liquids "Liquid-Liquid Phase Separation and Related Topics on Liquids".

[121] Patrick K. Wise and Dor Ben-Amotz. Interfacial adsorption of neutral and ionic solutes in a water droplet. *The Journal of Physical Chemistry B*, 122(13):3447–3453, 2018. PMID: 29244951.

[122] Edgar L. Camacho Vergara, Georgios M. Kontogeorgis, and Xiaodong Liang. Gas adsorption and interfacial tension with classical density functional theory. *Industrial and Engineering Chemistry Research*, 58(14):5650–5664, 2019.

[123] Elmar Sauer and Joachim Gross. Classical density functional theory for liquid-fluid interfaces and confined systems: A new functional for the perturbed-chain polar statistical associating fluid theory equation of state. *Industrial and Engineering Chemistry Research*, 56, 03 2017.

[124] V. Talanquer, Crystal Cunningham, and D. W. Oxtoby. Bubble nucleation in binary mixtures: A semiempirical approach. *The Journal of Chemical Physics*, 114(15):6759–6762, 04 2001.

[125] Ryuichi Okamoto and Akira Onuki. Density functional theory of gas–liquid phase separation in dilute binary mixtures. *Journal of Physics: Condensed Matter*, 28(24):244012, apr 2016.

[126] Andrew J. Archer, Blesson Chacko, and Robert Evans. The standard mean-field treatment of inter-particle attraction in classical dft is better than one might expect. *The Journal of Chemical Physics*, 147(3):034501, 07 2017.

[127] Robert D Deegan, Olgica Bakajin, Todd F. Dupont, Greb Huber, Sidney R Nagel, and Thomas A. Witten. Capillary flow as the cause of ring stains from dried liquid drops. *Nature*, 389(6653):827–829, oct 1997.

[128] A. J. Archer, R. Evans, and R. Roth. Microscopic theory of solvent-mediated long-range forces: Influence of wetting. *Europhysics Letters*, 59(4):526, aug 2002.

[129] A. J. Archer, R. Evans, R. Roth, and M. Oettel. Solvent mediated interactions close to fluid-fluid phase separation: Microscopic treatment of bridging in a soft-core fluid. *The Journal of Chemical Physics*, 122(8):084513, 02 2005.

[130] World Healt Organization. Infection prevention and control of epidemic- and pandemic-prone acute respiratory infections in health care. *National Library of Medicine*, 2014.

[131] Jan Gralton, Euan Tovey, Mary-Louise McLaws, and William D. Rawlinson. The role of particle size in aerosolised pathogen transmission: A review. *Journal of Infection*, 62(1):1–13, 2011.

[132] M. Kulmala, T. Vesala, and P.E. Wagner. An analytical expression for the rate of binary condensational particle growth: Comparison with numerical results. *Journal of Aerosol Science*, 23:133–136, 1992. Proceedings of the 1992 European Aerosol Conference.

[133] W. F. WELLS. On air-borne infection*: Study ii. droplets and droplet nuclei. *American Journal of Epidemiology*, 20(3):611–618, 11 1934.

[134] Roland R. Netz. Mechanisms of airborne infection via evaporating and sedimenting droplets produced by speaking. *The Journal of Physical Chemistry B*, 124(33):7093–7101, 2020. PMID: 32668904.

[135] R Peric and M Peric. *Journal of Applied Fluid Mechanics*, 13(06), November 2020.

[136] Majid Rezaei and Roland R. Netz. Water evaporation from solute-containing aerosol droplets: Effects of internal concentration and diffusivity profiles and onset of crust formation. *Physics of Fluids*, 33(9):091901, 09 2021.

[137] A. J. Archer, B. D. Goddard, and R. Roth. Stability of nanoparticle laden aerosol liquid droplets. *J. Chem. Phys.*, 159(19):194503, 11 2023.

[138] Andrea Fortini, Ignacio Martín-Fabiani, Jennifer Lesage De La Haye, Pierre-Yves Dugas, Muriel Lansalot, Franck D'Agosto, Elodie Bourgeat-Lami, Joseph L Keddie, and Richard P Sear. Dynamic stratification in drying films of colloidal mixtures. *Phys. Rev. Lett.*, 116(11):118301, 2016.

[139] Boshen He, Ignacio Martín-Fabiani, Roland Roth, Gyula I Tóth, and Andrew J Archer. Dynamical density functional theory for the drying and stratification of binary colloidal dispersions. *Langmuir*, 37(4):1399–1409, 2021.

[140] Mayukh Kundu and Michael P Howard. Dynamic density functional theory for drying colloidal suspensions: Comparison of hard-sphere free-energy functionals. *J. Chem. Phys.*, 157(18):184904, 2022.

[141] D. J. Lee, M. M. Telo da Gama, and Keith E. Gubbins. Adsorption and surface tension reduction at the vapor-liquid interface. *J. Chem. Phys.*, 89(8):1514–1519, 1985.

[142] K. Abe and K. Koga. Local solubility of nonpolar molecules in the liquid–vapor interfaces of water and simple liquids. *Journal of Molecular Liquids*, 200:7–11, 2014. Proceedings of the 7th Mini-Symposium on Liquids "Liquid-Liquid Phase Separation and Related Topics on Liquids".

[143] Zhidong Li and Jianzhong Wu. Toward a quantitative theory of ultrasmall liquid droplets and vapor—liquid nucleation. *Industrial & Engineering Chemistry Research*, 47(15):4988–4995, 2008.

[144] Xiao Jin, Ruijin Wang, Lizhong Huang, and Chun Shao. The morphology of dryout nanofluid droplet and underlying mechanisms based on coarse-grained molecular dynamic simulations. *Journal of Molecular Liquids*, 383:122064, 2023.

[145] Lingxiao Zhan, Heng Chen, Hao Zhou, Qianyuan Feng, Liyan Gu, Linjun Yang, and Zongkang Sun. Molecular dynamics study on evaporation of high-salinity wastewater droplet. *Applied Thermal Engineering*, 213:118752, 2022.

[146] Xin Li, Thomas Hede, Yaoquan Tu, Caroline Leck, and Hans Ågren. Cloud droplet activation mechanisms of amino acid aerosol particles: insight from molecular dynamics simulations. *Tellus B: Chemical and Physical Meteorology*, 65(1):20476, 2013.

[147] Weikang Chen, Joel Koplik, and Ilona Kretzschmar. Molecular dynamics simulations of the evaporation of particle-laden droplets. *Phys. Rev. E*, 87(5):052404, 2013.

[148] F. J. Martínez-Ruiz and F. J. Blas. Interfacial properties of binary mixtures of square-well molecules from monte carlo simulation. *J. Chem. Phys.*, 144(15):154705, 04 2016.

[149] D. M. Heyes and. Partial coordination numbers of square-well binary fluid mixtures. *Physics and Chemistry of Liquids*, 24(4):205–221, 1992.

[150] Kin-Chue Ng. Hypernetted chain solutions for the classical one-component plasma up to γ=7000. *J. Chem. Phys.*, 61(7):2680–2689, 10 1974.

[151] R Evans, J R Henderson, D C Hoyle, A O Parry, and Z A Sabeur. Asymptotic decay of liquid structure: oscillatory liquid-vapour density profiles and the fisher-widom line. *Mol. Phys.*, 80(4):755–775, 1993.

[152] JM Brader, R Evans, Matthias Schmidt, and H Löwen. Entropic wetting and the fluid-fluidinterface of a model colloid-polymer mixture. *J. Phys.: Condens. Matter*, 14(1):L1, 2001.